The Giant Antamina Deposit, Peru: Intrusive Sequence, Skarn Formation, and Mineralisation

Thesis submitted by

Stephanie A. Mrozek, M.Sc.

June 2018

For the Degree of Doctor of Philosophy
College of Science, Technology, and Engineering
James Cook University

Statement of Access

I, the undersigned author of this thesis, understand that James Cook University will make this thesis available for use within the university library and allow access in other approved libraries after its submission. All users consulting this thesis will have to sign the following statement:

> *In consulting this thesis I agree not to copy or closely paraphrase it in whole or in part without the written consent of the author, and to make proper public written acknowledgement for any assistance which have obtained from it.*

Beyond this, I do not wish to place any restrictions on access to this thesis.

Stephanie A. Mrozek

June 2018

Declaration

I declare that this thesis is my own work and has not been submitted in any form for another degree or diploma at any university or other institute or tertiary education. Information derived from the published or unpublished work of others has been acknowledged in the text and a list of references is given.

Stephanie A. Mrozek

June 2018

Statement of Contribution by Others

Nature of Assistance	Contribution	Names, Titles, and Affiliations of Co-Contributors
Intellectual Support	Proposal writing	Zhaoshan Chang (JCU)
	Data analysis	Zhaoshan Chang (JCU) Carl Spandler (JCU) Larry Meinert (US Geological Survey) Robert Holm (JCU)
	Editorial assistance	Zhaoshan Chang (JCU) Carl Spandler (JCU) Robert Holm (JCU)
Financial Support	Field Research	Compañía Minera Antamina
	Stipend	JCU International Postgraduate Research Award
	Research funding	Compañía Minera Antamina Society of Economic Geologists JCU SEES/CSTE
Data Collection	Research assistance	Shane Askew (JCU) Kevin Blake (JCU) Robert Creaser (University of Alberta) Richard Friedman (University of British Columbia) Chris Hall (University of Michigan) Yi Hu (JCU) Craig Johnson (US Geological Survey) Brendan Jones (JCU) Sebastien Meffre (University of Tasmania) Paul O'Sullivan (GeoSep Services) Peter Reiners (University of Arizona) Jay Thompson (University of Tasmania) Stuart Thomson (University of Arizona)

Acknowledgements

First and foremost, I thank my primary advisor, Zhaoshan Chang, for accepting me into the PhD program and for providing me with an unparalleled opportunity to live in tropical Queensland Australia whilst conducting research on Antamina in the high Andes of Peru. It would be an understatement to say that this opportunity has been life-changing. I owe a debt of gratitude for your generosity over the years; I don't know how I can ever repay you, though I suspect one way will be with published papers. Also, thank you Joy, for the kindest hospitality and so many delicious meals!

My sincerest appreciation is extended to Carl Spandler for always making time to discuss my research, for providing critical and insightful feedback, for strategising with me on solutions to every problem, and for always having my back through challenging times. Thank you, Carl!

I thank Larry Meinert for spending time with me in the field and for readily responding to every email request across the time zones, whether it was for decades-old data or a letter of reference. Cheers, Larry!

I thank Rob Holm for stepping up as an unofficial member of my advisory panel, for having an open door, creating some very helpful spreadsheets, showing me how to use Glitter and Isoplot many times, teaching me about U-Pb geochronology, and for being so patient and chill in every situation.

This project would not have been possible without the initiative of Steve Windle. Steve, I thank you for facilitating every aspect of my field work and for your gracious hospitality in Lima. I thank the Antamina geology crew, especially Cesar Raraz, Alberto Paz, Christian Mendoza, and David "Crazy" Paredes, for making me feel like a part of the team, spending time with me in the field, and being patient with my Spanglish. Esto es el "fin del huevo"…you guys Rock!

I am grateful to the CSE staff, especially: Judy, for clearing many administrative obstacles from my path; Melissa Crawford, for keeping it real and introducing me to fairy bread; Alaina, for always being a shining sun; and Bec Steele for bloody everything from pep talks, to eliminating paperwork, to wine. I thank the AAC staff, including Kevin, Shane, and Yi, for reliable, and sometimes spirited, analytical assistance.

Thanks to my geology mates, especially George, Jaime, Michael, Isaac, Gautier, Fredrik, Helge, Teimoor, Babo, Christa, Erin, and Jelle, for coffee and cathartic rant sessions. Thanks to my best mates, Astrid, Sophie, and Selma, for hours (days? possibly weeks?) of listening, talking, laughing, crying, and solving the seemingly big problems of our little worlds. You ladies are simply the best! x

Sincere gratitude is extended to The Society of Economic Geologists (SEG) for supporting me and my research through my MSc and PhD. Outside of my research, the SEG created many unique opportunities to attend conferences and field trips, and to interact with the brightest minds in my field. I look forward to serving the Society through research and mentorship for many years to come.

Before this project, a number of inspirational teachers and mentors helped me find my niche in geology. I thank Mr. Young, my highschool geography teacher, for adding a bit of geology to the curriculum by teaching about landforms and the rock cycle. Drs. Brenda Buck, Andrew Hanson, and Ben Dattilo, my undergraduate advisors, provided me with my first geological research experiences in pedology, sedimentology, and paleontology – as it turned out, I prefer altered rocks! Dr. Rainer Newberry, my MSc advisor and a true rockstar, introduced me to my first skarn in the Yukon 10 years ago. They called it "the next Antamina", and although it was not, it proved to be a solid stepping stone to the actual Antamina.

The time invested in this project amounts to almost 5 years of my life; it is difficult to capture the essence of this experience in just a few words. Australia is such an amazing place and I am grateful to many people for indirectly contributing to this work in the form of exceptional generosity and motivation during difficult times. I thank Tatjana for providing me with a soft landing in Townsville. I am grateful to Nicky Knoff for teaching me how to have lots of spine and lots of heart ("what's it going to take?"). Thank you to Dr. Chris Ball for keeping me in the game by treating my silly injuries with urgency and wit, and generally improving the quality of my life. Townsville was a great place to paddle an outrigger canoe or sail a Pacer on Sunday mornings – the coaches and crews reset my sanity and opened my eyes to another dimension of life in this beautiful part of the world.

It is unlikely that I would have even known about this project in the first place if it were not for my partner, friend, and colleague, Carlos, who introduced me to Zhaoshan and got the skarn conversation started at the SEG conference in Lima, Peru (2012). I cannot thank you enough, Carlos, for encouraging me to be brave and for believing in me when I doubted myself. I would not, and could not, have done this without your love and support.

Finally, from the bottom of my heart I thank, my parents and my sister, for cheering me on from the other side of the world, for visiting me, for phone calls, care packages, for asking about my work and then patiently listening to me talk about about endoskarns and exoskarns. I know you are proud of me, even if you have no idea what I have been talking about most of the time. Thank you for always encouraging me to pursue my dreams to the ends of the earth. There has been nothing more comforting than knowing I have your love and support, whether near or far.

Abstract

The Antamina Cu-Zn skarn, in the central Andes of Peru, is the largest skarn in the world with resources of ~2,968 Mt averaging 0.89% Cu, 0.77% Zn, 11 g/t Ag and 0.02% Mo as of 2015. The deposit measures ~2.5 km long by ~1.5 km wide with a vertical extension > 2.2 km and remains open at depth. The host rocks are structurally stacked limestones and marls of the Cretaceous Jumasha and Celendín formations. Skarn and mineralisation occur in and around the Antamina Porphyry Complex (APC), which consists of 4 porphyry centres emplaced between 10.95 ± 0.20 Ma and 10.24 ± 0.23 Ma (U-Pb zircon). The core of the main ore zone is composed of 3 contiguous porphyry centres (Oscarina, Taco-Bornita, Usupallares) oriented lengthwise from NE to SW; the fourth centre (Condorcocha) is located ~1 km north of Taco. This study combines field observations of cross-cutting relationships with U-Pb (zircon) and Re-Os (molybdenite) geochronology into a spatio-temporal model that explains how Antamina became a giant ore deposit.

At least 11 intrusive phases were identified at the Antamina deposit. The major porphyry phases documented in each intrusive centre at Antamina are classified as P1 (early), P2 (inter-mineralisation), and P3 (late inter-mineralisation). Sub-phases are denoted in alphabetical order as P2a, P2b, etc. General characteristics of the major phases are as follows: P1 is the causative skarn-forming intrusion in each porphyry centre. P1 ages range from 10.95 ± 0.20 Ma (Taco) to 10.24 ± 0.23 Ma (Usupallares). Endoskarn and exoskarn are genetically related to P1 porphyries. Stockwork quartz veins (≤ 40% volume) and hydrothermal biotite (potassic alteration) are locally abundant in the central porphyry complex. P2 intrusions cut P1 intrusions, related skarns, and early quartz veins. Quartz stockwork veins (± pyrite ± chalcopyrite ± molybdenite) extend outward from P2 porphyries and cross-cut P1 skarns. Locally, P2 contains xenoliths (up to several m long) of P1 exoskarn, P1 endoskarn, and refractory quartz vein fragments. P3 cross-cuts P1, P2, and early veins. Neither P2 nor P3 contain endoskarn alteration, although they do contain veins and disseminations of secondary biotite overprinted by sericite-chlorite alteration.

Molybdenite mineralisation occurs in two stages across the Taco-Bornita and Usupallares zones. Stage I molybdenite occurs in skarns; Re-Os ages include 10.58 ± 0.07 Ma and 10.44 ± 0.05 to 10.39 ± 0.05 Ma. Stage II molybdenite + quartz veins cut across P2 and P3 porphyries and Re-Os ages include 9.99 ± 0.04 and 9.68 ± 0.05 Ma. In general, U-Pb zircon and Re-Os molybdenite

ages decrease from northeast to southwest along the structurally-controlled axis of the deposit. Together, these ages constrain the duration of magmatic-hydrothermal activity at Antamina to ~1.1 Ma.

The skarns formed in sequence with porphyry emplacement, then coalesced to form a continuous body of skarn that comprises the giant Antamina deposit. Systematic patterns of alteration and mineralisation are centred on the multi-phase porphyry centre; outward from this centre, alteration consists of hydrothermal biotite (i.e., potassic alteration) transitioning into endoskarn, exoskarn, bleached marble, and fluid escape structures in the most distal reaches of the deposit. Skarn garnet colour changes from pink to red to brown in endoskarn and from red to brown and green (from proximal to distal) in exoskarn. Garnet becomes more andradite-rich and grossularite-poor from proximal to distal skarns, and clinopyroxene becomes more hedenbergite-rich and diopside-poor along the same trend. Mineralisation and metal zoning shows an outward progression from Mo ± Cu in the central porphyry, to Cu (± Ag, Bi)-Zn-Pb from proximal to distal exoskarns. The ore mineralogy is dominated by molybdenite, chalcopyrite, bornite, and sphalerite with lesser galena and minor Bi-Ag-S minerals. Fluid inclusions in a unidirectional solidification texture (UST) sample consist of four types assigned to primary and secondary assemblages. Primary inclusions are highly saline with liquid-vapour-solid phases and contain up to 5 translucent daughters plus a triangular opaque daughter. Secondary inclusions display variable proportions of liquid-vapour-solid phases, and are generally less saline and more vapour-rich than primary inclusions. Primary inclusions homogenise by halite disappearance, whereas secondary inclusions homogenise to the liquid state. Lithostatic pressure estimates from primary fluid inclusions range from 1.2 to 0.95 kbar, which equates to formation depth range from ~4.6 to 3.5 km.

The formation of the giant Antamina skarn deposit is attributed to the emplacement of multiple fertile porphyries along a NE-trending fault zone into reactive wall rocks between 10.95 ± 0.20 Ma (oldest U-Pb zircon age) and 9.68 ± 0.05 Ma (youngest Re-Os molybdenite age). Miocene surface uplift (on the order of 3.5 km), coupled with Pleistocene glaciation, exposed the top of the deposit, preserving the ore body at a favourable erosional level.

Table of Contents

List of Tables

List of Figures

List of Appendix Tables

List of Appendix Figures

Contents of Digital Appendices

Chapter 2

2.1. Whole rock geochemical methods and detection limits
2.2. Whole rock data
2.3. Total organic carbon analyses
2.4. Isocon data and worksheets

Chapter 3

3.1. U-Pb LA-ICP-MS zircon dating results
3.2. U-Pb LA-ICP-MS titanite dating results
3.3. U-Pb CA-TIMS zircon dating results
3.4. $^{40}Ar/^{39}Ar$ step heating data
3.5. WDS microprobe results for biotite
3.6. WDS microprobe results for plagioclase
3.7. Whole rock data for igneous samples

Chapter 4

4.1. WDS microprobe data for skarn and alteration minerals
4.2. Sulphur isotope data
4.3. Fluid inclusion physical properties and microthermometry results

Chapter 1:
Introduction

1.1. Thesis Structure

It is intended that the contents of this thesis will be published in internationally recognized, peer reviewed earth science journals. At the time of thesis submission, Chapter 2 has been accepted (pending minor revisions) to the journal Economic Geology. The remaining chapters have been written in a traditional monograph style; their contents will be combined into additional papers that will highlight the scientific contributions of this study. The chapters are stand-alone bodies of work that are related to the central theme of the thesis: resolving the intrusive sequence and its relationship to skarn formation at the giant Antamina deposit, Peru. There is minor repetition between chapter introductions, methods, and discussion topics (when necessary), but the results for each chapter are unique. Chapter 1 provides an introduction to the geology of Antamina from the regional to deposit scale, summarising the work of previous researchers. Chapter 2 presents new compositional data and discrimination diagrams for the host rocks and a method for quantifying mass changes during skarn formation. Chapter 3 presents new observations on the intrusive sequence and its relationship to skarn formation. New geochronology results from U-Pb zircon, Re-Os molybdenite, and $^{40}Ar/^{39}Ar$ biotite are presented in the context of the intrusive sequence. Chapter 4 presents the mineralisation and alteration paragenetic sequence, as well as mineral chemistry, and applies these to understanding deposit-scale zonation trends. Fluid inclusion results are used to estimate the pressure and depth of deposit formation. These results are interpreted in the context of previous work on the uplift history of the central Andes of Peru. Chapter 5 presents a summary of the work and some recommendations for future study. Each chapter contains a list of references and an appendix of A4-formatted tables and/or figures; larger format appendices are included in the digital supplement, as noted in the text.

1.2. Geological Setting of the Antamina Deposit

1.2.1. Tectonic Setting and Metallogeny

The Andes are a metallogenically diverse continental arc that hosts numerous world-class ore deposits along its tectonically-segmented length (Fig. 1.1). The Peruvian flat-slab segment is

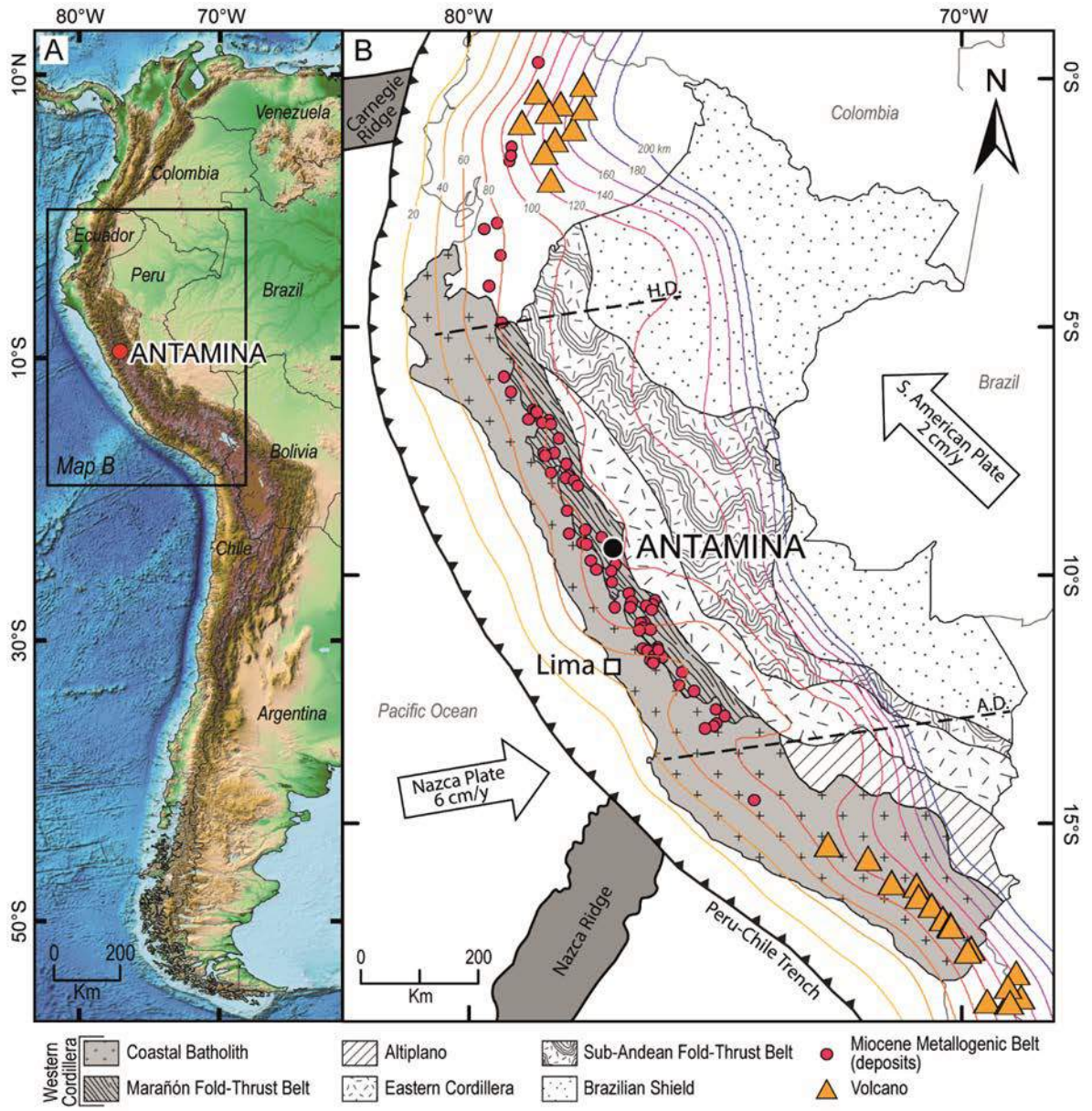

Fig. 1.1. Location and tectonic setting of the Antamina deposit, Peru. A. Global relief model of western South America showing the high topographic relief of the Andes and bathymetry of the western Nazca Plate (Amante and Eakins, 2009). B. Tectonic-magmatic-metallogenic domains of Peru. Antamina is located in the Marañón Fold-Thrust Belt (MFTB) of the Western Cordillera. The MFTB roughly corresponds with the Miocene Metallogenic Belt (Noble and McKee, 1999; Table A1.1), a volcanic gap (Table A1.2), and the Peruvian flat-slab zone, as indicated by Wadati-Benioff contours (Ramos and Folguera, 2009). Plate motion vectors are from Schellart et al. (2007). The Abancay deflection (A.D.) and Huancabamba deflection (H.D.) are indicated with dashed lines (see text for detail). Panel B modified after Myers (1975) and Scherrenberg et al. (2016).

one such example that hosts a > 900 km zone of mineralisation known as the Miocene metallogenic belt (MMB; Noble and McKee, 1999; Fig. 1.1). The MMB hosts a variety of base- and precious metal deposits with diverse mineralisation styles, including high-sulfidation epithermal Au-Ag (i.e., Yanacocha), porphyry-skarn Cu-Zn-Mo (i.e., Antamina), and carbonate replacement Zn-Pb-Ag-Cu (i.e., Cerro de Pasco), to name a few (Petersen, 1965; Noble and McKee, 1999; Bissig et al., 2008; Baumgartner et al., 2009; Laznicka, 2010; and Catchpole et al., 2015). This NNW-trending mineralized belt is roughly bounded by two major E-W shear zones, the Huancabamba deflection (5°S) and the Abancay deflection (14°S) (Sillitoe, 1988; Fig. 1.1). Based on the ages of these deposits, the timing of formation of the MMB corresponds with the mid-Miocene impingement of the Nazca Ridge bathymetric high in the Peru-Chile trench at between 15 and 5 Ma (Rosenbaum et al., 2005). This tectonic impingement resulted in shallowing of the Nazca plate subduction angle (Hu et al., 2016), a volcanic gap (McGeary et al., 1985), uplift of the central Peruvian Andes (McNulty and Farber, 2002; Ramos and Folguera, 2009), increased surface and tectonic erosion rates (von Huene and Lallemand, 1990; Gregory-Wodzicki, 2000; and Clift et al., 2003), and an increase in seismicity and deformation in the overriding plate (Rosenbaum and Mo, 2011; Fig. 1.1).

1.2.2. Regional Structure and Stratigraphy

Hydrothermal systems of the MMB are superimposed on the Marañón Fold-Thrust Belt (MFTB), a structurally and stratigraphically complex deformation zone between the Eastern Cordillera and Western Cordillera (Cordillera Blanca) in the central Peruvian Andes (Figs. 1.1 and 1.2). The lithology of the MFTB surrounding the Antamina district consists of Precambrian to Cambrian metamorphic basement rocks (Marañón Complex) overlain by Palaeozoic and Mesozoic shelf carbonates and clastic sedimentary rocks (Fig. 1.2), which record at least two marine transgressions related to early tectonism in the Andes (Love et al., 2004). This stratigraphic sequence is dominated by carbonate-rich units including the Permian Mitu Group, the Triassic-Jurassic Pucara Group, and Chicama Formation; and the Cretaceous Oyón Formation, Goyllarisquizga Group, Pariahuanca Formation, Jumasha Formation, and Celendín Formation (Fig. 1.2). Locally, these rocks host Eocene and Miocene intrusions and mineral deposits, and are sometimes capped by Miocene volcanic rocks (Fig. 1.2).

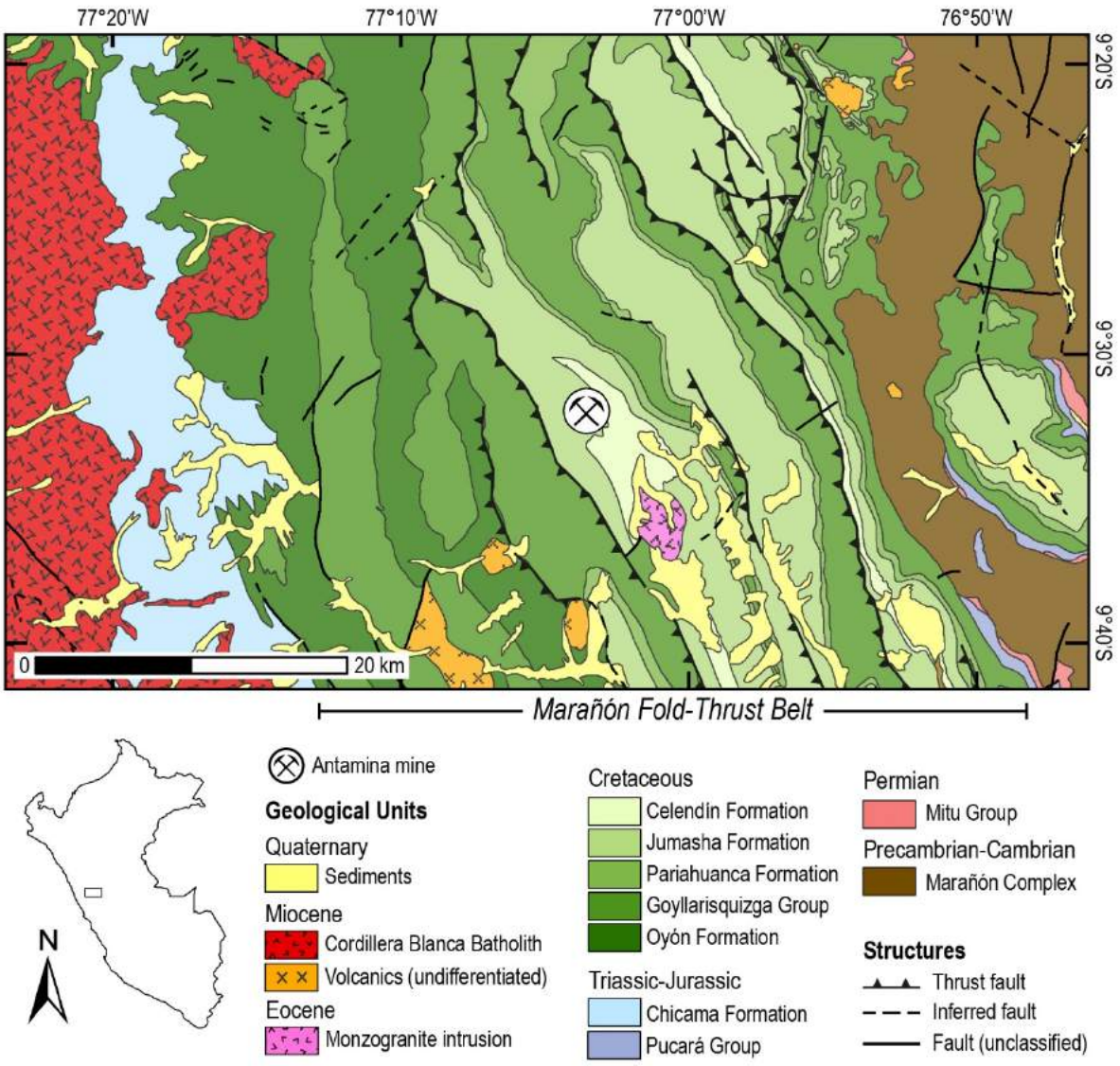

Fig. 1.2. Regional geological map showing the structural and stratigraphic setting of the Antamina deposit in the MFTB, modified after Wilson et al. (1967), Cobbing et al. (1996), and Jacay (1996).

East-vergent, compressional deformation of this stratigraphic package has taken place in at least five orogenic pulses since the late Cretaceous. Locally evident compressional events include the late Cretaceous Peruvian orogeny (Benavides-Cáceres, 1999), the Eocene Incaic orogenies (Noble et al., 1990; Benavides-Cáceres, 1999; Noble and McKee, 1999), and the Miocene Quechua I, II, and III orogenies (Benavides-Cáceres, 1999; Noble and McKee, 1999). During each orogenic period, compressional stress was accommodated through thick- and thin-skinned deformation (Scherrenberg et al., 2016). During the Miocene, interludes of local extension and transpression caused reactivation along some basement structures (associated with thick-skinned deformation), and facilitated an increase in magmatic-

hydrothermal activity at shallow crustal levels throughout the MFTB (Scherrenberg et al., 2016).

The folds and thrust faults that formed during these compressional events are evident at the district scale. Fig. 1.3 shows a carbonate-dominant stratigraphic package that has been folded into broad, NW-trending, syncline-anticline folds; these are cut across by sub-parallel thrust faults, which are cut across by transverse extensional faults; the Antamina deposit is situated at the junction between the Antamina anticline and a transverse fault.

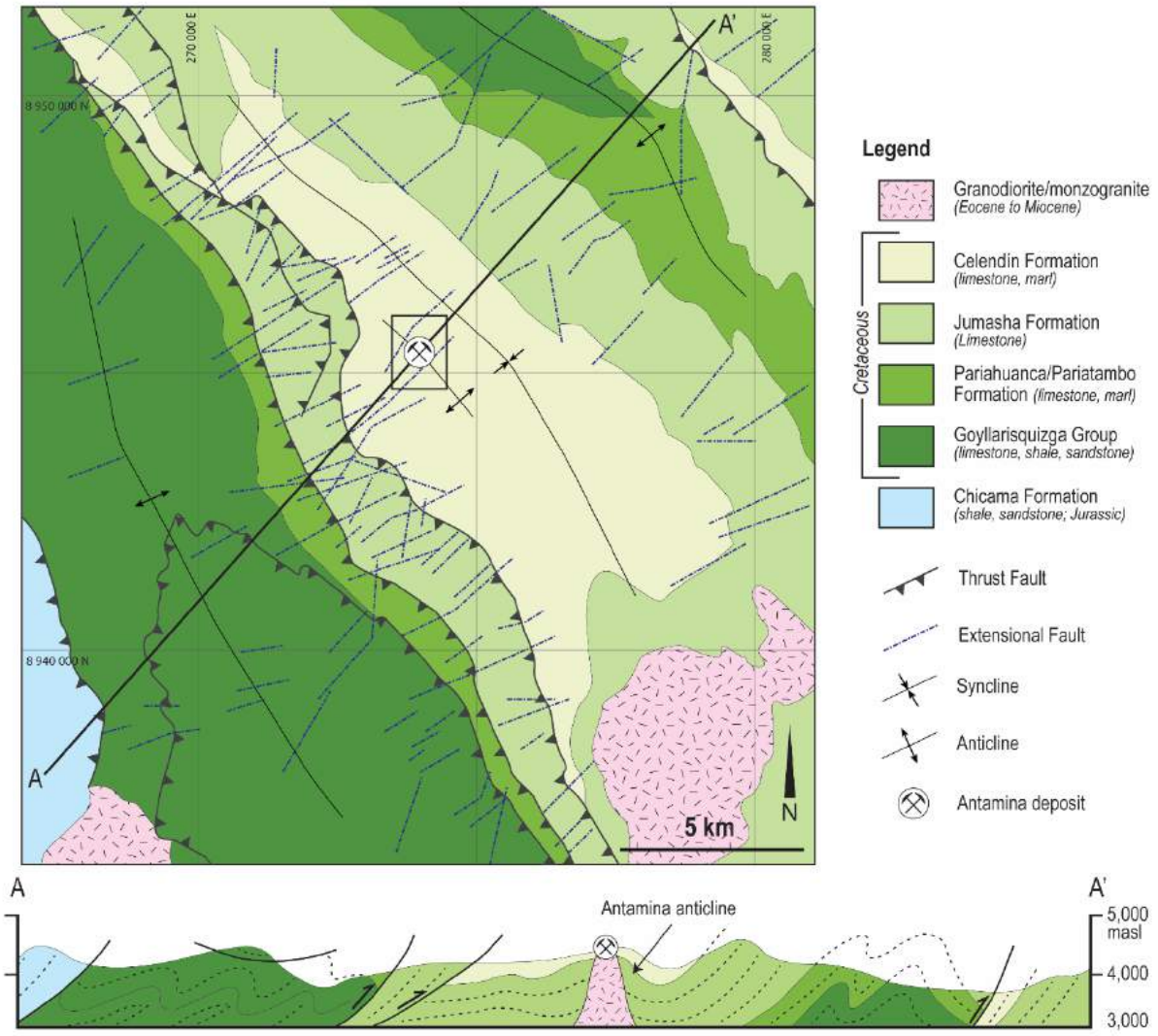

Fig. 1.3. District-scale geological map and cross section. Geology after Goodman (2012).

1.3. Deposit Geology

1.3.1. Host Rocks

Antamina is hosted in the transition zone between the middle Cretaceous Jumasha Formation and the Upper Cretaceous Celendín Formation. The Jumasha Formation consists predominantly of limestone and marly limestone, whereas the Celendín Formation is dominated by marl, shale, and lesser limestone (Benavides-Cáceres, 1956; Escalante et al., 2010). Both units are exposed in the vicinity of the mine, however precise location of the contact is not confidently known due to compositional similarities, local structural thickening (i.e., Jumasha Formation thrust atop the Celendín Formation) and the absence of fossil marker beds (Love et al., 2004; Redwood, 2004). Extensive contact metamorphism and pervasive metasomatic overprinting compound the problem of estimating true unit thickness and extent of these formations around the deposit.

1.3.2. Structure

The geometry of the Antamina deposit is largely controlled by the Valley Fault (VF) system (Love et al., 2003), also shown on some maps as the Valley Lateral Ramp (Hathaway, 1997;

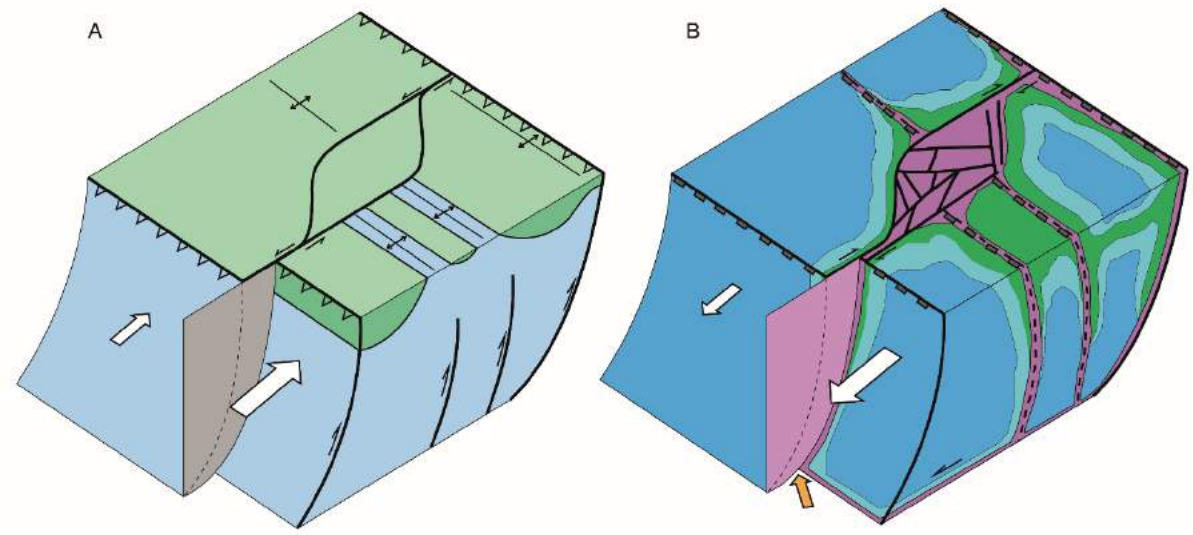

Fig. 1.4. Structure block diagram of the Antamina deposit. A. Structural preparation for the Antamina deposit includes subvertical faults and a dilational zone along the Valley Fault (VF). Arrows indicate stronger compression on the SE side of the Valley Lateral Ramp during the Quechua II orogeny. B. Dilation in the VF system controls the location of the Antamina porphyry complex, as well as skarn alteration and dykes (which exploit blind thrust faults, as shown in A). Modified after McCuaig (2003).

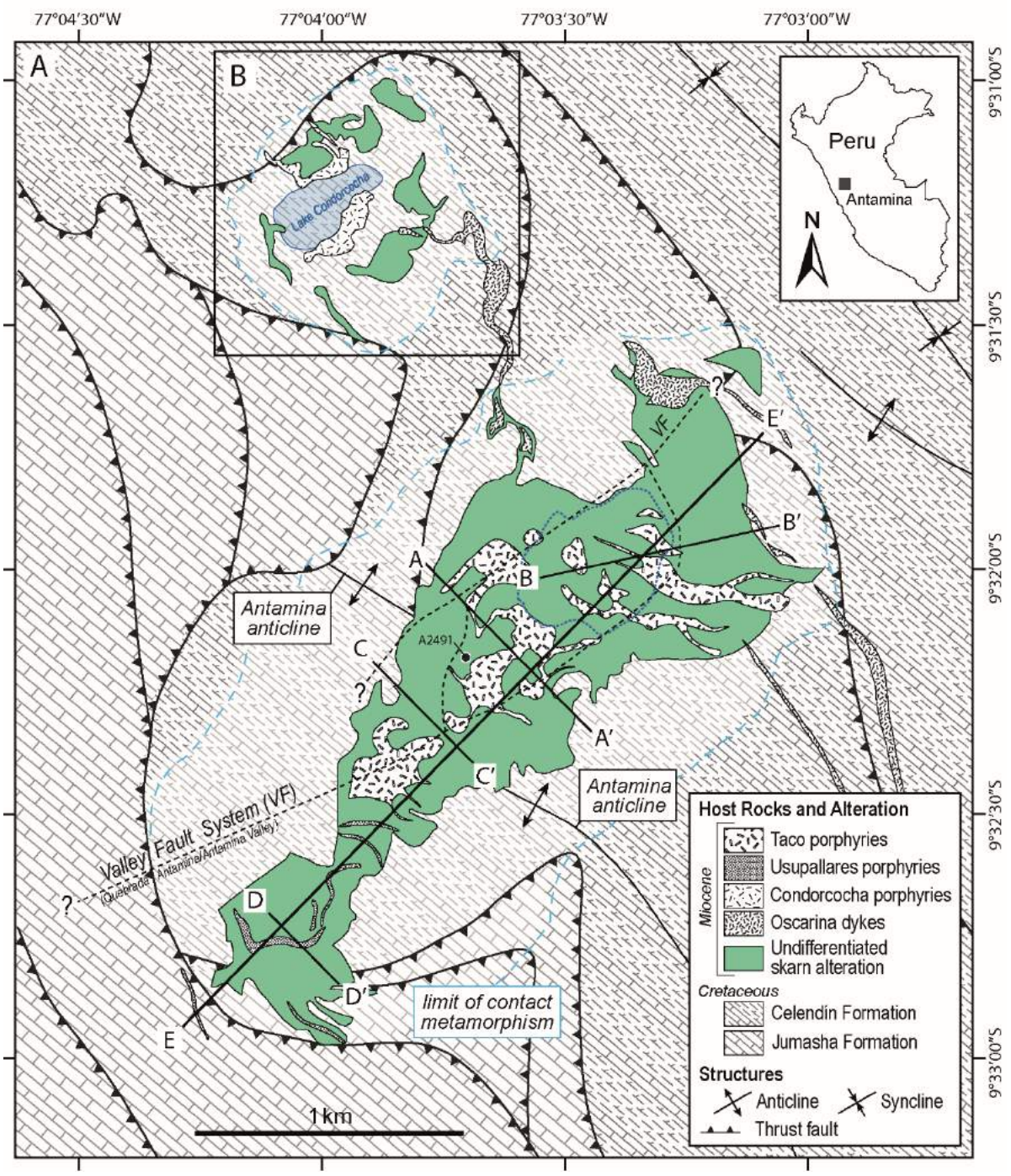

Fig. 1.5. Geological map of the Antamina deposit, Peru. Lithological and structural setting modified after Redwood (2004) and Escalante et al. (2010). Undifferentiated skarns include endoskarn and exoskarn. Cross sections are as follows: Taco (A-A'), Taco-Oscarina (B-B'), Bornita (C-C'), Usupallares (D-D'), and Antamina (long section, E-E'). Refer to text for details on each cross section.

McCuaig, 2003; Lipten and Smith, 2005), or as an unnamed lineament along the axis of Quebrada Antamina (i.e., the Antamina valley; Glover, 1997; Fig. 1.4). The VF system is a NE-striking, sub-vertical fault zone that defines the trend of the Antamina Valley (Figs. 1.4 and 1.5). Evidence for the structure stems from the apparent dextral offset of folds (i.e., the Antamina Anticline; Fig. 1.5) and thrust faults across the Antamina Valley (Love et al., 2003; McCuaig, 2003), although the main VF corridor has been largely overprinted by intense magmatic-hydrothermal activity in the centre of the deposit (Figs. 1.4 and 1.5). Love et al. (2003) and McCuaig (2003) suggest that the VF acted as a transfer fault or lateral ramp to partition strain across the axis of the deposit. The VF is thought to have formed in response to regional compression during the Quechua II orogeny (~10-9 Ma; Noble and McKee, 1999; Richards, 2003). A transpressional regime following the Quechua II orogeny caused dilation along the VF, which allowed magma and hydrothermal fluids to exploit the existing structural framework (McCuaig, 2003). The majority of the economic resource at Antamina is hosted in the zone of maximum dilation along the VF (Figs. 1.4 and 1.5). Northeast and southwest of this zone, the deposit narrows, both due to tapering of the VF and the greater structural influence of southwest-striking thrust faults (approximately normal to the VF) on intrusion geometry (McCuaig, 2003; Figs. 1.4 and 1.5).

1.3.3. Igneous Rocks

The Antamina Porphyry Complex (APC) is the name I have assigned to the multi-phase porphyry centre of the Antamina deposit (Taco and Usupallares porphyries; Fig. 1.5). In plan view, the APC is surrounded by skarns for up to 3 km by 1.5 km, with its long dimension oriented northeast along the axis of the Valley Fault (Fig. 1.5). Within the APC, two magmatic-hydrothermal centres have been documented in detail (this study): the Taco zone and the Usupallares zone (Fig. 1.5). The Taco zone occupies the northeast and central portions of the APC, while the Usupallares zone occupies the smaller southwest portion (Fig. 1.5). Two additional porphyry centres are included for comparison with the APC: the Condorcocha zone is a separate porphyry-skarn centre located approximately 1 km north of the Taco zone (Fig. 1.5), and the Oscarina dykes intersect the Taco and Condorcocha zones along their northeast margins (Fig. 1.5).

1.4. References

Amante, C., and Eakins, B.W., 2009, ETOPO1 1 arc-minute global relief model: procedures, data sources, and analysis: NOAA Technical Memorandum NESDIS NGDC-24. National Geophysical Data Center, NOAA. doi: 10.7289/V5C8276M.

Baumgartner, R., Fontboté, L., Spikings, R., Ovtcharova, M., Schaltegger, U., Schneider, J., Page, L., and Gutjahr, M., 2009, Bracketing the age of magmatic-hydrothermal activity at the Cerro de Pasco epithermal polymetallic deposit, central Peru: A U-Pb and $^{40}Ar/^{39}Ar$ study: Economic Geology, v. 104, p. 479-504.

Benavides-Cáceres, V., 1999, Orogenic evolution of the Peruvian Andes: The Andean Cycle: Society of Economic Geologists Special Publication 7, Chapter 3, p. 61-107.

Bissig, T., and Tosdal, R.M., 2009, Petrogenetic and metallogenetic relationships in the Eastern Cordillera Occidental of central Peru: The Journal of Geology, v. 119, p. 499-518.

Catchpole, H., Kouzmanov, K., Bendezú, A., Ovtcharova, M., Spikings, R., Stein, H., and Fontboté, L., 2015, Timing of porphyry (Cu-Mo) and base metal (Zn-Pb-Ag-Cu) mineralisation in a magmatic-hydrothermal system – Morococha district, Peru: Mineralium Deposita, v. 50, p. 895-922.

Clift, P.D., Pecher, I., Kikiwski, N., and Hampel A., 2003, Tectonic erosion of the Peruvian forearc, Lima Basin, by subduction and Nazca Ridge collision: Tectonophysics, v. 22. doi: 10.1029/2002TC001386.

Cobbing, J., and Sánchez Fernandez, A.W., Martinez Valladares, W., and Zárate Olazabal, H., 1996, Geología de los cuadrángulos de Huaraz, Recuay, La Unión, Chiquián y Yanahuanca (Hojas: 20-h, 20-i, 20-j, 21-i, 21-j), Instituto Geológico, Minero y Metalúrgico (INGEMMET), Boletín A 76, 297 p. http://repositorio.ingemmet.gob.pe/handle/ingemmet/199

Escalante, A., Dipple, G.M., Barker, S.L.L., and Tosdal, R., 2010, Defining trace-element halos to skarn deposits hosted in heterogeneous carbonate rocks: Case study from Cu-Zn Antamina skarn deposit, Peru: Journal of Geochemical Exploration, v. 105, p. 117-136.

Glover, J.K., 1997, Structural and stratigraphic setting of the Antamina deposit: Preliminary evaluation, executive summary: Lima, Peru, Compañía Minera Antamina, unpublished report, 4 p.

Goodman, S., 2012, Structural geology in the vicinity of the Antamina Deposit, Ancash Region, Peru: internal report for Compañía Minera Antamina S.A., 55 p.

Gregory-Wodzicki, K.M., 2000, Uplift history of the central and northern Andes: a review: Geological Society of America Bulletin, v. 112, p. 1091-1105.

Hathaway, L.H., 1997, Geological surface mapping and structural interpretation at Antamina Peru: Internal Report for Compañía Minera Antamina S.A., 35 p.

Hu, J., Liu, L., Hermosillo, A., and Zhou, Q., 2016, Simulation of late Cenozoic South American flat-slab subduction using geodynamic models with data assimilation: Earth and Planetary Science Letters, v. 438. http://dx.doi.org/10.1016/j.epsl.2016.01.011.

Jacay, J., 1996, Geología del cuadrángulo Singa (Hoja: 19-j), Instituto Geológico, Minero y Metalúrgico (INGEMMET), Boletín A 67, 173 p. http://repositorio.ingemmet.gob.pe/handle/ingemmet/189

Laznicka, P., 2010, Giant Metallic Deposits: Future Sources of Industrial Metals, 2nd edition. Berlin, Springer-Verlag, 950 p.

Lipten, E.J., and Smith, S.W., 2005, The geology of the Antamina copper-zinc deposit, Peru, South America: in Porter, T.M. (Ed.), Super Porphyry Copper & Gold Deposits: A Global Perspective, PGC Publishing, Adelaide, Australia, v. 1, p. 189-204.

Love, D.A, Clark, A.H., and Glover, K.J., 2004, The Antamina deposit, Ancash, Peru: The stratigraphic and structural setting of a giant copper-zinc skarn: Economic Geology, v. 99, p. 887-916.

McCuaig, T.C., 2003, Structural review of the Antamina mine, Peru: internal report for Compañía Minera Antamina S.A., 48 p.

McGeary, S., Nur, A., Ben-Avraham, Z., 1985, Spatial gaps in arc volcanism: the effect of collision or subduction of oceanic plateaus: Tectonophyiscs, v. 119, p. 195-221.

McNulty, B.A., and Farber, D.L., 2002, Active detatchment faulting above the Peruvian flat slab: Geology, v. 30, p. 567-570.

Myers, J.S., 1975, Vertical crustal movements of the Andes in Peru: Nature, v. 254, p. 672-674.

Noble, D.C., McKee, E.H., Mourier, T., and Megard, F., 1990, Cenozoic stratigraphy, magmatic activity, compressive deformation, and uplift in northern Peru: Geological Society of America Bulletin, v. 102, p. 1105-1113.

Noble, D.C., and McKee, E.H., 1999, The Miocene Metallogenic Belt of Central and Northern Peru: Society of Economic Geologists Special Publication 7, Chapter 5, p. 155-193.

Petersen, U., 1965, Regional geology and major ore deposits of central Peru: Economic Geology, v. 60, p. 407-476.

Ramos, V.A., and Folguera, A., 2009, Andean flat-slab subduction through time, in Murphy J.B., Keppie, J.D., and Hynes, A.J (eds.): Ancient Orogens and Modern Analogues. Geological Society, London, Special Publications, v. 327, p. 31-54.

Redwood, S.D., 2004, Geology and development history of the Antamina copper-zinc skarn deposit, Peru: Society of Economic Geologists Special Publication 11, Ch. 14, p. 259-277.

Richards, J.P., 2003, Tectono-magmatic precursors for porphyry Cu-(Mo-Au) deposit formation: Economic Geology, v. 98, p. 1515-1533.

Rosenbaum, G., Giles, D., Saxon, M., Betts, P.G., Weinberg, R.F., and Duboz, C., 2005, Subduction of the Nazca Ridge and the Inca Plateau: Insights into the formation of ore deposits in Peru: Earth and Planetary Science Letters, v. 239, p. 18-32.

Rosenbaum, R., and Mo, W., 2011, Tectonic and magmatic responses to the subduction of high bathymetric relief: Gondwana Research, v. 19, p. 571-582.

Schellart, W.P., Freeman, J., Stegman, D.R., Moresi, L., and May, D., 2007, Evolution and diversity of subduction zones controlled by slab width: Nature, v. 466, p. 308-311.

Scherrenberg, A.F., Kohn, B.P., Holcombe, R.J., and Rosenbaum, G., 2016, Thermotectonic history of the Marañón Fold-Thrust Belt, Peru: Insights into mineralisation in an evolving orogeny: Tectonophysics, v. 667, p. 16-36.

Sillitoe, R.H., 1988, Epochs of intrusion-related copper mineralisation in the Andes: Journal of South American Earth Sciences, v. 1, p. 89-108.

von Huene, R., and Lallemand, S., 1990, Tectonic erosion along the Japan and Peru convergent margins: Geological Society of America Bulletin, v. 102, p. 704-720.

Wilson, J., Reyes, L., and Garayar, J., 1967, Geología de los cuadrángulos de Mollebamba, Tayabamba, Huaylas, Pomabamba, Carhuaz y Huari (Hojas: 17-h, 17-i, 18-h, 18-i, 19-h, 19-i), Instituto Geológico, Minero y Metalúrgico (INGEMMET), Boletín A 16, 95 p. http://repositorio.ingemmet.gob.pe/handle/ingemmet/133.

1.5. Appendix

Table A1.1. Name and location of Miocene ore deposits shown in Fig. 1.1.

Name	Country	Lat.	Long.	Name	Country	Lat.	Long.
Junin	Ecuador	0.33	-78.58	Cerro de Pasco	Peru	-10.68	-76.27
Chaso Juan	Ecuador	-1.38	-79.12	Quicay	Peru	-10.70	-76.39
Telimbela	Ecuador	-1.57	-79.13	Iscay Cruz	Peru	-10.73	-76.71
Balzapamba-Las Guardias	Ecuador	-1.67	-79.15	Paraq	Peru	-10.73	-77.03
Chaucha	Ecuador	-2.93	-79.42	Colquijirca	Peru	-10.78	-76.27
Gaby-Papa Grande	Ecuador	-3.05	-79.68	Huaron	Peru	-11.03	-76.43
Fierro Urcu	Ecuador	-3.58	-79.33	Chungar	Peru	-11.05	-76.50
Rio Playas	Ecuador	-4.20	-79.58	Rio Pallanga	Peru	-11.15	-76.46
Rio Blanco	Peru	-4.94	-79.31	Carhuacayan	Peru	-11.18	-76.31
Canariaco	Peru	-6.04	-79.27	Santander	Peru	-11.19	-76.53
La Granja	Peru	-6.35	-79.13	Puy-Puy	Peru	-11.54	-76.15
Tantahuatay	Peru	-6.73	-78.68	Colqui	Peru	-11.57	-76.46
Hualgayoc	Peru	-6.75	-78.62	Morococha	Peru	-11.58	-76.18
Cerro Corona	Peru	-6.76	-78.61	Toromocho	Peru	-11.60	-76.13
Sipan	Peru	-6.92	-78.78	Venturosa	Peru	-11.62	-76.36
Minas Conga	Peru	-6.93	-78.36	Casapalca	Peru	-11.72	-76.22
Yanacocha	Peru	-6.99	-78.49	San Cristobal	Peru	-11.74	-76.05
El Galeno	Peru	-7.02	-78.32	Viso Aruri	Peru	-11.81	-76.30
Michiquillay	Peru	-7.30	-78.16	Millotingo	Peru	-11.82	-76.23
Sayapullo	Peru	-7.59	-78.47	Pacococha	Peru	-11.87	-76.25
Algamarca	Peru	-7.60	-78.24	Azulcocha	Peru	-12.05	-75.65
Igor	Peru	-7.65	-78.44	Yauricocha	Peru	-12.32	-75.72
El Toro	Peru	-7.82	-78.01	Cercapuquio	Peru	-12.43	-75.42
Quiruvilca	Peru	-7.99	-78.31	Huancavelica	Peru	-12.81	-74.97
Mundo Nuevo-Tamboras-Compaccha	Peru	-8.05	-77.97	Julcani	Peru	-12.93	-74.79
Angasmarca	Peru	-8.10	-78.01	Huachocolpa	Peru	-13.09	-74.96
Pasto Bueno	Peru	-8.15	-77.85	Palomo	Peru	-13.14	-75.02
Magistral	Peru	-8.27	-77.78	Castrovirreyna	Peru	-13.19	-75.20
Pashpap	Peru	-8.78	-77.99	Chalcobamba	Peru	-14.03	-72.33
Nueva California	Peru	-9.15	-77.63	Los Chancas	Peru	-14.16	-73.13
El Extrano	Peru	-9.23	-77.95	Cotabambas	Peru	-14.18	-72.35
Jacabamba	Peru	-9.31	-77.29	Constancia	Peru	-14.46	-71.77
Huarangayoc	Peru	-9.42	-77.68	Lahuani	Peru	-14.46	-72.99
Pierina	Peru	-9.45	-77.60	San Juan de Lucanas	Peru	-14.65	-74.19
Antamina	Peru	-9.53	-77.07	Tintaya	Peru	-14.91	-71.31
Ticapampa	Peru	-9.78	-77.52	Coroccohuayco	Peru	-14.95	-71.26
Huanzala	Peru	-9.86	-77.00	Antapaccay	Peru	-14.96	-71.35
Chururopampa	Peru	-9.98	-77.39	Quechua	Peru	-14.98	-71.31
Pachapaqui	Peru	-10.00	-77.09	Cuajone	Peru	-17.05	-70.71
Pacllon	Peru	-10.23	-77.07	Quellaveco	Peru	-17.11	-70.62
Raura	Peru	-10.44	-76.74	Queen Elizabeth	Chile	-19.87	-68.97
Atacocha-Milpo	Peru	-10.59	-76.21	Cerro Colorado	Chile	-20.04	-69.26
Uchucchacua	Peru	-10.62	-76.68	-	-	-	-

Data from Noble and McKee (1999).

Table A1.2. Name and location of active volcanoes shown in Fig. 1.1.

Name	Country	Latitude	Longitude
Reventader	Ecuador	-0.08	-77.67
Pichincha	Ecuador	-0.25	-78.60
Antizana	Ecuador	-0.48	-78.13
Sumaco	Ecuador	-0.57	-77.65
Cotopaxi	Ecuador	-0.63	-78.37
Quilotoa	Ecuador	-0.87	-78.92
Cumbal	Ecuador	-0.98	-77.88
Lunganate	Ecuador	-1.22	-78.25
Tungurahua	Ecuador	-1.47	-78.45
Sangay	Ecuador	-2.03	-78.33
Nevado Coropuna	Peru	-15.51	-72.70
Hualca-Gaulca	Peru	-15.80	-71.88
Vol. Misti	Peru	-16.30	-71.42
Ubinas	Peru	-16.35	-70.90
Omate	Peru	-16.58	-70.87
Ticsani	Peru	-16.76	-70.60
Tutupaca	Peru	-17.03	-70.37
Calientes	Peru	-17.15	-70.22
Yucamane	Peru	-17.18	-70.20
Nevado Chupiquina	Peru	-17.63	-69.80
Tacora	Peru	-17.68	-69.86
Nevado Sajama	Bolivia	-18.11	-68.88
Guallatiri	Bolivia	-18.41	-69.05
De Sacabaya	Bolivia	-18.61	-68.78
Cerro Tulapalca	Chile	-18.70	-69.47
Puquintica	Chile	-18.73	-69.01
Cerro Arintica	Chile	-18.73	-69.05
Isluga	Chile	-19.15	-68.83

Chapter 2:
Using whole rock geochemistry to evaluate element mobility and optimize skarn classification: An example from the Antamina deposit, Peru

Stephanie A. Mrozek[1], Zhaoshan Chang[1], Carl Spandler[1], Steve Windle[2,3], Cesar Raraz[2], Alberto Paz[2]

[1] EGRU (Economic Geology Research Centre) and Academic Group of Geosciences, James Cook University, Townsville, Queensland, 4811, Australia

[2]Compañía Minera Antamina, Av. El Derby #055, Surco, Lima, Peru

[3]Monazita SAC, Lima, Peru

Submitted to *Economic Geology*

2.1. Abstract

Distinguishing exoskarns from endoskarns can be problematic when textures are massive or mottled. In this study I assess the effectiveness of whole rock composition to distinguish massive exoskarn from endoskarn, using the Antamina skarn in Peru as an example. Whole rock data (up to 60 elements) were examined for 224 samples, including wall rocks (limestone, marl, marble, hornfels), intrusive rocks, and massive skarns. Cluster analysis was used to identify elements and elemental pairs that can distinguish wall rocks and intrusive rocks; these parameters were further tested for their capacity to distinguish massive exoskarns and endoskarns. Geochemical discriminators of skarn type include: TiO_2 vs. Y, HREE; Al_2O_3 vs. HREE, Y, Ni, and Sc, plus Al_2O_3 alone. Skarn samples plot as two non-overlapping data clusters defined by precursor; skarns plotting with the wall rock cluster are interpreted as exoskarns, while skarns plotting with the igneous cluster are interpreted as endoskarns. The process of identifying and applying these parameters, as I have done at Antamina, establishes a clear link between the skarns and their precursors. Antamina skarn samples previously logged by texture and garnet colour were re-evaluated using these geochemical parameters. I found that mottled skarn textures are not reliable for classification in the field, and classification by garnet colour must be used with caution. The effectiveness of the discriminating pairs identified in this study is likely due to the significantly different concentrations of these elements in the wall rocks versus igneous rocks, coupled with their immobility during skarn formation. Based on this immobility, isocon analysis reveals that both skarn types gained significant Fe_2O_3, MnO, MgO and base metals, and lost alkali elements Na_2O and K_2O. Exoskarn formation involves loss of volatiles and gain of SiO_2, whereas SiO_2 is lost and volatiles are gained during conversion of intrusive rock to endoskarn.

2.2. Introduction

The intensity of hydrothermal alteration during skarn formation can have a destructive effect on primary rock textures, rendering the rocks massive, ambiguous, and difficult to relate to a least-altered precursor. In mineralogically and geochemically zoned systems, such as skarns, successful exploration targeting relies heavily upon accurate classification of altered rocks, as zonation patterns can be used as vectors to ore (Newberry et al., 1991; Meinert, 1997; Meinert et al., 2005; and references therein). Understanding these patterns requires correct assumption of a precursor. In the field this is usually based on skarn texture and mineralogy, with highly interpretive results for the most altered samples. Where textures become unreliable, geochemistry can be used to examine the immobile element composition of a rock and establish a clearer link to its precursor, and hence, its significance in the skarn system.

Skarn formation is a metasomatic process driven by hydrothermal fluid-rock interaction. Skarns can replace both calcareous wall rocks and igneous rocks, forming exoskarns and endoskarns, respectively (Einaudi et al., 1981; Meinert et al., 2005). Both exoskarn and endoskarn occur as partial to massive replacements of wall rocks and igneous host rocks, however most skarns are dominated by exoskarn with only minor amounts of endoskarn (Meinert et al., 2005), because carbonate-rich wall rocks are more easily dissolved and replaced by acidic magmatic-hydrothermal fluids. More often than exoskarns, endoskarns retain residual patches of igneous rock, which provide an unambiguous link to the igneous precursor (Chang and Meinert, 2008a).

Endoskarn is an integral part of the skarn zoning pattern and accurate identification of endoskarn and exoskarn has important implications for exploration, mine geology, and metallurgy. Mineralogical zoning patterns around the causative intrusion are of the most important tools in skarn exploration (Meinert, 1997; Meinert et al., 2005; Chang and Meinert, 2008b). For mine geologists, the endoskarn-exoskarn contact marks a change in precursor, ore grade, and metal distribution, therefore accurate mapping of this contact can improve modelling of intrusion and orebody geometry and aid in ore zone prediction. For metallurgists, the contact can signify a change in ore hardness and grade, which can inform ore control procedures and optimize blending of ore types and metal recovery through the mill circuit.

Where endoskarn alteration is relatively weak, calc-silicate skarn minerals, such as garnet, clinopyroxene and wollastonite, occur in veins cutting intrusive rocks or as patchy replacements in intrusive rocks, e.g., at the Empire Zn-Cu skarn, Idaho (Chang and Meinert, 2008a). Such endoskarns are easy to recognise due to the presence of residual igneous textures. Where endoskarn development is strong and pervasive (i.e., proximal to the hydrothermal fluid source), calc-silicate veins coalesce into massive endoskarn and the igneous precursor texture is destroyed. Such endoskarns are difficult to distinguish from exoskarns, because both have similar mineralogy and lack residual precursor textures.

At Antamina, Peru (Fig. 2.1), some endoskarns occur distinctly as veins and patchy replacements in intrusive rocks, and some exoskarns (i.e., near the marble front) clearly inherit banded textures from layering in the wall rocks. In between there are extensive massive skarns, locally with mottled textures; this scenario provides an ideal location to test and develop tools to distinguish massive endoskarn and exoskarn. In this study, I use a suite of 224 samples from the Antamina deposit to demonstrate that geochemical discrimination of skarns, based on whole rock composition, is an effective way to distinguish massive endoskarn from exoskarn. Using the geochemical discriminators identified in this study, I re-examine the effectiveness of classifying the same skarn samples by texture and garnet colour, and I evaluate elemental loss and gain during skarn formation.

2.2.1. Geology of Antamina

Antamina is located approximately 270 km north of Lima, Peru, at 9°46’S, 77°06’W. It is the largest skarn deposit in the world, with a resource of ~2,968 Mt averaging 0.89% Cu, 0.77% Zn, 11 g/t Ag and 0.02% Mo (Glencore, 2015). The deposit is located in the Marañon Fold-Thrust Belt structural domain of the central Peruvian Andes, where it is hosted in a complexly deformed package of intercalated limestone, marl, and calcareous shale/siltstone assigned to the Cretaceous Jumasha and Celendín formations. Marble and calcareous hornfels are the inferred precursors to exoskarn at Antamina and they form the contact metamorphic halo that surrounds the deposit. Structural thickening, metamorphic recrystallization, and skarn alteration within the contact metamorphic halo make it difficult to confidently trace the stratigraphic contact between the two formations. Despite these complications, previous workers generally agree that the deposit is hosted in the transition zone between the Jumasha and Celendín formations (Love et al., 2004; Lipten and Smith, 2005; Escalante et al., 2010).

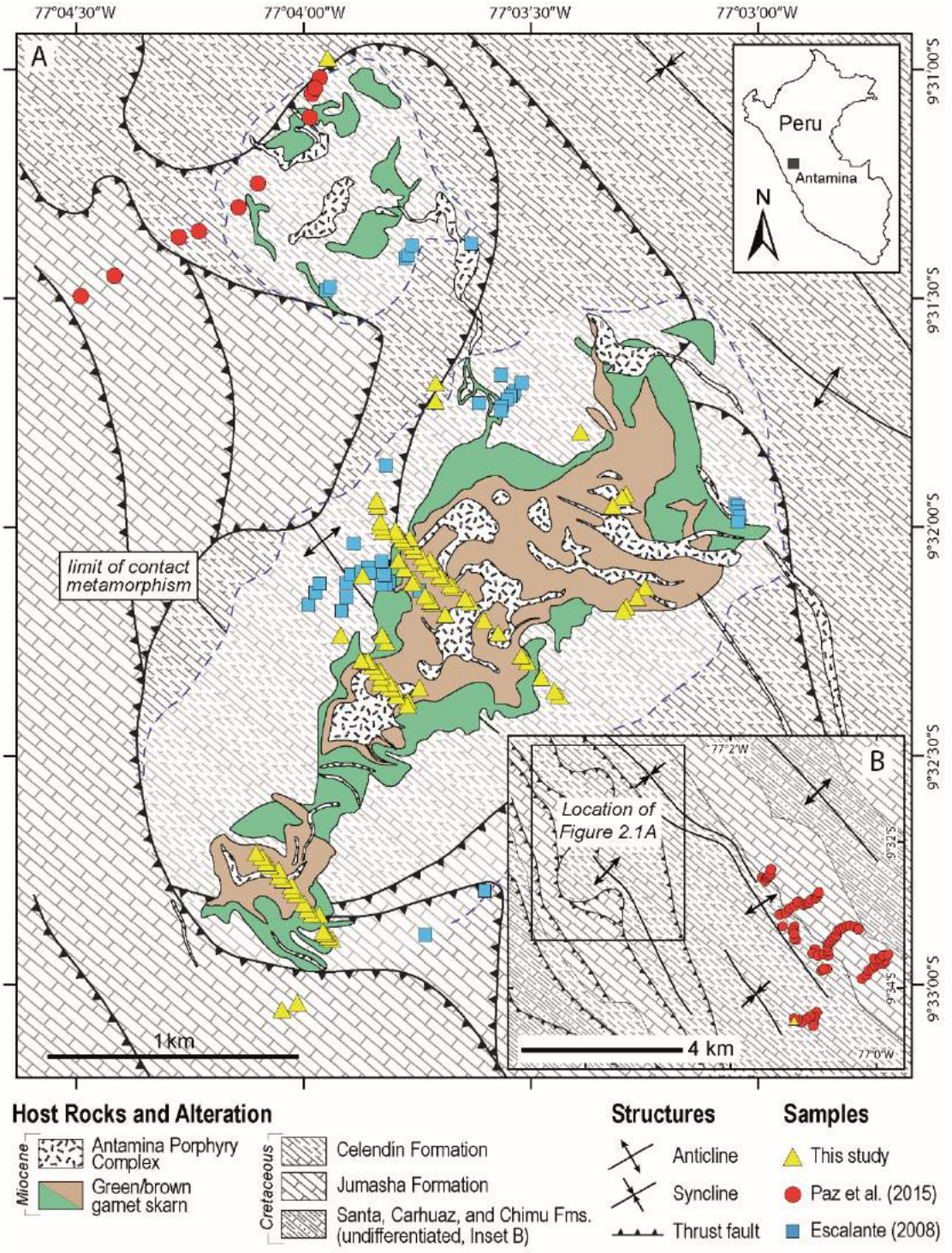

Fig. 2.1. Geological map of the Antamina deposit and district showing sample locations. The geology is modified after Redwood (2004) and Escalante et al. (2008, 2010). A. Near-mine sample distribution. B. District-scale sample distribution and location of near-mine samples shown in Figure 2.1A.

The Antamina orebody is centred on a Miocene (10.83 to 10.57 Ma; zircon U-Pb, Escalante et al., 2010) multi-phase porphyry intrusion complex, herein referred to as the Antamina Porphyry Complex (APC; Fig. 2.1). The APC comprises several intrusions, including early

and inter-mineral porphyries. All intrusive phases contain porphyry-style quartz stockworks and associated secondary biotite alteration, but only the early porphyries have endoskarn alteration along their margins (Mrozek et al., 2017). Early endoskarn and exoskarn are crosscut by later inter-mineral porphyries, indicating a complex intrusive history (Mrozek et al., 2017). Locally, epidote and chlorite alteration are common; however, a propylitic alteration zone is not well developed at Antamina. Evidence for hydrothermal alteration can be traced for up to approximately 1 km around the deposit based on trace element concentrations in fluid escape structures (Escalante et al., 2010). Hydrothermal activity continued until approximately 9 Ma, based on K-Ar ages of biotite and K-feldspar (McKee et al., 1979), and $^{40}Ar/^{39}Ar$ ages for hornblende, biotite, and sericite (Love et al., 2003).

Garnet is typically the dominant skarn mineral, indicating oxidized conditions of formation, although clinopyroxene-rich layers and lenses are locally common; these mineralogical heterogeneities are likely to be inherited from the host rocks. The skarn exhibits a well-developed garnet colour zonation from the APC outward to the marble front, which generally transitions from pink-red endoskarn to red-brown-green exoskarn (Lipten and Smith, 2005). All skarns are variably mineralized, with the general trend corresponding with proximal Cu-Mo to distal Zn-Pb. The principal ore minerals include chalcopyrite, sphalerite, and molybdenite, with localized bornite, galena, and lesser Bi-sulphides (Love et al., 2000). Late molybdenite-quartz-sericite veins cross-cut the APC and the surrounding skarns, including retrograde Cu-Zn skarn mineralisation (Love et al., 2000).

2.2.2. Characteristics of the Metasedimentary Wall Rocks

The host rocks have been subjected to at least 5 regional deformation events (Benavides-Cáceres, 1999; Ramos and Aleman, 2000), yet aside from intense fold-thrust development and localized contact metamorphism, the rocks have largely retained their sedimentary characteristics. Previous workers have suggested a marine-deltaic origin for the rocks surrounding Antamina, and have classified them as impure limestone, mudstone, wackestone, and marl (Benavides-Cáceres, 1956; Wilson, 1963; Escalante, 2008; Escalante et al., 2010).

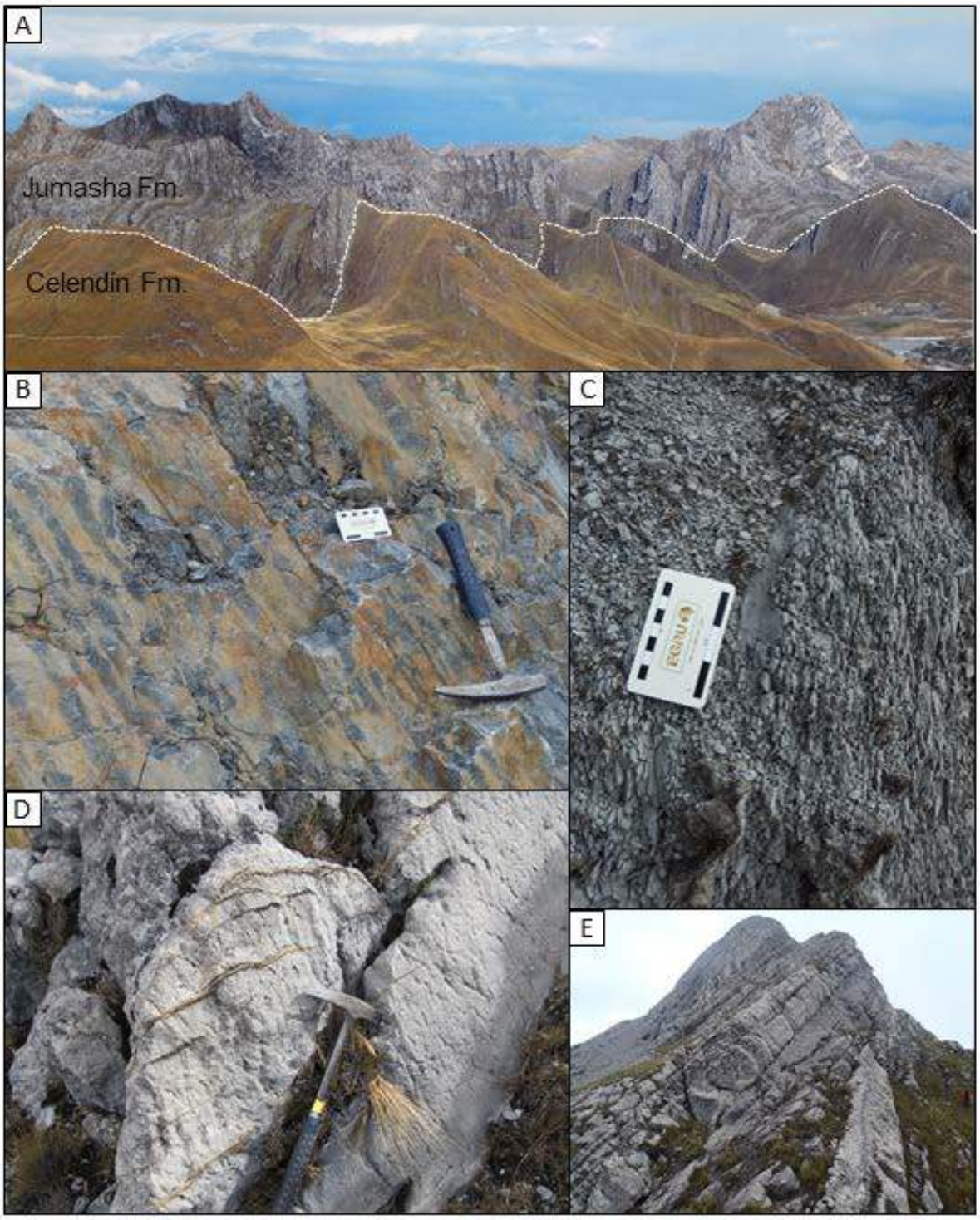

Fig. 2.2. Field characteristics of the Celendín and Jumasha Formations, within 3 km of Antamina. A. The break in slope marks the approximate location of the contact between the prominent Jumasha and recessive Celendín Formations. B. Weakly metamorphosed Celendín Formation, displaying interbedded marly (dark grey) and calcareous (light brown) layers. C. Thin-layered, dark grey, marly Celendín limestone. D. Massive, light grey Jumasha limestone with thin bioclastic layers. E. Thickly bedded, cliff-forming Jumasha limestone.

The mid-Cretaceous Jumasha Formation (Fig. 2.2 A, D-E) is a topographically prominent, medium-to-thickly bedded bioclastic limestone with lesser amounts of marl, dolomite, and

chert nodules (Benavides-Cáceres, 1956; Wilson, 1963; Escalante et al., 2010). Fresh and grey Celendín Formation. Unit thickness ranges from 200-800 m, although local structural thickening is observed around Antamina. The Late Cretaceous Celendín Formation (Fig. 2.2 A-C) is a fine-grained, moderately recessive unit dominated by thin intercalations of carbonate and calcareous shale/siltstone (Benavides-Cáceres, 1956; Wilson, 1963; Escalante et al., 2010). Thickness varies by location, from 225 m at the type locality to 115 m in other parts of the region (Wilson, 1963). Fresh rock surfaces are medium to dark grey reflecting an overall high organic carbon content; weathered surfaces display a creamy beige patina. Escalante (2008) used petrography to confirm that the limestone host rocks around Antamina contain a variable siliciclastic component and suggested that minerals other than calcite and pyrite are detrital in origin. Escalante (2008) also reported that the Celendín Formation has a more diverse mineralogy than the Jumasha Formation.

Contact metamorphism is restricted to an aureole up to 1 km surrounding the Antamina deposit (Fig. 2.1). Both the Celendín and Jumasha formations were affected, producing a colourful package of marble and fine-grained calcareous hornfels. Escalante (2008) identified five types of marble and four types of hornfels based on colour (Table A2.1). Many detrital minerals found in both marble and hornfels appear to be inherited from the limestones (i.e., quartz, feldspar, rutile, titanite, and apatite). There is also significant addition of some typical skarn minerals (i.e., diopsidic pyroxene, up to 53%; epidote, up to 18%), as well as trace amounts of sphalerite and chalcopyrite. The fine-grained pyroxene was likely from thermal metamorphism, whereas trace green pyroxene in narrow diffusive veins in marble was caused by prograde alteration. Other hydrothermal minerals were produced by retrograde skarn alteration (Table A2.1). The distribution of marble and hornfels types is controlled by sedimentary layering and proximity to the orebody. Bleached hornfels and marble extend at least 500 m outward from the orebody, but bleaching is also observed around dykes and veins distal to the main orebody. Green marble and hornfels containing diopside are transitional rock types observed between bleached (white) marble/hornfels and grey-tan marble/hornfels. The colour of tan marble and hornfels is attributed to phlogopitic biotite. A disseminated pyrrhotite aureole is notably present, approximately 75 m outward from the bleached halo (Escalante, 2008).

2.3. Sampling and Analytical Methods

A total of 224 rock samples were collected and analyzed for this study. Massive skarn samples (n = 66) and intrusion samples (n = 43) were selected from drill core and pit walls, with care taken to ensure that each sample was representative of the unit/interval and free of veins, xenoliths, contacts, and other heterogeneities. Nevertheless, minor alteration of some igneous rock samples is inevitable; 15 igneous rock samples with > 1% S, > 1,000 ppm Cu, > 100 ppm Mo, or > 250 ppm Pb have been filtered out of the dataset. Sample sizes ranged from 5-15 cm of NQ drill core or fist-sized hand samples from outcrops and high walls. Limestone ± marl samples (n = 106) were collected by Antamina exploration geologists (Paz et al., 2015) from within a 6 km radius of the mine, outside of the contact metamorphic halo, using the same selection criteria defined for the samples described above. Limestone samples were classified in the field as either Jumasha or Celendín Formation based on stratigraphic criteria used in regional exploration. Two additional samples of limestone and 7 of marble were collected for whole rock and total organic carbon (TOC) analyses. Fig. 2.1 presents the sample locations, with drill core samples projected to the surface.

All samples collected for this study were analyzed at ALS Chemex in Lima, Peru using a combination of techniques including X-ray fluorescence (XRF), inductively coupled plasma-atomic emission spectroscopy (ICP-AES), inductively coupled plasma-mass spectrometry (ICP-MS), atomic absorption (AA), and Leco analysis for 60 elements including major and trace elements, total S, total C, and LOI (loss on ignition). The sample digestion and measurement methods with analytical detection limits are presented in Digital Appendix 2.1. The complete data set is presented in Digital Appendix 2.2. Nine samples of undifferentiated limestone and marble from drill core and field samples were analyzed for total organic carbon (TOC) at the James Cook University Advanced Analytical Centre in Cairns, Australia. The analytical procedure is described in Wurster et al. (2012). The organic C content ranges 0.09-3.63 weight percent. The results are shown in Digital Appendix 2.3.

Whole rock analysis of an additional 41 samples from Escalante et al. (2010) are also used in this study, including 12 hornfels, 1 intrusive rock, and 28 marble samples. No unit names were assigned to the hornfels and marble samples (Escalante et al., 2010). For these samples the elements measured are the same as in our samples except that; 1) Sc and total C were not

analyzed for all the samples; 2) some samples were not analyzed for Au, and; 3) Cd, Li, As, Bi, Hg, Sb, Se, Te, and S were not analyzed in the intrusive sample (Escalante et al., 2010). Marble and hornfels are treated as metasedimentary wall rocks, as they are mainly the product of thermal metamorphism that is likely to be isochemical (e.g., Meinert et al., 2005). In total, the dataset has 265 samples, including 44 intrusive samples, 155 wall rock samples, and 66 skarn samples (Digital Appendix 2.2).

Isocon analysis (Grant, 1986; Grant, 2005) was conducted using the complete data set in order to quantify element mobility through skarn formation, regardless of precursor or degree of alteration. The isocon method uses a modified version of Gresens' (1967) equation for calculating mass balance by recalculating and plotting the chemical components of a least-altered rock against those of an altered equivalent in X-Y space using a common conversion factor to scale the data (Digital Appendix 2.4). Elements deemed to be immobile are used to plot a best-fit linear array anchored through the origin to define the isocon, or line of 'equal concentration'. The isocon slope quantifies the total mass change of the system. In this study, we used averaged sets of rocks to minimize the effect of compositional heterogeneity as in Oliver et al. (2004). Detailed explanations of the mass balance calculation procedure are presented in Grant (1986), Leitch and Lentz (1994), and Trepanier et al. (2016).

2.4. Results

2.4.1. Host Rock Geochemistry

Samples of the Jumasha Formation have higher concentrations and a narrower range of total carbon (9.85-13.1 wt. % C) and less SiO_2 (0.70-11.2 wt. %) and Al_2O_3 (0.15-3.14 wt. %) than samples from the Celendín Formation (3.15-11.6 wt. % C; 3.85-46.2 wt. % SiO_2; 0.9-12.6 wt. % Al_2O_3; Fig. 2.3). Some Jumasha samples are essentially pure limestone with up to 13.1 weight percent total C, 55.4 weight percent CaO, and little SiO_2 (minimum 0.70 wt. %) and Al_2O_3 (minimum 0.15 wt. %; Fig. 2.3); their composition is close to stoichiometric calcite (12.00 wt. % C and 56.03 wt. % CaO). Despite the fact that dolomite was not previously identified in sample of the Jumasha Formation (Table A2.1), some limestone samples from the Jumasha Formation contain up to ~3.4 weight percent MgO, indicating that they are dolomitic. Samples of the Celendín Formation are more variable in composition (~25-97 wt.

% calcite) and may contain more silicate minerals (up to ~75 wt. %). The low-carbon Celendín rocks are the calcareous shale-siltstone observed in the field (Fig. 2.2).

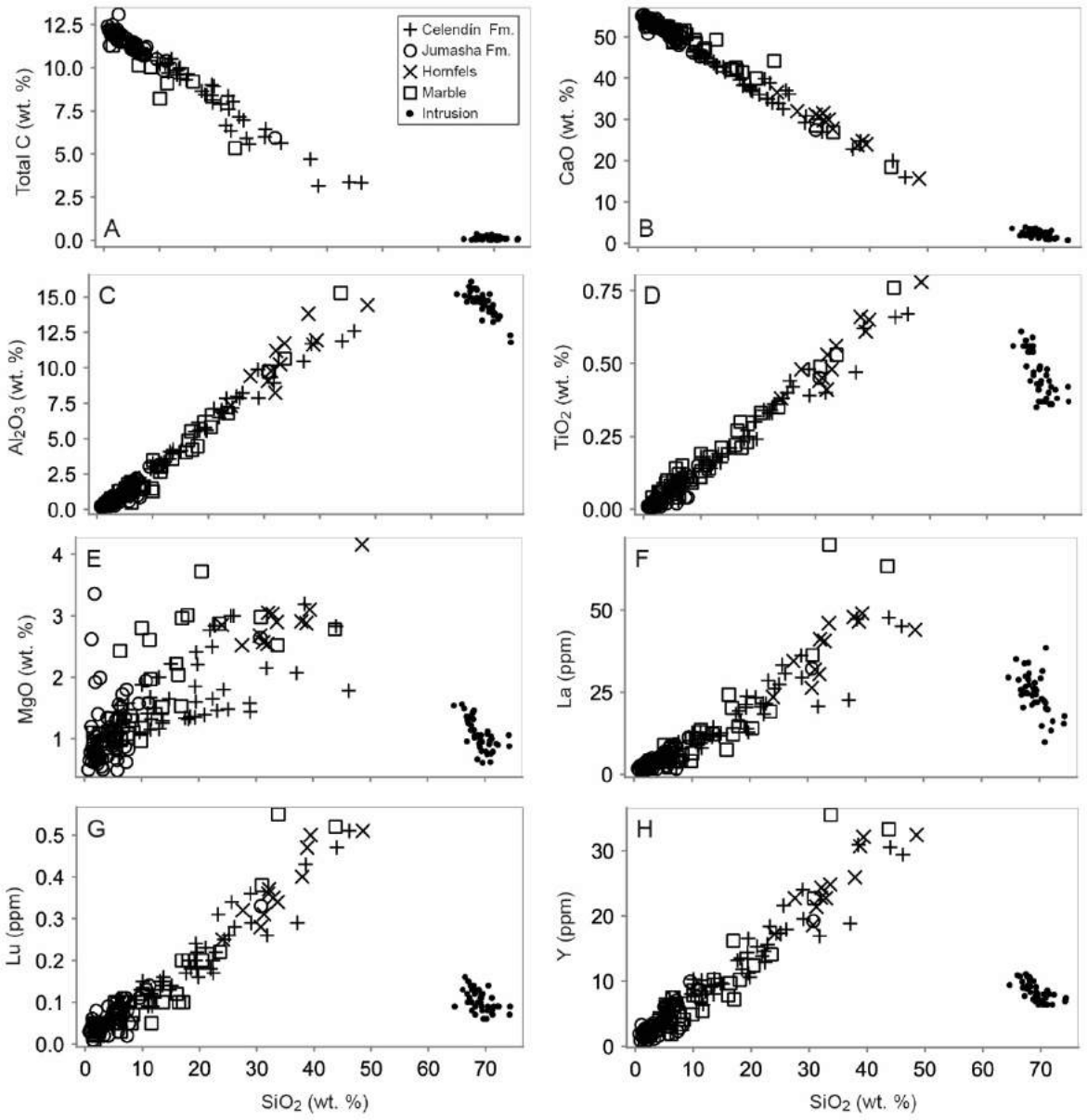

Fig. 2.3. Composition of wall rocks and intrusive rocks. Note that the 40 marble and hornfels samples from Escalante et al. (2010) do not have total carbon analysis therefore are not shown in the SiO_2-Total C diagram. These samples were not assigned stratigraphy unit names (Jumasha or Celendín), either.

The decrease in total C concentration in the wall rocks correlates with a decrease in CaO content and an increase in SiO_2 and Al_2O_3. The total C is dominated by carbon from carbonates, as the organic content is fairly low (Digital Appendix 2.3). Therefore, the trend indicates that the decrease in carbonate is compensated by an increase in silicate minerals (Fig. 2.3 A-B). This is consistent with the petrographic findings of Escalante (2008) in that

the wall rocks contain various proportions of calcite and quartz-aluminosilicate minerals (Table A2.1). Given the tight inverse linear relationship between total C and SiO_2 (Fig. 2.3 A), SiO_2 content is used as a proxy for the clastic component of the wall rocks.

Fe_2O_3, K_2O, Na_2O, and most lithophile trace elements (e.g. REE, Y) have positive linear correlations with SiO_2 (Fig. 2.3; Fig. A2.1) in both Jumasha and Celendín samples, indicating that these elements are related to the clastic components in the sedimentary host rocks. The MnO content is low (0.005-0.16 wt. %), with slightly higher concentrations in rocks containing > 10 wt. % SiO_2 (Fig. A2.1). Barium concentrations range from 17.1 to 429 ppm and do not seem to be related to any specific rock type (Fig. A2.1). The Sr content ranges from ~250 to 2,100 ppm, with some carbonate-rich rocks containing the highest Sr concentrations (Fig. A2.1); however, samples with lower Sr do not have clear correlation patterns between calcite/clastic component ratio and Sr content.

As would be expected, the intrusive rocks contain significantly higher SiO_2 with a narrower range (64.6-74.3 wt. % vs. 0.70-48.55 wt. %) and significantly lower total carbon (0.01-0.35 wt. % vs. 3.15-13.1 wt. %) and CaO (0.70-5.31 wt. % vs. 15.7-55.4 wt. %; Fig. 2.3) than the wall rocks. This is due to higher wall rock carbonate and lower wall rock silicate concentrations compared to the intrusive rocks. In general, the intrusive rocks contain more K_2O, Na_2O and Ba and have narrower compositional ranges than the wall rocks (Fig. 2.3 and Fig. A2.1). The intrusive rocks have similar Al_2O_3, TiO_2, and Zr concentrations and lower Ni, Lu, Y and V contents compared with the SiO_2-rich sedimentary rocks (> 30 wt. %, Celendín Formation; Fig. 2.3 and Fig. A2.1). The intrusive rocks and wall rocks have similar ranges of total Fe and MnO content (Fig. A2.1), although some intrusive rock samples extend to higher MnO concentrations (up to 0.19 wt. % MnO).

2.4.2. Seeking Geochemical Discriminators for Endoskarn and Exoskarn

In order to find elements or element pairs that can effectively discriminate massive endoskarn from exoskarn, I first identified parameters that can separate the least-altered intrusive rocks and the sedimentary host rocks, then among them seek elements that can discriminate the skarn types.

Among the 60 individual elements, only SiO_2, CaO, and total C can fully separate wall rocks and igneous rocks (Fig. 2.3). The three parameters, however, cannot discriminate massive endoskarn and exoskarn, as shown in Fig. A2.2, in which the composition of the skarns is between sedimentary rocks and intrusive rocks in terms of the SiO_2 and CaO content, and all of the skarns have less total C than all wall rocks.

All elements in the dataset were plotted as X-Y pairs. It was found that 73 element pairs could be used to distinguish the igneous versus sedimentary rocks, although many pairs involve geochemically similar elements (e.g., Al_2O_3 vs. La and Al_2O_3 vs. Ce). A summary of the most relevant pairs are listed in Table 2.1, and the representative plots are shown in Fig. 2.4. After addition of the skarn data to the X-Y plots, a number of plots were found to distinguish skarn types. Skarn data points plot in two groups in the TiO_2 vs. HREE plot; one group in the domain defined by the sedimentary wall rocks and the other group in the domain defined by igneous rocks (Fig. 2.4). Given the unequivocal clustering and the strong correlation with the precursor, these groups are considered to represent exoskarn and endoskarn, respectively. Among the pairing elements, TiO_2 vs. Y shows one of the best cases of clustering and matching, and has the highest abundance. Therefore, TiO_2-Y is proposed to be the best discriminating plot and is used to separate the skarns in this dataset into endoskarn and exoskarn (Fig. 2.4 A).

Table 2.1. Elements and element pairs that can discriminate massive endoskarn and exoskarn at Antamina.

Element	Pairing Elements								
TiO_2	HREE	Y	Al_2O_3	Ni	Sc	LREE	Ga	Zr, Hf	Th
Al_2O_3	HREE	Y	Th	TiO_2	LREE	Ni	Sc	Ga	Zr, Hf
Y	Al_2O_3	TiO_2	LREE	Zr, Hf	Th	Sc	HREE	Ga	Ni

Element pairs clearly discriminate endo- and exoskarns.
Element pairs weakly discriminate endo- and exoskarns.
Element pairs cannot discriminate endo- and exoskarns.

LREE: La to Sm
HREE: Dy to Lu

Using the endoskarn vs exoskarn classification defined by the TiO_2-Y plot, other elemental pairs capable of discriminating sedimentary and intrusive rocks were divided into three groups regarding their effectiveness in separating endoskarn and exoskarn. First order discriminants (i.e., element pairs that can clearly separate endoskarn and exoskarn) include

TiO_2 vs. HREE and Y; and Al_2O_3 vs. HREE, Y, Ni and Sc (Table 2.1; Fig. 2.4). Other TiO_2 pairs listed in Table 2.1 have analogous behaviour to TiO_2-Y in that they can clearly separate the skarns and display maximum cluster overlap between the skarns and their corresponding precursors (Fig. 2.4). In the plots involving Al_2O_3, the endoskarns have a larger Al_2O_3 concentration range than that of the intrusive rocks; however, the skarns are still clearly distinguishable (Fig. 2.4). Second order discriminants include element pairs that can separate endoskarn and exoskarn with no overlapping (or only minor overlapping) of the clusters.

These pairs include TiO_2 vs. Ni; Al_2O_3 vs. LREE, TiO_2, V, and MgO; Ni vs. Nb, Sm, Zr and Sc; HREE vs. Nd, Sm, Hf, and Th (Fig. 2.4, Table 2.1). Second-order pairs may be used to discriminate the skarn types, but some data points will have an ambiguous interpretation. The third order group includes element pairs that cannot distinguish endoskarn and exoskarn, as the two skarn domains overlap. These include all pairs involving Na_2O and Ga; Fig. 2.4 G and H present one example with minor overlap (i.e., Ga vs. Y), and one example with significant overlap (i.e., Na_2O vs. Y), respectively.

It was found that although Al_2O_3 alone cannot discriminate intrusions from wall rocks (Fig. 2.3 C), the Al_2O_3 contents of exoskarn (0.63-11.05 wt. %) and endoskarn (11.90-20.00 wt. %) do not overlap (Fig. A2.3). Therefore, Al_2O_3 by itself is an easy-to-use discriminator of skarn types at Antamina. The gap between the range of exoskarn and endoskarn values is small (11.05-11.90 wt. %), and the midpoint value, 11.5 weight percent Al_2O_3, is proposed to be the discriminatory criterion (Fig. A2.3).

Isocon analysis of endoskarn versus intrusions (Fig. 2.5 A; Digital Appendix 2.4) appears to involve little mass change, as indicated by the isocon slope of 1.02, while exoskarn formation shows an overall mass loss of approximately 15% percent (Fig. 2.5 B; Digital Appendix 2.4). Immobile elements in both endoskarn and exoskarn include REE, Y, TiO_2 and Al_2O_3 (Fig. 2.5). In both endoskarn and exoskarn, significant mass increases are observed in metals (Cu, Mo, Zn, Pb, U) and some major skarn mineral components (i.e., Fe_2O_3, MnO, and MgO). Alkalis (K_2O, Na_2O) decrease by more than 50 percent in both endoskarn and exoskarn. LOI increases by more than 50 percent in endoskarn, but decreases by more than 50 percent in exoskarn.

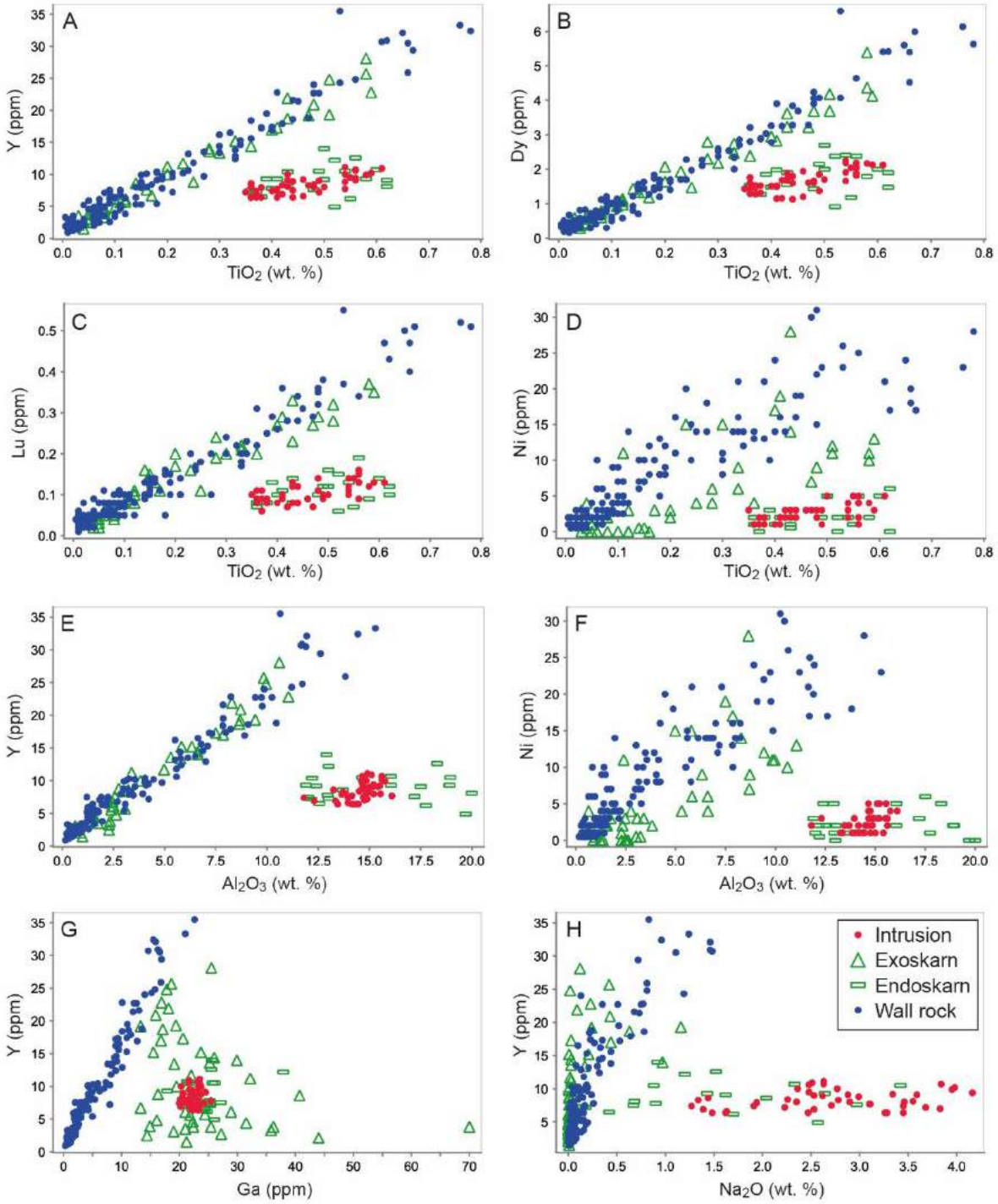

Fig. 2.4. Element pairs that can clearly distinguish intrusive rocks and sedimentary wallrocks, but function differently in distinguishing endoskarns and exoskarns. The division of endoskarn and exoskarn is based on the TiO_2-Y plot. TiO_2-Dy and TiO_2-Lu representing the TiO_2-HREE plots, and Al_2O_3-Y representing Al_2O_3-HREE plots (see Table 2.1) can also clearly distinguish endo- and exoskarns. TiO_2-Ni represents pairs that can barely distinguish endo- and exoskarns, with the endo- and exoskarn domains in the diagram not overlapping but very close. Na_2O-Y and Ga-Y plots represent pairs that cannot distinguish endoskarns and exoskarns.

2.4.3. Texture and Garnet Colour as Indicators of Skarn Precursor

Mottled textures (Fig. 2.6) and garnet colours are the most commonly used classification criteria for distinguishing massive endoskarn and exoskarn at Antamina. Mottled textures were believed to be inherited from the porphyritic texture of the intrusive rocks, and as such, would indicate an endoskarn precursor. I have found that this criterion is not reliable. For example, the samples shown in Fig. 2.6 A-C have mottled textures but their whole rock

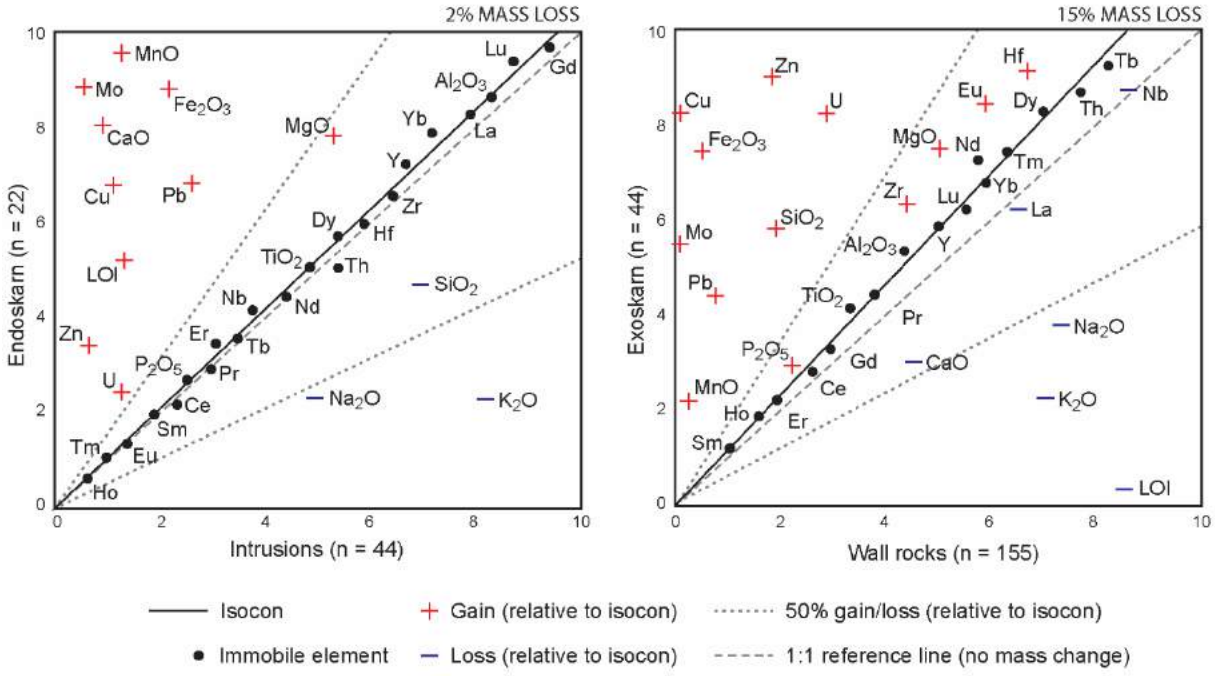

Fig. 2.5. Isocon plots showing mass change during skarn formation. Least-altered precursors are plotted along the X-axis, while altered equivalents are plotted along the Y-axis. The total mass change for the system is indicated at the top right of each plot. Elements plotting along the isocon line (black circles) are immobile. Those species plotting below the isocon indicate mass loss, while those above the isocon indicate mass gain. A: element mobility and mass changes during endoskarn formation. B: element mobility and mass changes during exoskarn formation. Data and calculations are presented in Digital Appendix 2.4.

geochemistry indicates that they are actually exoskarns (Fig. 2.7). In contrast the samples in Fig. 2.6 D-F are endoskarns based on their geochemical signature (Fig. 2.7).

Garnet colour (pink, red, brown, green) was recorded for each skarn sample in this study, then plotted using the TiO_2-Y discriminator. Typically, a sample may contain more than one colour of garnet; the dominant garnet colour recorded for each sample is presented in Fig. 2.7. At Antamina, only pink and green garnet correspond strongly with endoskarn and exoskarn, respectively (Fig. 2.7). Red and brown garnet are observed both in endoskarn and exoskarn (Fig. 2.7).

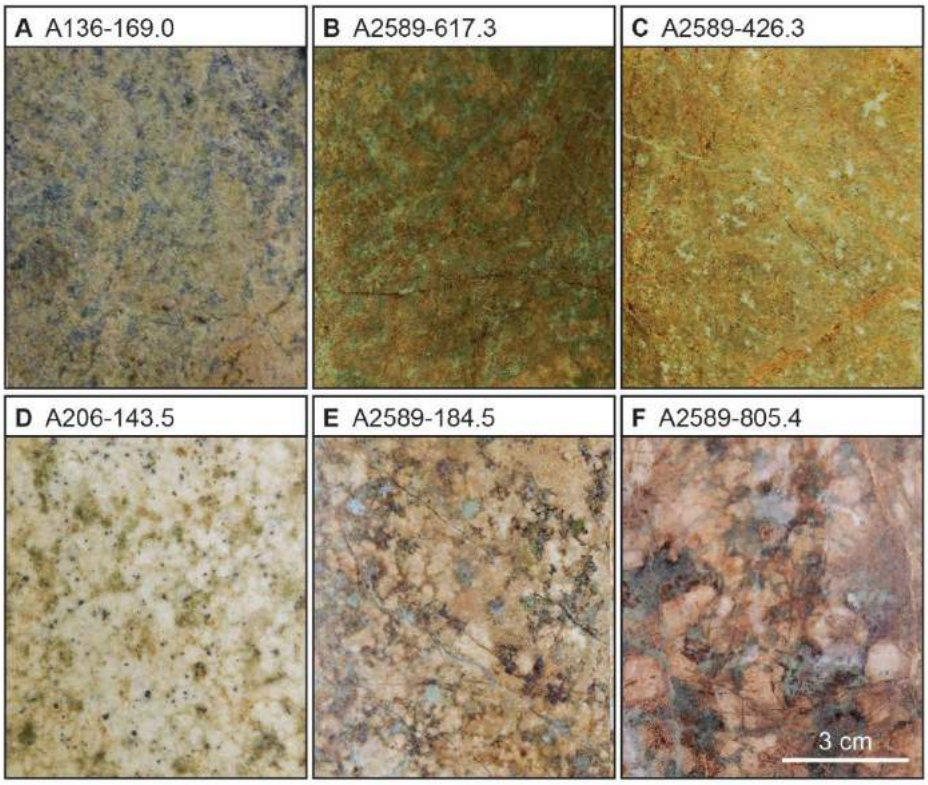

Fig. 2.6. Both endoskarns and exoskarns can have mottled textures. A, B and C are exoskarns, whereas D, E and F are endoskarns, based on the geochemical discrimination. Scale bar applies to all images.

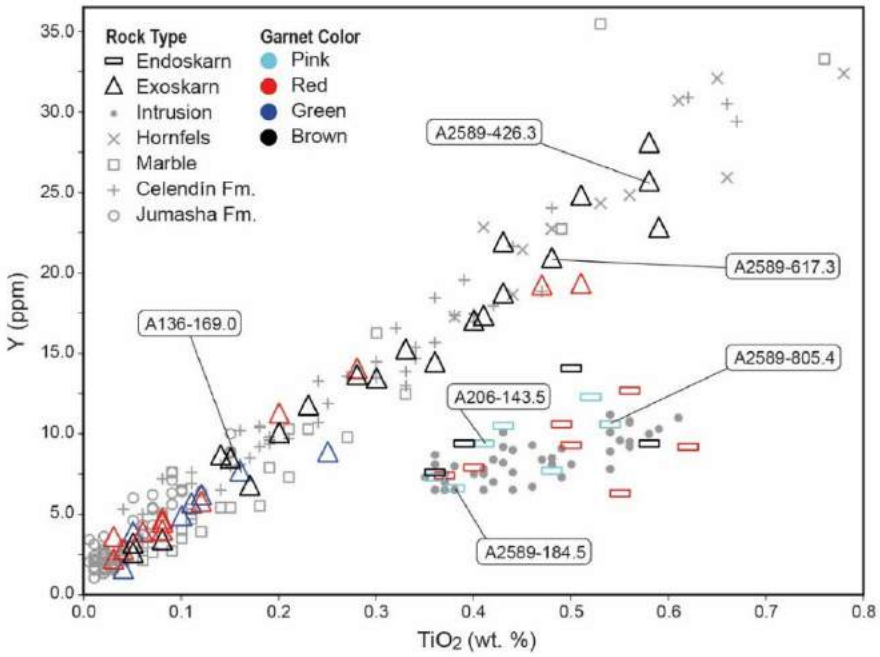

Fig. 2.7. Skarns reclassified by whole rock geochemistry and plotted by garnet colour. Pink garnet occurs exclusively in endoskarn, while green garnet occurs exclusively in exoskarn. Red and brown garnet occur in both endoskarn and exoskarn, therefore they are not diagnostic of skarn type. Mottled-textured skarns presented in Fig. 2.6 are labelled; note that both endoskarn and exoskarn can display mottled textures, and mottled textures are not limited to the samples identified in this plot.

2.5. Discussion

2.5.1. Geochemical Distinction of Endoskarn and Exoskarn

In this study I identified several combinations of elements, plus the Al_2O_3 content, that can be used to effectively discriminate massive skarn types (endoskarn vs. exoskarn) at Antamina. These geochemical discriminators involve Al_2O_3 and high field strength elements (HFSE), including Ti, Y, HREE, Hf, Th, Zr, and Nb (Table 2.1 and Fig. 2.4). These geochemical discriminators are effective probably because; 1) the intrusive and metasedimentary wall rocks have significantly different signatures (i.e., non-overlapping clusters) in terms of these discriminators, and 2) the elements involved are typically immobile, particularly in a carbonate-rich (pH buffered) environment, therefore the geochemical fingerprint of the precursor is passed on to the skarns. As a result, the discriminating elements and element pairs are effective for any combination of prograde and retrograde skarn alteration.

The compositional differences between the igneous rocks and the wall rocks are shown in Fig. A2.1 and Fig. 2.3. The calcareous wall rocks have various amounts of siliciclastic impurities, particularly in the Celendín Formation. The wall rocks contain various amounts of Al_2O_3 and HFSE, mostly in the siliciclastic components. Escalante (2008) reported the mineralogy of hornfels and marbles, which are the thermal metamorphic products of the calcareous wall rocks (Table A2.1). The Al_2O_3 is mostly in the feldspars (up to 85 volume % of the rocks), whereas the HFSE may be in the accessory LREE-epidote, rutile, titanite, apatite, zircon, and biotite. The amount of these generally immobile elements is broadly in proportion to the ratio of siliciclastic component/calcite in the wall rocks (Fig. 2.3 and Fig. A2.1).

2.5.2. Element Loss and Gain During Skarn Formation

Being able to clearly distinguish the precursor of various skarn types, I can now confidently evaluate element mobility (loss or gain) during both prograde skarn formation and retrograde alteration using isocon analysis (Fig. 2.5). The immobility of discriminating elements at Antamina (Fig. 2.5) is in agreement with previous studies showing that HFSE and Al are among the most immobile under a variety of geologic conditions (Floyd and Winchester, 1978; Finlow-Bates and Stumpfl, 1981; Whitney and Olmsted, 1998; Jiang et al., 2005; Lentz, 2005; Ranjbar et al., 2016). Although the solubility and mobility of these elements can

be enhanced in strongly acidic fluids, their solubilities drop dramatically with increasing pH. For example, at 250°C total dissolved Al in fluids in equilibrium with alunite + kaolinite + quartz is ~2000 ppm at a pH of 2 but drops to only ~1 ppm when the pH is 4 (Stoffregen, 1987). In high-sulfidation epithermal environments, strongly acidic fluids (pH < 2) can remove Al from rocks to form vuggy residual quartz (up to 99% SiO_2; Stoffregen, 1987; Hedenquist et al., 2000).

In carbonate-rich environments where most skarns form, fluid acidity ranges from weak to neutral due to buffering by excess carbonate; such fluids will not be able to mobilize HFSE or Al_2O_3. In impure carbonates, like those that host the Antamina skarns, these elements can be hosted in authigenic feldspar, titanite, rutile, zircon, and apatite (Table A2.1; Deer et al., 1992; Hammerli et al., 2016; Mao et al., 2016). During skarn formation, the mineralogy of the host rocks changes significantly; however the low solubilities of these immobile elements allows them to be re-incorporated in skarn minerals as they form (Huggins et al., 1977; Nicolescu et al., 1998, Gaspar et al., 2008). Consequently, immobile element signatures in the Antamina skarns are inherited from the host rocks, as evidenced by the isochemical behaviour of elements outlined in Fig. 2.5.

Endoskarn formation resulted in a mass loss of 2%, while a 15% mass loss during exoskarn formation was observed. The greater mass loss calculated in exoskarn may be due to increased porosity (reduced density) as a result of prograde dissolution by acidic magmatic-hydrothermal fluids and retrograde alteration of the prograde exoskarn mineral assemblage. In general, exoskarn samples gain porosity and lose density during prograde formation and retrograde alteration. In contrast, endoskarn samples are rarely porous, despite being subjected to the same intensity of metasomatism. This may be related to the silicate-rich composition of the precursor being more resistant to dissolution than the carbonate-rich wall rocks.

In both endoskarn and exoskarn, increases in Fe_2O_3, MnO, and MgO are related to the formation of garnet and clinopyroxene during prograde skarn alteration; these components are likely to be derived from the magmatic-hydrothermal fluids. SiO_2 is also added to exoskarn during prograde skarn formation, but its source may be partly from SiO_2 stripping from the intrusions during endoskarn formation (as indicated by a loss of SiO_2 in the endoskarn vs. intrusions isocon plot; Fig. 2.5 A). Metals (Cu, Mo, Zn, Pb, U) increase

significantly in both endoskarn and exoskarn as a result of retrograde alteration. Volatile (LOI) increases in endoskarn may be related to the formation of hydrous or CO_2-bearing retrograde minerals (chlorite, amphibole, calcite), while decreases in exoskarn LOI are related to CO_2 being driven off of marble (mostly calcite) during prograde skarn formation.

The only elements lost in significant quantities (50 to 75%) from both endoskarn and exoskarn are the alkali elements (K_2O, Na_2O). The most common skarn minerals do not incorporate these elements into their crystal lattice. Some of this element loss may actually be related to alkali gain in the intrusive samples due to retrograde alteration (i.e., sericite), but significant amounts of these elements were likely transported to distal parts of the system via hydrothermal fluid escape structures (Meinert et al., 2005). At Antamina I can only speculate that these alkalis were transported to overlying rock packages that have now been lost to erosion. Nevertheless, if alkali element loss is a common feature of skarn formation, then upflow and reaction of these fluids may provide some of the alkalis for the alteration assemblages that are characteristic of overlying porphyry-epithermal environments. Elements for these alteration assemblages are primarily considered to be magma sourced, but some contribution from skarn alteration of wallrock would be consistent with Pb isotope evidence supporting a wallrock component to porphyry alteration fluids (Cooke et al., 2014), and would ease the requirements for very large magma volumes to source alkali elements for porphyry alteration envelopes (Cathles and Shannon, 2007).

2.5.3. Mottled Texture

I have found that the mottled textures displayed by some exoskarns at Antamina are not reliable for distinguishing endoskarn from exoskarn, as both skarn types can exhibit mottled textures (Fig. 2.6). Endoskarns typically inherit mottled textures from porphyritic and coarse-grained phaneritic igneous precursors. However, exoskarns may also inherit mottled textures (Fig. 2.6) from impure carbonate precursors like those at Antamina. Any host rock containing patches or layers of siliciclastic impurities may produce a mottled exoskarn texture through a process of repetitive dissolution and fragmentation. For example, open space is created when carbonate dissolution occurs faster than calc-silicate replacement can fill voids, which causes the more resistant siliciclastic layers to become unsupported and collapse into fragments; metasomatic replacement of these rocks will produce exoskarns with mottled textures.

2.5.4. Garnet Colour

At Antamina, green and pink garnet can be used with a high degree of confidence to classify skarns, because they never occur together and they correlate well with exoskarn and endoskarn, respectively (Fig. 2.7). Red and brown garnet should be used with caution as they occur in all skarn types (Fig. 2.7). Spatially, pink garnet occurs in endoskarn, green garnet occurs in distal exoskarn near the marble front, and red ± brown garnet occur in both exoskarn and endoskarn proximal to the intrusion-wall rock contact. As such, garnet colour can also be used, with caution, to establish broad-scale zoning patterns where rock exposure or spatial context is limited (i.e, exploration drill core).

2.5.5. Applicability in Other Skarns

The geochemical discriminators discovered at Antamina may be applicable to other skarns but need to be used with caution. Calcareous wall rocks may vary significantly in compositions from deposit to deposit, and the intrusive rocks may also have different compositions, as skarns may be caused by a wide range of intrusive rocks, with the SiO_2 content ranging from ~53 to 78 weight percent (Meinert, 1995). Accordingly, the Al_2O_3 and HFSE content of various intrusive rocks and the temperature and composition of alteration fluids may be significantly different from the situation at Antamina. Therefore, it is unlikely that the geochemical discriminators I have identified at Antamina are would be universally applicable; however, this approach to skarn classification is particularly well-suited for deposit-scale studies where the detailed geology is known and a range of rock types, from least-altered to strongly altered, are available for analysis. Applying our procedures to other skarn localities, I suggest that the compositions of both the wall rocks and the intrusive rocks should be characterised prior to identification of geochemical discriminators of skarn type.

2.6. Conclusions

The results of this study demonstrate that whole rock major and trace element composition can be used to discriminate precursors (igneous versus wall rock) of skarns, which is particularly useful where the skarns are massive or mottled and the original textures have been destroyed by intense hydrothermal alteration. The most effective discriminators at Antamina are element pairs of TiO_2 vs. Y, HREE; Al_2O_3 vs. HREE, Y, Ni, and Sc, plus

Al_2O_3 alone (endoskarns contain > 11.5 wt. % Al_2O_3, whereas exoskarns contain < 11.5 wt. %). The parameters identified in this study at Antamina may be applicable elsewhere, although a pilot study following the procedure of this study is recommended.

2.7. Acknowledgements

This study was funded by Compañía Minera Antamina (analytical funds and in kind support) and a Society of Economic Geologists Graduate Student Research Grant awarded to S. Mrozek. I thank J.A. Grant for answering questions related to isocon calculations, and Christian Mendoza, David Paredes, Frederick Sanchez, and the Antamina exploration crew for providing limestone samples and access to the whole rock data set. I also thank Dr. Rob Holm and Dr. Carlos Jimenez who provided constructive reviews on the manuscript.

2.8. References

Benavides-Cáceres, V., 1999, Orogenic evolution of the Peruvian Andes: the Andean Cycle, Chapter 3, Society of Economic Geologists Special Publication 7: Geology and ore deposits of the central Andes, p. 61-100.

Benavides-Cáceres, V.E., 1956, Cretaceous system in northern Peru: Bulletin of the American Museum of Natural History, v. 108, p. 353-494.

Cathles, L.M., and Shannon R., 2007, How potassium silicate alteration suggests the formation of porphyry ore deposits begins with the nearly explosive but barren expulsion of large volumes of magmatic water: Earth and Planetary Science Letters, v. 262, p. 92-108.

Chang, Z., and Meinert, L.D., 2008a, The Empire Cu-Zn Mine, Idaho: exploration implications of unusual skarn features related to high fluorine activity: Economic Geology, v. 103, p. 909-938.

Chang, Z., and Meinert, L.D., 2008b, Zonation in skarns: complexities and controlling factors. In: Proceedings of the PACRIM Congress (11), p. 303-306, PACRIM Congress 2008, 24-26 November 2008, Gold Coast, QLD, Australia.

Cooke, D.R., Hollings, P., Wilkinson, J.J. and Tosdal, R.M., 2014, Geochemistry of porphyry deposits: Treatise in Geochemistry, second edition, v. 13, p. 357-381.

Deer, W.A., Howie, R.A., and Zussman, J., 1992, An Introduction to the Rock-Forming Minerals: Essex, UK, Pearson Education Ltd., 696 p.

Einaudi, M.T., Meinert, L.D., and Newberry, R.J., 1981, Skarn deposits, *in* Skinner, B. J., ed., Economic Geology 75th Anniversary Volume: El Paso, Economic Geology Publishing Co, p. 317-391.

Escalante, A.D., 2008, Patterns of distal alteration zonation around Antamina Cu-Zn skarn and Uchucchacua Ag base metal vein deposits, Peru: mineralogical, chemical, and isotopic evidence for fluid composition, and infiltration, and implicaitons for mineral exploration. The University of British Columbia, 817 p.

Escalante, A., Dipple, G.M., Barker, S.L.L., and Tosdal, R., 2010, Defining trace-element alteration halos to skarn deposits hosted in heterogeneous carbonate rocks: Case study from the Cu–Zn Antamina skarn deposit, Peru: Journal of Geochemical Exploration, v. 105, p. 117-136.

Finlow-Bates, T., Stumpfl, E.F., 1981. The behaviour of so-called immobile elements in hydrothermally alterated rocks associated with volcanogenic submarine-exhalative ore deposits: Mineralium Deposita, v. 16, p. 319-328.

Floyd, P.A., and Winchester, J.A., 1978, Identification and discrimination of altered and metamorphosed volcanic rocks using immobile elements: Chemical Geology, v. 21, p. 291-306.

Gaspar, M., Knaack, C., Meinert, L.D., Moretti, R., 2008, REE in skarn systems: A LA-ICP-MS study of garnets from the Crown Jewel gold deposit: Geochimica et Cosmochimica Acta, v. 72, p. 185-205.

Glencore, 2015, Annual Report (http://www.glencore.com/assets/investors/doc/ reports_and_results/ 2015/GLEN-2015-Annual-Report.pdf).

Grant, J.A., 1986, The Isocon Diagram – A Simple Solution to Gresens' Equation for Metasomatic Alteration: Economic Geology, v. 81, p. 1976-1982.

Grant, J.A., 2005, Isocon analysis: a brief review of the method and applications: Physics and Chemistry of the Earth, v. 30, p. 997-1004.

Gresens, R.L., 1967, Composition-volume relationships of metasomatism: Chemical Geology, v. 2, p. 47-55.

Hammerli, J., Spandler, C, and Oliver, N.H.S., 2016, Element redistribution and mobility during upper crustal metamorphism of metasedimentary rocks: an example from the eastern Mount Lofty Ranges, South Australia: Contributions to Mineralogy and Petrology, v. 171, p. 1-21.

Hedenquist, J.W., Arribas, A.R., and Gonzalez-Urien, E., 2000, Exploration for epithermal gold deposits: SEG Reviews, Chapter 7, v. 13, p. 245-277.

Huggins, F.E., Virgo, D., and Huchenholz, H.G., 1977, Titanium-containing silicate garnets. II. The crystal chemistry of melanites and schorlomites: American Mineralogist, v. 62, p. 646-665.

Jiang, S-Y., Wang, R-C., Xu, X-S., and Zhao, K-D., 2005, Mobility of high field strength elements (HFSE) in magmatic-, metamorphic-, and submarine-hydrothermal systems: Physics and Chemistry of the Earth, v. 30, p. 1020-1029.

Leitch, C.H.B., and Lentz, D.R., 1994, The Gresens approach to mass balance constraints of alteration systems: methods, pitfalls, examples, in Lentz, D.R., ed., Alteration and Alteration Processes Associated with Ore-Forming Systems: Geological Association of Canada, Short Course Notes, v. 11, p. 161-192.

Lentz, D.R., 2005, Mass-balance analysis of mineralized skarn systems: implications for replacement processes, carbonate mobility, and permeability evolution. In: Mao, J., Bierlein, F.P. (Eds.), Mineral Deposit Research: Meeting the Global Challenge: Proceedings of the Eight Biennial SGA Meeting, Beijing, China, Chapter 4–18, p. 421–424.

Lipten, E.J., and Smith, S.W., 2005, The Geology of the Antamina Copper-Zinc Deposit, Peru, South America, in Porter T.M., ed., Super Porphyry Copper & Gold Deposits: A Global Perspective, v. 1: Adelaide, PGC Publishing, p. 189-204.

Love, D.A., Clark, A.H., and Schwarz, F.P., 2000, The Antamina deposit, Ancash, Peru: Anatomy and petrology of a giant copper skarn [abs.]: Geological Society of America Abstracts with Programs, v. 32, no. 7, p. A137.

Love, D.A., Clark, A.H., Ullrich, T.D., Archibald, D.A., and Lee, J.K.W., 2003, ^{40}Ar-^{39}Ar evidence for the age and duration of magmatic-hydrothermal activity in the giant Antamina Cu-Zn skarn deposit, Ancash, north-central Peru [abs.]: Geological Association of Canada/Mineralogical Association of Canada/Society of Economic Geologists Abstracts, v. 28, Abstract no. 396 CD-ROM.

Love, D.A., Clark, A.H., and Glover, J.K., 2004, The lithologic, stratigraphic, and structural setting of the giant Antamina copper-zinc skarn deposit, Ancash, Peru: Economic Geology, v. 99, pp. 887-916.

McKee, E.H., Noble, D.C., Scherkenbach, D.A., Drexler, J.W., Mendoza, J., and Eyzaguirre, V.R., 1979, Age of porphyry intrusion, potassic alteration, and related Cu-Zn skarn mineralisation, Antamina district, northern Peru: Economic Geology, v. 74, p. 928-930.

Mao, M., Rukhlov, A.S., Rowins, S.M., Spence, J., and Coogan, L.A., 2016, Apatite trace element compositions: a robust new tool for mineral exploration: Economic Geology, v. 111, pp. 1187-1222.

Meinert, L.D., 1997, Application of skarn deposit zonation models to mineral exploration: Exploration and Mining Geology, v. 6, p. 185-208.

Meinert, L.D., Dipple, G.M., and Nicolescu, S., 2005, World skarn deposits, *in* Hedenquist, J. W., Thompson, J. F. H., Goldfarb, R. J., and Richards, J. P., eds., Economic Geology One Hundredth Anniversary Volume 1905-2005: Littleton, CO, Society of Economic Geologists, p. 299-336.

Mrozek, S.A., Chang, Z., Meinert, L., and Creaser, R., 2017, Using field observations and geochronology to constrain the age of magmatic-hydrothermal activity at the Antamina deposit, Peru [ext. abs.]: International Congress of Prospectors and Explorers (ProExplo), 10th, Lima, Peru, 2017, Extended Abstract, p. 47-51.

Newberry, R.J., Einaudi, M.T., and Eastman, H.S., 1991, Zoning and genesis of the Darwin Pb-Zn-Ag skarn deposit, California: a reinterpretation based on new data: Economic Geology, v. 86, p. 960-982.

Nicolescu, S., Cornell, D.H., Södervall, U., and Odelius, H., 1998, Secondary ion mass spectrometry analysis of rare earth elements in grandite garnet and other skarn related silicates: European Journal of Mineralogy, v. 10, p. 251-259.

Oliver, N.H.S, Cleverley, J.S., Mark, G., Pollard, P.J., Fu, B., Marshall, L.J., Rubenach, M.J., Williams, P.J., and Baker, T., 2004, Modeling the role of sodic alteration in the genesis of iron oxide-copper-gold deposits, eastern Mount Isa block, Australia: Economic Geology, v. 99, p. 1145-1176.

Paz, A., Raraz, C., Windle, S., Paredes, D., Mendoza, C., 2015, Caracterizacion litogeoquimica de las formaciones Jumasha y Celendín con elementos mayors y elementos de traza, relacionados con mineralizacion de Cu-Zn cercanos al yacimiento minero Antamina [ext. abs.]: International Congress of Prospectors and Explorers (ProExplo), 9th, Lima, Peru, 2015, Extended Abstract.

Ramos, V.A., and Aleman, A., 2000, Tectonic evolution of the Andes, in Cordani, U.G., Milani, E.J., Thomaz Filho, A., and Campos, D.A., eds., Rio de Janeiro, p. 635-685.

Ranjbar, S., Tabatabaei-Manesh, S.M., Mackizadeh, M.A., Tabatabaei, S.H., Parfenova, O.V., 2016, Geochemistry of Major and Rare Earth Elements in Garnet of the Kal-e Kafi Skarn, Anarak Area, Central Iran: Constraints on Processes in a Hydrothermal System: Geochemistry International, v. 54, p. 423-438.

Stoffregen, R.E., 1987, Genesis of acid-sulfate alteration and Au-Cu-Ag mineralisation at Summitville, Colourado: Economic Geology, v. 82, p. 1575-1591.

Trepanier, S., Mathieu, L., Daigneault, R., and Faure, S., 2016, Precursors predicted by artificial neural networks for mass balance calculations: quantifying hydrothermal alteration in volcanic rocks: Computers & Geosciences, v. 89, p. 32-43.

Whitney, P.R., and Olmsted, J.F., 1998, Rare earth element metasomatism in hydrothermal systems: The Willsboro-Lewis wollastonite ores, New York, USA: Geochimica et Cosmochimica Acta, v. 62, p. 2965-2977.

Wilson, J.J., 1963, Cretaceous stratigraphy of central Andes of Peru: American Association of Petroleum Geologists Bulletin, v. 47 (1), p. 1-34.

Wurster, C.M., Robertson, J., Westcott, D.A., Dryden, B., Zazzo, A., and Bird, M.I., 2012, Utilization of sugarcane habitat by feral pig (*sus scrofa*) in northern tropical Queensland: evidence from the stable isotope composition of hair: PLoS ONE, v. 7, e43538.

2.9. Appendix

Table A2.1. Summary of host rock mineralogical composition at Antamina (after Escalante, 2008).

Rock Type[1]	Calcite	Quartz	Plagioclase	Albite	K-Feldspar	Amphibole	Augite	Tremolite	Wollastonite	Diopside	Scapolite	Grossular	Vesuviante	Biotite	Phlogopite
Limestone	70-92	2-12	2	2-8	tr-5	-	tr	-	-	-	-	-	-	tr	-
Hornfels															
Tan	40-60	5-10	10-20	tr	1-35	-	-	1	-	4	-	tr	-	0.5-10	1-2
Gray	60	tr-2	5	tr	5-15	tr	-	-	-	15-20	-	tr	-	-	-
Greenish gray	14-33	tr-1	1-14	tr-1	20-60	-	-	-	-	6-35	tr	-	-	-	-
Pale green-white	5-30	tr-1	5-25	1	18-60	-	tr	-	-	15-53	tr	1	-	tr	-
Marble															
Tan	25-70	3-6	0.5-3	-	20-55	-	-	2	tr	1	-	-	-	-	10-15
Gray	65-80	tr-10	5-18	tr	0.5-10	-	tr	0.5	-	2	7-8	tr	-	tr	2-3
Greenish gray	70	2	5-8	-	5-10	tr	tr	2-3	tr	10-12	-	tr	-	-	-
Massive white	84-92	tr-0.5	1-2	-	tr-2	-	-	tr-1	-	3-5	0.5-3	tr	tr	-	0.5
Diffusional white	20-30	2-10	tr-1	1	30-50	-	0.5	tr	-	5-20	-	-	-	-	-

Rock Type[1]	Illite	Chlorite	Clinochlore	Epidote	LREE-Epidote	Dolomite	Ankerite	Pyrite	Sphalerite	Pyrrhotite	Chalcopyrite	Rutile	Titanite	Apatite	Zircon
Limestone	tr	0.5-3	0.5	-	-	-	tr	0.5	-	0.5	-	tr	tr	tr	-
Hornfels															
Tan	-	2-6	-	2-3	1-2	-	-	1-5	-	-	-	tr	0.5-3	tr-0.5	-
Gray	-	-	tr	1-2	-	tr	-	tr-3	tr	-	-	-	0.5-1	tr-1	-
Greenish gray	-	tr-3	-	tr-18	0.5-2	-	-	tr-2	-	-	-	-	tr-1	tr	-
Pale green-white	-	tr-0.5	-	tr-3	1-2	-	-	tr-2	1	-	-	-	0.5-2	tr-0.5	-
Marble															
Tan	-	0.5	0.5	-	-	-	-	1-2	tr	tr	-	-	0.5-4	tr	-
Gray	-	1	-	0.5	-	-	-	2	-	1-2	tr	-	0.5-2	tr	tr
Greenish gray	-	-	tr	tr-0.5	-	-	-	1	tr	-	-	-	tr	tr-1	-
Massive white	-	-	tr	-	-	-	-	1-2	tr	-	-	-	0.5	tr-0.5	-
Diffusional white	-	tr	-	-	-	-	-	3-10	1	1	tr	-	0.5-1	0.5	-

[1]As defined by Escalante (2008). All values are reported in volume per cent.
tr: trace (<0.5 %).

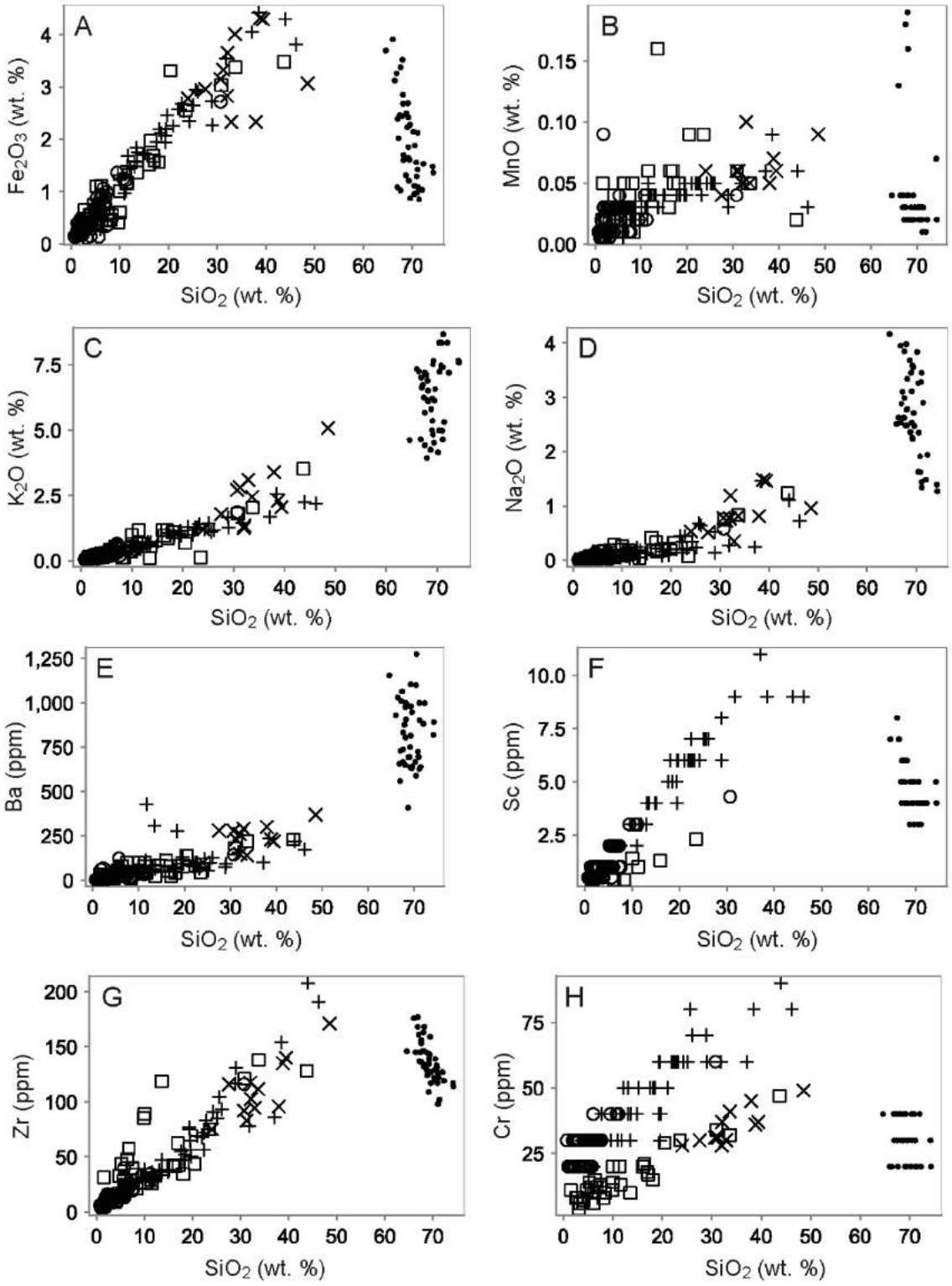

Fig. A2.1. Geochemical characteristics of the Antamina host rocks. Continued on next page.

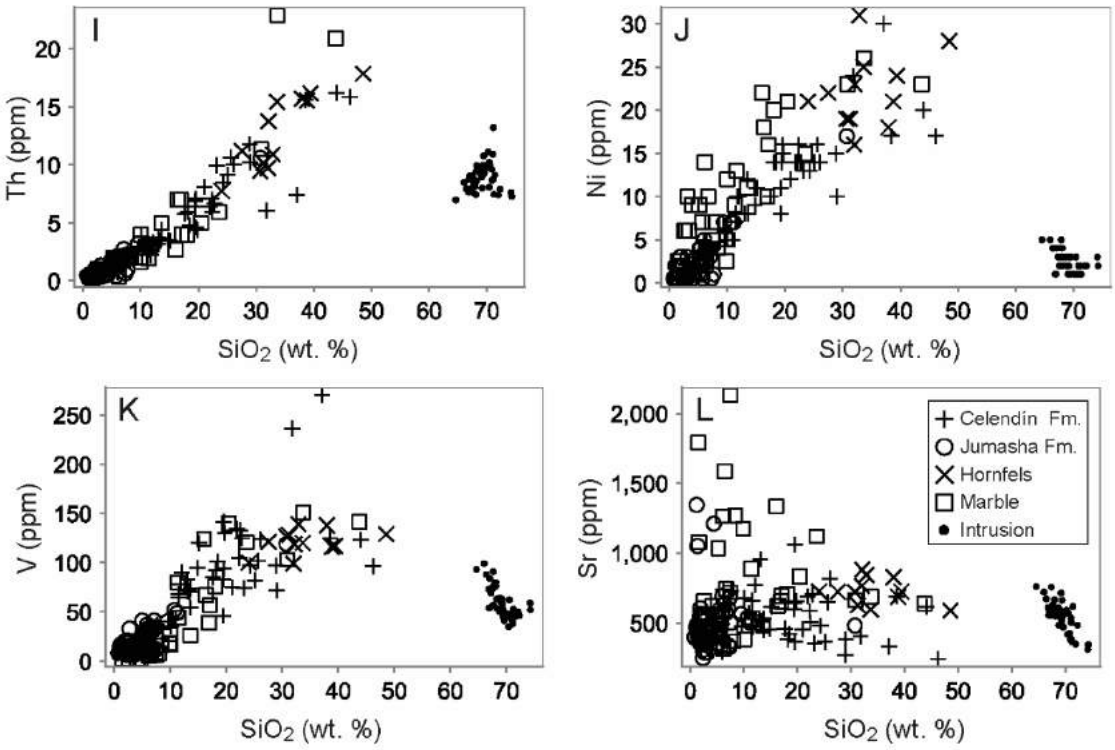

Fig. A2.1. Continued from previous page. Geochemical characteristics of the Antamina host rocks using selected major and minor elements.

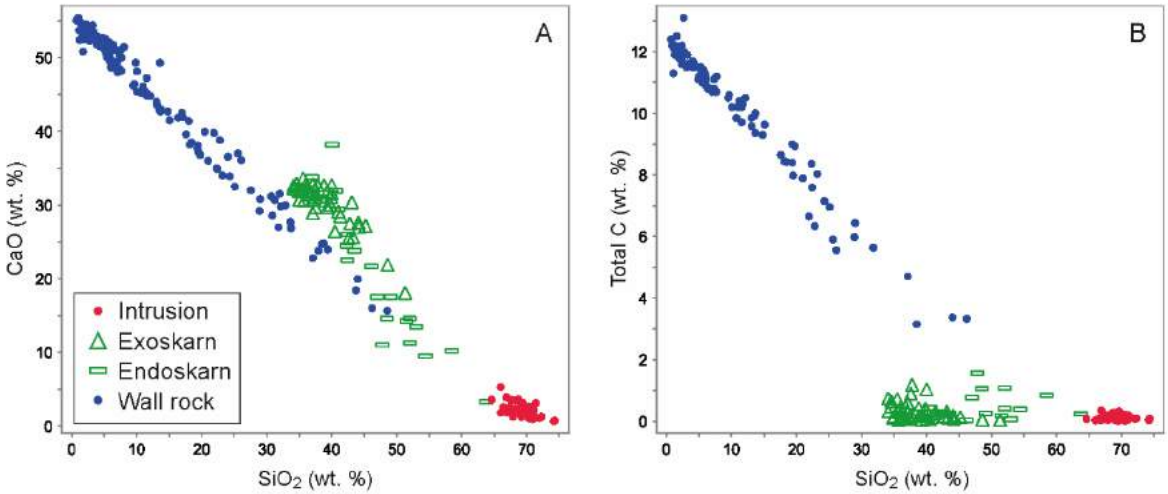

Fig. A2.2. SiO_2 (wt. %) vs. CaO (wt. %) and Total C (wt. %) contents of skarns, intrusions, and wall rocks.

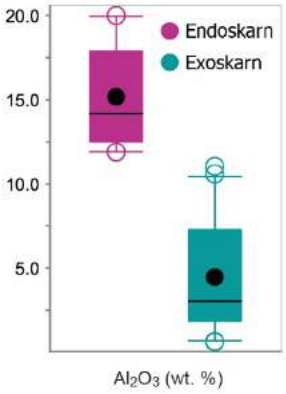

Fig. A2.3. Box and whisker plot comparing Al_2O_3 contents of endoskarn and exoskarn.

Chapter 3:
An age-constrained model for skarn formation at the giant Antamina deposit, Peru

3.1. Abstract

The Antamina Cu-Zn-Mo deposit, in Peru, consists of a Miocene multi-phase porphyry complex surrounded by the largest continuous body of skarn known in the world today. At least 11 porphyry phases have been identified through field observations of cross-cutting relationships; only two display a genetic link to the surrounding skarns (i.e., they contain endoskarn alteration). All of the porphyries contain magmatic biotite ± hornblende and quartz stockwork veins, therefore it is likely that each one contributed hydrothermal fluids to enhance the size of this giant ore deposit. The porphyry phases have been classified based on relative timing of emplacement in four zones across the deposit (Taco-Bornita, Usupallares, Oscarina, and Condorcocha. Different porphyry phases are present in each zone and the relative timing of each phase is denoted by the abbreviation P1, P2, P3, etc., where P1 is the oldest and P3 is the youngest phase. U-Pb zircon (LA-ICP-MS and CA-TIMS) ages range from 10.95 ± 0.20 to 10.24 ± 0.23 Ma for ten porphyry phases dated in this study. The Taco-Bornita zone comprises the bulk of the economic resource at Antamina and hosts 5 porphyry phases (10.95 ± 0.20 to 10.25 ± 0.20 Ma). The Usupallares zone (southwest of the Taco-Bornita zones) hosts three porphyry phases (10.44 ± 0.14 to 10.24 ± 0.23 Ma). Skarns completely surround the Taco-Bornita and Usupallares zones. The Oscarina zone hosts at least two subparallel porphyry dykes that cut across skarns in the northeast Taco zone (10.81 ± 0.02 to 10.54 ± 0.11 Ma). The Condorcocha zone hosts at least three porphyry phases (two observed and one inferred) and a small skarn located approximately 1 km northwest of the Taco zone; only one age was obtains for P2-Condorcocha, 10.61 ± 0.12 Ma. One endoskarn titanite sample returned a discordant U-Pb age of 11.2 ± 1.3 Ma, which spans the entire range of U-Pb ages for the deposit. Three new $^{40}Ar/^{39}Ar$ hydrothermal biotite ages include 11.4 ± 0.5 to 10.5 ± 0.4 Ma in P1-Taco and 10.2 ± 0.2 Ma in P2-Taco. Molybdenite mineralisation occurs in two stages across the Taco-Bornita and Usupallares zones. Stage I molybdenite occurs in skarns; Re-Os ages include 10.58 ± 0.07 Ma and 10.44 ± 0.05 to 10.39 ± 0.05 Ma. Stage II molybdenite + quartz veins cut across P2 and P3 porphyries and Re-Os ages include 9.99 ± 0.04 and 9.68 ± 0.05 Ma. In general, U-Pb zircon and Re-Os molybdenite ages decrease from northeast to southwest along the structurally-controlled axis of the deposit. The formation of the giant Antamina skarn deposit is attributed to the emplacement of multiple fertile porphyries along a NE-trending, dilational structural corridor, into reactive calcareous wall rocks, over approximately 1.1 Ma, starting as early as ~11 million years ago.

3.2. Introduction

3.2.1. Research Subject

Skarn deposits are related in space and time to a magmatic-hydrothermal fluid sourced from an intrusion. This can be an adjacent intrusion or an intrusion at depth that is connected via structural pathways. One of the key questions in skarn research is: which is the causative intrusion(s)? Because porphyry deposits are often comprised of more than one intrusive phase, a study on the skarn-porphyry connection requires careful documentation of each phase and its relative timing relationship to the skarns under investigation.

This chapter presents new observations on the intrusive sequence and its relationship to skarn formation at Antamina. Specifically, this research focused on determining the number of intrusive phases present in 4 zones of the deposit (based on 4 cross sections; Fig. 1.5). Within each zone, cross-cutting relationships were documented in order to determine the relative timing of emplacement of each phase, and its relationship to the skarns. New geochronology ages were obtained for key porphyry phases in the context of the intrusive sequence. In addition to the intrusions, hydrothermal biotite, molybdenite, and skarn titanite were dated to provide additional age constraints on the formation and duration of the Antamina magmatic-hydrothermal system. These data are combined into an age-constrained model for porphyry and skarn formation at Antamina. Building upon the deposit geology that is summarized in Chapter 1, this chapter begins with a review of the porphyry nomenclature from previous work on Antamina.

3.2.2. Evolution of the Nomenclature of the Antamina Porphyries

Two different approaches to porphyry classification have been used by previous workers at Antamina: one based on relative timing (Pacheco, 1997; Sillitoe, 1997), and another based on texture and mineralogy (McKee et al., 1979; CMA, 2007; Love et al., 2003; Lipten and Smith, 2005; Escalante, 2008). Sillitoe (1997) noted abrupt contacts between the porphyry units at Antamina and suggested a classification scheme based on relative timing (i.e., early- and inter-mineral porphyries). Around the same time, Pacheco (1997) suggested a more elaborate classification scheme, employing categories for early-, inter-, late-, and post-mineral porphyries with sub-categories based on alteration intensity, vein type and density, mineralisation, and location in the deposit. Sometime between 1997 and 2000, the relative

timing classification scheme was abandoned for the texture and mineralogy-based scheme that remains in use today, which includes rock units named IPPA (plagioclase-rich porphyry), IPPAMO (plagioclase-rich porphyry with K-feldspar megacrysts), IPPAO (plagioclase and K-feldspar rich porphyry), and IPPEO (K-feldspar porphyry with minor plagioclase) (Lipten and Smith, 2005). In the case of the Oscarina dykes, Escalante (2008) assigned different names to these dykes based on their location along strike: exposures along the northeast margin of the Taco zone were referred to as the Quarry Bench and Ridge Road dykes (Table A3.1); only exposures to the south of the Taco zone were called Oscarina dykes. In this study I refer to all of the dykes emplaced along the same structural trend (between Condorcocha and south of the Taco zone) as the Oscarina dykes.

Due to the textural and mineralogical similarities across the entire deposit, I found that classification of the Antamina porphyries was most straightforward when performed in the context of crosscutting relationships. Therefore, in this study I employ a porphyry classification scheme based on relative timing of emplacement. As a result, the unit names I have assigned to the porphyries do not always match those published in earlier literature. Whenever necessary, the correlative published name and reference is provided for clarity.

3.3. Methods

Several methods were employed to establish the intrusive sequence for the APC, Condorcocha, and Oscarina, and understand the magmatic-hydrothermal evolution of the Antamina deposit, including; (1) documentation of cross-cutting relationships observed in drill core and outcrops; (2) U-Pb dating of magmatic zircon by laser ablation-inductively coupled plasma-mass spectrometry (LA-ICP-MS) and chemical abrasion-thermal ionization mass spectrometry (CA-TIMS); (2) U-Pb dating of hydrothermal titanite in exoskarn by LA-ICP-MS; (3) $^{40}Ar/^{39}Ar$ dating of secondary biotite, and; (4) Re-Os dating of molybdenite. Geochronology samples were selected from key intrusive phases in each of the four porphyry zones with the intention of bracketing the age of magmatism, hydrothermal alteration, and mineralisation.

3.3.1. Whole Rock Geochemistry

Whole rock geochemical analyses were conducted at ALS Chemex in Lima, Peru using a combination of techniques including X-ray fluorescence (XRF), inductively coupled plasma-atomic emission spectrometry (ICP-AES), inductively coupled plasma-mass spectrometry (ICP-MS), and atomic absorption (AA), for 60 elements including major and trace elements and LOI (loss on ignition). The sample digestion and measurement methods with analytical detection limits are presented in Digital Appendix 2.1.

3.3.2. U-Pb Dating of Zircon and Titanite by LA-ICP-MS

Ten porphyry zircon samples, and one endoskarn titanite sample were selected for U-Pb dating. Mineral separation and sample preparation was carried out at the James Cook University (JCU) Mineral Separation Laboratory in Townsville, Australia and at the University of Tasmania (UTAS) in Hobart, Australia. The JCU heavy mineral extraction and sample preparation procedures are described by Holm et al. (2013) and Tucker et al. (2013). Least-altered, representative samples were selected for dating; when necessary, groundmass was separated from xenoliths and/or quartz veins using a trim saw prior to crushing. Samples were crushed and milled to 500 µm, washed and decanted several times to remove the clay-sized fraction, then dried overnight in an oven. The high-density mineral fraction (including zircon, titanite, etc.) was extracted using a combination of heavy liquids (lithium heteropolytungstate (LST), density = 2.85 g/mL) and Frantz magnetic separation (magnetic current settings up to 1.2 A, side slope 10°). Zircons or titanite in the non-magnetic fraction > 1.2 A were hand-picked under a binocular microscope and mounted in an epoxy resin puck. The puck was polished to reveal mid-sections of grains before carbon coating. In order to document zoning, inclusions, and microstructures in the zircons, cathodoluminescence (CL) images were obtained prior to laser ablation (for samples analysed at JCU; no CL images were obtained for samples analysed at UTAS).

U-Pb dating by LA-ICP-MS technique (e.g., Chang et al., 2006) was conducted at the JCU Advanced Analytical Centre (AAC) in Townsville, Australia using a GeoLas Pro 193 nm ArF Excimer laser ablation system coupled with a Bruker (previously Varian) 820-MS inductively coupled plasma-mass spectrometer (ICP-MS), following the method described by Tucker et al. (2013). Laser energy density was set to 6 J/cm^2, and laser spot size and repetition rate

were set to 44 µm and 10 Hz, respectively. Total analysis time was 60 seconds; background concentrations were measured for the first 30 seconds (gas blank measurement, laser operating with shutter closed), followed by 30 seconds of sample ablation. Standard bracketing was used to correct for elemental fractionation, mass bias, and instrumental drift (Gehrels et al., 2008). For zircon analyses, NIST 612 reference material standard glass (USGS working values, 2009) was analysed (for calibration of U and Th concentrations, using Si as the internal standard and assuming stoichiometry) at the start, middle, and end of each laser session. Two to three analyses each of a primary zircon standard (GJ-1, 608.5 ± 0.4 Ma; Jackson et al., 2004) and secondary standard (Temora-2, 416.8 ± 0.3 Ma; Black et al., 2004) were conducted at the start and end of each session, as well as between every 10-12 unknown zircon analyses (Fig. A3.1). For titanite analysis, bracketing external standards included NIST 612 and MKED1 (Spandler et al., 2016), Khan, and OLT1, with ^{43}Ca used as the internal standard. Data reduction for titanite and zircon was performed off-line using GLITTER 4.0 software (Van Achterbergh et al., 2001). Time-resolved isotope signals from standards and samples were filtered for spikes indicative of inclusions or other heterogeneities. The overall data quality for this titanite sample are poor, yielding no concordant ages. Therefore the final age was determined using a common Pb-correction and a best-fit line through the discordant array.

Additional U-Pb dating (LA-ICP-MS) of zircon was conducted at the University of Tasmania in Hobart. The analyses in this study were performed on an Agilent 7500cs quadrupole ICP-MS with a 193 nm Coherent ArF laser and the Resonetics S155 ablation cell. The downhole fractionation, instrument drift and mass bias correction factors for Pb/U ratios on zircons were calculated using 2 analyses on the primary standard (91500 standard of Wiendenbeck et al. 1995) and one analysis on each of the secondary standard zircons (Temora standard of Black et al., 2003 and GJ-1 of Jackson et al., 2004) analysed at the beginning of the session and every 15 unknown zircons (roughly every 1/2 hour) using the same spot size and conditions as used on the samples. The correction factor for the ^{207}Pb/^{206}Pb ratio was calculated using large spots of NIST 610 analysed every 30 unknowns and corrected using the values recommended by Baker et al. (2004).

Each analysis on the zircons began with a 30 second blank gas measurement followed by a further 30 seconds of analysis time when the laser was switched on. Zircons were sampled on

32 micron spots using the laser at 5 Hz and a density of approximately 2 J/cm^2. A flow of He carrier gas at a rate of 0.35 litres/minute carried particles ablated by the laser out of the chamber to be mixed with Ar gas and carried to the plasma torch. Isotopes measured were ^{49}Ti, ^{56}Fe, ^{90}Zr, ^{178}Hf, ^{202}Hg, ^{204}Pb, ^{206}Pb, ^{207}Pb, ^{208}Pb, ^{232}Th and ^{238}U with each element being measured every 0.16 s with longer counting time on the Pb isotopes compared to the other elements. Element abundances on zircons were calculated using the method outlined by Kosler (2001) using Zr as the internal standard element, assuming stoichiometric proportions and using the NIST 610 as the external standard. Data reduction was performed off-line using an in-house spreadsheet.

The reduced data (for both JCU and UTAS samples) were exported to Microsoft Excel and age calculations were conducted using Isoplot/Ex 4.15 (Ludwig, 2012). The young ages of these samples (~10 Ma) required that all analyses be corrected for initial Th/U disequilibrium following Holm et al. (2013); ^{230}Th is excluded during zircon crystallization (due to isotope fractionation), which results in a deficit of measured ^{206}Pb as a ^{230}Th decay product (Schärer, 1984; Parrish, 1990). The upward correction of ^{206}Pb/^{238}U ages (on the order of 100 k.y.) utilizes Th/U concentrations determined from LA-ICP-MS and whole rock analyses for each sample, taken to represent the Th/U concentration of the melt (Crowley et al., 2007). A conservative discordance cut-off of 15% was applied to all data points before calculating the weighted average age of each sample (e.g., Buys et al., 2014; Holm and Poke, 2018). The youngest zircon population passing the 15% discordance cut-off (minimum n = 3 zircons, MSWD $\leq$ 1.5) was selected to represent the crystallization age of each sample; in many cases, older and/or younger zircons did not meet these criteria and are not included in the age calculations. Errors were propagated at the 2σ level and the ages are reported at the 95% confidence interval level. The complete U-Pb zircon and titanite (LA-ICP-MS) data sets are presented in Digital Appendices 3.1 and 3.2.

3.3.3. U-Pb Dating of Zircon by CA-TIMS

U-Pb dating by CA-TIMS was conducted at the Pacific Centre for Isotopic and Geochemical Research at the University of British Columbia in Vancouver, Canada, using the procedure modified from Mundil et al. (2004), Mattinson (2005), and Scoates and Friedman (2008). Zircons were handpicked under alcohol from heavy mineral separates of the rock samples. The clearest, crack- and inclusion-free grains are selected, photographed and then annealed in

quartz glass crucibles at 900˚C for 60 hours. Annealed grains are transferred into 3.5 mL PFA screw top beakers, ultrapure HF (up to 50% strength, 500 mL) and HNO_3 (up to 14 N, 50 mL) are added and caps are closed finger tight. The beakers are placed in 125 mL PTFE liners (up to four per liner) and about 2 mL HF and 0.2 mL HNO_3 of the same strength as acid within beakers containing samples are added to the liners. The liners are then slid into stainless steel Parr™ high pressure dissolution devices, which are sealed and brought up to a maximum of 200˚C for 8-16 hours (typically 175˚C for 12 hours). Beakers are removed from liners and zircon is separated from leachate. Zircons are rinsed with >18 MΩ.cm water and sub-boiled acetone. Then 2 mL of sub-boiled 6N HCl is added and beakers are set on a hotplate at 80˚-130˚C for 30 minutes and again rinsed with water and acetone. Masses are estimated from the dimensions (volumes) of grains. Single grains are transferred into clean 300 mL PFA microcapsules (crucibles), and 50 mL 50% HF and 5 mL 14 N HNO_3 are added. Each is spiked with a $^{233\text{-}235}$U-^{205}Pb tracer solution (EARTHTIME ET535), capped and again placed in a Parr liner (8-15 microcapsules per liner). HF and nitric acids in a 10:1 ratio, respectively, are added to the liner, which is then placed in Parr high pressure device and dissolution is achieved at 240˚C for 40 hours. The resulting solutions are dried on a hotplate at 130˚C, 50 mL 6N HCl is added to microcapsules and fluorides are dissolved in high pressure Parr devices for 12 hours at 210˚C. HCl solutions are transferred into clean 7 mL PFA beakers and dried with 2 mL of 0.5 N H_3PO_4. Samples are loaded onto degassed, zone-refined Re filaments in 2 mL of silicic acid emitter (Gerstenberger and Haase, 1997).

Isotopic ratios are measured a modified single collector VG-54R or 354S (with Sector 54 electronics) thermal ionization mass spectrometer equiped with analogue Daly photomultipliers. Analytical blanks are 0.2 pg for U and up to 1 pg for Pb. U fractionation was determined directly on individual runs using the EARTHTIME ET535 mixed $^{233\text{-}235}$U-^{205}Pb isotopic tracer and Pb isotopic ratios were corrected for fractionation of 0.30%/amu, based on replicate analyses of NBS-982 reference material and the values recommended by Thirlwall (2000). Data reduction employed the excel-based program of Schmitz and Schoene (2007). Standard concordia diagrams were constructed and regression intercepts, weighted averages calculated with Isoplot (Ludwig, 2003). Unless otherwise noted all errors are quoted at the 2 sigma or 95% level of confidence. Isotopic dates are calculated with the decay constants l_{238}=1.55125E-10 and l_{235}=9.8485E-10 (Jaffe et al., 1971). EARTHTIME U-Pb synthetic solutions are analysed on an on-going basis to monitor the accuracy of results. Data

uncertainties are reported at the 95% confidence interval level. The complete data set is presented in Digital Appendix 3.3.

3.3.4. Re-Os Dating of Molybdenite

Five molybdenum samples (two endoskarn, one exoskarn, and two quartz + molybdenite veins in intrusions) were selected for Re-Os dating. Molybdenite extraction, sample preparation, and Re-Os analysis was carried out at the Canadian Centre for Isotopic Microanalysis at the University of Alberta, Canada. A molybdenite mineral separate was produced by metal-free crushing followed by gravity and magnetic concentration methods. Methods used for molybdenite analysis are described in detail by Selby and Creaser (2004) and Markey et al. (2007). The ^{187}Re and ^{187}Os concentrations in molybdenite were determined by isotope dilution mass spectrometry using Carius-tube, solvent extraction, anion chromatography and negative thermal ionization mass spectrometry techniques. A mixed double spike containing known amounts of isotopically enriched ^{185}Re, ^{190}Os, and ^{188}Os analysis is used. Isotopic analysis is made using a ThermoScientific Triton mass spectrometer by Faraday collector. Total procedural blanks for Re and Os are less than < 3 picograms and 2 picograms, respectively, which are insignificant for the Re and Os concentrations in molybdenite. The molybdenite powder HLP-5 (Markey et al., 1998) is analyzed as a standard, and over a period of one year an average Re-Os date of 220.66 ± 0.21 Ma (1 standard deviation uncertainty, n = 5) is obtained. This Re-Os age date is identical to that reported by Markey et al. (1998) of 221.0 ± 1.0 Ma. The age uncertainty is quoted at the 2σ level, and includes all known analytical uncertainty, including uncertainty in the decay constant of ^{187}Re.

3.3.5. ^{40}Ar/^{39}Ar Dating of Hydrothermal Biotite

Three samples of hydrothermal biotite were dated using ^{40}Ar/^{39}Ar geochronology at the Argon Geochronology Laboratory at the University of Michigan, USA. Biotite grains (0.5-3 mm) were handpicked under a binocular microscope. The pure mineral separates were wrapped in Al foil and irradiated for 90 MWhr at location 8B at the McMaster Nuclear Reactor at McMaster University in Hamilton, Ontario in irradiation packages mc48 and mc52. Standard hornblende MMhb-1 was used as a neutron fluence monitor with an assumed age of 520.4 Ma (Samson and Alexander, 1987). Following irradiation, the samples were

incrementally heated with a Coherent Innova 5 W continuous argon-ion laser until complete fusion was achieved. Samples were loaded into 3 adjacent 2 mm diameter wells and degassed each laser power setting for 30 seconds.

Dating was conducted using a standard procedure described by Frey et al. (2007) and Rooney et al. (2013). Argon isotopes were measured using a VG1200S mass spectrometer with a source operating at 150 μA total emission and equipped with a Daly detector operating in analog mode. Mass discrimination was monitored daily using ~4 x 10^{-9} ccSTP of atmospheric Ar. Fusion system blanks were run every five fusion steps and blank levels from argon masses 36 through 40 (~2 x 10^{-14}, ~3 x 10^{-14}, ~1 x 10^{-14}, ~3 x 10^{-14}, and 2 x 10^{-12} ccSTP respectively) were subtracted from sample gas fractions. Corrections were also made for the decay of ^{37}Ar and ^{39}Ar, as well as interfering nucleogenic reactions from K, Ca, and Cl as well as the production of ^{36}Ar from the decay of ^{36}Cl. The step heating data are presented in Digital Appendix 3.4 and the age spectra in Fig. A3.2. The plateau ages (and error-weighted plateau ages) are used for age reporting. The age uncertainties have incorporated 1% combined uncertainties of external factors including decay constants, standard ages and the ^{40}K/K ratio, and are at the 2-sigma level.

3.3.6. Major Element Mineral Compositions

Major element compositions of selected minerals in polished thin sections were determined *in situ* using a JEOL JXA-8200 Superprobe equipped with a wavelength-dispersive spectroscopy (WDS) system, housed in the AAC at JCU. WDS analyses were collected for plagioclase and biotite in selected Antamina porphyry samples. The microprobe was operated at 15 keV acceleration voltage, 20 nA current, and 5 μm beam size. Analytical conditions are as follows [element analysed (standard, line, crystal)]: Na (albite, Kα, TAP), Fe (hematite, Kα, LIF), Mn (spessartine, Kα, LIFH), F (F-TAP, Kα, TAP), Cl (tugtupite, Kα, PETJ), Si (wollastonite, Kα, TAP), Ti (rutile, Kα, LIF), Al (almandine, Kα, TAP), Ca (wollastonite, Kα, PETJ), Mg (olivine, Kα, TAP), and K (orthoclase, Kα, PETJ). Element concentrations were calculated by applying φρz corrections. The complete data set for igneous biotite and plagioclase is available in Digital Appendix 3.5 and 3.6, respectively.

3.4. Results

3.4.1. Cross-Cutting Relationships

The intrusion paragenesis was determined in each zone through careful examination of crosscutting relationships (described below) and porphyry unit names were assigned based on the relative timing of emplacement, for example, “P1a-Taco”. The prefix “P” denotes “porphyry” and is followed by a number to indicate timing (i.e., P2 cuts P1; P3 cuts both units). Where sub-units were later identified, a letter (in alphabetical order) follows the number to denote additional order (i.e., P2b cuts P2a and P1; all are cut by P3). The name of the zone is denoted after the unit (i.e., P1-Taco, P2a-Taco, etc.); for instance, P1-Taco and P1-Usupallares are the earliest intrusions in each respective zone, however they are different units. Using this naming scheme, the intrusive sequence was recorded for the APC, Condorcocha, and Oscarina.

Contact relationships between porphyries (of different relative timing) and skarns provide important clues for determining the intrusion paragenesis. The APC is comprised of early and inter-mineralisation porphyries; all of the porphyries are at least weakly mineralized, not all contain endoskarn alteration. Only early porphyries contain endoskarn alteration, because they were emplaced during (or slightly before) skarn formation; they occur early in the intrusion paragenesis (i.e., P1; Fig. 3.1 A) and are commonly cross-cut by inter-mineralisation porphyries and/or quartz stockwork veins (Fig. 3.1 B-C).

The endoskarn-exoskarn contact is a lithological boundary that has been overprinted by skarn alteration; it marks the original emplacement contact between wall rock (marble) and an early porphyry (P1). Contacts between early porphyries (or skarns) and inter-mineralisation porphyries are typically sharp and can be marked by truncated veins, chilled margins, and abrupt changes in rock type and/or alteration style (Fig. 3.1 C-D). At Antamina, most porphyry units contain stockwork veins, and in general, the volume of stockwork veins increases with the relative age of each porphyry unit. As such, each progressively younger porphyry unit truncates veins and alteration assemblages in older units (Fig. 3.1 D-E). Xenoliths entrained in younger porphyries also provide compelling evidence for the relative timing of porphyry emplacement (Fig. 3.1 E).

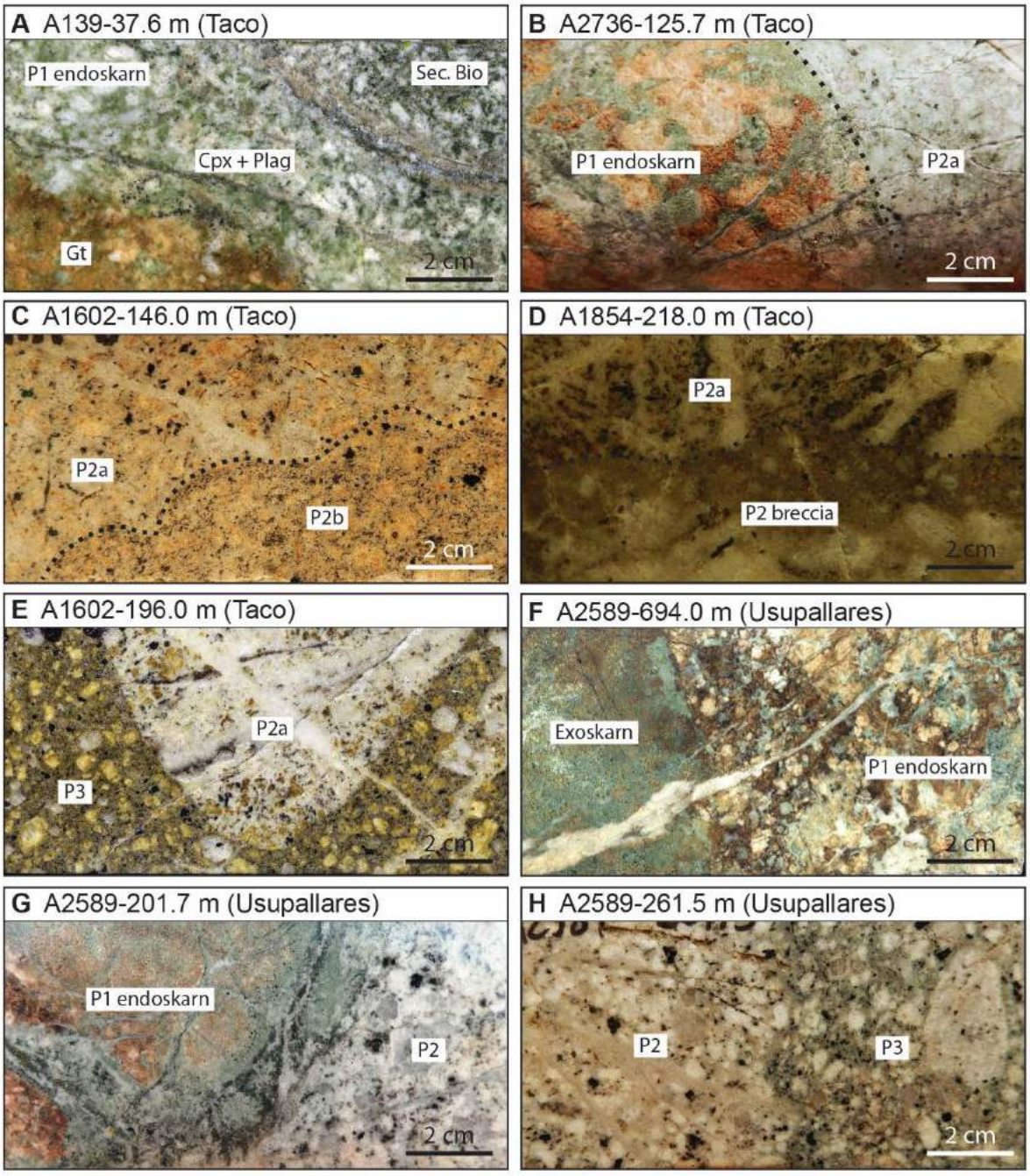

Fig. 3.1. Examples of some cross-cutting relationships used to determine the intrusion sequence at Antamina. A. P1-Taco altered to endoskarn, indicating that it was emplaced early in the paragenesis. B. P1-Taco altered to endoskarn and cross-cut by quartz + sulphide stockwork veins. C. Fine grained P2b-Taco cuts across P2a-Taco. Note the truncated quartz vein. D. P2 breccia truncates quartz stockwork veins in P2a-Taco. E. A xenolith of P2a-Taco is enclosed in P3-Taco. F. Metasomatic contact between P1-Usupallares (endoskarn) and exoskarn, Usupallares area. G. P1-Usupallares (endoskarn) is cross-cut by P2-Usupallares. H. P2-Usupallares and associated quartz stockwork veins are truncated by P3-Usupallares.

At Antamina, molybdenum mineralisation occurred in two stages: Stage I occurs as sinuous veins and patchy replacements in both P1 (Taco and Usupallares), endoskarn, and exoskarn (Fig. 3.2 A-C), whereas Stage II occurs as straight-edged veins of molybdenite + quartz cutting across all porphyries and skarns (Fig. 3.2 D-E). The mineral paragenesis is described in detail in Chapter 4.

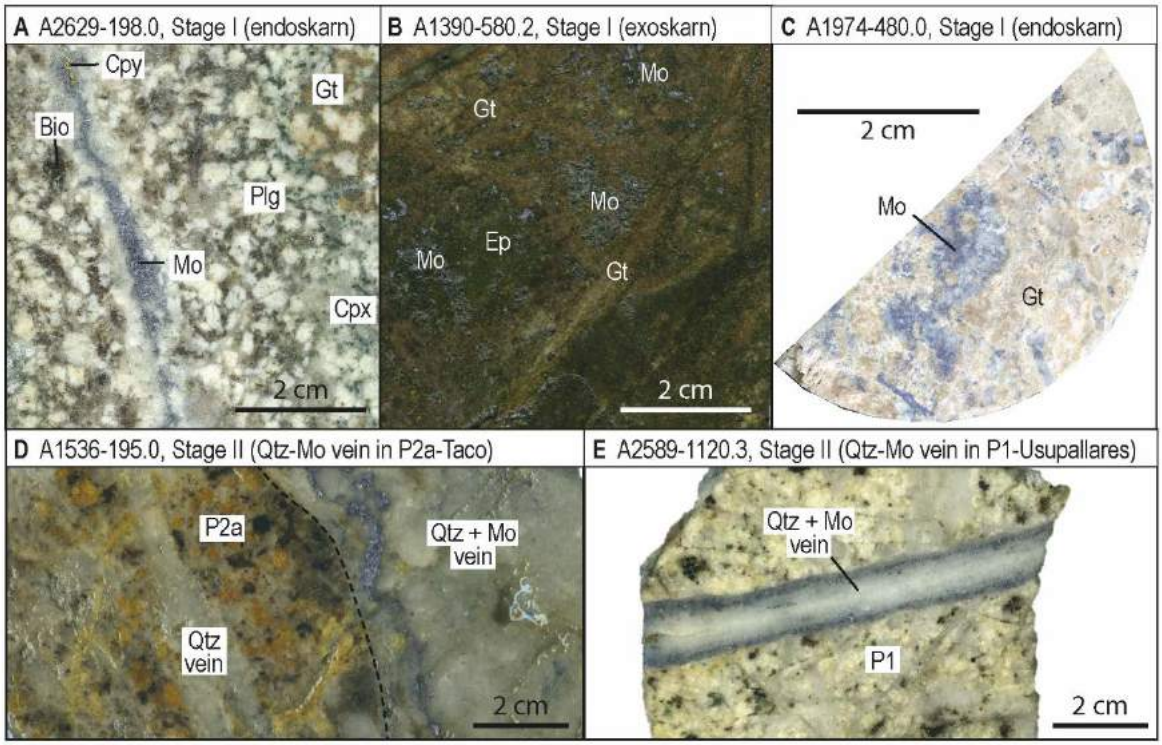

Fig. 3.2. Molybdenite mineralisation stages and samples selected for Re-Os dating. A. Stage I molybdenite vein in P1 endoskarn, Taco-Oscarina zone. B. Stage I molybdenite in exoskarn, Taco zone. C. Stage I molybdenite in P1 endoskarn, Usupallares zone. D. Stage II molybdenite + quartz vein in P2a, Taco zone. E. Stage II molybdenite + quartz vein in P1, Usupallares zone.

3.4.2. Igneous Rock Types – Mineralogy and Textures

All of the samples are porphyritic and contain 50-80% phenocrysts, except for P1-Oscarina with 40% phenocrysts (Table 3.1). Most phenocrysts are a few millimetres in size. Megacrystic K-feldspar (≥ 40 mm) occurs in ~50% of the phases observed and is not diagnostic of any specific phase or location in the deposit. Quartz phenocrysts range from 3-10% of the rock volume and are typically rounded and embayed in the Taco and Oscarina zones. All phases contain plagioclase phenocrysts, with the compositions ranging from An_{23}

Table 3.1. Texture, mineralogy, and modal composition of Antamina porphyries.

	P1-Taco	P2a-Taco	P2b-Taco	P3-Taco	P1-Usupallares	P2-Usupallares	P3-Usupallares	P1-Oscarina	P2-Oscarina	P2-Condorcocha	P3-Condorcocha
Rock Type*	Trachyandesite porphyry	Trachyandesite porphyry	Trachyandesite porphyry	Trachyandesite porphyry	Trachyandesite porphyry	Trachyandesite porphyry	Trachyandesite porphyry	Trachyandesite porphyry	Trachyte porphyry	Trachyandesite porphyry	Andesite porphyry
Texture	Porphyritic	Porphyritic (megacrystic)	Porphyritic	Porphyritic (megacrystic)	Porphyritic (megacrystic)	Porphyritic (megacrystic)	Porphyritic (megacrystic)	Porphyritic	Porphyritic	Porphyritic	Porphyritic
Phenocrysts	75%	80%	65%	60%	80%	85%	65%	40%	60%	65%	50%
Quartz	3-5%, anh, emb, ≤ 5 mm	5-8%, sub, emb, 5-10 mm	5-7%, sub, emb, ≤ 5 mm	2-8%, sub, emb, 4-10 mm	7-10%, sub, 5-10 mm	7-10%, sub-euh, 5-15 mm	7-10%, sub, 8-10 mm	3-5%, anh, emb, 5-8 mm	5-7%, anh, 5-8 mm	7-10%, sub, 7-10 mm	3-5%, sub, 5-8 mm
Plagioclase	40-55%, sub, 2-5 mm, An_{23-45}	40-50%, sub, 4-10 mm, An_{27-30}	35-45%, sub, 1-3 mm	15-30% sub glom, 4-10 mm, An_{26-35}	40-45%, anh, 5-8 mm, An_{25-38}	40-45%, sub-euh, 5-8 mm, An_{25-30}	30-40%, sub, 8-10 mm	10-15%, sub, 5-8 mm	20-30%, sub, 3-5 mm	20-30%, anh-sub, 5-8 mm	15-25%, sub, 1-3 mm
K-feldspar	2-5%, anh, 2-4 mm	10-15%, euh mgx ≤ 50 mm	10-15%, sub, 2-4 mm	10-15%, euh mgx ≤ 10%, ≤ 50 mm	15-20%, anh, 2-4 mm	15-20%, sub-euh, 2-4 mm; mgx ≤ 10%, ≤ 70 mm	10-15%, sub, 5-15 mm	10-15%, sub, 5-8 mm	15-20%, sub, 3-5 mm	15-20%, sub, 5-8 mm	10-15%, sub, 2-4 mm
Biotite	10-15%, 3-5 mm	10-15%, 2-3	8-10%, 2-3	7-10%, 3-5 mm	5-10%, 5-7 mm	5-10%, 5-7 mm	8-15%, 3-5 mm	7-10%, 3-5 mm	5-10%, 2-3	8-12%, 3-5 mm	7-10%, 3-5 mm
Amphibole	≤ 3%, 1-4 mm	Nil	Nil	Nil	Nil	Nil	Nil	≤ 5%, 2-5 mm	3-5%, 2-5 mm	1-3%, 2-5 mm	3-5%, 2-5 mm
Groundmass	25%	20%	35%	40%	20%	15%	35%	60%	40%	35%	50%
Quartz	7-10%	7-10%	10-15%	10-15%	7-10%	5-10%	5-10%	10-15%	5-10%	5-10%	5-10%
Plagioclase	10-15%	7-10%	10-15%	10-15%	5-10%	5-10%	7-10%	15-20%	10-15%	10-15%	10-15%
K-feldspar	5-15%	~5%	~5%	10-15%	~5%	~5%	10-15%	20-25%	10-15%	10-15%	10-15%
Biotite	3%	2%	5%	5%	2%	2%	5%	5%	2%	5%	3%
Qtz Stock-work Veins	Abundant	Abundant	Abundant	Common	Common	Common	Rare	Rare	Rare	Common	Rare
Accessory Minerals	Mt, Ap, Tit, Zrn	Mt, Ap, Tit, Zrn	Mt, Ap, Tit, Zrn	Mt, Ap, Tit, Zrn	Mt, Ap, Tit, Zrn	Mt, Ap, Tit, Zrn	Mt, Ap, Tit, Zrn	Mt, Ap, Tit, Zrn	Mt, Ap, Tit, Zrn	Mt, Ap, Tit, Zrn	Mt, Ap, Tit, Zrn
Pervasive Alteration	≤ 45% sec Bio; endo; Chl aft Bio	≤ 20% sec Bio; Chl aft Bio	≤ 20% sec Bio; Chl aft Bio	≤ 20% sec Bio; Chl aft Bio	≤ 15% sec Bio; endo; Chl aft Bio	≤ 15% sec Bio; Chl aft Bio	≤ 10% Chl aft Bio	≤ 10% Chl aft Bio; minor Cal + Epi + Prh**	≤ 5% Chl aft Bio; minor Cal + Ill**	≤ 20% sec Bio; minor endo; Chl aft Bio	≤ 10% Chl aft Bio; minor Ser
Comments	Contains unidirectional solidification textures (UST).	Displays some textural and compositional similarities to P2b-Taco.	Displays some textural and compositional similarities to P2a-Taco.	Narrow dikes, typically along pre-existing contacts.	Megacrystic texture preserved in some endoskarns.	Similar texture and composition, compared to P1-Usupallares, but lacks endoskarn.	Abundant xenoliths (skarn, intrusions), Qtz vein fragments.	Dike along thrust fault, intercepts NE Taco zone.	Dike along thrust fault, intercepts NE Taco zone.	No spatial overlap with Taco and Usupallares.	Dike along thrust fault. Connects Taco zone to Condorcocha.

Minerals: An: anorthite; Ap: apatite; Bio: biotite; Cal: calcite; Chl: chlorite; Epi: epidote; Ill: illite; Mt: magnetite; Or: orthoclase; Prh: prehnite; Qtz: quartz; Ser: sericite; Tit: titanite; Zrn: zircon.
Other: aft: after; anh: anhedral; emb: embayed; endo: endoskarn; euh: euhedral; glom: glomerocryst; mgx: megacryst; mm: millimeter; Nil: not observed; sec: secondary; sub: subhedral.
Qtz stockwork veins: Abundant: up to 40% volume; Common: up to 20% volume; Rare: less than 5% by volume. *Nomenclature and classification after Winchester and Floyd (1977). **Determined by XRD.

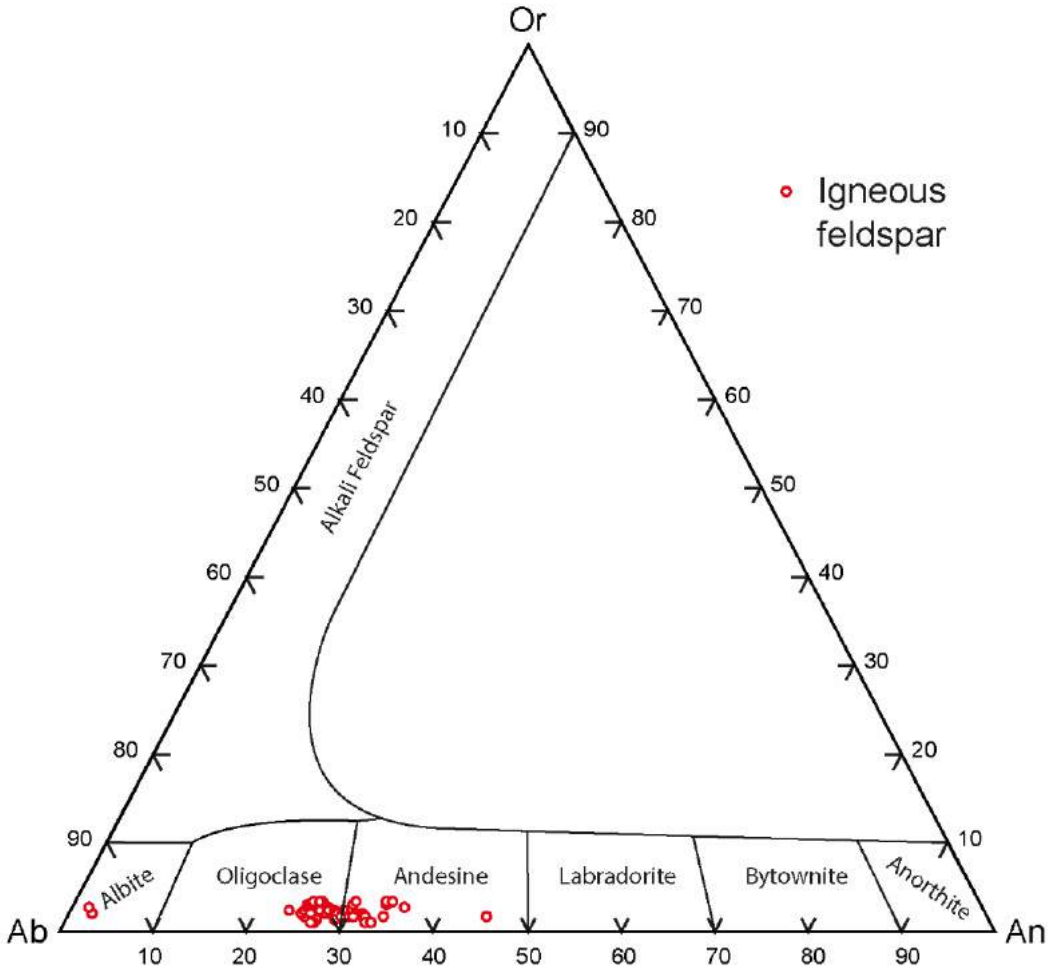

Fig. 3.3. Ternary plot of igneous plagioclase compositions from the Antamina porphyries, determined by microprobe analysis.

to An_{45} (Fig. 3.3 and Digital Appendix 3.6), based on electron microprobe analysis. Igneous biotite was observed in all samples and contains up to ~2.31 wt. % F and up to 0.2 wt. % Cl (Table 3.2 and Digital Appendix 3.5). Amphibole was only observed in early porphyry phases and dykes along the northeast margin of the APC, including P1-Taco, P1-Oscarina, P2-Oscarina, P2-Condorcocha, and P3-Condorcocha. All porphyry phases contain 5-15% biotite, and accessory minerals magnetite, apatite, titanite and zircon. Microprobe analyses of plagioclase and biotite are summarised in Fig. 3.3 and Table 3.2, respectively.

Table 3.2. Representative microprobe analyses of biotite from Antamina porphyries. Total Fe (listed as FeO) is assumed to be Fe^{2+} (as in Droop, 1987).

Rock Unit	P1-Taco	P2a-Taco	P3-Taco	P1-Usupallares	P2-Usupallares	P1-Oscarina
Sample	A2084-985	A1391-488	A1391-498	A2589-1142.5	A2589-367.5	AT13-029
Point no.	91	39	28	110	167	156
SiO_2	39.6	37.15	37.44	37.61	37.44	37.07
TiO_2	3.73	3.76	3.77	3.90	3.41	3.92
Al_2O_3	12.79	13.42	13.25	13.06	12.88	13.44
FeO	10.48	15.96	15.21	12.85	15.35	18.19
MnO	0.10	0.18	0.13	0.14	0.13	0.27
MgO	18.12	14.80	14.80	16.16	14.94	12.81
CaO	0.00	0.01	0.04	0.00	0.01	0.01
Na_2O	0.14	0.14	0.18	0.20	0.25	0.25
K_2O	10.1	9.92	9.91	10.0	9.93	9.58
F	1.11	1.45	0.98	1.08	1.06	0.47
Cl	0.06	0.14	0.14	0.08	0.17	0.09
Total	96.23	96.93	95.85	95.09	95.57	96.10

3.4.3. Geochemistry

The whole rock geochemical composition of all analysed igneous samples is provided in Digital Appendix 3.7 and a summary of representative sample compositions is provided in Table 3.3. The Antamina porphyries display a narrow range of major element compositions dominated by trachyte, trachyandesite, and andesite porphyries (Fig. 3.4). The compositional range of most of the individual rock types straddles the division between andesite and trachyandesite, however P2-Oscarina (n = 1) and P3-Condorcocha (n = 2) plot exclusively as trachyte and andesite, respectively (Fig. 3.4). Effort was made to select the least-altered samples, however due to the geological context of the samples, some alteration is to be expected (LOI ≤ 2.72 wt. %; Digital Appendix 3.7).

Trace element data are presented in Fig. 3.5 and Fig. 3.6. All samples show patterns within the range of typical arc magmas, with a distinct depletion in Nb and HFSE (such as Zr, Hf, and Ti), and enrichment in LILE, including Ba, Rb, K, and Pb. All samples display LREE enrichment (average La/Sm = 6.5) and HREE depletion (average Sm/Yb = 5.0), with samples from Taco, Usupallares, and Condorcocha showing greater depletion than the Oscarina dykes (Fig. 3.5). In general, all samples display listric-shaped REE patterns, which are likely to be

Table 3.3. Representative major and trace element data for selected Antamina porphyry samples.

Sample ID	P1-Oscarina AT13-029	P2-Oscarina A2810-186	P1-Taco A2084-985	P1-Taco A545-163	P2a-Taco A1854-670.8	P2b-Taco A1602-303	P3-Taco A1854-192	P1-Usupallares A2589-1120	P2-Usupallares A2589-367.5	P3-Usupallares A2589-301	P1-Condorcocha M-22
Al2O3	14.95	13.20	13.70	13.35	14.70	12.50	15.40	14.75	14.35	16.10	15.01
CaO	0.76	1.84	1.05	2.74	1.74	0.48	1.84	2.39	2.64	2.11	2.00
Fe2O3	3.94	2.28	1.08	1.65	2.28	2.05	2.39	2.14	0.98	2.02	3.83
K2O	9.19	7.85	8.67	6.21	6.13	8.53	6.62	4.15	4.98	6.73	4.05
MgO	1.04	0.17	1.00	0.87	0.95	1.00	1.30	0.79	0.62	1.25	1.32
MnO	0.03	0.08	0.01	0.02	0.03	0.06	0.04	0.03	0.02	0.02	0.06
Na2O	0.70	0.07	1.34	2.53	2.71	1.13	2.88	3.83	3.28	3.10	3.88
P2O5	0.18	0.07	0.14	0.13	0.15	0.15	0.20	0.13	0.13	0.18	0.16
SiO2	64.2	70.6	71.2	69.1	69.5	72.4	67.0	70.2	71.0	67.2	67.8
SrO	0.06	0.01	0.04	0.07	0.07	0.04	0.07	0.07	0.07	0.07	0.07
TiO2	0.50	0.05	0.42	0.37	0.44	0.40	0.56	0.37	0.36	0.54	0.49
LOI	2.47	2.72	0.83	1.83	0.30	0.54	0.63	0.47	1.06	0.81	0.90
Total	105.7	101.7	99.8	100.8	99.4	100.6	99.4	99.5	100.0	101.2	99.6
Ba	1115	194	902	750	947	869	730	667	695	1010	709
Ce	47.7	52.1	40.5	49.5	48.7	26.9	50.2	56.9	45.7	43.4	43.9
Cr	20	20	20	20	30	20	40	20	30	40	8.3
Cs	5.87	16.9	6.80	4.63	3.17	4.20	4.99	1.94	3.79	10.5	2.00
Dy	1.62	3.16	1.68	1.53	1.60	1.40	1.82	1.47	1.29	1.66	1.77
Er	0.83	1.70	0.68	0.56	0.72	0.60	0.93	0.57	0.60	0.81	0.90
Eu	0.26	0.44	0.60	0.78	0.77	0.59	0.96	0.90	0.76	0.82	0.79
Ga	20.9	14.8	22.5	20.2	21.6	20.3	24.5	23.3	22.0	25.4	19.4
Gd	2.39	3.53	2.12	2.20	2.27	1.62	3.06	2.31	2.18	2.72	2.52
Hf	3.5	3.3	3.2	2.9	3.8	3.5	4.6	3.4	3.6	4.0	3.5
Ho	0.25	0.56	0.27	0.22	0.28	0.21	0.37	0.22	0.24	0.25	0.32
La	22.4	29.6	19.8	25.9	25.5	12.8	25.1	29.2	21.8	20.3	22.0
Lu	0.13	0.20	0.07	0.11	0.12	0.1	0.15	0.06	0.08	0.11	0.13
Nb	8.0	29	7.1	6.0	7.2	5.9	6.5	6.3	5.6	6.0	7.9
Nd	23.0	19.6	18.6	19.9	20.2	14.3	24.7	23.3	20.6	22.0	20.2
Pr	5.65	5.74	4.54	5.11	5.50	3.42	6.17	5.86	5.37	5.34	5.24
Rb	320	243	218	119	138	209	158	97.9	132	209	104
Sm	3.90	4.08	3.20	3.16	3.55	2.21	4.22	3.62	3.43	3.89	3.47
Sn	3	2	2	2	2	2	3	2	3	3	2
Sr	440	31.7	627	588	548	296	581	591	535	581	589
Ta	0.7	2.3	0.6	0.6	0.6	0.6	0.6	0.6	0.5	0.5	0.7
Tb	0.29	0.56	0.31	0.28	0.29	0.23	0.36	0.28	0.25	0.34	0.34
Th	9.1	12	6.7	8.3	9.3	7.7	9.0	11	11	7.9	9.0
Tm	0.13	0.27	0.09	0.12	0.08	0.08	0.14	0.09	0.09	0.11	0.14
U	3.98	4.14	1.35	2.72	2.06	1.09	1.91	3.70	2.88	2.77	3.10
V	78	5	53	53	51	69	84	45	44	69	67
W	7	3	5	3	6	7	6	2	4	5	1
Y	7.8	18	7.2	6.9	7.5	6.5	9.1	7.0	6.4	7.7	8.7
Yb	0.87	1.7	0.66	0.51	0.67	0.59	0.73	0.70	0.43	0.65	0.90
Zr	136	113	122	109	127	128	161	122	117	137	118
Ag	3.8	1.6	2.5	2.5	0.0	1.1	0.0	2.5	0.0	0.7	963
Cu	163	4	88	52	160	2370	623	24	198	682	2227
Li	20	40	50	20	20	30	30	20	10	20	16
Mo	2	1	19	63	65	128	31	1	6	18	1
Ni	3	1	2	1	3	3	1	1	1	4	4
Pb	10000	119	4	8	9	7	8	11	10	12	13
Sc	5	2	4	4	5	4	6	4	3	5	6
Zn	1720	60	12	21	24	25	30	37	26	34	379
As	123	107	4	1	1	1	1	1	10	22	1
Bi	0.71	0.03	0.04	0.12	0.73	0.12	0.04	0.09	0.27	0.28	0.35
Hg	0.034	0.04	0.003	0.008	0.017	0.009	0.013	0.007	0.011	0.013	2.5
Sb	6.8	0.1	1.6	0.0	0.2	0.3	0.6	0.1	1.2	3.6	0.1
Se	1.6	0.6	0.4	0.3	0.5	1.3	0.3	0.3	0.3	0.4	0.2
Te	1.4	0.1	0.0	0.0	0.0	0.0	0.0	0.0	0.0	0.0	0.0

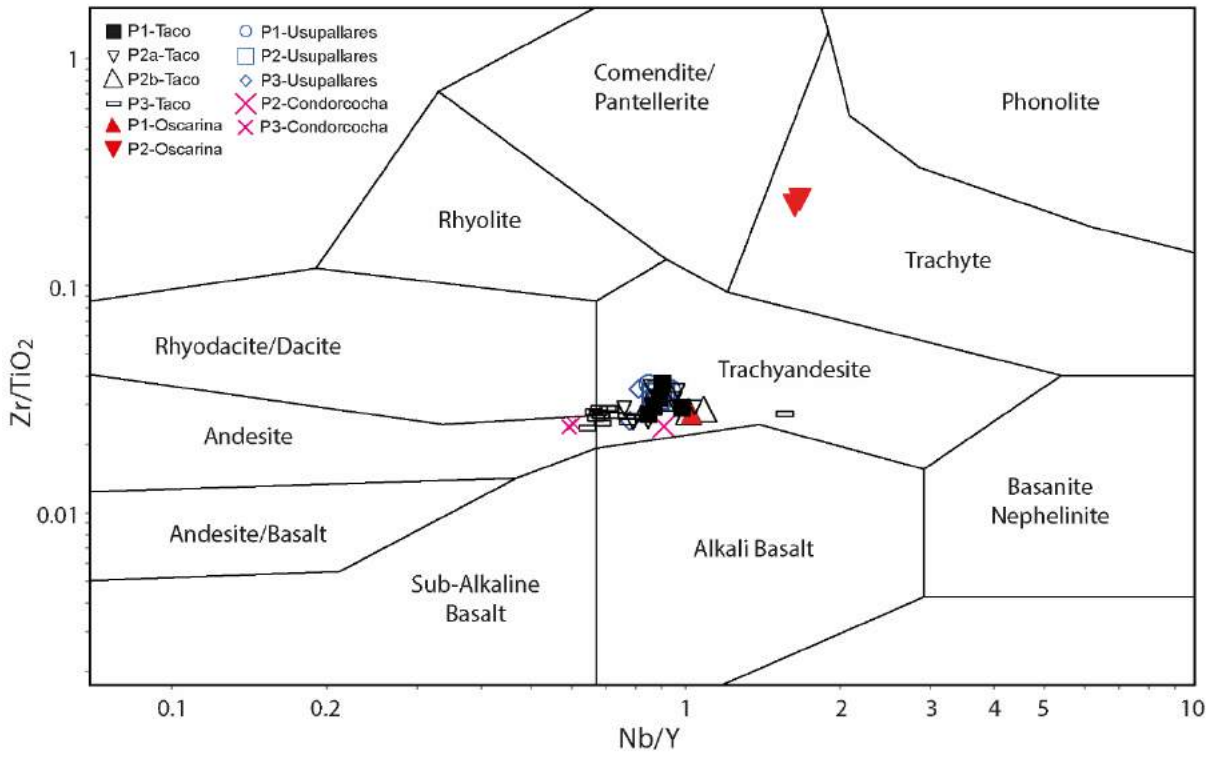

Fig. 3.4. Trace element classification of the Antamina porphyries (after Winchester and Floyd, 1977). All of the samples display porphyry textures. The complete geochemical data set is provided in Digital Appendix 3.7.

derived from fractionation in the presence of amphibole (i.e., Richards and Kerrich, 2007). Negative Eu anomalies are observed in the Oscarina samples, but not in any other samples; this may be due to high magmatic *f*O2 or suppression of plagioclase fractionation under high pH_2O conditions (e.g., Kay et al., 1991; Lang and Titley, 1998; Richards et al., 2001). Lead enrichment in P1- and P2-Oscarina is due to mineralisation (Fig. 3.5 B); LOI values for these samples range from 2.30-2.72 wt. % (i.e., Table 3.3 and Digital Appendix 3.7). All samples, except for P2-Oscarina, display adakite-like signatures ($Sr/Y \geq 20$; Fig. 3.6), which could also be a result of high-pressure magmatic fractionation.

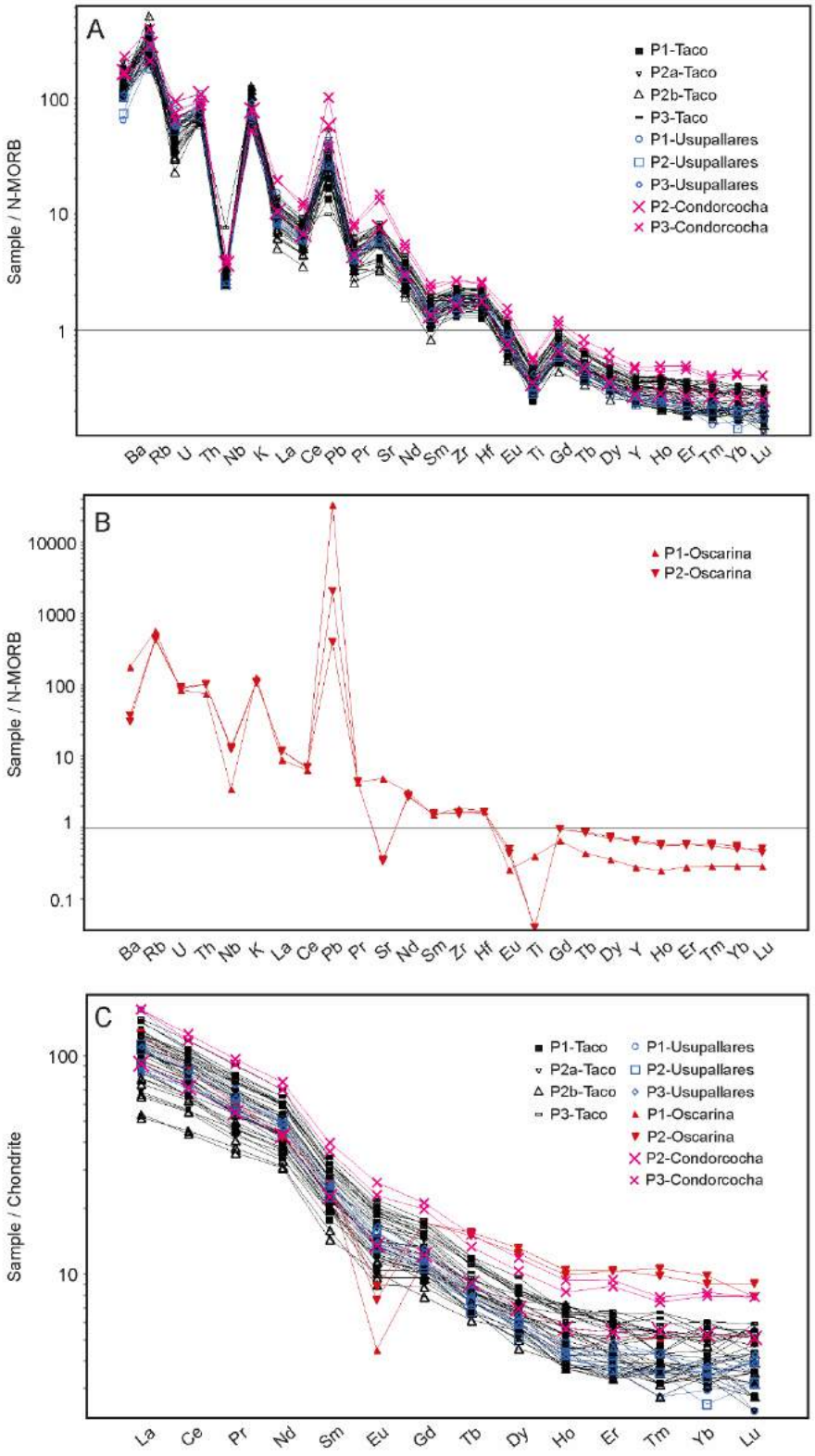

Fig. 3.5. Multi-element N-MORB and chondrite normalized plots for selected major, minor, and trace elements, including rare earth elements (after Sun and McDonough, 1989). All samples show patterns within the range of typical arc magmas; Pb enrichment in P1- and P2-Oscarina (B) is due to mineralisation. Panel C shows that the Oscarina magmas also have depleted Eu and enriched HREE relative to all other samples. The complete data set is available in Digital Appendix 3.7.

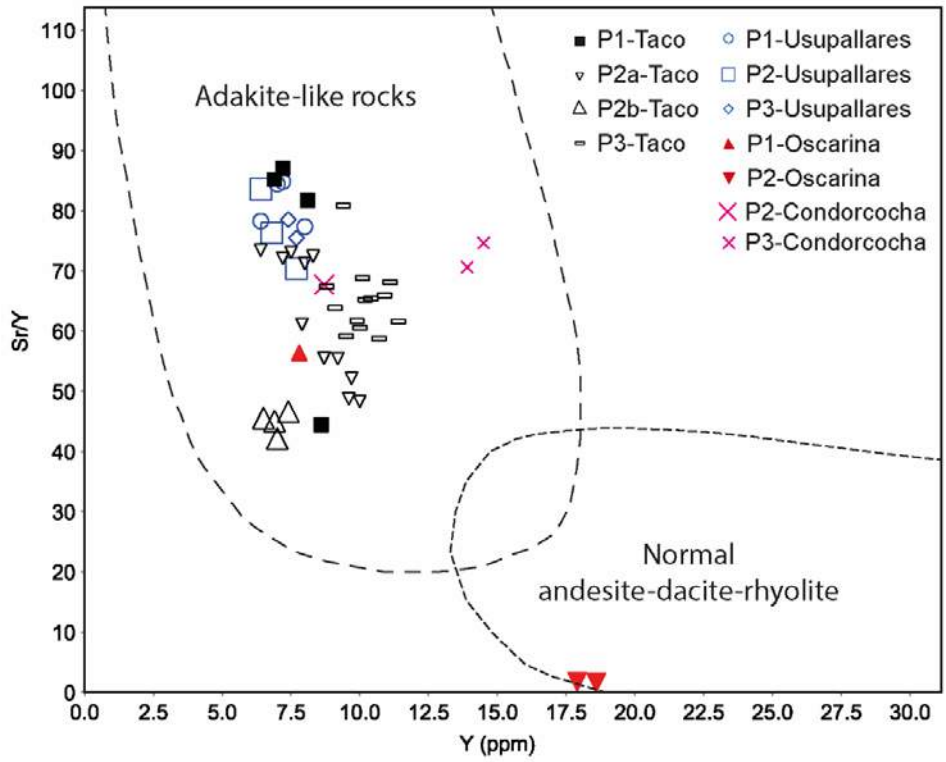

Fig. 3.6. Sr/Y versus Y plot for the Antamina porphyries (after Defant and Drummond, 1993).

3.4.4. Intrusive Sequence - Taco Zone

The Taco zone encompasses approximately 85% of the porphyry-skarn alteration and mineralisation that defines the economic resource at Antamina. This zone is characterized by at least 4 nested porphyry phases surrounded by skarns (from oldest to youngest they are P1, P2a, P2b, and P3 (Fig. 3.7 A-D, Fig. 3.8).P1-Taco (trachyandesite porphyry) is the oldest unit observed in this zone. It was emplaced as a series of dykes ranging in width from less than one meter to tens of meters. Least-altered P1-Taco is porphyritic and contains up to 75% phenocrysts of quartz, plagioclase, and K-feldspar; biotite and amphibole are also present, but have largely been replaced by secondary biotite and endoskarn (Table 3.1). This unit contains continuous pervasive and massive endoskarn alteration along the P1-wall rock (exoskarn) contact (Fig. 3.8). P1 and its associated skarns are cut across by P2 and P3 porphyries (Fig. 3.7 F and H). Frequently P1 (and associated skarns are incorporated into P2 and P3 as xenoliths and sometimes as large blocks or dismembered zones, which can include endoskarn and exoskarn, surrounded by P2 (Fig. 3.7 K). Stockwork quartz veins also cut across P1 porphyry, endoskarn, and exoskarn, and locally account for up to 40% of the total rock volume in P1 (Table 3.1).

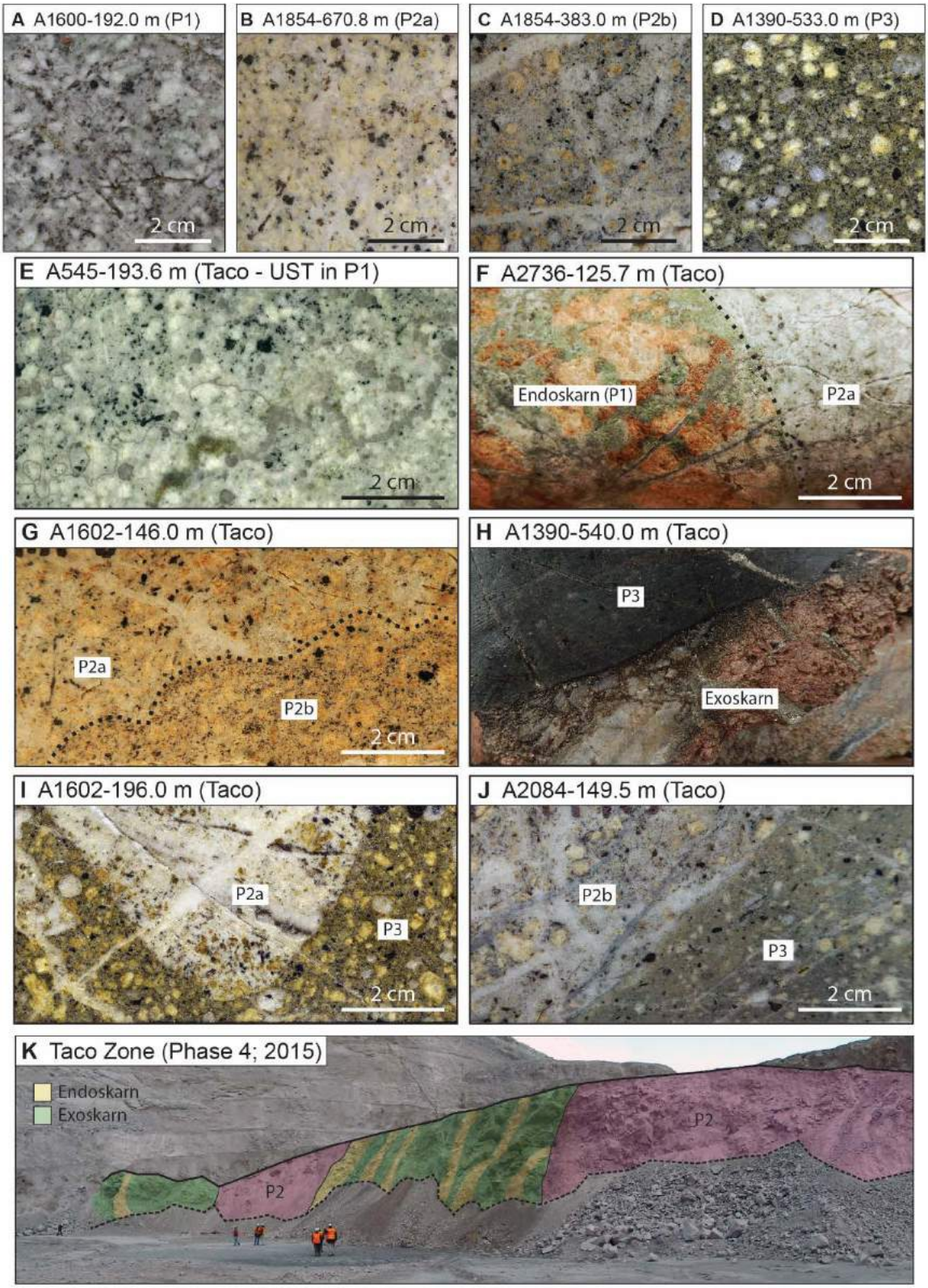

Fig. 3.7. Porphyries and cross-cutting relationships in the Taco zone. See text for detail.

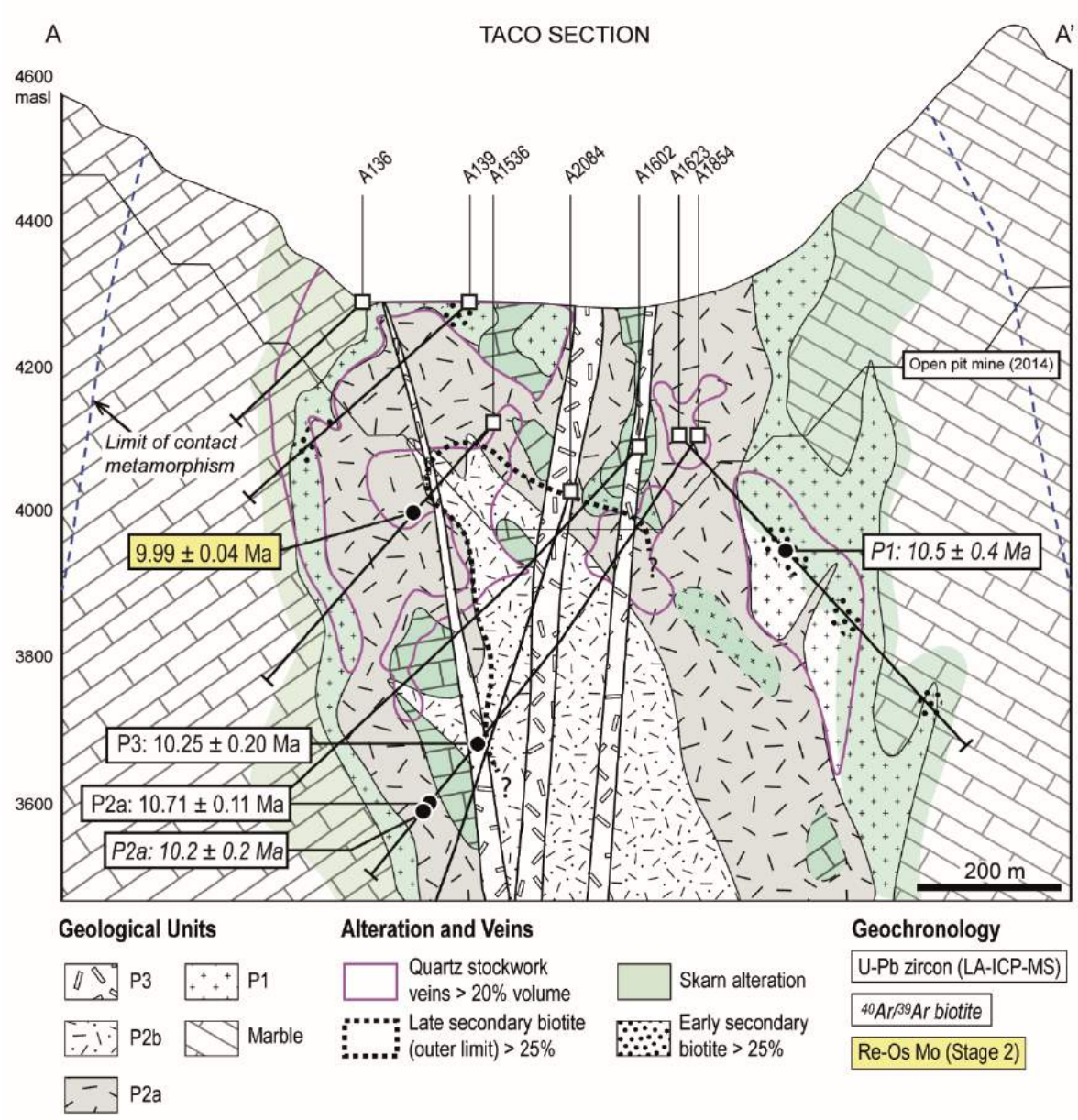

Fig. 3.8. Cross section A-A' through the central Taco zone. Section reference line is shown in Fig. 1.5.

A comb quartz unidirectional solidification texture (UST) was recognized in P1-Taco, in drill hole A545 between approximately 150-200 meters depth, in the northeast section of the Taco zone (Fig. 3.7 E, Fig. 3.9). The UST layers are 0.5-5 mm thick with porphyritic aplite interlayers. The UST aplite groundmass consists of fine-grained quartz and K-feldspar with up to 30% phenocrysts of quartz, K-feldspar, and biotite with lesser plagioclase and hornblende (Table 3.1).

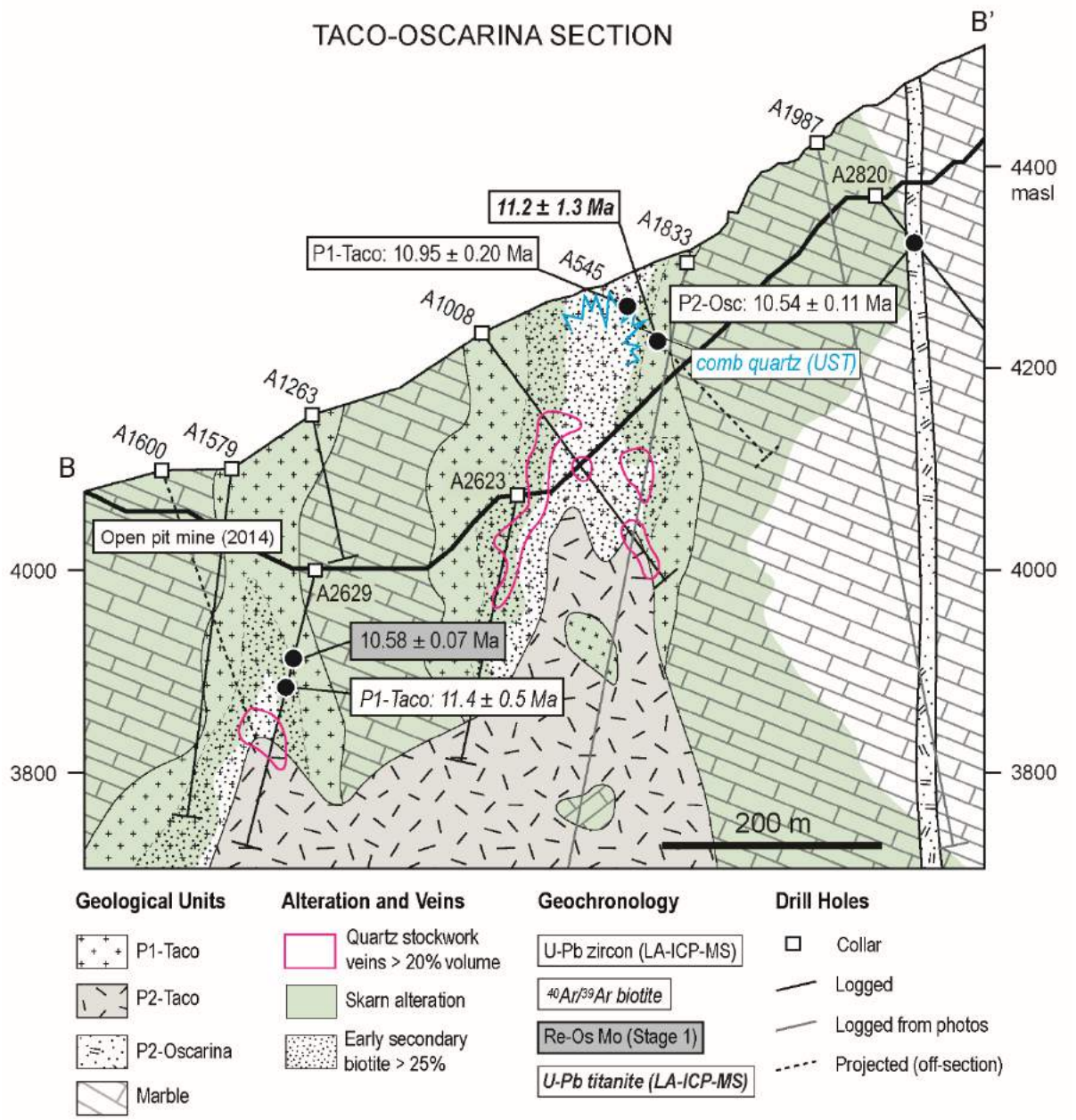

Fig. 3.9. Cross section B-B' through the Taco and Oscarina zones. Section reference line is shown in Fig. 1.5.

P2-Taco (trachyandesite porphyry) forms broad dykes and a stock that occupies the centre of the Taco zone (Fig. 3.8). P2-Taco is comprised of two compositionally similar trachyandesite porphyries, P2a and P2b (Fig. 3.7 B-C). Compared with P1-Taco, P2 contains up to 5% more quartz and up to 10% K-feldspar phenocrysts, and the plagioclase with slightly higher Na contents (Table 3.1 and Digital Appendix 3.6). Texturally, P2a is slightly coarser grained compared to P2b and displays a variably megacrystic porphyry texture; however in the absence of megacrysts the two units are difficult to tell apart. P2b-Taco truncates veins in

P2a-Taco (Fig. 3.7 G). Neither P2a nor P2b contain endoskarn alteration, and they cut across endoskarn and exoskarn (e.g., Fig. 3.7 F). Stockwork quartz veins are variable in abundance and account for up to 25% volume of P2a and P2b, with local increases up to ~40%.

P3-Taco (trachyandesite porphyry) is the youngest porphyry phase observed in the Taco section (Fig. 3.7 D). The true thickness and morphology of this unit are not accurately known as it has only been observed in drill core and as isolated blocks in the open pit mine. Drill thickness is highly variable from < 1 m to tens of meters. In drill core, P3 dykes display sharp contacts (straight edges, occasionally chilled margins) with all older units (Fig. 3.7 I-J). Key mineralogical features of P3-Taco include plagioclase glomerocrysts and K-feldspar megacrysts, which lack perthite exsolution textures and can exceed 50 mm in length (Table 3.1). Compared to P1- and P2-Taco, P3-Taco contains significantly fewer stockwork veins (Table 3.1).

3.4.5. Intrusive Sequence – Bornita Zone (Taco South)

The Bornita zone is located approximately 500 m southwest of the Taco zone (Fig. 3.10). The geology of this section is correlative with the Taco zone; igneous units include P1-Taco and P2a-Taco (Fig. 3.8). The dyke morphology of these porphyry phases is more evident in the Bornita zone even though a post-mineralisation fault cuts through the centre of the section (Fig. 3.10); displacement appears to be oblique-normal and offset is minor (≤ 50 m).

3.4.6. Intrusive Sequence - Usupallares Zone

The Usupallares zone is located SW of the Taco zone and is connected via a narrow isthmus of skarn (Fig. 3.11). Tapering of the Valley Fault dilational zone may have influenced intrusion morphology in this zone, as most porphyries were emplaced as narrow (typically < 10 m wide) dykes and the entire zone is ≤ 500 m wide (Fig. 3.11). Three major porphyry phases have been identified in this zone: P1, P2, and P3 (Fig. 3.11 and Fig. 3.12 A-C). Compositions trachyandesite, and all phases have plagioclase-phyric porphyry textures with K-feldspar megacrysts (Table 3.1).

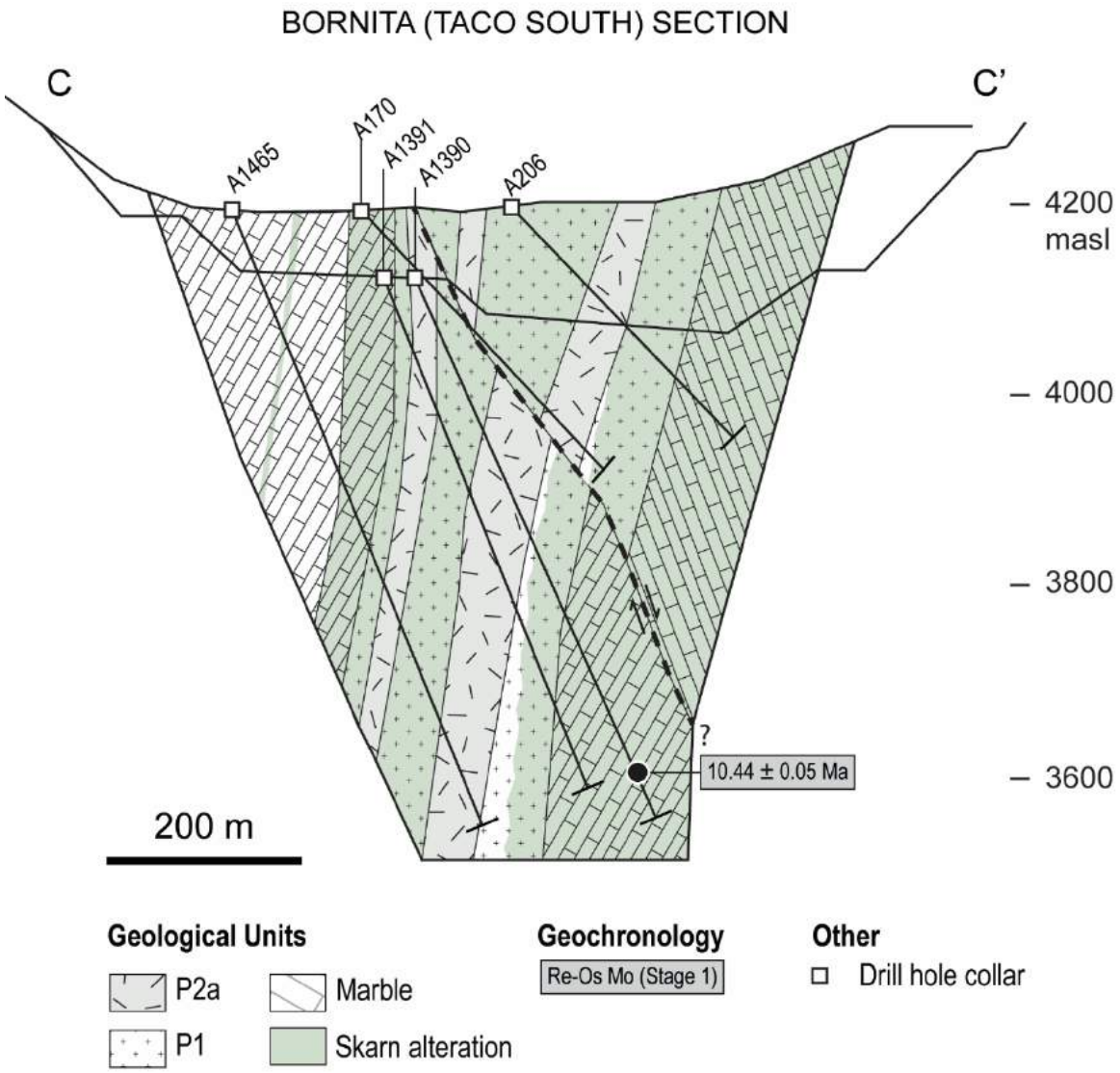

Fig. 3.10. Cross section C-C' through the Bornita (Taco south) zone. Section reference line is shown in Fig. 1.5.

P1-Usupallares (trachyandesite porphyry) is the oldest phase in this zone and, like P1-Taco, it displays endoskarn alteration along outer margins in contact with exoskarn-altered country rock (Fig. 3.11 and Fig. 3.12 A). Endoskarn-altered dyke margins grade into a core of less-altered P1 porphyry with weak secondary biotite alteration (Fig. 3.11). In the Usupallares zone, P1 and P2 have similar textures and compositions (Table 3.1), however P2 (Fig. 3.12 B) lacks endoskarn alteration and cuts across P1 with sharp contacts (Fig. 3.11 and Fig. 3.12 E), which confirms the relative timing of emplacement and the genetic relationship between P1 endoskarn and P1 exoskarn. Both P1- and P2-Usupallares contain up to 20% (by volume) quartz veins. Quartz veins also cut across P1 endoskarn and exoskarn.

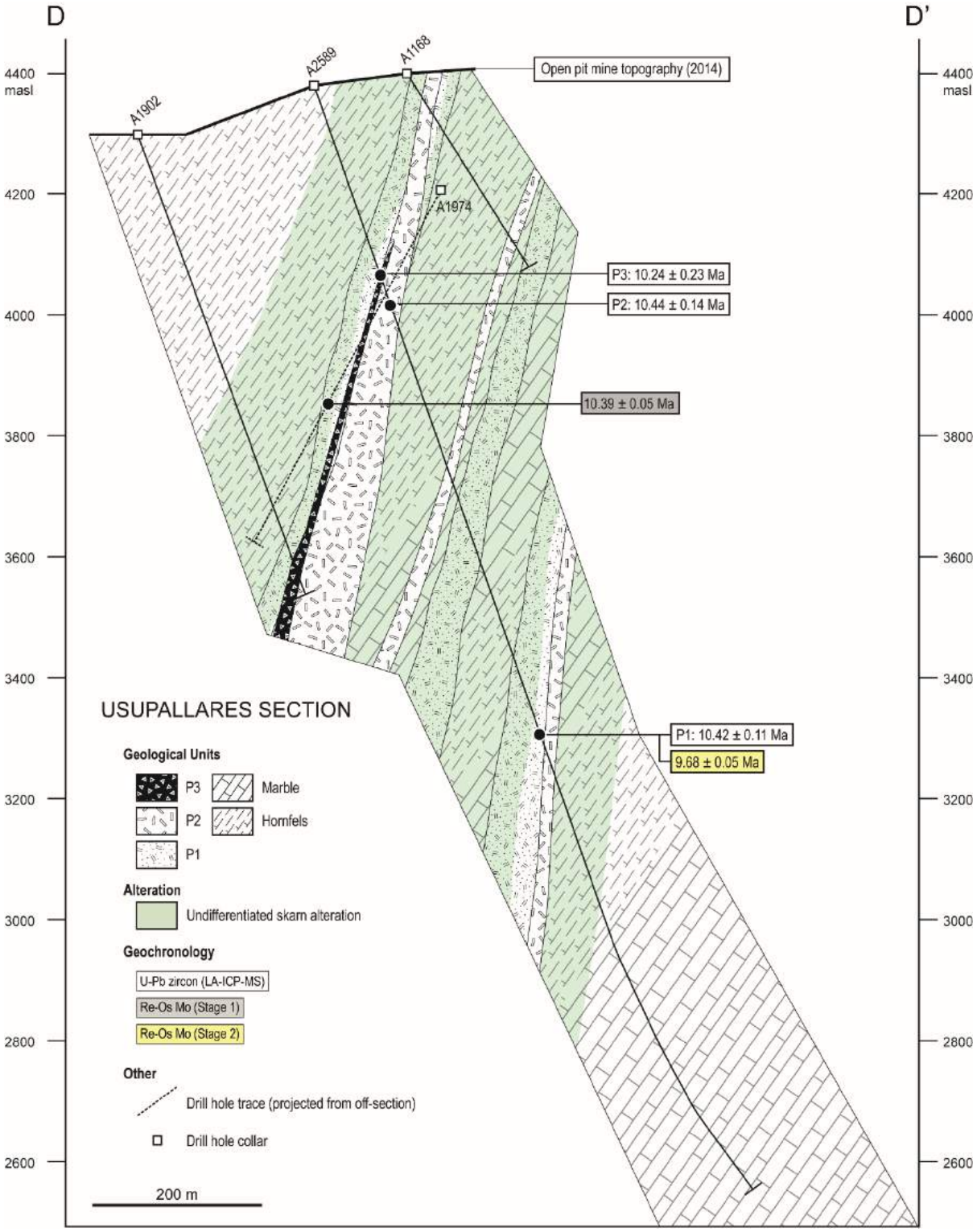

Fig. 3.11. Cross section D-D' through the Usupallares zone. Section reference line is shown in Fig. 1.5.

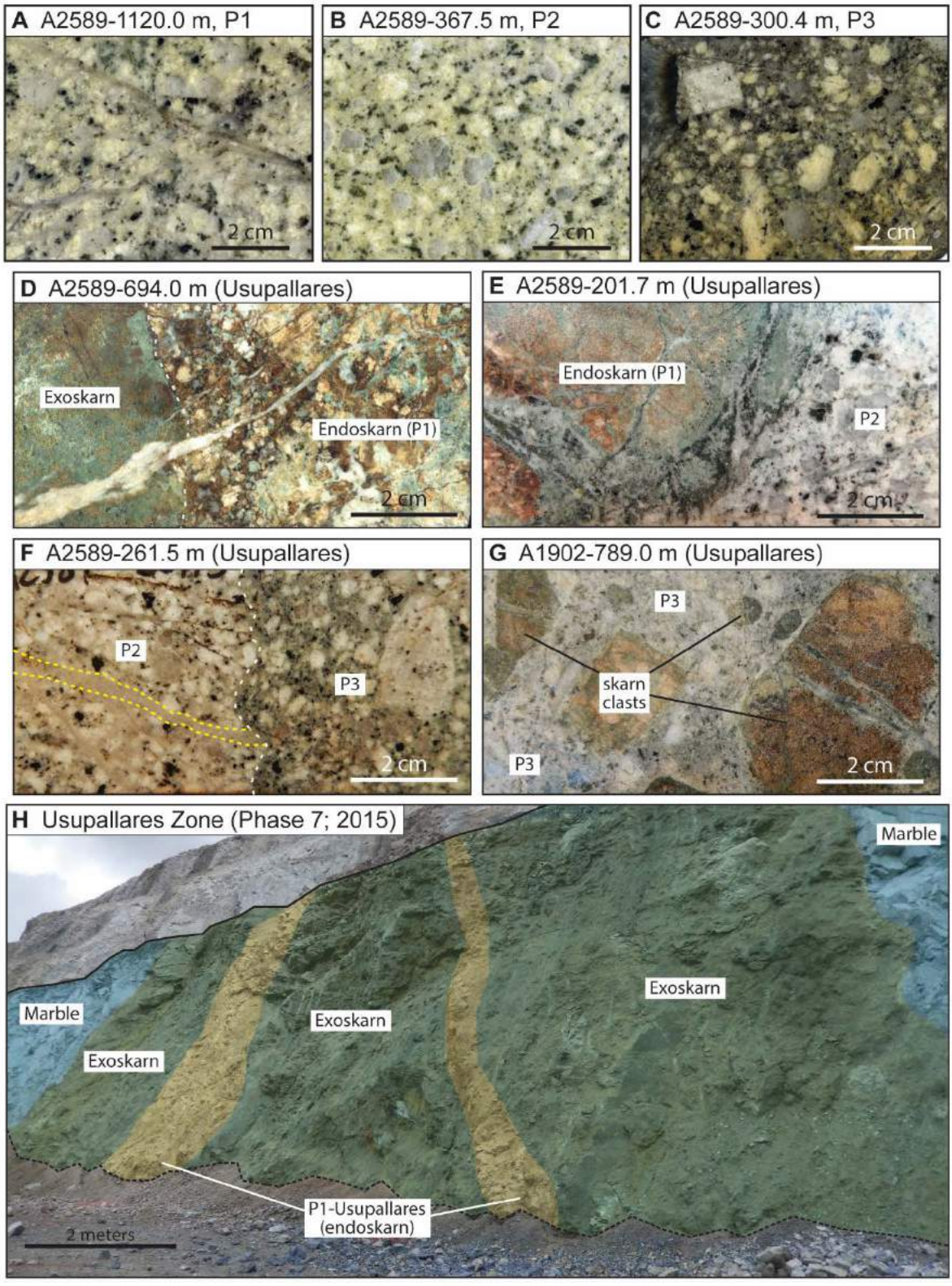

Fig. 3.12. Porphyries and cross-cutting relationships in the Usupallares zone.

P3-Usupallares (andesite porphyry) has a dark grey groundmass and abundant skarn xenoliths (Fig. 3.12 C), which gives it a distinctly different appearance compared to P1- and P2-Usupallares. P3-Usupallares occurs as narrow dykes along P1-P2 contacts and is the youngest porphyry unit observed in the Usupallares zone (Fig. 3.11). P3-Usupallares cuts across P2-Usupallares and truncates veins in it (Fig. 3.12 F), and contains clasts of skarns related to P1 (Fig. 3.12 G). It lacks endoskarn alteration, and rarely contains quartz veins (Fig. 3.12 C, G).

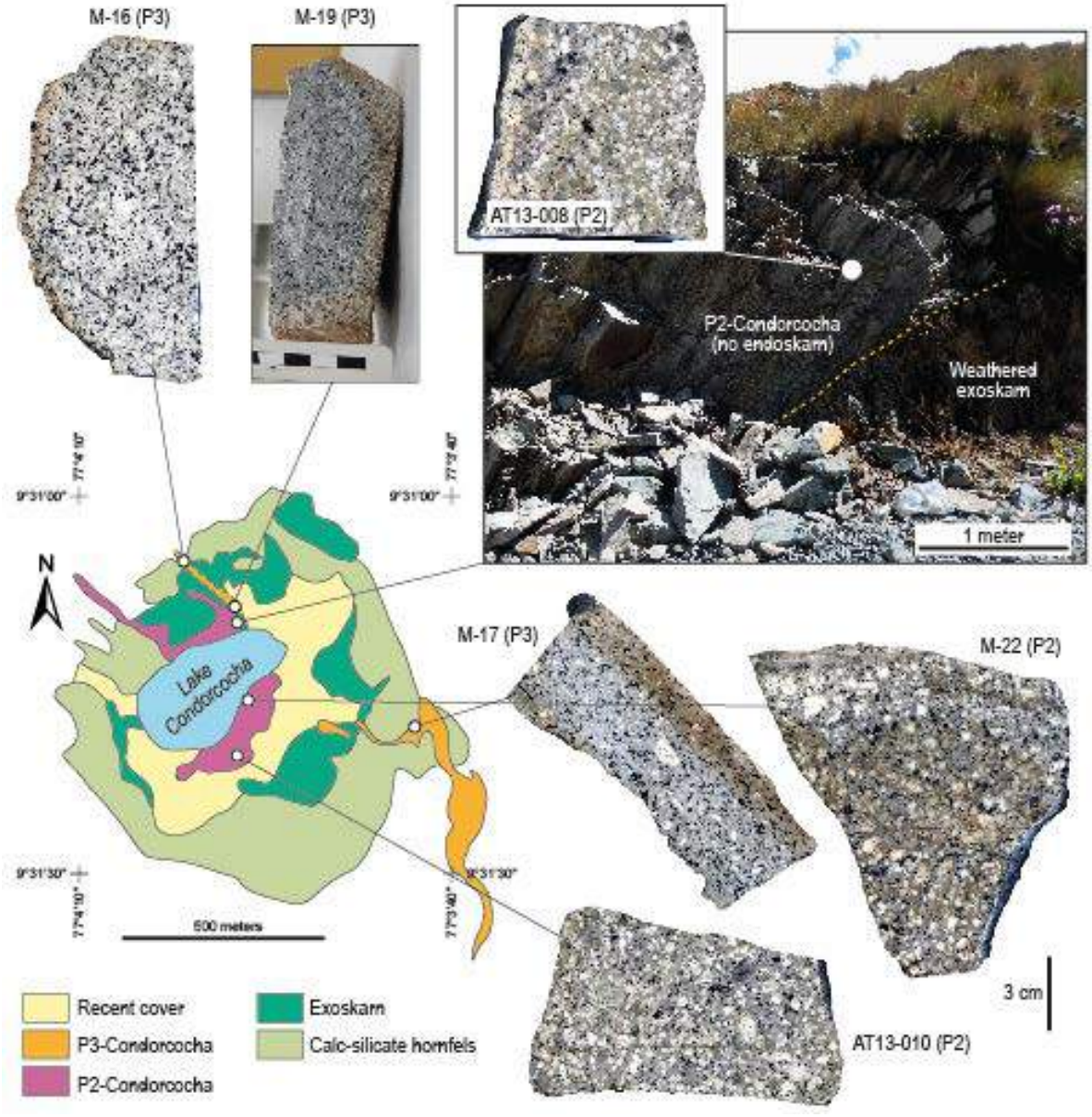

Fig. 3.13. Porphyries and cross-cutting relationships in the Condorcocha zone. Map shows detailed geology from Fig. 1.5, Inset B (modified after Escalante et al., 2010).

3.4.7. Intrusive Sequence - Condorcocha Zone

The Condorcocha zone is located approximately 1 km NNW of the Taco zone where it forms an isolated porphyry centre, approximately 600 m wide, surrounded by a weakly mineralised skarn that is partially concealed under Lake Condorcocha (Fig. 1.5 and Fig. 3.13). Two porphyry phases have been identified here and a third (the causative intrusion) is inferred based on field relationships. In the field, only exoskarn was observed (no endoskarn), but given that much of the skarn is concealed under Lake Condorcocha, P1-Condorcocha is inferred beneath the lake surface or at depth (Fig. 3.13). P1-exoskarn is cut across by P2-Condorcocha, which is a trachyandesite porphyry that lacks endoskarn but contains hydrothermal biotite veinlets (potassic alteration) and quartz stockwork veins, locally up to 20% rock volume (Fig. 3.13). P3-Condorcocha is an andesite porphyry dyke with up to 5% hornblende, up to 10% biotite, and no quartz stockworks. Based on mapping by Antamina geologists, it cuts across P1-Condorcocha skarns and P2-Condorcocha (Fig. 3.13). Alteration of P3-Condorcocha consists of minor chlorite after biotite and amphibole (Table 3.1). P3-Condorcocha occurs along strike of the Oscarina dykes (described below) and is texturally and compositionally similar to the Fortuna dykes of Escalante (2008).

3.4.8. Intrusive Sequence - Oscarina Zone

The Oscarina zone comprises a set of dykes that intersect the northeast margin of the Taco and Condorcocha zones (Figs. 1.5 and 3.9). The dykes were emplaced along steeply dipping (~80°), SE-striking (~140°), regional thrust faults (McCuaig, 2003) and exploration mapping shows that the dykes are intermittently exposed for approximately 7 km (Fig. 1.5). Both P1- and P2-Oscarina display porphyritic textures with 40-60% groundmass; phenocrysts include quartz, K-feldspar, plagioclase, biotite and hornblende (Table 3.1). P1-Oscarina is a trachyandesite porphyry with localised patches of calcite + epidote ± prehnite alteration (Fig. 3.14 A and Table 3.1). P2-Oscarina is a trachyte porphyry that contains patchy, weak pervasive calcite + chlorite + illite/muscovite alteration (Fig. 3.14 B and Table 3.1). The Oscarina dykes lack endoskarn alteration and cut across limestone and marble to the east of the deposit (Fig. 3.14 C), and skarns in the northeast Taco zone (Figs. 3.9 and 3.14 D). Quartz veins are rare in the Oscarina dykes.

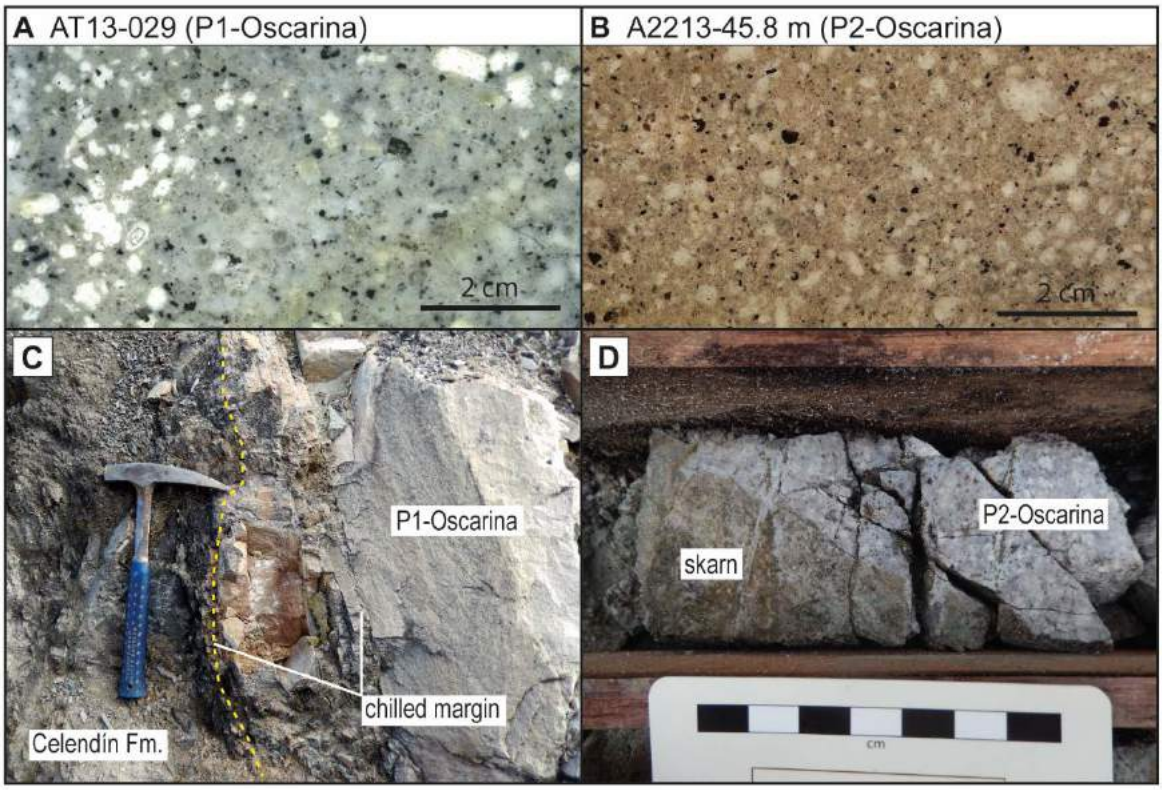

Fig. 3.14. Porphyries and cross-cutting relationships in the Oscarina zone.

3.4.9. U-Pb Zircon Dating Results

Ten igneous rocks were sampled for U-Pb zircon dating (Figs. 3.15 and 3.16). The selected samples represent the porphyry phases most commonly encountered at Taco, Usupallares, Oscarina, and Condorcocha and were selected based on cross-cutting relationships and lowest alteration intensity. Samples include P1-Taco (A2084-985.0, A545-178.5), P2a-Taco (A1854-670.8), P3-Taco (A1854-192.0), P1-Usupallares (A2589-1120.0), P2-Usupallares (A2589-367.5), P3-Usupallares (A2589-300.4), P1-Oscarina (AT13-029), P2-Oscarina (A2820-186.0), and P2-Condorcocha (M-22).

Zircons extracted from these samples share some common features: they are euhedral and prismatic (ranging from short and equant to elongate and acicular in all samples), up to 400 m long, and are invariably pale pink (Fig. 3.17 A-B). Cathodoluminescence (CL) imaging (Fig. 3.17 C-F) reveals that the Antamina zircons display magmatic oscillatory zoning. several are ‘antecrysts’, which are early magmatic zircons incorporated into later magmatic pulses (e.g., Miller et al., 2007); these display typical magmatic CL textures, but are slightly older than

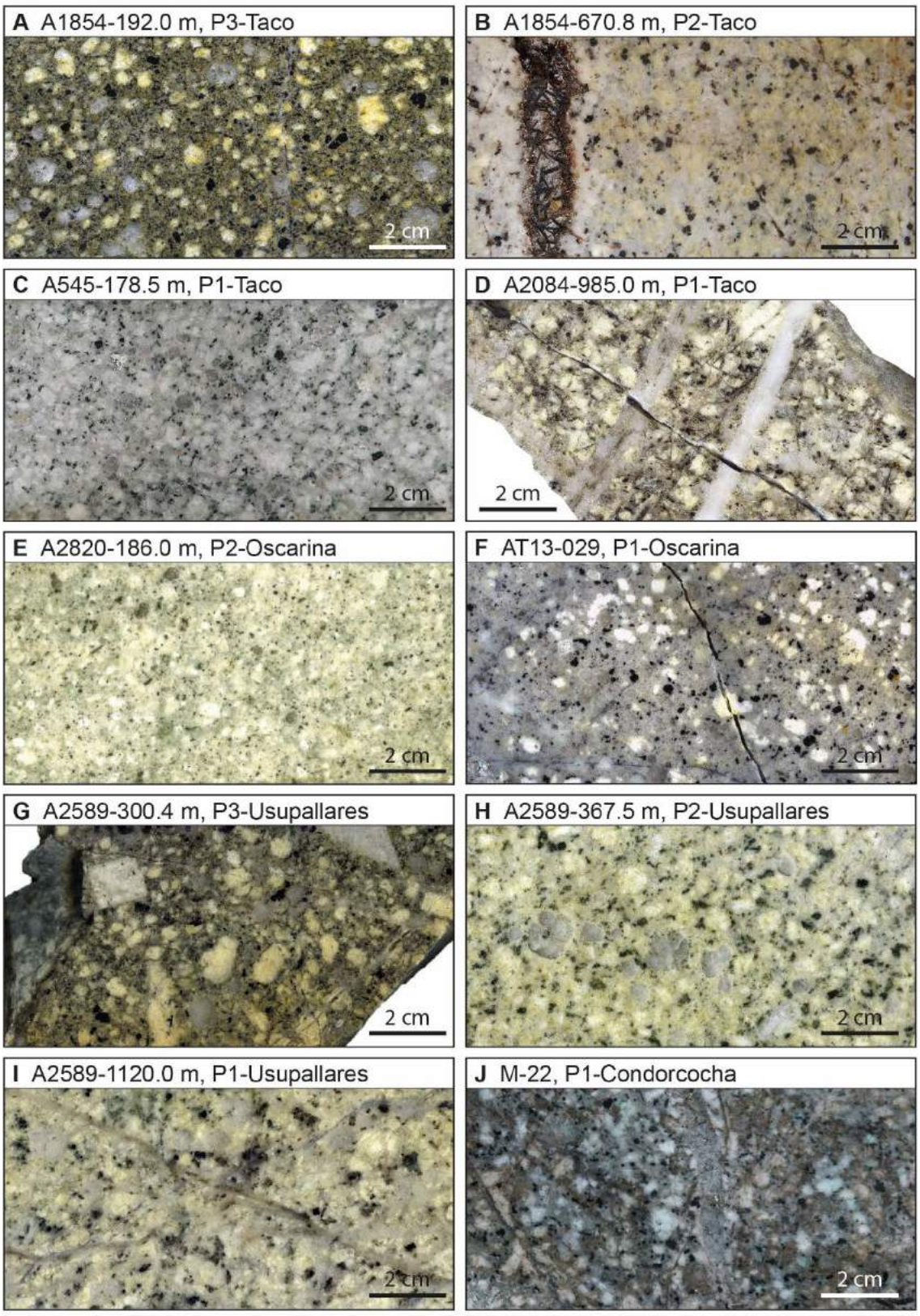

Fig. 3.15. Porphyry samples dated in this study using the U-Pb zircon dating method.

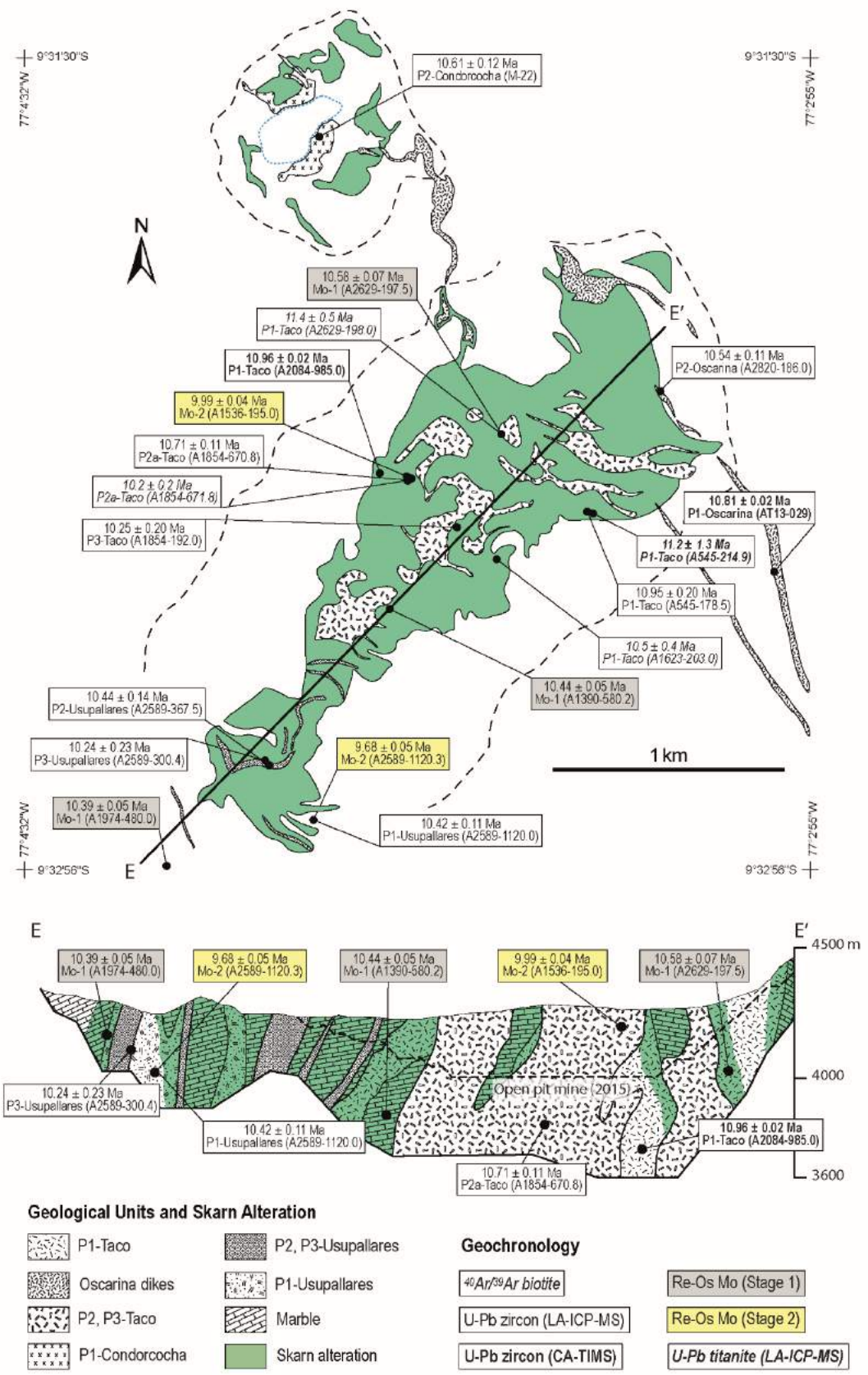

Fig. 3.16. Map and cross section E-E' showing sample location, age, and dating method. Map modified after Redwood (2004) and Escalante et al. (2010). Cross section geology is based on logged drill core (this study).

juvenile magmatic zircons. Commonly, a juvenile magmatic zircon rim surrounds an antecryst core of similar brightness (Fig. 3.17 C-F). A few inherited (Paleozoic to Eocene) zircons were encountered in approximately 60% of the samples dated; CL features of these zircons typically include bright xenocryst cores surrounded by darker magmatic rims (e.g., Fig. 3.17 C-F). Due to the presence and abundance of antecrysts and inherited xenocrysts, zircon rims were targeted during laser ablation dating. Analysis of inherited or antecrystic zircon domains were not included in our age calculations.

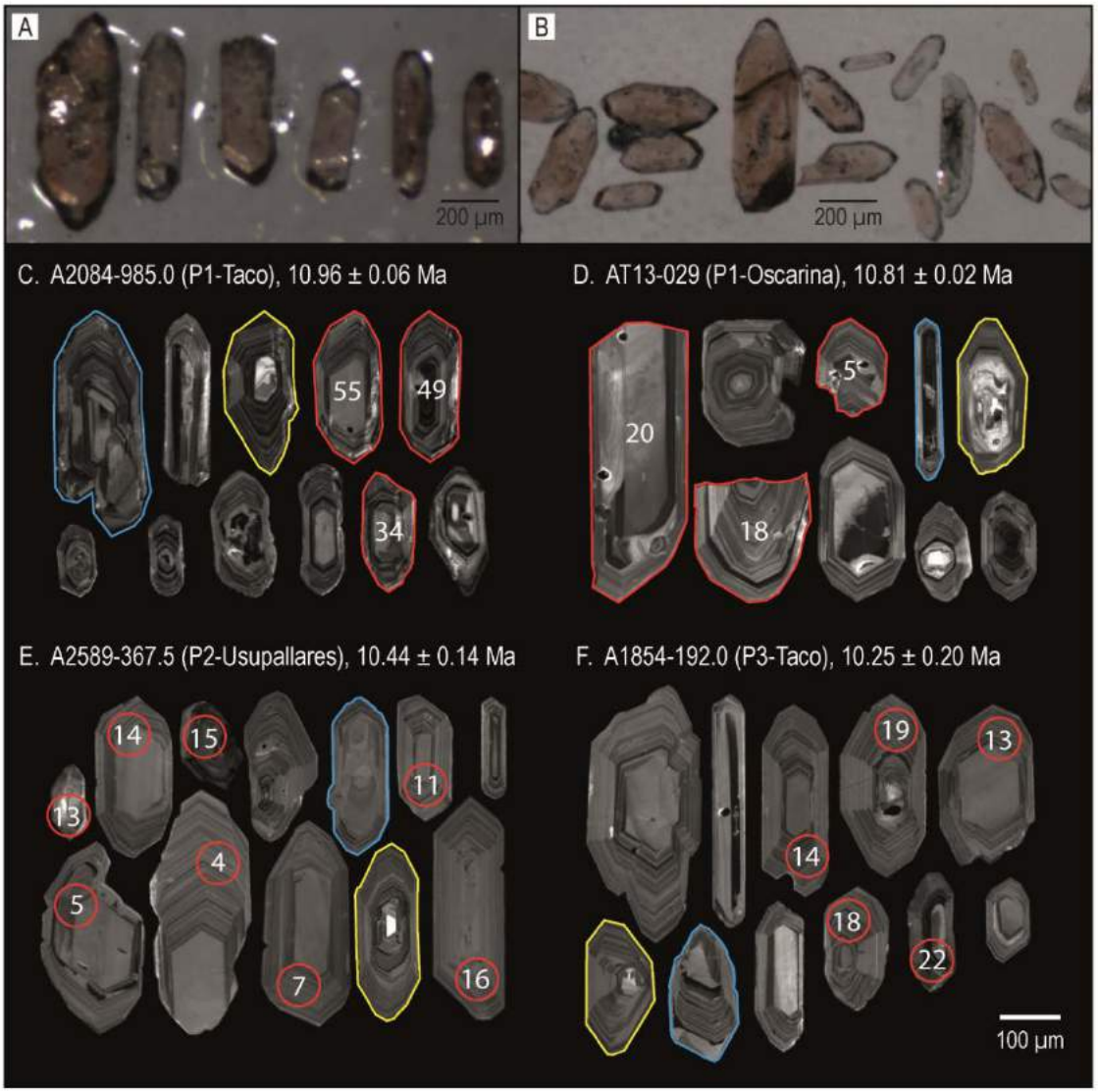

Fig. 3.17. Transmitted light and cathodoluminescence (CL) images of representative zircons from four different intrusive phases at Antamina. A-B. Transmitted light images of light pink to brown zircons from samples A2084-985.0 (P1-Taco) and A2589-367.5 (P2-Usupallares), respectively. Note the pale pink-brown colour of the zircons observed in all of the Antamina porphyies. C-D: Zircons dated by the CA-TIMS method (A2084-985.0 and AT13-029; red outlines). E-F: Samples A2589-367.5 and A1854-192.0 were dated by the LA-ICP-MS method. Laser ablation spots are denoted by red circles. Zircons outlined in yellow display bright inherited cores, while zircons outlined in blue are magmatic antecrysts. See text for detail.

Table 3.4 provides a summary of zircon U-Pb dating results. Weighted mean and Tera-Wasserburg concordia plots (Tera and Wasserburg, 1972) are provided in Fig. 3.18. In most cases, Tera-Wasserburg plots show significant age dispersion and overlap along Concordia over 2-3 Ma (e.g., Fig. 3.18); therefore weighted mean $^{206}Pb/^{238}U$ ages were calculated using the method described above (for U-Pb zircon, LA-ICP-MS), and are herein reported as crystallization ages. Tera-Wasserburg concordia plots are included to illustrate the spread of the data and to highlight the points used in our weighted mean age calculations, but they have not been used to calculate ages.

Table 3.4. New U-Pb (LA-ICP-MS and CA-TIMS) zircon ages for the Antamina Porphyry Complex.

Sample ID	Rock Type	Intrusive phase	Age (Ma)	±2σ (Ma)	MSWD	Probability	n	Method
Taco								
A1854-192.0	Megacrystic quartz monzonite porphyry	P3	10.25	0.20	1.4	0.23	5	LA-ICPMS
A1854-670.8	Megacrystic granite porphyry	P2a	10.71	0.11	0.63	0.82	13	LA-ICPMS
A2084-985.0	Quartz monzonite porphyry	P1	10.96	0.06	1.6	0.20	3	CA-TIMS
A545-178.5	Quartz monzonite porphyry	P1	10.95	0.20	0.02	0.98	3	LA-ICPMS
Usupallares								
A2589-300.4	Megacrystic quartz monzonite porphyry	P3	10.24	0.23	0.97	0.38	3	LA-ICPMS
A2589-367.5	Megacrystic granite porphyry	P2	10.44	0.14	1.4	0.21	8	LA-ICPMS
A2589-1120.0	Megacrystic granite porphyry	P1	10.42	0.11	0.78	0.69	15	LA-ICPMS
Oscarina								
A2820-186.0	Granite porphyry	P2	10.54	0.11	0.98	0.44	7	LA-ICPMS
AT13-029	Quartz monzonite porphyry	P1	10.81	0.02	0.46	0.63	3	CA-TIMS
Condorcocha								
M-22	Quartz monzonite porphyry	P2	10.61	0.12	0.86	0.59	13	LA-ICPMS

P1-Taco (A2084-985.0, A545-178.5): P1-Taco is the oldest unit identified in the APC based on cross-cutting relationships. Two samples of P1 were collected from drill core in the Taco section (Fig. 3.8, Fig. 3.9, and Fig. 3.16). Sample A2084-985.0 displays strong potassic alteration and abundant quartz stockwork veins (Fig. 3.15 A), whereas sample A545-178.5 displays only traces of chlorite alteration after weak potassic alteration (Fig. 3.15 B). Sample A2084-985.0 returned a weighted mean $^{206}Pb/^{238}U$ age of 10.96 ± 0.06 Ma (MSWD = 1.6) based on 3 CA-TIMS analyses (Table 3.4, Fig. 3.18 A-B). Sample A545-178.5 was collected from the northeast extension of the Taco section (Fig. 3.9) and returned an age of 10.95 ± 0.20 Ma (MSWD = 0.02) for 3 LA-ICP-MS zircon analyses (Table 3.4, Fig. 3.18 C-D). They are statistically identical, however the CA-TIMS date has much higher precision. Sample A545-178.5 contained zircon antecrysts and two inherited zircon grains dated at ~34 Ma (Eocene) and ~165 Ma (Middle Jurassic); these are not included in the age calculation.

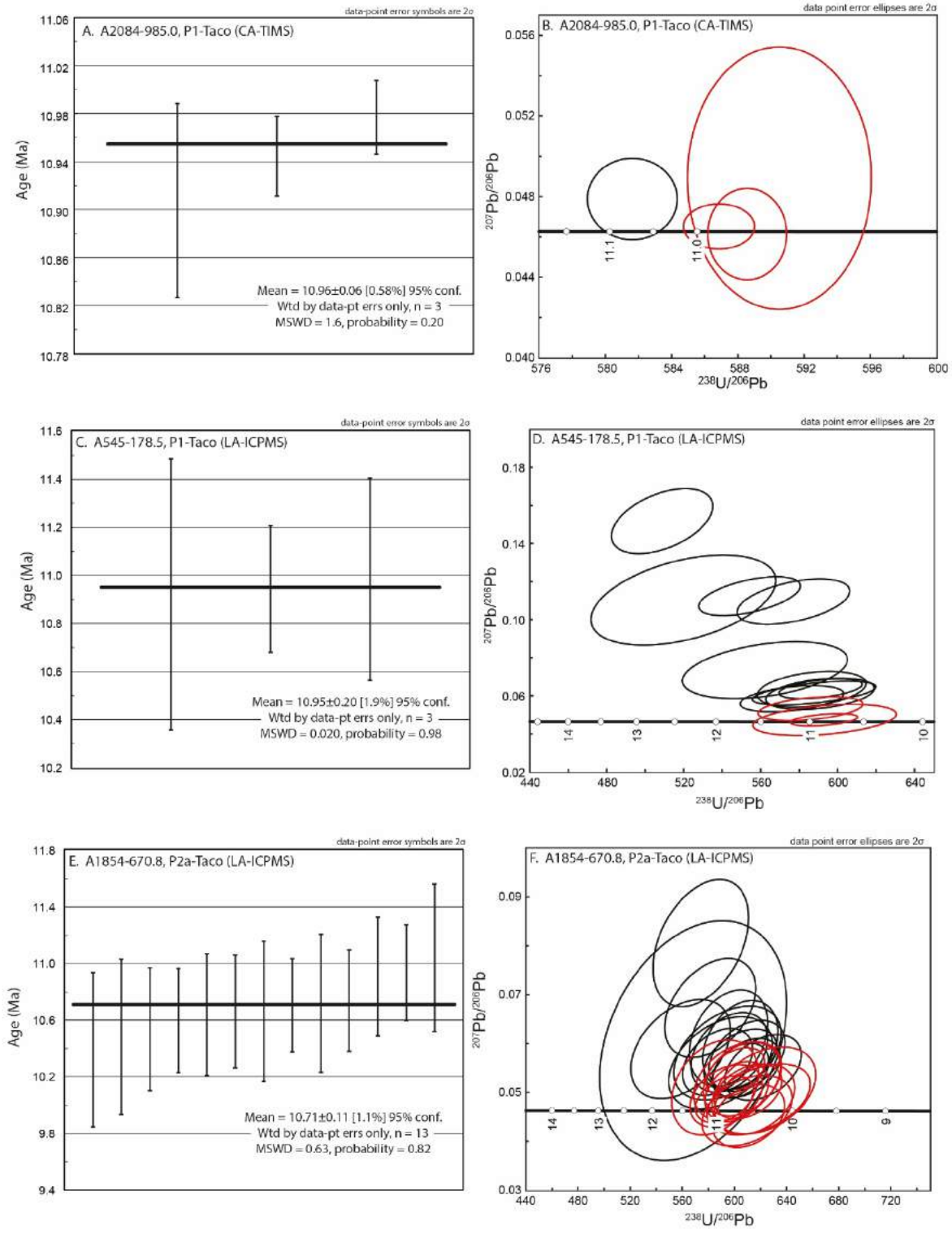

Fig. 3.18. Weighted mean and Tera-Wasserburg concordia plots (Tera and Wasserburg, 1972) for U-all zircon samples dated by Pb geochronology (LA-ICP-MS and CA-TIMS). Ages were calculated using weighted means; concordia plots are presented only to show the spread of the data. Continued on next page.

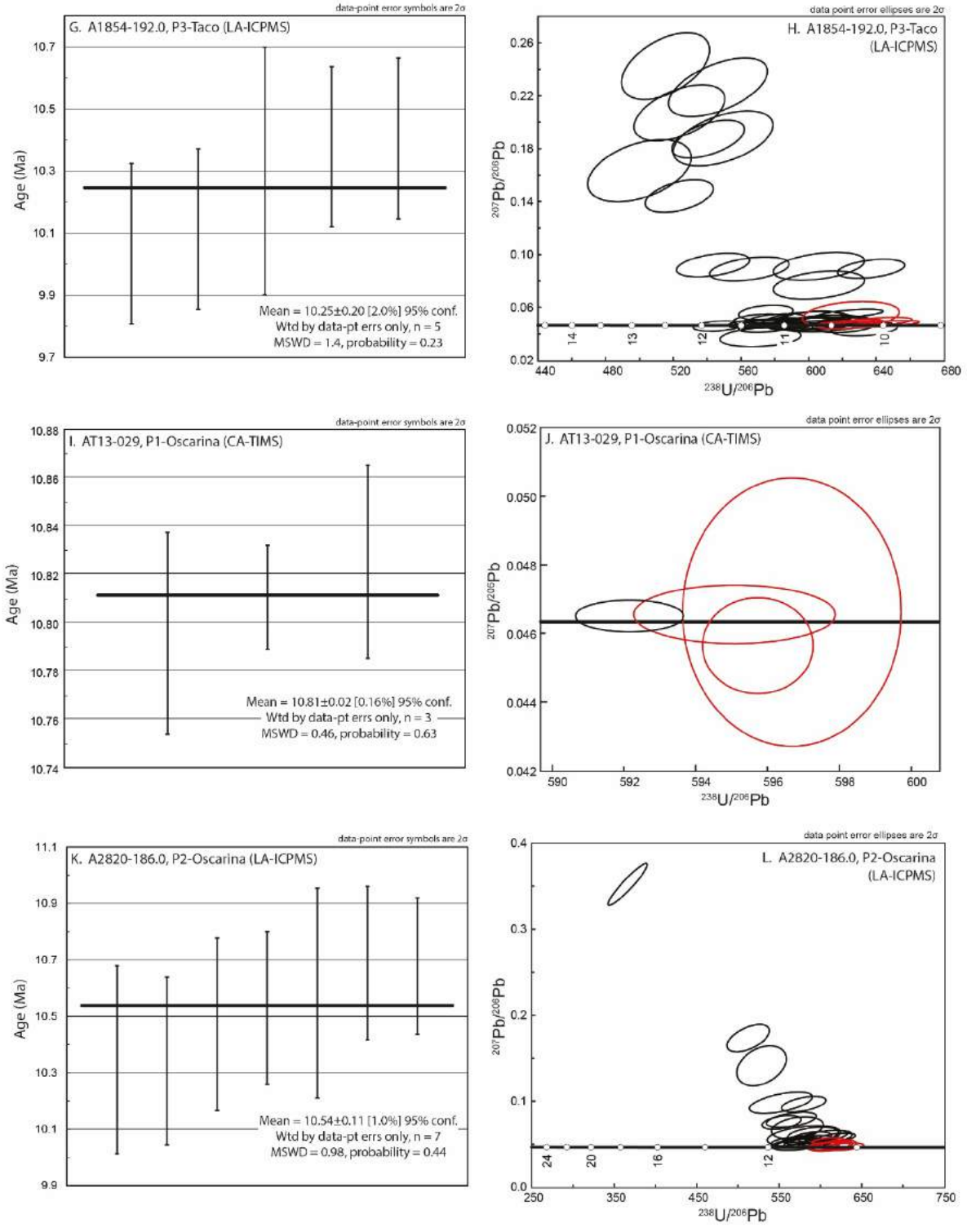

Fig. 3.18. Continued.

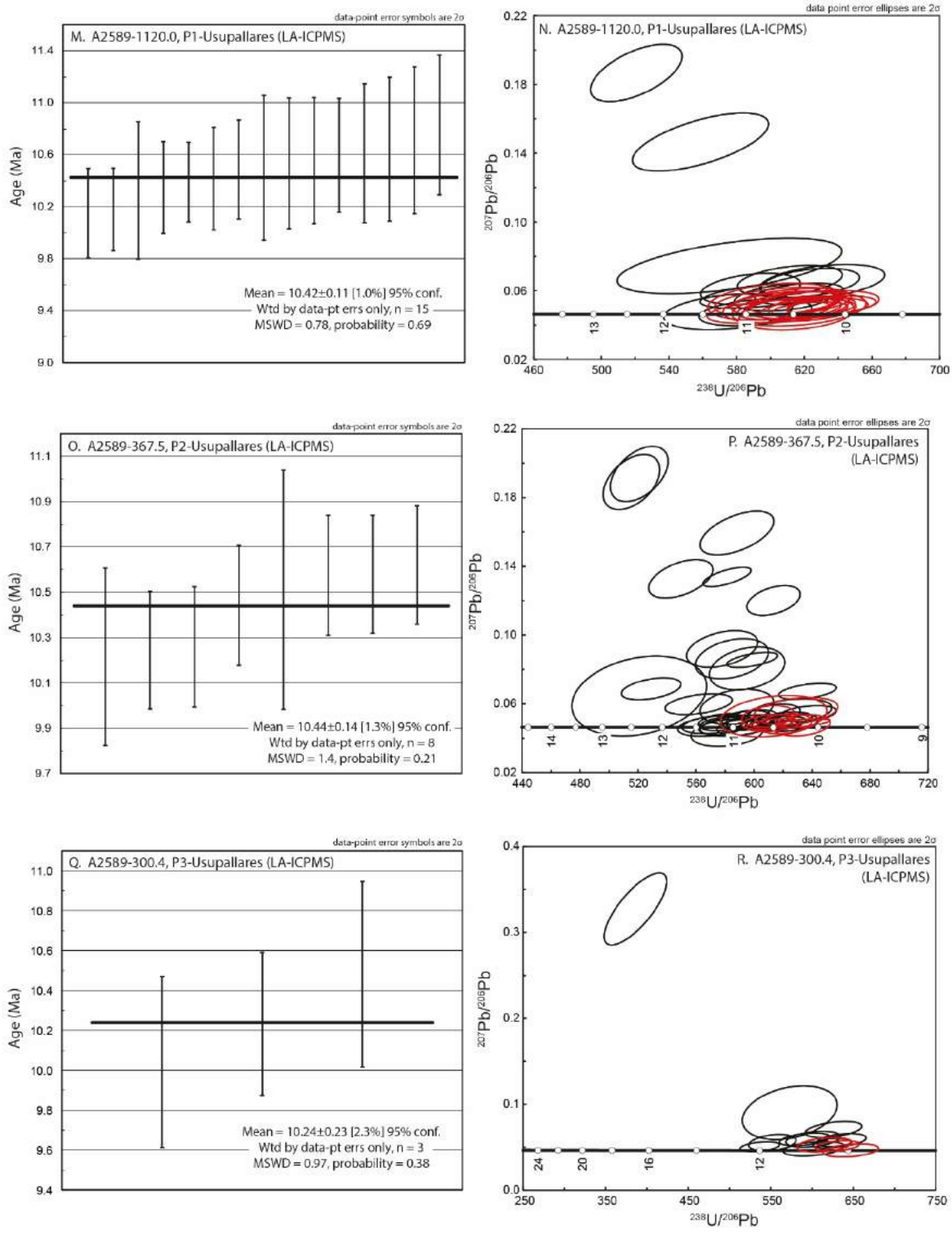

Fig. 3.18. Continued.

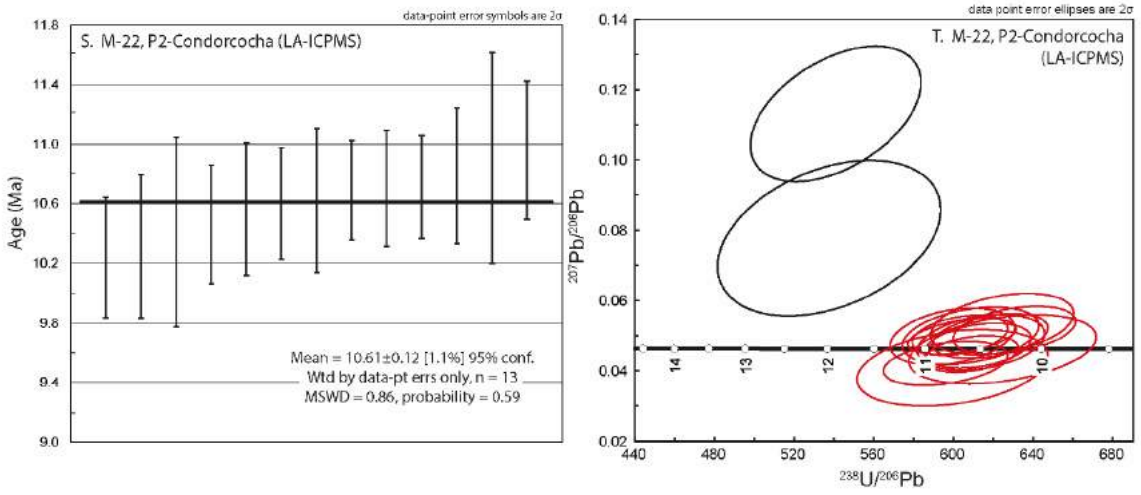

Fig. 3.18. Continued.

P2a-Taco (A1854-670.8): One sample of P2a was collected from the drill hole A1854 in the central Taco section (Figs. 3.8 and 3.16). The sample contained some veins and clots of light brown hydrothermal biotite (also dated in this study; Fig. 3.15 C). Sample A1854-670.8 yielded an age of 10.71 ± 0.11 Ma (MSWD = 0.63) based on 13 grains (Table 3.4, Fig. 3.18 E-F). This sample contained zircon antecrysts up to 11.43 ± 0.65 Ma (not included in the final age calculation) and no inherited zircons.

P3-Taco (A1854-192.0): One P3 dyke was sampled (Figs. 3.8 and 3.16). Overall, this sample has a well-defined porphyry texture with sharp mineral boundaries and no veining (Fig. 3.15 D). Alteration consists of minor chloritization after hydrothermal biotite. An age of 10.25 ± 0.20 Ma (MSWD = 1.4) is reported for 5 zircon grains (Table 3.4, Fig. 3.18 G-H). This sample contained zircon antecrysts up to 11.41 ± 0.26 Ma and two inherited zircon grains dated at ~80 Ma (Upper Cretaceous) and ~207 Ma (Upper Triassic); these are not included in the final age calculation.

P1-Oscarina (AT13-029): This sample was collected from a surface outcrop of an Oscarina dyke behind the haul truck maintenance bay, outside of the open pit mine (Fig. 3.16). The sample is a sub-equigranular biotite hornblende trachyandesite porphyry with up to 5% secondary biotite after primary biotite and hornblende (Fig. 3.15 E). Age determination by CA-TIMS yielded 10.81 ± 0.02 Ma (MSWD = 0.46) for 3 zircons (Table 3.4, Fig. 3.18 I-J).

P2-Oscarina (A2820-186.0): This sample was collected from the northernmost dyke in the Oscarina zone, along the northeast margin of the APC (Figs. 3.9 and 3.16). The sample is an equigranular trachyte porphyry with < 10% chloritized hornblende (Fig. 3.15 F). An age of 10.54 ± 0.11 Ma (MSWD = 0.98) for 7 zircons was determined by LA-ICP-MS (Table 3.4, Fig. 3.18 K-L). Together with sample AT13-029 (P1-Oscarina), these samples constrain the age of the Oscarina dykes from 10.81 ± 0.02 to 10.54 ± 0.11 Ma. The oldest zircon antecryst is 11.46 ± 0.34 Ma, and two inherited zircon grains were dated at ~102 Ma (Lower Cretaceous) and ~255 Ma (Permian); these are not included in the final age calculation.

P1-Usupallares (A2589-1120.0): This sample shows weak secondary biotite alteration and patchy endoskarn alteration, and is cross-cut by a quartz-molybdenum-pyrite vein (also dated in this study; Figs. 3.11, 3.15 G, and 3.16). Fifteen zircon grains yielded a weighted mean age of 10.42 ± 0.11 Ma (MSWD = 0.78; Table 3.4, Fig. 3.18 M-N). This sample contained zircon antecrysts up to 11.28 ± 0.62 Ma (not included in the final age calculation) and no inherited zircons.

P2-Usupallares (A2589-367.5): This sample comes from the northernmost P2-dyke in the Usupallares section (Figs. 3.12 and 3.16). It displays minor secondary biotite alteration and < 2% quartz vein density (Fig. 3.15 H). Based on 8 zircons, the sample yielded a weighted mean age of 10.44 ± 0.14 Ma (MSWD = 1.4; Table 3.4, Fig. 3.18 O-P). This sample contained zircon antecrysts up to 12.17 ± 0.93 Ma and one inherited zircons dated at ~417 Ma (Lower Devonian); these are not included in the final age calculation.

P3-Usupallares (A2589-300.4): This sample is from a narrow (~50 cm) P3 dyke (Figs. 3.11 and 3.16). Like other P3 dykes, this specific dyke has a dark groundmass and is essentially free of cross-cutting veins; however unlike other P3 samples, this dyke contains xenoliths of P2, skarn, quartz vein fragments, and traces of chalcopyrite (Fig. 3.15 I). In order to date this unit, groundmass was separated from xenoliths using a trim saw; xenolith-free groundmass was send to UTAS for dating (as described above). Based on 3 zircon analyses, an age of 10.24 ± 0.23 Ma (MSWD = 0.97) was obtained (Table 3.4, Fig. 3.18 Q-R). This age is coeval with P3-Taco dykes (10.25 ± 0.20 Ma) observed 500 m to the northeast of Usupallares (Fig. 3.16). This sample also contained antecrysts up to 12.03 ± 0.44 Ma and two inherited zircons dated at ~90 Ma (Upper Cretaceous) and ~223 Ma (Upper Triassic), which are not included in the final age calculation.

P2-Condorcocha (M-22): This sample is from an outcrop of the Condorcocha stock (Figs. 3.13 and 3.16). It is a crowded trachyandesite porphyry with approximately 15% fine-grained secondary biotite in the groundmass, and is cross-cut by 5% quartz-pyrite stockwork veins (Fig. 3.15 J). Based on 13 zircons, an age of 10.61 ± 0.12 Ma (MSWD = 0.86) is reported for the Condorcocha stock (Table 3.4, Fig. 3.18 S-T). This sample contained zircon antecrysts up to 11.59 ± 0.98 Ma (not included in the final age calculation) and no inherited zircons.

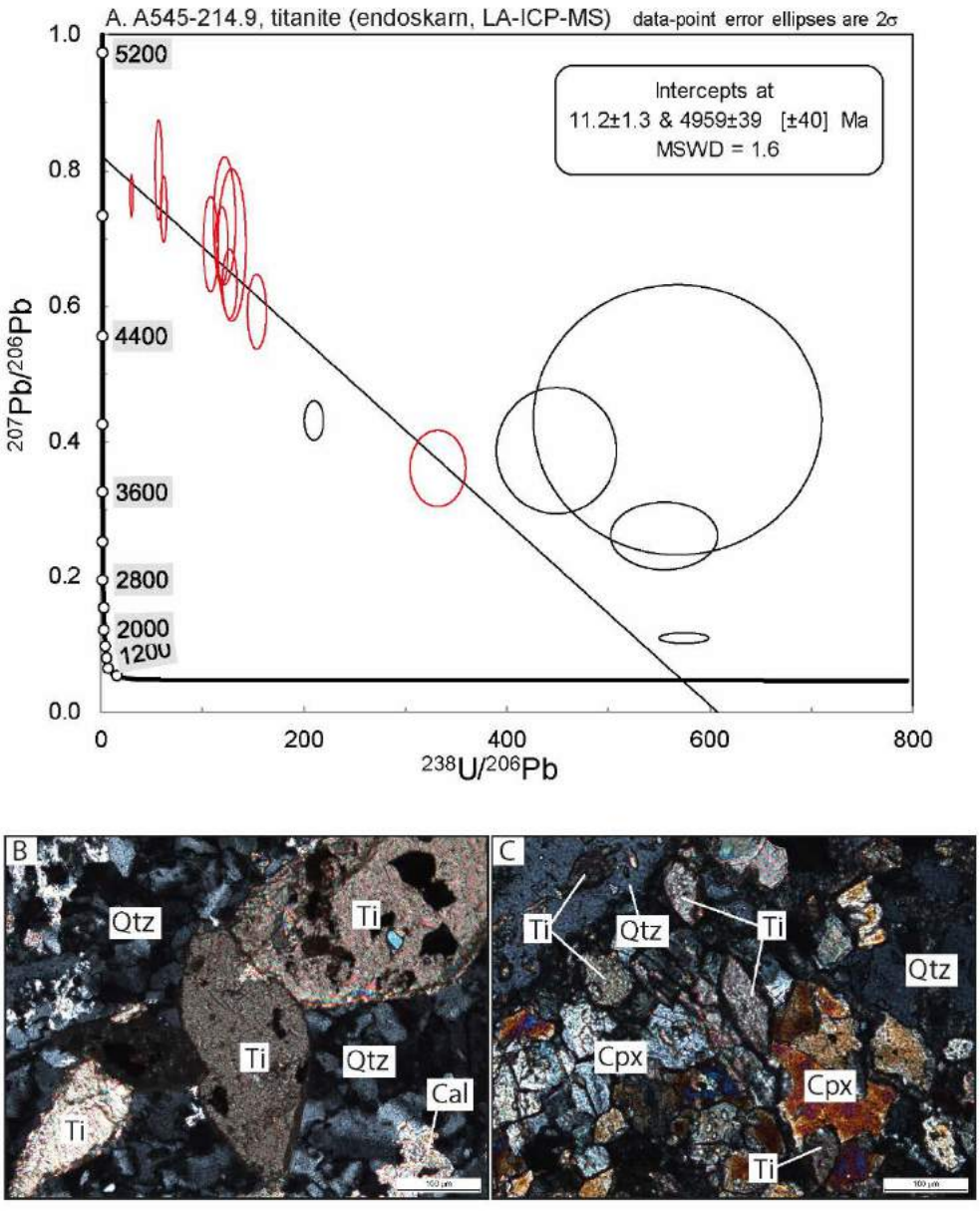

Fig. 3.19. U-Pb (LA-ICP-MS) age and 2σ error for endoskarn titanite sample A545-214.5, northeast Taco zone. B-C: photomicrographs showing the mineralogical context and size variability of titanite in the ablated sample (cross-polarized light). Abbreviations: Cal: calcite, Cpx: clinopyroxene, Qtz: quartz, Ti: titanite.

3.4.10. U-Pb Titanite Dating Results

Endoskarn sample A545-214.9 (northeast Taco zone; Fig. 3.16) returned an age of 11.2 ± 1.3 Ma (MSWD = 1.6), based on 10 analyses of five titanite grains (Fig. 3.19). Four analyses were excluded from the final age estimate due to signal interference from inclusions. The sample contained many titanite grains that were too small to accommodate the 44 µm laser beam, whereas some larger titanite grains were ablated in 2-3 spots (as noted in Digital Appendix 3.2).

3.4.11. $^{40}Ar/^{39}Ar$ Biotite Dating Results

Three new hydrothermal biotite ages are reported in this study, two samples from P1-Taco groundmass and one from a biotite vein cutting across P2a-Taco.

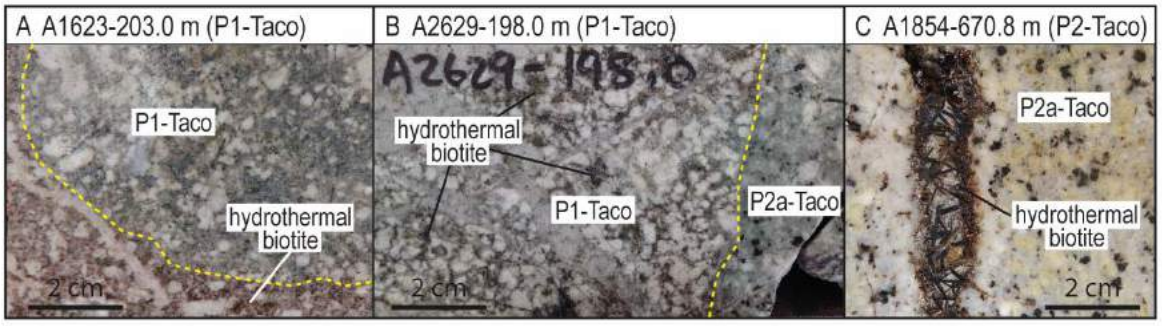

Fig. 3.20. Hydrothermal biotite samples dated in this study using the $^{40}Ar/^{39}Ar$ step-heating method.

P1-Taco (A2629-198.0 and A1623-203.0): Sample A2629-198.0 is located approximately 400 m northeast of the central Taco zone and sample A1623-203.0 is located approximately 300 m southeast of the central Taco zone (Fig. 3.16). These samples contain pervasive secondary biotite with incipient clinopyroxene endoskarn alteration (Fig. 3.20 A) and some quartz veins (Fig. 3.20 B). Care was taken to avoid including quartz vein fragments in the mineral separates, which also contained fine (≤ 0.5 mm) medium-dark brown biotite flakes. Two analytical runs (denoted as -a and -b) were completed for each sample A2629-198.0 and A1623-203.0 (Table 3.5). For both samples the "-a" analyses are preferred due to the 100% ^{39}Ar gas release plateau (Fig. A3.2 A, C). In contrast, the "-b" analyses show some evidence for disturbance; A2629-198.0-b has high apparent ages at low temperature (Fig. A3.2 B) and A1623-203.0-b spectrum displays a slight saddle shape (Fig. A3.2 D). Despite these minor

differences, the two sets of results are similar. The presence of a Ca-rich mineral (most likely clinopyroxene ± calcite) is also noted in the high Ca/K part of each spectrum (Fig. A3.2 A-D). These may be inclusions or contaminants from the host rock; in either case they do not appear to have significantly affected the age spectra. It is interesting to note that the total gas ages are more similar than the plateau ages for each sample, indicating that some of the disturbance features of the "-b" analyses may be due to internal redistribution of ^{39}Ar between inclusions and the biotite host mineral; this could explain the younger plateau ages reported for "-b" analyses (Table 3.5). The preferred ages for A2629-198.0 and A1623-203.0 are 11.4 ± 0.5 Ma and 10.5 ± 0.4 Ma, respectively (Table 3.5; Fig. A3.2 A-D).

Table 3.5. $^{40}Ar/^{39}Ar$ hydrothermal biotite ages for the Taco zone, Antamina deposit.

Sample ID	Unit	Plateau age (Ma)	1σ (Ma)	% ^{39}Ar released	Total gas age (Ma)	1σ (Ma)	Preferred age (Ma)	2σ (Ma)	Comment
A1854-671.8-a	P2a-Taco	10.21	0.05	98.8	10.12	0.08	**10.2**	**0.2**	Error weighted plateau age
A1854-671.8-b	P2a-Taco	10.10	0.07	50.3	10.73	0.07			
A1623-703.0-a	P1-Taco	10.50	0.16	100	10.67	0.21	**10.5**	**0.4**	Plateau age
A1623-703.0-b	P1-Taco	9.68	0.15	82.7	11.04	0.15	-	-	-
A2629-198.0-a	P1-Taco	11.41	0.24	100	11.14	0.29	**11.4**	**0.5**	Plateau age
A2629-198.0-b	P1-Taco	9.84	0.20	91.1	10.86	0.31	-	-	-

A sample of hydrothermal biotite in P2a-Taco (A1854-670.8) was collected from the central Taco zone (Fig. 3.16). It contained clots and veins of coarse-grained (1-2 mm), light brown biotite flakes that were easily separated from the igneous groundmass (Fig. 3.20 C). No quartz veins are noted in this sample. The sample returned an error weighted plateau age of 10.2 ± 0.2 Ma (Table 3.5; Fig. A3.2 E-F). In comparison, zircon from this same sample returned a U-Pb age of 10.71 ± 0.11 Ma (Table 3.5).

3.4.12. Re-Os Molybdenite Dating Results

Five molybdenite samples were dated in order to constrain the age of mineralisation with respect to porphyry emplacement and skarn formation. All Re-Os dates reported here represent the age of mineralisation (Table 3.6); these are the first Re-Os ages reported for Antamina (Fig. 3.16).

Table 3.6. Re-Os molybdenite ages for the Antamina deposit.

Sample ID	Zone	Rock Type	Re (ppm)	± 2σ	^{187}Re (ppb)	± 2σ	^{187}Os (ppm)	± 2σ	Age (Ma)	± 2σ	Paragenetic Stage*
Quartz-molybdenite veins in intrusions											
A2589-1120.3	Usupallares	P1	29.51	0.08	18548	49	2.991	0.007	9.68	0.05	Stage II
A1536-195.0	Taco	P2a	133.5	0.30	83928	217	13.964	0.012	9.99	0.04	Stage II
Skarns											
A1974-480.0	Usupallares	Endoskarn	69.08	0.23	43420	150	7.514	0.019	10.39	0.05	Stage I
A1390-580.2	Taco	Exoskarn	78.01	0.20	49034	127	8.528	0.025	10.44	0.05	Stage I
A2629-198.0	Taco	Endoskarn	75.92	0.24	47720	150	8.409	0.042	10.58	0.07	Stage I

Molybdenite samples were selected from endoskarn, exoskarn, and veins in P1-Usupallares, and P2a-Taco (Fig. 3.2). Two non-overlapping mineralisation ages are observed in skarns, from 10.58 ± 0.07 to 10.44 ± 0.05 and 10.39 ± 0.05 Ma. Two younger, also non-overlapping, ages are reported for veins hosted in P2a-Taco and P1-Usupallares, 9.99 ± 0.04 and 9.68 ± 0.05 Ma, respectively (Table 3.6; Fig. 3.16). In the northeast Taco zone, molybdenite from endoskarn is younger (10.58 ± 0.07 Ma; A2629-198.0) than hydrothermal biotite in the groundmass of the same sample (11.4 ± 0.5 Ma); the nearest P1 U-Pb zircon age is 10.95 ± 0.20 Ma, approximately 600 m to the southeast (Fig. 3.16). In the Bornita zone, the age of molybdenite in exoskarn (10.44 ± 0.05 Ma; A1390-580.2) overlaps with hydrothermal biotite in P1-Taco (10.5 ± 0.4 Ma; A1623-703.0), approximately 500 m to the northeast (Fig. 3.16). In the Usupallares zone, a molybdenite age in endoskarn (10.39 ± 0.05 Ma; A1974-480.0) is indistinguishable from P1-, P2-, and P3-Usupallares zircon ages (10.44 ± 0.14 to 10.24 ± 0.23 Ma) approximately 700 m to the northeast (Fig. 3.16). A molybdenum + quartz vein in P2a-Taco is younger (9.99 ± 0.04 Ma; A1536-195.0) than zircon in its equivalent host rock (10.71 ± 0.11 Ma, A1854-670.8; Fig. 3.18 E). Similarly, another molybdenum + quartz vein from the Usupallares zone is younger (9.68 ± 0.05 Ma; A2589-1120.0) than its P1 host rock (10.42 ± 0.11 Ma; A2589-1120.3; Fig. 3.18 M).

3.5. Discussion

3.5.1. Role of P1 in Skarn Formation

All of the porphyry phases documented at Antamina display evidence for mineralising potential, including the presence of magmatic biotite ± hornblende, quartz stockwork veins, and weak to strong potassic alteration. However, only two of the documented phases (P1-

Taco and P1-Usupallares) display endoskarn alteration, which provides a clear genetic link to the surrounding exoskarns. P1-Condorcocha has an associated skarn, but is inferred under cover. P1-Oscarina, P2-Oscarina, and P3-Condorcocha contain hornblende and biotite, but lack potassic alteration, endoskarn, and quartz stockwork veins, indicating lower temperatures of formation and weaker mineralising potential. Here we examine the relationship between P1 porphyries and skarn formation at Antamina.

Emplacement of P1-Taco (10.95 ± 0.20 Ma) was accompanied by multiple pulses of magmatic fluid exsolution (and hydrothermal alteration), as indicated by the presence of UST quartz layers and locally high densities of quartz stockworks in the Taco zone. Comb-layered quartz is an igneous texture that forms in the cupola zone of shallow felsic intrusions and each layer is indicative of fluid exsolution and release from a crystallising magma (Lowenstern and Sinclair, 1996). Release of magmatic fluids is also indicated by quartz stockwork veins, which form in response to hydraulic fracturing of wall rocks (including the crystallised margin of P1-Taco), and subsequent fluid egress (e.g., Burnham, 1997). Interaction of these magmatic-hydrothermal fluids with calcareous wall rocks drove the formation of endoskarns and exoskarns associated with P1-Taco. Stockwork veins observed in P1-Usupallares indicate a similar process took place at approximately 10.42 ± 0.11 Ma, leading to the formation of slightly younger skarns southwest of the Taco zone. Between the Taco and Usupallares zones, the skarns coalesce, creating one continuous aureole of skarn alteration around (and in) the APC.

Titanite dated from a P1-Taco endoskarn (11.2 ± 1.3 Ma) overlaps the entire range of magmatic and hydrothermal ages reported in this study. The poor quality of the analyses have contributed to the large error, which is likely due to the presence of inclusions or open-system behaviour during skarn formation.

3.5.2. P2 and P3 Inter-Mineralisation Porphyries

In the Taco zone, P2a-, P2b- and P3 (10.71 ± 0.11 Ma to 10.25 ± 0.2 Ma) cut across P1 and its associated skarns, thereby constraining the age of the early skarn formation. Similarly, in the Usupallares zone, P2 and P3 (10.44 ± 0.14 to 10.24 ± 0.23 Ma) constrain the age of P1 skarns. Inter-mineralisation porphyries (P2, P3) in the Taco and Usupallares zones may have also contributed metals to the earlier skarns, thereby increasing the endowment of the whole

system. These inter-mineralisation porphyries share many similarities with P1 in terms of magmatic-hydrothermal potential; they all contain magmatic biotite, quartz stockworks, and localized potassic alteration. One key difference is that they lack endoskarn alteration. The absence of endoskarn in these inter-mineralisation porphyries does not preclude their skarn-forming potential, though it does indicate that there was a lack of proximal reactive wall rock and Ca available to drive skarn alteration. Magmatic-hydrothermal fluids associated with the emplacement of P1 consumed most (if not all) of the proximal carbonate rocks during early skarn formation. As a result, any fluids released from these inter-mineralisation porphyries would have to be transported to the marble front before any further skarn-forming reactions could take place. It is conceivable that any reactive wallrocks encountered by these fluids would form another generation of skarn, coalescing with early P1 skarns. Quartz stockworks cutting across P1-skarns provide some evidence that hydrothermal fluids were transported away from the porphyry centres into existing skarns, and beyond.

3.5.3. Condorcocha

The $^{238}U/^{206}Pb$ zircon age reported for P2-Concorcocha (10.61 ± 0.12 Ma; this study) is within error of the previously reported $^{40}Ar/^{39}Ar$ ages for biotite (11.02 ± 0.09 Ma; Love et al., 2003) and hornblende (10.85 ± 0.25 Ma; Escalante, 2008) from the same area. The $^{238}U/^{206}Pb$ zircon age of P2-Condorcocha (10.61 ± 0.12 Ma; this study) overlaps with P2a-Taco (10.71 ± 0.11 Ma), P2-Oscarina (10.54 ± 0.11 Ma), and P1- to P2-Usupallares (10.42 ± 0.14 to 10.44 ± 0.14 Ma). The timing of emplacement coincides with a peak in magmatic-hydrothermal activity in the adjacent APC, where porphyry emplacement, skarn formation, and mineralisation was actively taking place. Given the ~1 km proximity of Condorcocha to Antamina, and the age and textural similarities, it is reasonable to question why Condorcocha did not acquire a metalendowment on the same scale as Antamina. Field evidence indicates that the APC comprises at least seven syn-mineralisation porphyry phases, in contrast to Condorcocha where only two porphyry phases (P1 inferred and P2 documented) comprise the main stock, which are cut by a later porphyry (P3). This indicates that the emplacement of multiple fertile porphyry phases (versus one or two) can have a cumulative effect on enhancing the grade and tonnage of a magmatic-hydrothermal ore deposit.

3.5.4. Oscarina Dykes

The Oscarina dykes were emplaced along thrust faults roughly perpendicular to the orientation of the APC. Based on $^{40}Ar/^{39}Ar$ ages, Escalante (2008) concluded that the Oscarina dykes were slightly older than the APC intrusions. Our new U-Pb zircon ages (Table 3.4), however, show that P1-Oscarina (10.81 ± 0.02 Ma) was emplaced after P1-Taco (10.96 ± 0.06 Ma). Cross-cutting relationships were not observed between the Oscarina dykes and any of the Taco porphyries, although the dykes lack endoskarn alteration and quartz stockwork veins, and cut across Taco exoskarns (Fig. 3.9 and Fig. 3.14 D). Based on these observations, the Oscarina dykes do not appear to be related to skarn formation at Antamina. Furthermore, their different structural orientation (Fig. 1.5), geochemical composition (Fig. 3.5 B-C), and lack of high-temperature alteration assemblages (potassic, endoskarn; Table 3.1) may indicate that they were sourced from a separate magma chamber, or via a different fractionation process, than the APC porphyries.

3.5.5. Protracted and Pulsed Magmatism

Based on the age dispersion along concordia (on the order of approximately 1.8 to 3.6 million years) and overlap observed in these porphyry samples, it appears that a protracted period of zircon growth and recycling was a standard process in the magma reservoir(s) underlying the Antamina deposit. Some degree of overlap is expected due to the precision of the LA-ICP-MS dating method (compared to the higher precision TIMS method); nonetheless, some samples show a distinct age gap between the oldest and youngest concordant zircon. For example, A1854-192.0 (P3-Taco) shows approximately 1.9 Ma of age dispersion [(oldest zircon + 2σ error) – (youngest zircon - 2σ error)] along concordia and an age gap [(oldest zircon - 2σ error) – (youngest zircon + 2σ error)] of approximately 0.8 Ma between the oldest (age + 2σ error) and youngest (age - 2σ error) concordant zircons (Fig. 3.18). Likewise, zircon ages from A2589-367.5 (P2-Usupallares) are dispersed along concordia by approximately 2.2 Ma with an age gap of approximately 0.9 Ma (Fig. 3.18). While the youngest concordant zircons in each sample have been selected to represent the age of final crystallization, the older concordant zircons are most likely to be antecrysts recycled in the same magma chamber (e.g., Miller et al., 2007). It is through this process that each successively younger porphyry phase obtained a range of zircon ages spanning up to approximately 3 million years with no overlap between the oldest and youngest concordant

ages. This idea is supported by zircon CL textures displaying magmatic rims surrounding partially resorbed cores of similar brightness (Fig. 3.17). While the LA-ICP-MS data lack the precision of CA-TIMS, a subtle inheritance trend is still apparent, which is reasonable for a porphyry system.

It is interesting to note that many of the samples also contain zircons inherited either from the source or the host rocks. These zircons range in age from Lower Devonian to Eocene and can be recognized by their bright CL response (Fig. 3.17). Geological units that correspond with these ages comprise the bedrock that hosts and underlies the Antamina deposit. This indicates that there has been some amount of crustal interaction and assimilation with these magmas, which is an expected process in a subduction-related continental arc (Hildreth and Moorbath, 1988).

3.5.6. Timing of Mineralisation

In the Taco zone, Stage I molybdenite ages range from 10.58 ± 0.07 to 10.44 ± 0.05 Ma and overlap with P2a (10.71 ± 0.11 Ma) and P3 (10.25 ± 0.20 Ma) U-Pb zircon ages; these ages are significantly younger than P1 zircon ages in the Taco zone (10.95 ± 0.20. Ma). In the Usupallares zone, Stage I molybdenite (10.39 ± 0.05 Ma) overlaps with all of the intrusions in that zone, from P1 (10.42 ± 0.14) to P3 (10.24 ± 0.23 Ma). Stage II molybdenite ranges from 9.99 ± 0.04 Ma in the Taco area to 9.68 ± 0.05 Ma in the Usupallares area; these ages do not appear to overlap with any of the porphyries dated in this study.

Because zircon ages record early-stage magma crystallisation (at temperatures near or exceeding 900°C) and molybdenite deposition occurs once temperatures have cooled to hydrothermal conditions (approximately <450°C), the molybdenite stages identified in this study cannot be definitively linked to any specific porphyry. However, these new Re-Os molybdenite ages display a spatial relationships with the Antamina porphyries. Both Stage I and Stage II molybdenite ages decrease from northeast (Taco) to southwest (Usupallares) along the axis of the deposit (Fig. 3.16). This pattern of southwest-sweeping mineralisation along the axis of the APC is in cadence with the northeast to southwest younging of U-Pb ages in the APC porphyries (Fig. 3.16). Together, the zircon and molybdenite ages constrain the duration of magmatic-hydrothermal activity in the APC to approximately 1.52 million years, with the main phase occurring over a maximum duration of 0.52 Ma (P2a-Taco (10.71

± 0.11 Ma) to P2-Usupallares (10.44 ± 0.14 Ma), including Stage I molybdenite (10.39 ± 0.05 Ma)).

3.5.7. Width and Lateral Continuity of the Antamina Skarn

Field evidence indicates that P1-Taco and P1-Usupallares were emplaced as dykes extending upward into the wall rock, likely from a shallow stock (e.g., Fig. 3.7 K). This irregular porphyry geometry increased the reaction surface area at the porphyry-wall rock interface and each apophysis acted as a conduit for skarn-forming fluids, as evidenced by the pervasive endoskarn alteration of both P1-Taco and P1-Usupallares dykes. Additional factors such as the redox potential of the magma and wall rock, volume and duration of fluids released, as well as formation depth likely contributed to the width, lateral extent, and continuity of the Antamina skarns. All of the porphyries examined in this study contain magnetite (no ilmenite), which is indicative of oxidised magmas. The wall rocks are medium grey to black, with various amount of organic carbon; some rocks contain up to 3.6% organic carbon (Chapter 2 and Digital Appendix 2.3). The high organic carbon content is not favourable for skarn formation, as during thermal metamorphism the organic carbon may be heated and converted to CO_2. This CO_2 in the system will suppress subsequent skarn formation, as the process of skarn formation also produces CO_2 (e.g., quartz + carbonate → wollastonite + CO_2). The higher XCO_2 caused by reaction of organic carbon will retard or even stop the skarn forming reactions. On the other hand, skarn formation at shallow depths tends to be more laterally extensive than at greater depths (e.g., Chang and Meinert, 2008), because at shallow depths the wall rocks are more amenable to brittle deformation and fracturing, which provides effective fluid flow channels to allow escape of the CO_2 generated during thermal metamorphism, and more extensive penetration of skarn-forming magmatic hydrothermal fluids into the country rocks (Meinert, 2005). In contrast, at depths exceeding ~8 km wall rocks tend to be ductile, which significantly decreases the fracture densities of the rocks, thereby blocking fluid flow and resulting in narrower skarn zones (Chang and Meinert, 2008). In addition, at greater depths the water solubility in magmas is higher (e.g., Burnham, 1997), which is unfavourable for hydrothermal fluid exsolution and skarn formation. A shallow depth of emplacement for P1-Taco is supported by the narrow thermal metamorphic halo (~500-800 m wide), ~800-1000 m wide skarn zone and numerous apophyses (presumably taking advantage of brittle fractures in the shallow crust) surrounded by skarn.

The combination of multiple pulses of oxidizing magma emplaced in a shallow crustal setting may have subdued the reducing potential of the wall rocks to favour the development of laterally extensive, coalesced skarns at Antamina.

3.5.8. Structural Controls

Skarn alteration zones are narrower in the Usupallares zone (~500 m) compared to the Taco zone (~800-1000 m), and at Usupallares it is possible to see the outward zoning of endoskarn-exoskarn-marble over tens of meters along open pit highwalls (e.g., Fig. 3.12 H). This is likely due to the influence of the Valley Fault; the Taco zone coincides with maximum dilation along this structure, whereas Usupallares formed in a structurally-controlled hanging valley perpendicular to the main Valley Fault zone (Fig. 1.5). In addition to a shallow depth of emplacement, the Valley Fault probably influenced fluid flow, the width of alteration zones, and the overall shape of the deposit (McCuaig, 2003).

3.5.9. Formation of the Giant Antamina Deposit

In the largest porphyry districts around the world, economic deposits are typically formed by clusters of fertile porphyry phases emplaced in several pulses on the order of millions to hundreds of thousands of years; examples include El Teniente, Chile (Maksaev et al., 2004), Tampakan, Philippines (Rohrlach and Loucks, 2005), Grasberg, Indonesia (Pollard et al., 2005), Yanacocha, Peru (Longo et al., 2010), and Coroccohuayaco, Peru (Chelle-Michou et al., 2015). The ages in context with the intrusion paragenesis at Antamina show that this giant deposit formed in several short magmatic-hydrothermal pulses rather than a protracted period of intense magmatic-hydrothermal activity. The bulk of the economic resource formed in the Taco zone over approximately half a million years; this does not include Stage II molybdenite mineralisation, which formed at least 0.02 million years after P3-Taco emplacement. P1- and P2-Usupallares were emplaced during P2- and P3-Taco magmatism and the Usupallares zone formed over approximately 0.9 million years. The southeastwardly progressive younging of relatively short duration magmatic-hydrothermal events was likely controlled by dilation along the Valley Fault; the coalescing of skarns and porphyries along this structural corridor resulted in the formation of the giant Antamina deposit.

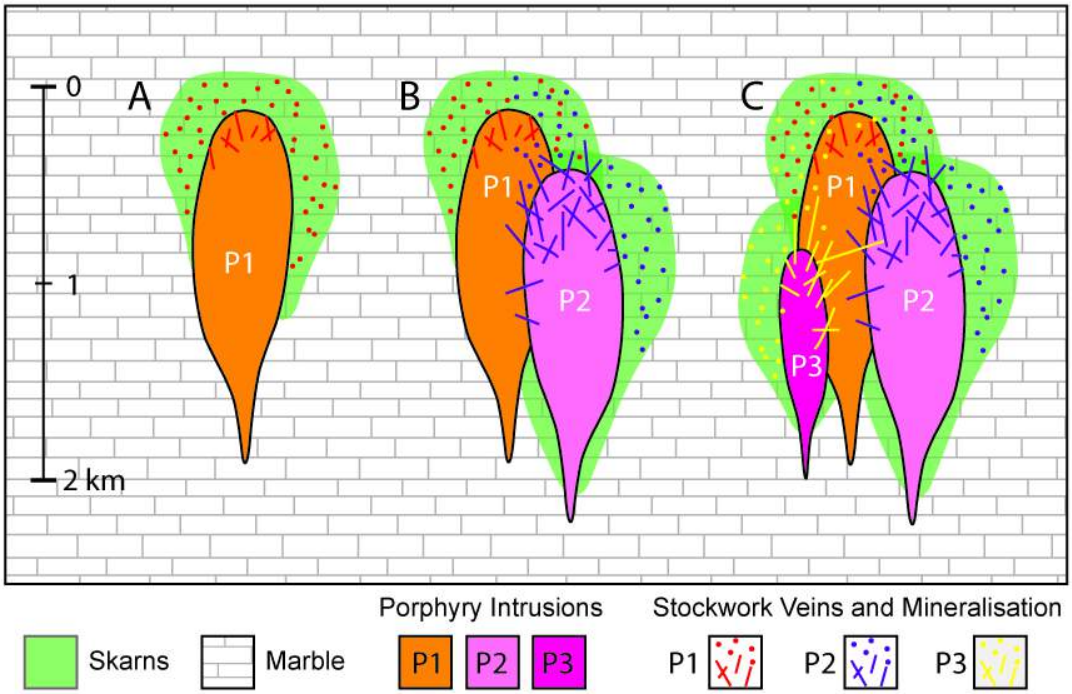

Fig. 3.21. A model for the vertical and lateral extent of the Antamina skarn deposit. A. Intrusion of P1into marble forms early skarns and mineralisation. Stockwork veins form in P1, but they do not propagate into the wall rock as porphyry-style alteration; skarns form instead. B. Intrusion of P2. Stockwork veins associated with P2 cut across P1 and earlier skarns, but where marble is available skarns form. C. Intrusion of P3/late porphyries. Associated stockwork veins cut across P1, P2, and earlier formed skarns. If marble is available, new skarns are formed. In case B and C, newly formed skarns coalesce with existing skarns. In A, B, and C mineralisation is added to the skarns and porphyries in each step, thereby enhancing the ore grade as well as the vertical and lateral extent of skarn alteration.

3.5.10. Exploration

Considerations for district-scale exploration include the composition of the host rocks, structural controls, the number of porphyry phases emplaced, and the presence of multiple fertility indicators (composition, mineralogy, texture) in an intrusive centre. Intrusive centres comprised of several hydrous (i.e., containing hornblende and/or biotite) porphyries are favoured over isolated stocks for enhancing the magmatic-hydrothermal potential. Multiple generations of quartz stockwork veins indicate good hydrothermal potential of a magma. Additional, more obvious, indicators of fertility include the presence of hydrothermal alteration (potassic or skarn) and visible mineralisation. The high Sr/Y (42-87, average 65) in all Antamina porphyries, except for P2-Oscarina, indicate that they are prospective for porphyry Cu ± Mo ± Au (and associated skarn) deposits (Richards, 2011). The REE patterns observed for all porphyries (with exception to P1- and P2-Oscarina) show enriched LREE and depleted HREE, which is consistent with amphibole fractionation and is another

prospectivity indicator (Richards, 2011). These geochemical compositions, coupled with the presence of biotite ± hornblende, are indicative of a high magmatic water contents that are needed to drive the formation of large mineralised systems. Structurally-focused porphyry emplacement (e.g., McCuaig, 2003) into reactive wall rocks is ideal; the lateral and/or vertical migration in porphyry emplacement coupled with uplift over time allows progressively younger magmas to interact with carbonate wall rocks, which is necessary for skarn formation and mineralisation.

3.6. Conclusions

Formation of the giant Antamina skarn-porphyry deposit occurred over a relatively short time period on the order of up to 1 Ma, based on the approximate time elapsed between emplacement of P1-Taco (10.95 ± 0.20 Ma) and P3-Usupallares (10.24 ± 0.23 Ma). In this study I have identified several factors that played an important role in promoting skarn formation at Antamina, including the emplacement of at least 11 fluid-rich porphyries, structural focussing of magmas and hydrothermal fluids, and an abundant supply of carbonate in favourable host rock for skarn formation and mineralisation. While each factor alone is not unique to Antamina, it is the combination of these factors at the right time and location that enhanced the otherwise typical ore-forming processes in this active arc setting.

Eleven porphyry phases have been documented in the APC, Oscarina, and Condorcocha zones; all phases (except the Oscarina dykes) contain quartz stockwork veins and weak to moderate potassic alteration, but only 3 display a genetic relationship to their surrounding skarns (P1-Taco, P1-Usupallares, and P1-Condorcocha). Uranium-Pb zircon ages for all of the porphyries show dispersion (~2-3 million years) and overlap along Concordia, indicative of recycling and recharge in a large composite magma chamber. In contrast, U-Pb zircon ages the adjacent Condorcocha stock show a single age population and less complex magmatic history. The APC is comprised of intermediate composition porphyries (trachyte-trachyandesite-andesite compositions), they contain biotite ± hornblende, and all phases are cross-cut by quartz stockwork veins. Porphyry emplacement was strongly influenced by the pre-existing structural framework, including a series of NW-trending thrust faults intersected by the NE-trending Valley Fault system. In general, porphyry ages (U-Pb zircon) and mineralisation ages (Re-Os molybdenite) display younging to the southwest along the axis of

the Valley Fault from Taco to Usupallares (NE to SW). Exceptions include the Oscarina dykes and the Condorcocha stock, both of which have different structural controls and potentially different source magma chambers from the APC. The formation of the giant Antamina porphyry-skarn deposit can be attributed to the emplacement of multiple fertile porphyries along a NE-trending, dilational structural corridor, into reactive calcareous wall rocks, over a relatively short timeframe, between 10.95 ± 0.20 to 10.24 ± 0.23 Ma.

3.7. References

Baker, J., Peate, D., Waight, T. and Meyzen, C., 2004. Pb isotopic analysis of standards and samples using a Pb-207-Pb-204 double spike and thallium to correct for mass bias with a double-focusing MC-ICP-MS. Chemical Geology, 211, 275-303.

Black, L.P., Kamo, S.L., Allen, C.M., Davis, D.W., Aleinikoff, J.N., Valley, J.W., Mundil, R., Campbell, I.H., Korsch, R.J., Williams, I.S., Foudoulis, C., 2004, Improved Pb-206/U-218 microprobe geochronology by the monitoring of a trace-element-related matrix effect; SHRIMP, ID-TIMS, ELA-ICP-MS, and oxygen isotope documentation for a series of zircon standards: Chemical Geology, v. 205, p. 115-140.

Black, L.P., Kamo, S.L., Allen, C.M., Aleinikoff, J.N., Davis, D.W., Korsch, R.J., and Foudoulis, C., 2003. TEMORA 1: a new zircon standard for Phanerozoic U-Pb geochronology. Chemical Geology 200 (1), 155e170. http://dx.doi.org/10.1016/S0009-2541(03)00165-7.

Burnham, C.W., 1997, Magmas and hydrothermal fluids, in H.L.Barnes (ed.), Geochemistry of Hydrothermal Ore Deposits, 3rd edition, John Wiley & Sons, p. 63-123.

Buys, J., Spandler, C., Holm, R.J., and Richards, S.W., 2014, Remnants of ancient Australia in Vanuatu: implications for crustal evolution in island arcs and tectonic development of the southwest Pacific: Geology, v. 42, p. 939-942.

Chang, Z., and Meinert, L.D., 2008, Zonation in skarns – complexities and controlling factors. In: Proceedings of the PACRIM Congress, Gold Coast, QLD, Australia, v. 11, p. 303-306.

Chang, Z., Vervoort, J. D., McClelland, W. C., and Knaack, C., 2006, U-Pb dating of zircon by LA-ICP-MS: Geochemistry, Geophysics, Geosystems, v. 7, Q05009. http://dx.doi.org/10.1029/ 2005GC001100.

Chelle-Michou, C., Chiaradia, M., Selby, D., Ovtcharova, M., and Spikings, R.A., 2015, High-resolution geochronology of the Coroccohuayco porphyry-skarn deposit, Peru: a rapid product of the Incaic Orogeny: Economic Geology, v. 110, p. 423-443.

CMA (Compañía Minera Antamina), 2007, Core logging manual and coding instructions, v. 2.10, 22 p.

Crowley, J.L., Schoene, B., Bowring, S.A., 2007, U-Pb dating of zircon in the Bishop Tuff at the millennial scale: Geology, v. 35, p. 1123-1126.

Defant, M.J., and Drummond, M.S., 1993, Mount. St. Helens: Potential example of the partial melting of the subducted lithosphere in a volcanic arc: Geology, v. 21, p. 547-550.

Droop, G.T.R., 1987, A general equation for estimating Fe^{3+} concentrations in ferromagnesian silicates and oxides from microprobe analyses using stoichiometries criteria: Mineralogical Magazine, v. 51, p. 431-435.

Escalante, A., Dipple, G.M., Barker, S.L.L., and Tosdal, R., 2010, Defining trace-element halos to skarn deposits hosted in heterogeneous carbonate rocks: Case study from Cu-Zn Antamina skarn deposit, Peru: Journal of Geochemical Exploration, v. 105, p. 117-136.

Escalante, A.D., 2008, Patterns of distal alteration zonation around Antamina Cu-Zn skarn and Uchucchacua Ag-base metal vein deposits, Peru: Mineralogical, chemical, and isotopic evidence for fluid composition, and infiltration, and implications for mineral exploration: PhD Thesis, The University of British Columbia, Canada, 817 p.

Frey, H.M., Lange, R.A., Hall, C.M., Delgado-Granados, H., and Carmichael, I.S.E., 2007, A Pliocene ignimbrite flare-up along the Tepic-Zacoalco rift: Evidence for the initial stages of rifting between the Jalisco block (Mexico) and North America: Geological Society of America Bulletin, v. 119, p. 49-64.

Gehrels, G.E., Valencia, V.A., Ruiz, J., 2008. Enhanced precision, accuracy, efficiency, and spatial resolution of U-Th-Pb ages by LA-MC-ICPMS. Geochemistry, Geophysics, Geosystems 9, Q03017. http://dx.doi.org/10.1029/2007GC001805.

Gerstenberger, H., and Haase, G., 1997. A Highly effective emitter substance for mass spectrometric Pb isotopic ratio determinations. Chem. Geol. 136, 309-312.

Glencore, 2015, Annual Report: http://www.glencore.com/assets/investor/doc/reports_ and_results/2015/GLEN-2015-Annual-Report.pdf.

Hathaway, L.H., 1997, Geological surface mapping and structural interpretation at Antamina Peru: internal report for Compañía Minera Antamina S.A., 35 p.

Hildreth, W., and Moorbath, S., 1988, Crustal contributions to arc magmatism in the Andes of central Chile: Contributions to Mineralogy and Petrology, v. 98, p. 455-489.

Holm, R.J., Spandler, C., Richards, S.W., 2013, Melanesian arc far-field response to collision of the Ontong Java Plateau: Geochronology and petrogenesis of the Simuku Igneous Complex, New Britain, Papua New Guinea: Tectonophysics, v. 603, p. 198-212.

Holm, R.J., and Poke, B., 2018, Petrology and crustal inheritance of the Cloudy Bay Volcanics as derived from a fluvial conglomerate, Papuan Peninsula (Papua New Guinea): An example of geological inquiry in the absence of *in situ* outcrop: Cogent Geoscience, https://doi.org/10.1080/23312041.2018.1450198.

Jackson, S.E., Pearson, N.J., Griffin, W.L., Belousova, E.A., 2004. The application of laser ablation-inductively coupled plasma-mass spectrometry to in situ U-Pb zircon geochronology: Chemical Geology, v. 211, p. 47-69.

Jaffey, A.H., Flynn, K.F., Glendenin, L.E., Bentley, W.C., Essling, A.M., 1971. Precision measurement of half-lives and specific activities of ^{235}U and ^{238}U. Phys. Rev. C4, 1889–1906.

Kosler, J., 2001, Laser-ablation ICPMS study of metamorphic minerals and processes. In: Sylvester P. J. ed. Laser-ablation-ICPMS in the earth sciences; principles and applications Mineralogical Association of Canada Short Course Handbook 29, 185-202.

Kay, S.M., Mpodozis, C., Ramos, V.A., and Munizaga, F., 1991, Magma source variation for mid-late Teriary magmatic rocks associated with a shallowing subduction zone and a thickening crust in the central Andes (28 to 33°): Geological Society of America Special Paper 265, p. 113-137.

Lang, J.R., and Titley, S.R., 1998, Isotopic and geochemical characteristics of Laramide magmatic systems in Arizona and implications for the genesis of porphyry copper deposits: Economic Geology, v. 93, p. 138-170.

Le Maitre, R.W., Bateman, P., Dudek, A., Keller, J., Lameyre Le Bas, M.J., Sabine, P.A., Schmid, R., Sorensen, H., Streckeisen, A., Woolley, A.R., and Zanettin, B., 1989. A classification of igneous rocks and glossary of terms: Recommendations of the IUGS Subcommission on the Sustematics of Igneous Rocks. Blackwell Scientific, London.

Lipten, E.J., and Smith, S.W., 2005, The geology of the Antamina copper-zinc deposit, Peru, South America: in Porter, T.M. (Ed.), Super Porphyry Copper & Gold Deposits: A Global Perspective, PGC Publishing, Adelaide, Australia, v. 1, p. 189-204.

Lowenstern, L.B., and Sinclair, W.D., 1996, Exsolved magmatic fluid and its role in the formation of comb-layered quartz at the Cretaceous Logtung W-Mo deposit, Yukon Territory, Canada: Trans. R. Soc. Edinb. Earth Sci., v. 87, p. 291-303.

Longo, A.A., Dilles, J.H., Grunder, A.L., and Duncan, R., 2010, Evolution of calc-alkaline volcanism and associated hydrothermal gold deposits at Yanacocha, Peru: Economic Geology, v. 105, p. 1191-1241.

Love, D.A., Clark, A.H., Ullrich, T.D., Archibald, D.A., and Lee, J.K.W., 2003, $^{40}Ar/^{39}Ar$ evidence for the age and duration of magmatic-hydrothermal activity in the giant Antamina Cu-Zn skarn deposit, Ancash, north-central Peru (abs.): Geological Association of Canada-Mineralogical Association of Canada-Society of Economic Geologists, Joint Annual Meeting, Vancouver, British Columbia, Abstracts Volume, v. 28, CD-ROM.

Ludwig, K.R., 2012, User's Manual for Isoplot 3.75-4.15: A Geochronological Toolkit for Microsoft Excel. Berkeley Geochronology Center Special Publication No. 5.

Maksaev, V., Munizaga, F., and McWilliams, M., 2004, New chronology for El Teniente, Chilean Andes, from U/Pb, $^{40}Ar/^{39}Ar$, Re-Os and fission-track dating: Implications for the evolution of a supergiant porphyry Cu-Mo deposit: Society of Economic Geologists Special Publication, v. 11, p. 15-54.

Markey, R.J., Stein, H.J., and Morgan, J.W., 1998, Highly precise Re-Os dating for molybdenite using alkaline fusion and NTIMS: Talanta, v. 45, p. 935–946.

Markey, R.J., Stein, H.J., Hannah J.L., Selby, D., and Creaser, R.A., 2007, Standardizing Re-Os geochronology: A new molybdenite Reference Material (Henderson, USA) and the stoichiometry of Os salts: Chemical Geology, v. 244, p. 74-87.

Mattinson, J.M., 2005, Zircon U-Pb chemical abrasion ("CA-TIMS") method: Combined annealing and multi-step partial dissolution analysis for improved precision and accuracy of zircon ages: Chemical Geology, v. 220, p. 47–66.

McCuaig, T.C., 2003, Structural review of the Antamina mine, Peru: internal report for Compañía Minera Antamina S.A., 48 p.

McKee, E.H., Noble, D.C., Scherkenbach, D.A., Drexler, J.W., Mendoza, J., and Eyzaguirre, V.R., 1979, Age of porphyry intrusion, potassic alteration, and related skarn mineralisation, Antamina district, northern Peru: Economic Geology, v. 74, p. 928-930.

Miller, J.S., Matzel, J.E.P., Miller, C.F., Burgess, S.D., and Miller, R.B., 2007, Zircon growth and recycling during the assembly of large, composite arc plutons: Journal of Volcanology and Geothermal Research, v. 167, p. 282-299.

Mundil, R., Ludwig, K. R., Metcalfe, I., and Renne, P. R. (2004). Age and timing of the Permian Mass Extinctions: U/Pb Dating of Closed-System Zircons, Science, v. 305, p. 1760-1763.

Pacheco, A.M., 1997, Intrusivo en el Skarn Antamina: internal report for Compañía Minera Antamina S.A., 26 p.

Parrish, R.R., 1990, U-Pb dating of monazite and its application to geological problems: Canadian Journal of Earth Sciences, v. 27, p. 1431-1450.

Pollard, P.J., Taylor, R.G., and Peters, L., 2005, Ages of intrusion, alteration, and mineralisation at the Grasberg Cu-Au deposit, Papua, Indonesia: Economic Geology, v. 100, p. 1005-1020.

Redwood, S.D., 2004, Geology and development history of the Antamina copper-zinc skarn deposit, Peru: Society of Economic Geologists Special Publication 11, Ch. 14, p. 259-277.

Richards, J.P., Boyce, A.J., and Pringle, M.S., 2001, Geological evolution of the Escondida area, northern Chile: A model for spatial and temporal localization of porphyry Cu mineralization: Economic Geology, v. 96, p. 271-305.

Richards, J.P., 2011, High Sr/Y arc magmas and porphyry Cu ± Mo ± Au deposits: just add water: Economic Geology, v. 106, p. 1075-1081.

Rohrlach, B.D., and Loucks, R.R., 2005, Multi-million-year cyclic ramp-up of volatiles in a lower crustal magma reservoir trapped below the Tampakan copper-gold deposit by Mio-Pliocene crustal compression in the southern Philippines, in Porter T.M., ed., Super porphyry copper and gold deposits: a global perspective: Adelaide, Australia, PGC Publishing, p. 369-407.

Rooney, T.O., Mohr, P., Dosso, L., and Hall, C., 2013, Geochemical evidence of mantle reservoir evolution during progressive rifting along the western Afar margin: Geochimica et Cosmochimica Acta, v. 102, p. 65-88.

Samson S.D., and Alexander E.C., 1987, Calibration of the interlaboratory $^{40}Ar/^{39}Ar$ dating standard, Mmhb-1: Chemical Geology, v. 66, p. 27-34.

Schärer, U., 1984, The effect of initial ^{230}Th disequilibrium on young U-Pb ages: the Makalu case, Himalaya: Earth and Planetary Science Letters, v. 67, p. 191-204.

Schellart, W.P., Freeman, J., Stegman, D.R., Moresi, L., and May, D., 2007, Evolution and diversity of subduction zones controlled by slab width: Nature, v. 466, p. 308-311.

Scoates, J.S. and Friedman, R.M., 2008, Precise age of the platiniferous Merensky Reef, Bushveld Complex, South Africa, by the U-Pb ID-TIMS chemical abrasion ID-TIMS technique, Economic Geology, v. 103, p. 465-471.

Schmitz, M.D. and Schoene, B., 2007, Derivation of isotope ratios, errors, and error correlations for U-Pb geochronology using 205Pb-235U-(233U)-spiked isotope dilution thermal ionization mass spectrometric data, Geochemistry, Geophysics, Geosystems, 8: Q08006, doi:10.1029/2006GC001492.

Selby, D. and Creaser, R.A., 2004, Macroscale NTIMS and microscale LA-MC-ICP-MS Re-Os isotopic analysis of molybdenite: Testing spatial restrictions for reliable Re-Os age determinations, and implications for the decoupling of Re and Os within molybdenite: Geochimica et Cosmochimica Acta, v. 68, p. 3897-3908.

Sillitoe, R.H., 1997, Comments on the geological model for the Antamina copper-zinc skarn deposit, Peru: Internal Report for Compañía Minera Antamina S.A., 7 p.

Spandler, C., Hammerli, J., Sha, P., Hilbert-Wolf, H., Hu, Y., Roberts, E., and Schmitz, M., 2016, MKED1: A new titanite standard for in situ analysis of Sm-Nd isotopes and U-Pb geochronology: Chemical Geology, v. 425, p. 110-126.

Stacey, J.S., and Kramers, J.D. 1975. Approximation of terrestrial lead isotopic evolution by a two-stage model. Earth and Planetary Science Letters, 26: 207–221.

Sun, S., and McDonough, W.F., 1989, Chemical and isotopic systematics of oceanic basalts: implications for mantle composition and processes: Geological Society, London, Special Publication, v. 42, p. 313-345.

Tera, F., and Wasserburg, G.J., 1972, U-Th-Pb systematics in three Apollo 14 basalts and the problem of initial Pb in lunar rocks: Earth and Planetary Science Letters, v. 14, p. 281-304.

Thirlwall, M. F., 2000. Inter-laboratory and other errors in Pb isotope analyses investigated using a ^{207}Pb-^{204}Pb double spike, Chemical Geology, 163, p. 299-322.

Tucker, R., Roberts, E., Hu, Y., Kemp, A., Salisbury, S., 2013. Detrital zircon age constraints for the Winton formation, Queensland: contextualizing Australia's late Cretaceous dinosaur faunas. Gondwana Research, v. 24, 767e779. http://dx.doi.org/10.1016/j.gr.2012.12.009.

Van Achterbergh, E., Ryan, C.G., Jackson, S.E., Griffin, W.L., 2001. Appendix 3, data reduction software for LA-ICP-MS. In: Sylvester, P. (Ed.), Laser-Ablation-ICPMS in the Earth Sciences - Principles and Applications. Mineralogical Association of Canada, Short Course Series, pp. 239-243.

Wiedenbeck, M., Alle, P., Corfu, F., Griffin W.L., Meier, M., Oberli, F., von Quadt A., Roddick, J.C., Speigel W., 1995, 3 Natural Zircon Standards for U-Th-Pb, Lu-Hf, Trace-Element and REE Analyses. Geostandards Newsletter 19, 1-23.

3.8. Appendix

Table A3.1. Previously published geochronology for the Antamina and Condorcocha deposits.

Sample ID	UTM East	UTM North	Location	Description	Mineral	Method	Age (Ma)	± 2σ (Ma)	Reference
L-14	8945138	273508	Taco Pit	K-altered Qtz monzonite ppy	K-feldspar	K-Ar	9.6	0.2	McKee et al. (1979)
CMA 335	8945425	273862	Taco Pit	K-altered Qtz monzonite ppy	Ser	Ar-Ar	9.75	0.07	Love et al. (2003)
CMA 206	8944898	273464	Taco Pit	Late white endoskarn	Ser, Plg	Ar-Ar	9.8	0.1	Love et al. (2003)
CMA 009	8945310	274050	Taco Pit	Phyllic altered Qtz monzonite ppy	Ser	Ar-Ar	9.81	0.06	Love et al. (2003)
CMA 190	8945308	274047	Taco Pit	K-altered Qtz monzonite ppy	K-feldspar	Ar-Ar	9.87	0.07	Love et al. (2003)
CMA 238	8945482	273670	Taco Pit	Phyllic altered Qtz monzonite ppy	Ser	Ar-Ar	9.9	0.1	Love et al. (2003)
CMA 179	8945306	274043	Taco Pit	K-altered Qtz monzonite ppy	Plg	Ar-Ar	9.98	0.09	Love et al. (2003)
CMA 206	8944898	273464	Taco Pit	Early massive endoskarn	Ser, Plg	Ar-Ar	10.00	0.16	Love et al. (2003)
CMA 009	8945310	274050	Taco Pit	Phyllic altered Qtz monzonite ppy	Bio	Ar-Ar	10.09	0.07	Love et al. (2003)
R-16	8945138	273508	Taco Pit	K-altered Qtz monzonite ppy	Bio	K-Ar	10.1	0.6	McKee et al. (1979)
CMA 226	8945180	274100	Taco Pit	Coarse grained ppy	Bio	Ar-Ar	10.18	0.07	Love et al. (2003)
2PAT-02	8945299	273553	Taco Pit	Endoskarn	Bio	Ar-Ar	10.29	0.36	Escalante (2008)
CMA 238	8945480	273670	Taco Pit	Phyllic altered Qtz monzonite ppy	Bio	Ar-Ar	10.12	0.07	Love et al. (2003)
CMA 335	8945425	273862	Taco Pit	K-altered Qtz monzonite ppy	Bio	Ar-Ar	10.18	0.07	Love et al. (2003)
CMA 179	8945310	274040	Taco Pit	K-altered Qtz monzonite ppy	Bio	Ar-Ar	10.3	0.07	Love et al. (2003)
CMA 190	8945310	274048	Taco Pit	K-altered Qtz monzonite ppy	Bio	Ar-Ar	10.39	0.08	Love et al. (2003)
2PAT-18	8945324	273621	Taco Pit	Late dike	Zircon	U-Pb	10.52	0.17	Escalante (2008)
2PAT-11	8945467	273755	Taco Pit	Bio-Plg-ppy	Zircon	U-Pb	10.73	0.1	Escalante (2008)
ANT-183	8943982	272830	Usupallares	I-2-C ppy	K-feldspar	Ar-Ar	10.1	0.1	Love et al. (2003)
ANT-WEST-F	8944026	272599	Usupallares	K-altered, plg-rich ppy with Ksp megacrysts	K-feldspar	K-Ar	10.4	0.4	McKee et al. (1979)
2PAT-08	8945101	273564	Usupallares	Bio-orthoclase-megacryst dike	Zircon	U-Pb	10.56	0.21	Escalante (2008)
ANT-1	8945516	274970	Oscarina	Potassic-propylitic altered Qtz monzonite ppy	Bio	K-Ar	9.1	0.4	McKee et al. (1979)
ANT-EES	8946248	274233	Ridge Road	Phyllic altered Qtz monzonite ppy	K-feldspar	K-Ar	10.2	0.3	McKee et al. (1979)
2PAT-06	8945202	274744	Oscarina dike	Hbl-Bio-Plg ppy	Hbl	Ar-Ar	10.6	1.1	Escalante (2008)
2PAT-06	8945202	274744	Condorcocha	Hbl-Bio-Plg ppy	Bio	Ar-Ar	10.76	0.16	Escalante (2008)
4PAA231	8945984	273918	Quarry Bench	Qtz feldspar ppy dike	Bio	Ar-Ar	10.85	0.07	Escalante (2008)
4PAA127	8947008	273049	Condorcocha	Qtz feldspar ppy dike	Hbl	Ar-Ar	10.85	0.25	Escalante (2008)
4PAA230	8946100	273819	Quarry Bench	Qtz feldspar ppy dike	Bio	Ar-Ar	10.93	0.09	Escalante (2008)
4PAA125	8946332	273323	Fortuna dike	Silicified dacite ppy dike	Bio	Ar-Ar	10.94	0.08	Escalante (2008)
ANT-198	8947000	273000	Condorcocha	Qtz feldspar ppy dike	Bio	Ar-Ar	11.02	0.09	Love et al. (2003)

Abbreviations: Biotite (Bio); hornblende (Hbl); plagioclase (Plg); quartz (Qtz); sericite (Ser); porphyry (ppy).

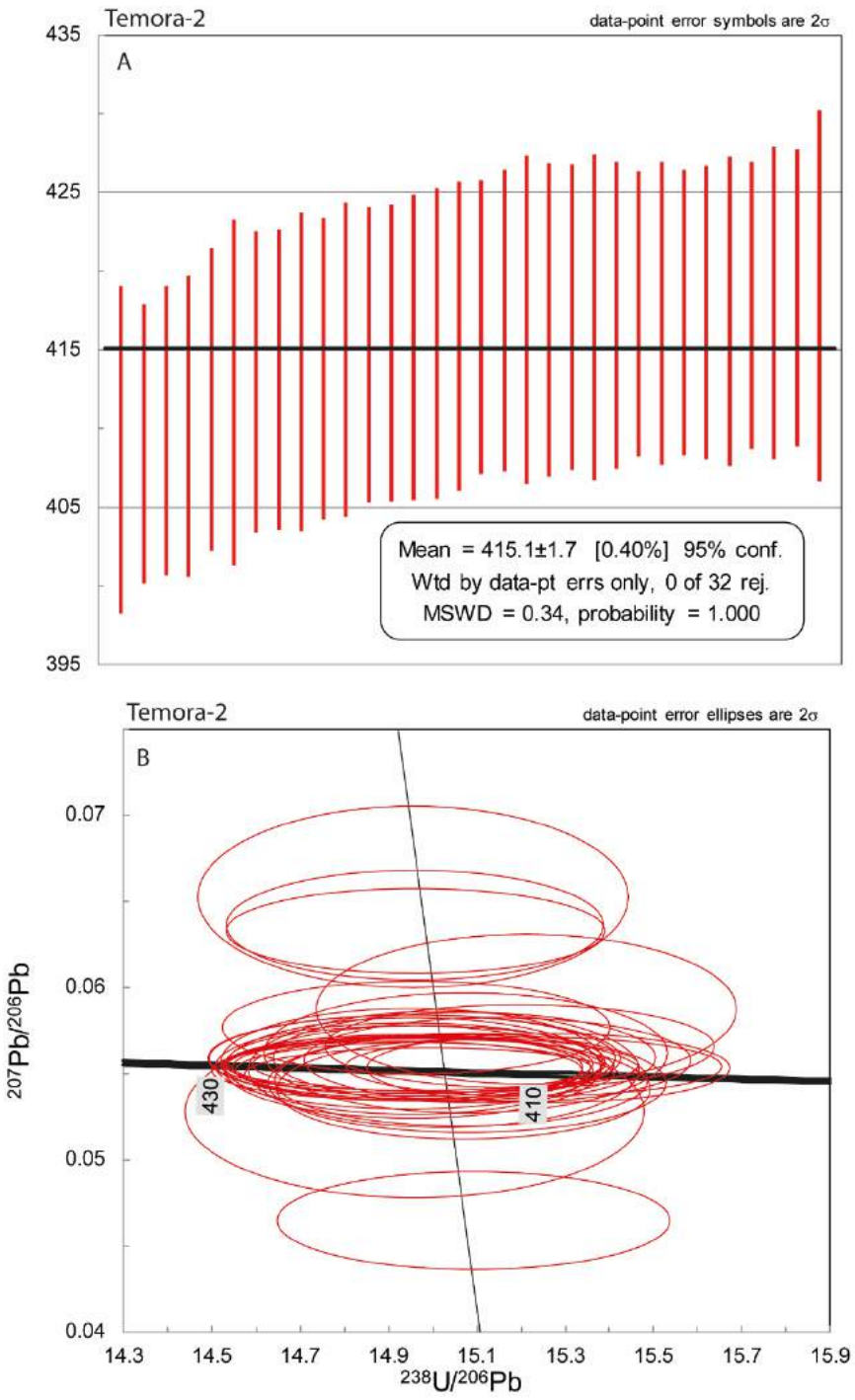

Fig. A3.1. Weighted average and Concordia plot for Temora-2 U-Pb zircon geochronology standard.

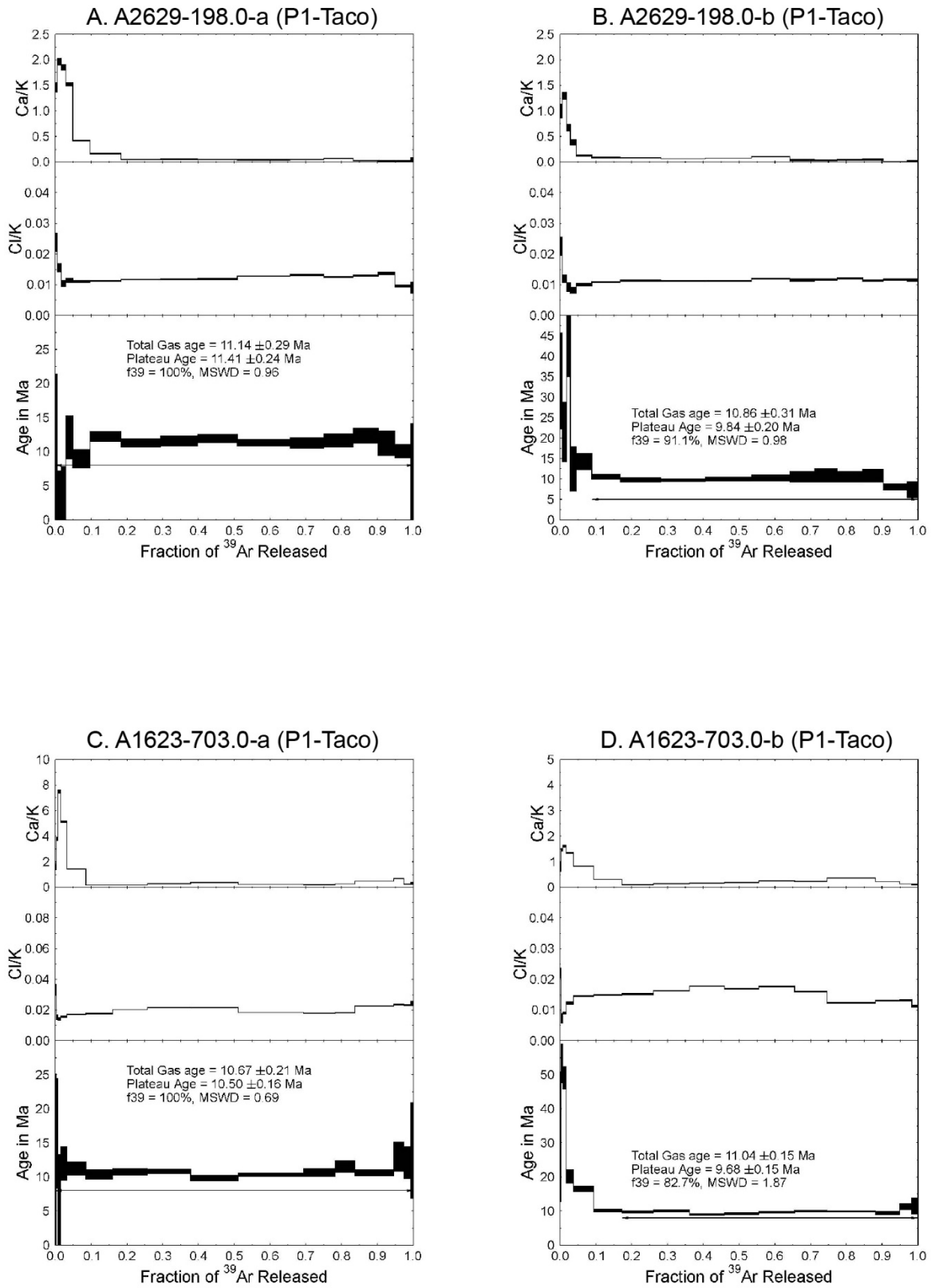

Fig. A3.2. Age spectra plots of $^{40}Ar/^{39}Ar$ step-heating experiments on hydrothermal biotite. Continued on next page.

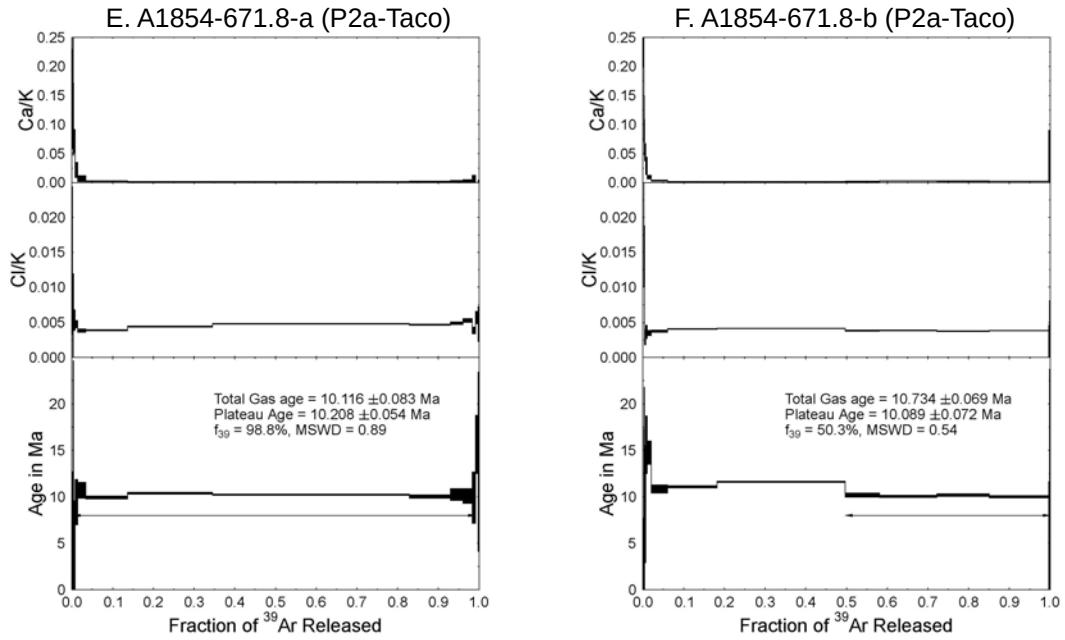

Fig. A3.2. Age spectra plots of $^{40}Ar/^{39}Ar$ step-heating experiments on hydrothermal biotite. Continued from previous page.

Chapter 4:
Alteration and Mineralisation

4.1. Abstract

The Antamina Cu-Zn-Mo deposit, in Peru is the largest skarn in the world with resources of ~2,968 Mt, averaging 0.89% Cu, 0.77% Zn, 11 g/t Ag and 0.02% Mo as of 2015. The deposit displays systematic patterns of alteration and mineralisation centred on a multi-phase porphyry centre that is surrounded by skarns. Outward from the centre of the Taco zone the alteration consists of potassic alteration (hydrothermal biotite) transitioning into endoskarn, then exoskarn, bleached marble, and fluid escape structures in the most distal reaches of the deposit. Within the skarns there are systematic zoning patterns defined by garnet colour, garnet:clinopyroxene ratio, and garnet and clinopyroxene compositions. Garnet colour changes from pink to red to brown in endoskarn and from red to brown and green (from proximal to distal) in exoskarn. Overall, the skarn mineralogy is dominated by garnet with lesser clinopyroxene, and the change in abundance is partly controlled by the fO_2 of the wall rocks, as well as distance from the central porphyry complex; garnet > clinopyroxene typically occurs proximal to the endoskarn contact and in wall rocks with low organic carbon contents, such as marble in the Jumasha and/or Celendín formations. Clinopyroxene > garnet tends to occur in distal exoskarns or in wall rock precursors with higher organic carbon contents, such as the Celendín Formation in the Usupallares section. Garnet becomes more andradite-rich and grossularite-poor from proximal to distal skarns, and clinopyroxene becomes more hedenbergite-rich and diopside-poor along the same spatial trend. Mineralisation and metal zoning shows an outward progression from Mo ± Cu in the central porphyry, to Cu (± Ag, Bi)-Zn-Pb from proximal to distal exoskarns. The ore mineralogy is dominated by molybdenite, chalcopyrite, bornite, and sphalerite with lesser galena and minor Bi-Ag-S minerals. Fluid inclusions in a unidirectional solidification texture (UST) sample from P1-Taco consist of four types assigned to primary and secondary assemblages. Primary inclusions are highly saline with liquid-vapour-solid phases and contain up to 5 translucent daughters plus a triangular opaque daughter. Secondary inclusions display variable proportions of liquid-vapour-solid phases, but are generally less saline and more vapour-rich than primary inclusions. Primary inclusions homogenise by halite disappearance, whereas secondary inclusions homogenise to the liquid state. Lithostatic pressure estimates from primary fluid inclusions range from 1.2 to 0.95 kbar, which equates to a depth of formation range from ~4.6 to 3.5 km. Coupled with estimates of surface uplift and erosion in the Central Peruvian Andes (from the early Miocene to present), the ideal depth of formation is

between 4.0 to 3.5 km, which is within error of the estimates derived from fluid inclusion microthermometry in this study.

4.2. Introduction

This research was conducted for the purpose of establishing the broad- and local-scale zoning patterns intrinsic to the porphyry-skarn transition at Antamina. Understanding these patterns is important because zoning trends in magmatic-hydrothermal systems, such as skarns and porphyries, can be used to understand fluid origins and to improve the prediction of ore zones. This chapter combines new results from core logging and field observations to refine the current understanding of orebody geometry at Antamina.

Skarns and porphyry deposits typically display well-developed mineralogical zoning patterns that can be used to understand fluid origins and to predict the location of ore zones. Establishing the composition and distribution of alteration minerals is a fundamental aspect of any study of these deposit types. Many skarns and porphyries are related in time and space, so the study of one can provide insight on the other.

Porphyry deposits are one of the most thoroughly studied deposits types and typical porphyry alteration zoning is well-documented; the simplified alteration pattern includes a multi-phase intrusive centre containing potassic alteration surrounded by propylitic alteration on the sides and advanced argillic alteration on the top, cut by phyllic alteration (Gustafson and Hunt, 1975; Sillitoe, 2010). However, if the wall rocks are calcareous, skarns may form along the margins of a porphyry deposit or a subeconomic intrusion (Meinert, 2005; Sillitoe, 2010). The skarns will also display systematic mineralogical zoning that is largely dependent on the composition and oxidation state of the intrusions and wall rocks (i.e., Meinert, 1995; Chang and Meinert, 2008). Generalised patterns include garnet colour becoming lighter away for the causative intrusion, and proximal garnet to distal clinopyroxene ± wollastonite if the causative intrusion is oxidized and the wallrocks are reduced. Beyond the skarn alteration, a zone of contact metamorphosed and pervasively bleached country rock transitions into progressively narrower bleached veins along fluid escape structures. From a combined-system approach, these patterns provide a framework in which to examine the porphyry-skarn transition.

Previous studies on the Antamina deposit have identified several features typical of porphyries and skarns. These include a multi-phase porphyry centre surrounded by well-developed skarns. The skarns zoned outward from the porphyry centre as follows: brown garnet endoskarn, mixed brown and green garnet indeterminate skarn, mixed brown and green garnet exoskarn, green garnet exoskarn, diopside exoskarn, wollastonite exoskarn, hornfels, marble, and limestone (Lipten and Smith, 2005). The principal ore minerals include chalcopyrite, sphalerite, and molybdenite, with lesser bornite, galena, and Cu-Bi-Ag-Fe sulphides. In general, metal zoning patterns show that Mo is largely confined to the APC (and stockwork veins extending outward from the deposit centre), Cu is most abundant in proximal endoskarns and exoskarns, and Zn is concentrated in distal exoskarns near the marble front.

The work of previous researchers established the broad-scale zoning patterns of alteration and mineralisation, however many questions remain. To answer these questions, samples from outcrops and drill core were studied to determine mineralogy and mineral chemistry. The major alteration styles and zoning patterns were characterised from the central porphyry complex outward beyond the distal skarns. Fluid inclusions in quartz from a unidirectional solidification texture (UST) provide insight on fluid chemistry and depth of deposit formation. The results of this chapter are combined into a model for skarn and ore formation in the context of a dynamic early Miocene magmatic arc undergoing active uplift and erosion.

4.3. Samples and Methods

4.3.1. Core Logging and Sampling

Thirty-one drill holes were logged, accounting for approximately 15,500 m of drill core from five cross sections (Fig. 1.5). A summary of the drill holes logged in this study is presented in Table A4.1. Core logging criteria included: rock type and description, garnet/clinopyroxene ratio, garnet colour, intrusion alteration and intensity, and retrograde alteration and intensity. Representative samples of drill core (½ NQ diameter) were selected from each rock type. A total of 869 samples were documented in the field and/or collected for analysis by the methods described in this section. Several samples were polished and scanned at high resolution to document specific features of alteration and/or mineralisation.

4.3.2. Petrography

Polished thin sections of the representative rock types were prepared by Lanfang Hongxin Geology and Exploration Service Co. Ltd. in Hebei, China. Photomicrographs were acquired using Leica DM 4000 microscope.

4.3.3. Electron Microprobe WDS Spot Analyses

Major-element compositions of selected minerals in polished thin sections were determined *in situ* using a JEOL JXA-8200 Superprobe equipped with five wavelength-dispersive spectroscopy (WDS) detectors, housed in the Advanced Analytical Centre (AAC) at James Cook University (JCU). WDS spot analyses were collected for sphalerite (n = 40) and silicates, including garnet (n = 176), clinopyroxene (n = 186), feldspars (n = 48), vesuvianite (n = 7), epidote (n = 27), chlorite (n = 24), and amphibole (n = 23), and biotite (Digital Appendix 4.1). Microprobe operating conditions and analytical conditions [element analysed (standard, line, crystal)] for each routine are listed as follows: Sphalerite: 20 keV acceleration voltage, 20 nA current, absolute minimum (2-3 µm) beam diameter, and 10 µm working distance; Zn (Tsphal20k, Kα, LIF), Fe (a1marc20k, Kα, LIFH), S (Tsphal20k, Kα, PETJ). Silicates: 15 keV acceleration voltage, 20 nA current, 5 µm beam size, and 10 µm working distance; Na (albite, Kα, TAP), Fe (hematite, Kα, LIF), Mn (spessartine, Kα, LIFH), F (F-TAP, Kα, TAP), Cl (tugtupite, Kα, PETJ), Si (wollastonite, Kα, TAP), Ti (rutile, Kα, LIF), Al (almandine, Kα, TAP), Ca (wollastonite, Kα, PETJ), Mg (olivine, Kα, TAP), and K (orthoclase, Kα, PETJ).

4.3.4. WDS Element Mapping

The distribution of selected elements was mapped using an electron microprobe equipped with WDS detectors (as above). Maps were created for comb-layered quartz (UST) and to locate zircon in skarn-altered rocks. Zircon maps were acquired using a 50 µm electron beam with an accelerating voltage of 15 kV, a beam current of 100 nA, a step size of 50 µm and 100 ms dwell time. Spectrometers collected data for P (Kα, TAP), Ti (Kα, LIF), Zr (Lα, PETH), Al (Kα, TAP), and Ca (Kα, PETJ). Comb quartz maps were acquired using a 6 µm electron beam with an accelerating voltage of 20 kV, a beam current of 200 nA, step size of 6 µm and 100 ms dwell time. Spectrometers collected data for Si (Kα, TAP), Fe (Kα, LIF), Ti

(Kα, LIFH), Al (Kα, TAP), and K (Kα, PETJ). Another comb quartz map was acquired using a 3 µm electron beam with an accelerating voltage of 20 kV, a beam current of 500 nA, step size of 4 µm and 150 ms dwell time. Spectrometer settings were the same as for the previous comb quartz map. Element maps were processed offline using ImageJ software.

4.3.5. X-Ray Diffraction

The qualitative mineralogy of selected samples was determined using X-ray diffraction (XRD). Hand-picked mineral separates and whole rock samples were crushed and milled to a finely-ground, homogenous powder (at least 0.5 grams). The powder was mounted in a sample holder and analysed using a Siemens D5000 Diffractometer equipped with Theta/2Theta goniometer and copper anode X-ray tube housed at the JCU AAC. The data were collected and analysed using Bruker DiffracPlus software, the search/match option, and the ICDD PDF-2 (2011) database. Interpretation was performed by an Intertek minerals specialist in Townsville, Queensland, Australia. Mineral abundances were reported as follows: dominant (> 50%), major (> 10%), minor (< 10%), trace (< 1%), and possible (may be present; designation is not unambiguous).

4.3.6. Sulfur Isotopes

Twenty-one samples were selected for analysis from Stage 2 sulphides in skarns and calc-silicate hornfels. Prepared mineral separates that included pyrite, sphalerite, galena, and bornite were selected for ^{34}S analyses. Isotopic analyses were conducted at the USGS stable isotope lab Denver, Colourado. Mineral separates were combined with vanadium pentoxide powder (catalyst for combustion) in tin capsules and analyzed by continuous flow mass spectrometry, following pyrolysis of the sample to SO_2 gas using methods modified from Giesemann et al. (1994). Instrumentation includes a CE Elantech Inc. Flash 2000 Elemental Analyzer with a Conflo III interface, coupled to a Thermo-Finnigan Delta Plus XP continuous flow mass spectrometer. Samples were analyzed alongside internationally accepted standards, including NBS123 and IAEA-S-3 (Coplen et al., 2001). Values of $\delta^{34}S$ are expressed relative to the Vienna Cañon Diablo Troilite (VCDT) with a precision of 0.2‰, based on replicate analyses.

4.3.7. Fluid Inclusions

Doubly-polished fluid inclusion sections, approximately 300 µm thick, were prepared by Langfang Hongxin Geology and Exploration Service Co. Ltd. in Hebei, China. Each section was mounted on a glass slide using acetone-soluble glue, which was removed through repeated cycles of soaking and refreshing in concentrated acetone until no glue residue remained. Petrographic observations were made for each section and schematic maps were drawn to scale for areas of interest. Each map includes layers representing the z-dimension at 5°-10° increments for precise spatial orientation and to facilitate the depiction of 3D sample details in 2D. Physical parameters (length, width, degree of fill, number of phases, etc.) were recorded prior to breaking the sample into smaller chips, up to 8 mm, to fit in the sample carrier on the heating-freezing stage.

Microthermometry was conducted using a Linkam MDS600 heating-freezing stage with temperature limits of -190°C to 600°C, attached to an Olympus BX52 microscope equipped with 40x and 50x long working distance objectives. The stage conditions (heating/freezing), temperature limits, and real-time video observation were controlled through Linksys32 software provided by Linkam. Low-temperature calibration was conducted using a standard CO_2-H_2O fluid inclusion (manufactured by FluidInc) in which the solid to liquid phase changes of CO_2 (-56.6°C) and H_2O (0.0°C) were reproduced to within ± 0.3°C prior to taking measurements on the test samples. For higher temperatures the stage was calibrated based on the critical homogenesation of pure H_2O in synthetic quartz fluid inclusions (374.1°C),

Phase transitions measured in the test samples include the last ice melting temperature (Tm) and/or the homogenization temperature (Th). Effort was made to obtain both Tm and Th for each inclusion measured, however due to physical limitations (small size, poor clarity, metastable behaviour, etc.), this was not always possible. In order to observe Tm, the sample was cooled to at least -100°C, then heated to 0°C at an initial rate of 20°C/min, then progressively slowing to a rate of < 2°C/min approaching the phase change. Homogenization temperatures were measured using the strategy, heating at higher rate initially then progressing to a slower heating rate approaching the phase change. Measurement of Th was determined by observing the gradual shrinking and subsequent disappearance of the vapor bubble, followed by at least 10°C of rapid cooling to test for bubble reappearance. Failure of the vapour bubble to immediately reappear was a good indication of complete

homogenization; however, an error of ± 5°C is applied to all Th measurements to account for the difficulty in observing this phase change once the bubble size diminishes beyond visual recognition.

Solid, liquid, and vapour phase compositions were measured using a WITec Alpha300 R confocal Raman microscope housed in the JCU AAC. An Ar+ ion laser operating at 44 mW was used to produce an excitation wavelength of 532 nm line. The scanning range of spectra was set between 100 and 4000 cm^{-1} with an accumulation time of 10 seconds for each scan, and a spectral resolution of 0.65 cm^{-1}. The Raman shift of a monocrystalline silicon piece was measured to be 520.7 cm^{-1} before the analysis. Further information on the analysis procedure is available in Burke (2001).

4.4. Results

The Antamina deposit displays a continuum of alteration styles between porphyry and skarn end-members and, with few exceptions, all rocks at Antamina have been altered to some degree. Three major stages of alteration are recognised across the porphyry-skarn transition at Antamina: potassic and prograde alteration (Stage 1), retrograde alteration and Cu-Mo-Zn-Pb mineralisation (Stage 2), and late phyllic alteration and Mo mineralisation (Stage 3; Fig. 4.1). Most of the features described in this section are common across the Taco, Oscarina, and Usupallares zones, unless otherwise specified.

4.4.1. Stage 1: Potassic and Prograde Skarn Alteration

Early alteration consists of hydrothermal biotite ± K-feldspar (potassic alteration) in intrusive rocks, and garnet ± clinopyroxene in prograde endoskarn and exoskarn (Fig. 4.2 A-D). Hydrothermal biotite occurs as a disseminated and selectively pervasive replacement of igneous biotite and/or amphibole (Fig. 4.2 A), or as veinlet-controlled alteration (equivalent of A-veinlets of Titley, 1982). In these potassic-altered rocks, disseminated pyrite is visible with the naked eye and the rocks are weakly magnetic, indicating that disseminated magnetite is present (Fig. 4.1). In the central Taco zone (below 3,500 m above sea level), purple anhydrite + quartz veins were observed in potassically-altered rocks (Fig. 4.2 B).

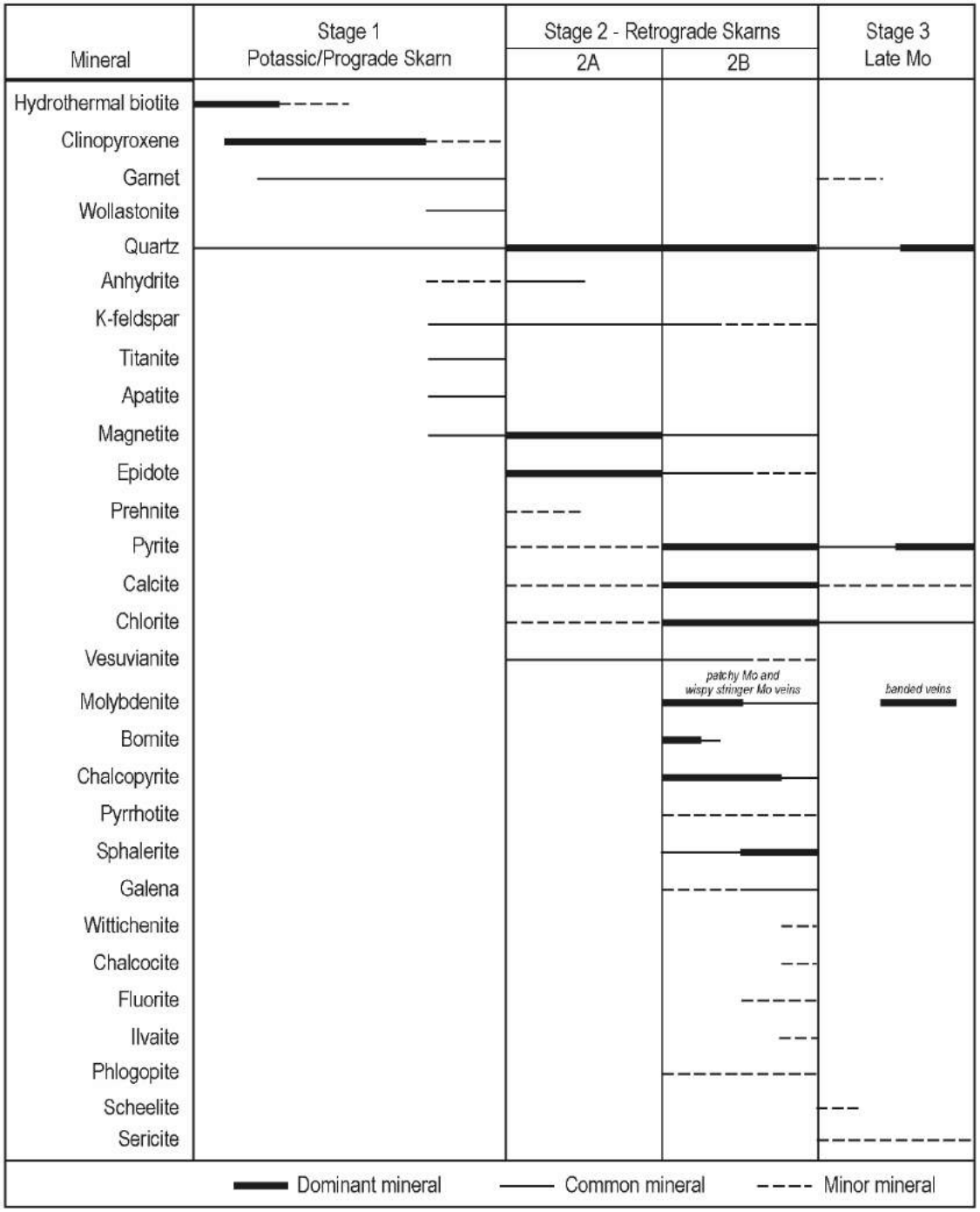

Fig. 4.1. Alteration and mineralisation paragenesis chart for the Antamina deposit. See text for detail.

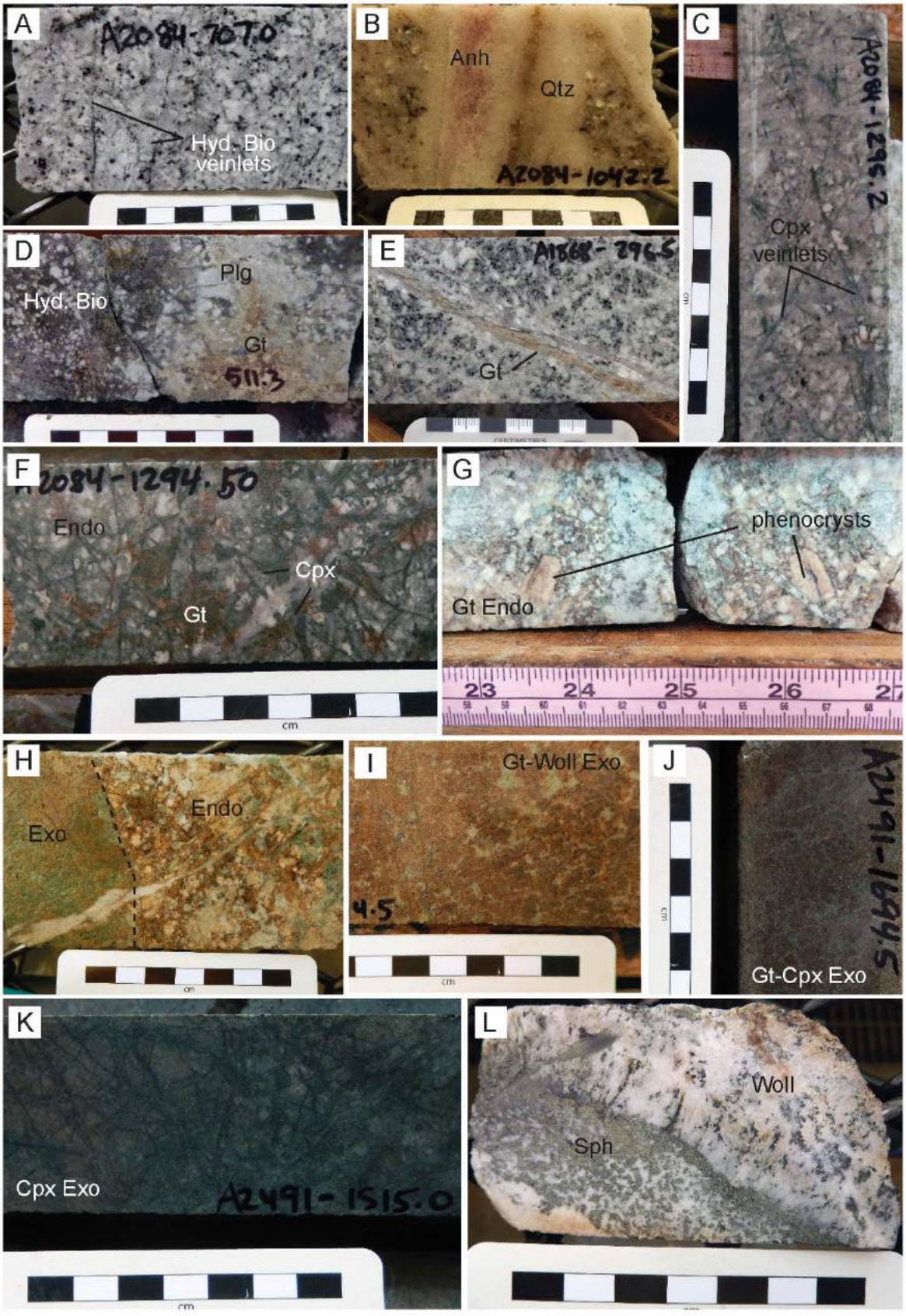

Fig. 4.2. Caption on next page.

Fig. 4.2. Stage 1 (early) potassic and prograde skarn alteration. A. Hydrothermal biotite A-veinlets in P1-Taco. B. Quartz-anhydrite vein cutting across P1-Taco. C. Cpx veinlets and weak potassic alteration in P1-Taco. D. Strong potassic alteration + endoskarn in A1623-511.3, P1-Taco. E. Endoskarn vein cutting across P1-Taco. F. Moderately strong endoskarn (porphyry texture still apparent) showing cpx veinlets. G. Garnet endoskarn in P1-Usupallares, porphyritic texture preserved, A2589-198.3. H. Exoskarn-endoskarn contact in A2589-694.0, P1-Usupallares. I. Red garnet + wollastonite exoskarn, Taco zone. J. Garnet + clinopyroxene exoskarn, Taco zone. K. Clinopyroxene exoskarn cut across by Stage 2 chlorite, Taco zone. L. Wollastonite exoskarn with Stage 2 sphalerite, A206-332.0, Taco zone. All scales in cm. Abbreviations: Hyd. Bio: hydrothermal biotite; Gt: garnet; Cpx: clinopyroxene; Endo: endoskarn; Exo: exoskarn; Sph: sphalerite; Woll: wollastonite.

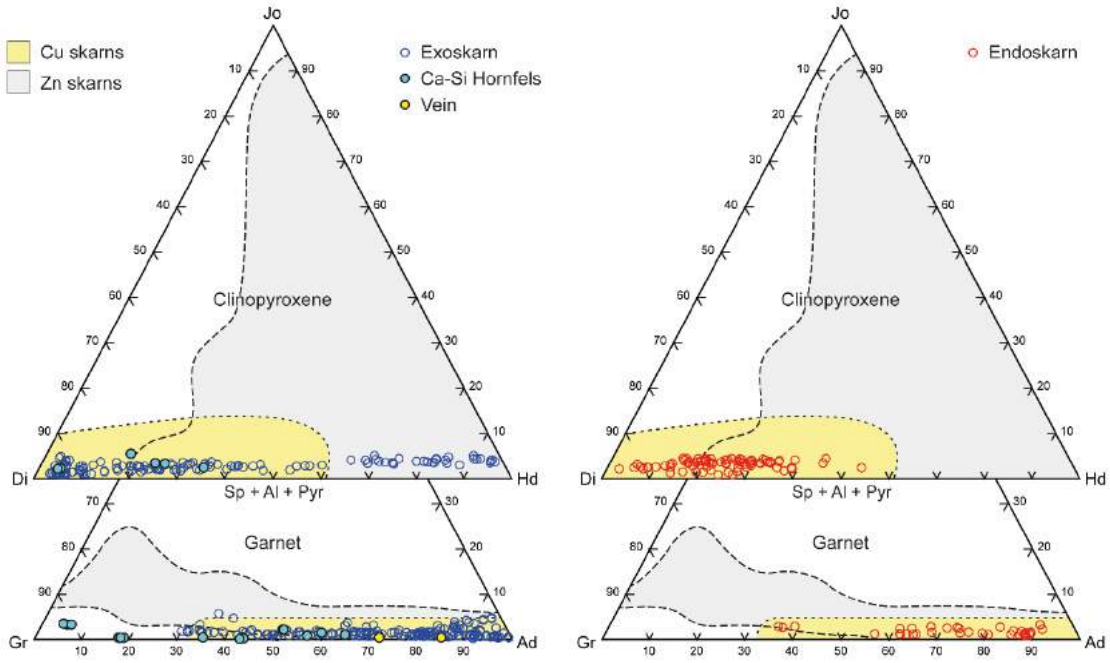

Fig. 4.3. Ternary composition plots of skarn garnet and clinopyroxene. Compositions are expressed in terms of end members Ad: andradite, Gr: grossularite; Sp: spessartine; Al: almandine; Pyr: pyrope; Di; diopside; Hd: hedenbergite; Jo: johanssenite. Fields for Zn and Cu skarns are after Meinert et al. (2005).

Endoskarn and exoskarn formed early during prograde skarn alteration in igneous rocks and wall rocks, respectively. Both endoskarn and exoskarn occur as massive to partial replacements of their respective host rocks, but are sometimes difficult to tell apart due to the range of inherited textures that are not always diagnostic of skarn type (Chapter 2). Prograde skarn mineralogy is dominated by garnet with lesser clinopyroxene ± wollastonite (Fig. 4.2 E-L). Garnet compositions, measured in mol % andradite (Ad) – grossularite (Gr) – and spessartine-almandine-pyrope (Sp+Al+Pyr) end members, range from $Ad_{35\text{-}91}Gr_{04\text{-}62}$ in endoskarn and $Ad_{30\text{-}99}Gr_{01\text{-}89}$ in exoskarn; the Sp+Al+Pyr contents of all skarn garnets do not exceed 5.8 mol % (Fig. 4.3 and Digital Appendix 4.1). Endoskarn garnet is pink to red and exoskarn garnet is red-brown-green. Garnet in calc-silicate hornfels ranges from $Ad_{7\text{-}64}$, and in one vein sample $Ad_{72\text{-}85}$ (Fig. 4.3). Clinopyroxene colour is invariably medium to dark

green (Fig. 4.2) and the compositions range from Hd_{1-98} in exoskarn, Hd_{3-55} in endoskarn, and Hd_{5-33} in calc-silicate hornfels (Fig. 4.3). The johannsenite component is all less 10 mol percent. Plagioclase (common) and K-feldspar (rare) are present in both endoskarn and exoskarn; plagioclase compositions, measured in mol % anorthite endmember, (An) range from ~An_{19-60} in endoskarn (n = 34) and ~An_{41-44} in exoskarn (n = 3; Fig. 4.4, Digital Appendix 4.1). K-feldspar also occurs in both skarn types (Fig. 4.4, Digital Appendix 4.1). Endoskarn occurs in P1 porphyries in the Taco, Usupallares, and Condorcocha zones (P1-Oscarina cuts across skarn alteration); it was not observed in any P2 porphyry, indicating that this alteration stage is related to early magmatic-hydrothermal activity. Prograde endoskarn alteration is well-developed along the outer margin of P1 (Fig. 4.5). The transition from skarn to porphyry-style alteration (toward the centre of P1) is marked by either a gradational change from endoskarn (clinopyroxene ± garnet) to potassic (hydrothermal biotite) alteration (Fig. 4.5), or by the presence of endoskarn veins infiltrating potassic-altered igneous rocks (Fig. 4.2 C-F). The endoskarn veins observed at Antamina are similar to those described by Chang and Meinert (2008); they are composed of garnet ± clinopyroxene, range in size from 1 mm up to about 1 cm, display irregular shapes and edges, are discontinuous, and may join other endoskarn veins to form coalesced skarn-altered zones. Exoskarn occurs as a massive replacement of marble wall rocks in contact with early P1 porphyries. As a result, exoskarn forms a shell around the early, endoskarn-altered porphyries that comprise the centre of the Antamina deposit (Fig. 4.5). The prograde exoskarn mineralogy is dominated by garnet ± clinopyroxene and lesser, distal wollastonite (Fig. 4.2 H-L).

4.4.2. Stage 2: Retrograde Skarn Alteration and Cu-Mo-Zn-Pb Mineralisation

Retrograde alteration is common in both endoskarn and exoskarn at Antamina, and the intensity is structurally controlled, with the strongest alteration noted along contacts or veins. The dominant retrograde assemblage consists of quartz + sulphides ± calcite ± epidote ± vesuvianite ± chlorite ± magnetite, with lesser fluorite, phlogopite, and rare ilvaite (Figs. 4.6 to 4.11). Quartz + sulphides ± calcite fills interstices between garnet and clinopyroxene, and forms veins that cut across the skarns (Fig. 4.6 A). Chlorite occurs as a selvage around some quartz + sulphide ± calcite veins, and as a partial replacement of garnet-clinopyroxene (Fig. 4.6 G). Vesuvianite and epidote replace garnet and/or clinopyroxene (Fig. 4.6 B, I-K, C-E) and occurs as veins/ selvages with quartz ± calcite ± pyrite ± magnetite (Fig. 4.6 F).

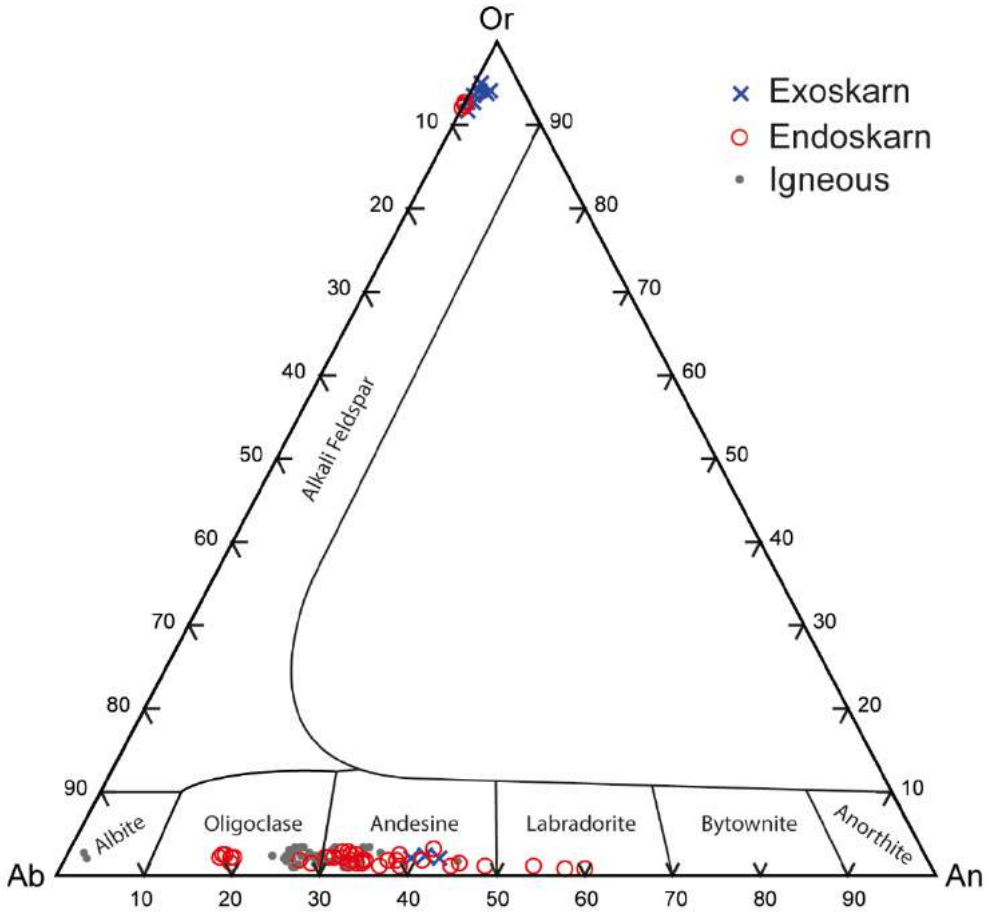

Fig. 4.4. Ternary plot of plagioclase and K-feldspar compositions in endoskarn and exoskarn (igneous compositions from Antamina porphyries are included for comparison).

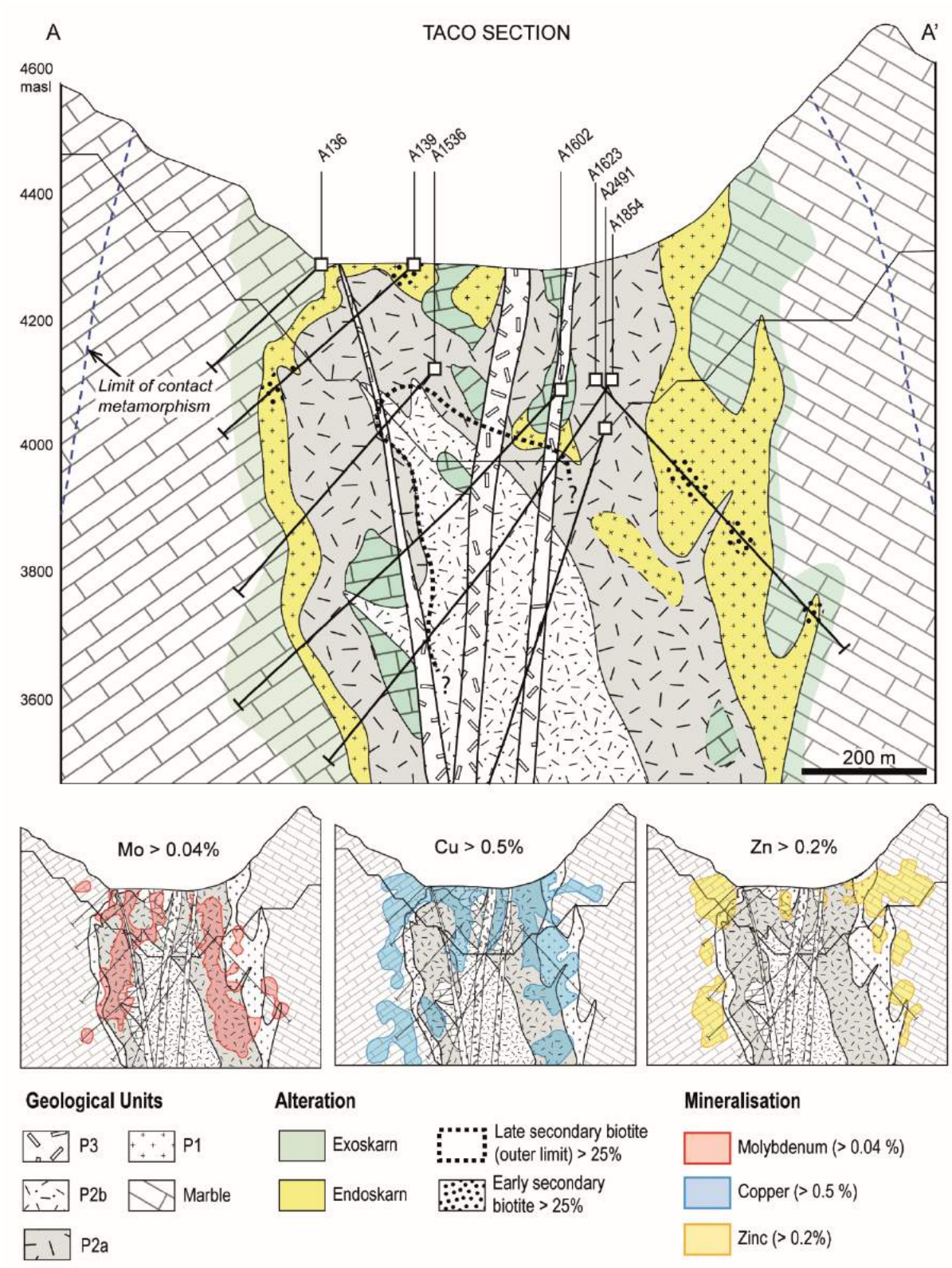

Fig. 4.5. Alteration and metal zoning in the Taco section (cross section A-A').

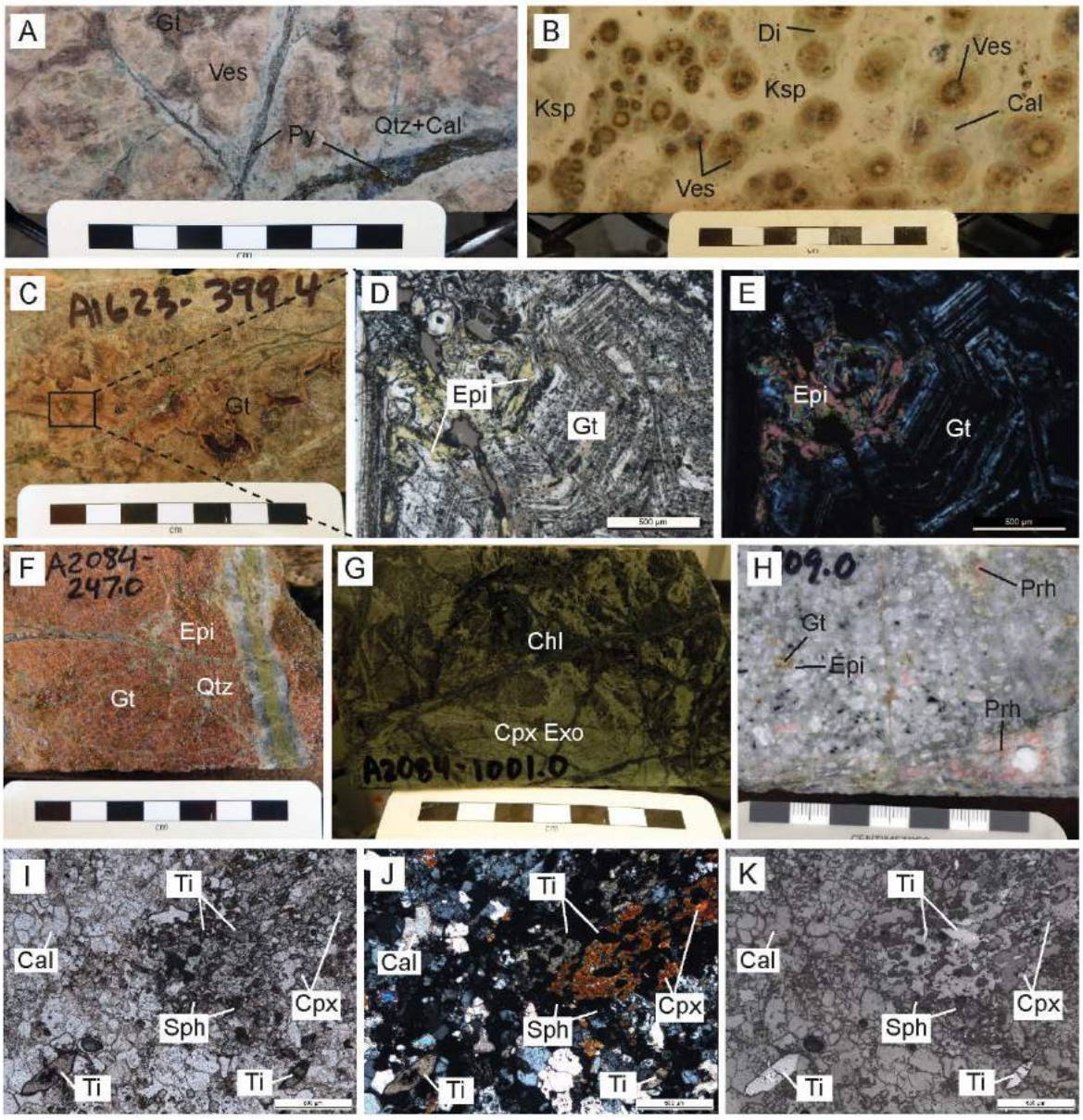

Fig. 4.6. Stage 2 retrograde alteration assemblages. A. Quartz-sulphide-calcite vein cuts across prograde garnet endoskarn. Garnet is partially replaced by vesuvianite. B. Vesuvianite-diopside after garnet in calc-silicate hornfels. C-E. Massive garnet exoskarn partially replaced by epidote (photomircographs D: plane polarised light, E: cross-polarised light). F. Epidote-quartz vein cuts across garnet exoskarn. D. Chlorite veinlets cut across clinopyroxene exoskarn. H. Epidote after garnet and prehnite after feldspar(?) in P1-Oscarina. I-K: photomicrographs showing the replacement of prograde clinopyroxene and titanite by calcite and sphalerite (I: plane polarised light, J: cross-polarised light, K: reflected light). Abbreviations: Cal: calcite; Chl: chlorite; Cpx: clinopyroxene; Di: diopside; Epi: epidote; Gt: garnet; Ksp: K-feldspar; Prh: prehnite; Py: pyrite; Qtz: quartz; Sph: sphalerite; Ti: titanite; Ves: vesuvianite.

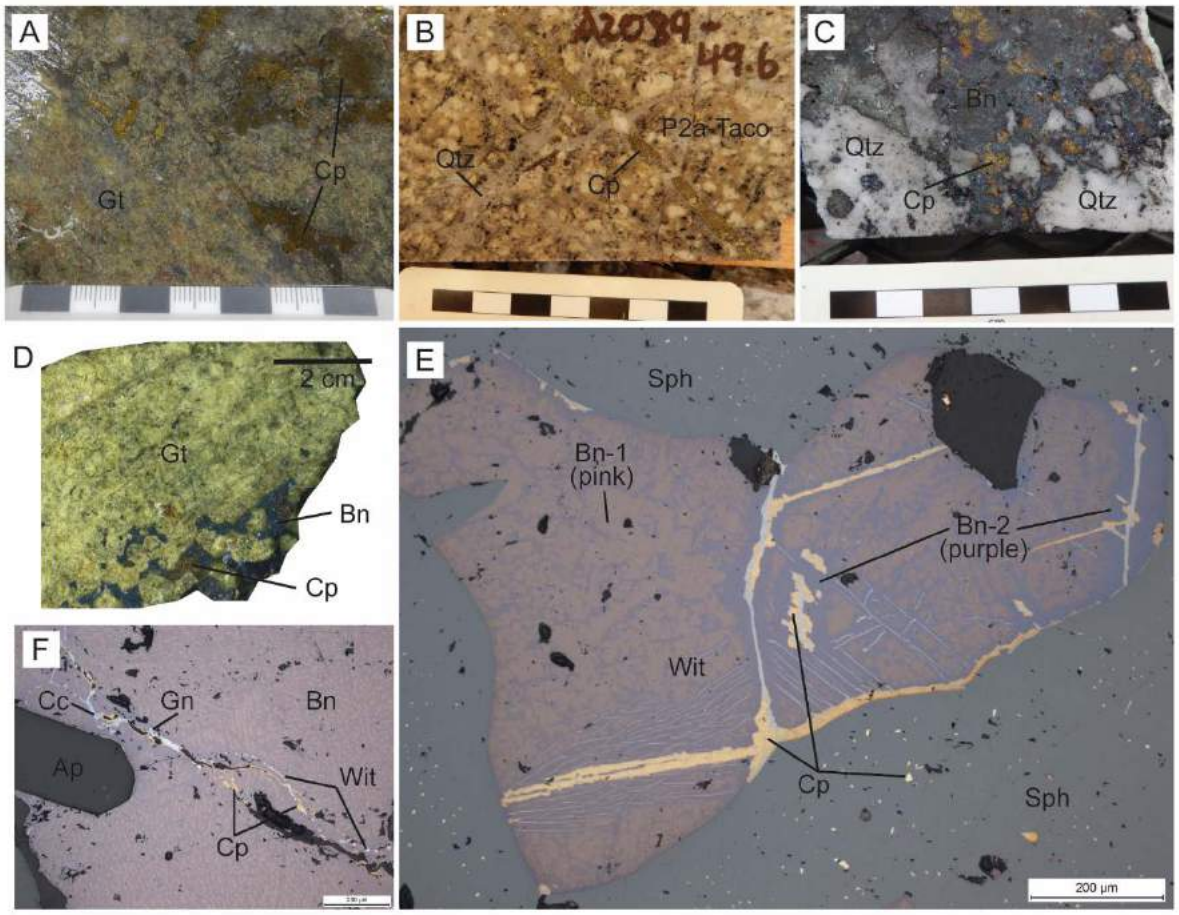

Fig. 4.7. Stage 2 chalcopyrite and bornite mineralisation. A. Chalcopyrite replacement in brown garnet exoskarn. B. Intermineralisation chalcopyrite vein cuts a quartz vein and is cut by a later quartz vein. C. Bornite-chalcopyrite-quartz vein. D. Proximal green garnet exoskarn replaced by bornite-chalcopyrite. E-F. Reflected light photomicrographs of sulphides in (D), showing bornite exsolution textures (Bn-1, Bn-2), and related sulphides. See text for detail. Abbreviations: Ap: apatite; Bn: bornite; Bn-1: bornite solid solution composition #1; Bn-2: bornite solid solution composition #2; Gt: garnet; Cp: chalcopyrite; Gn: galena; Qtz: quartz; Sph: sphalerite; Wit: wittichenite.

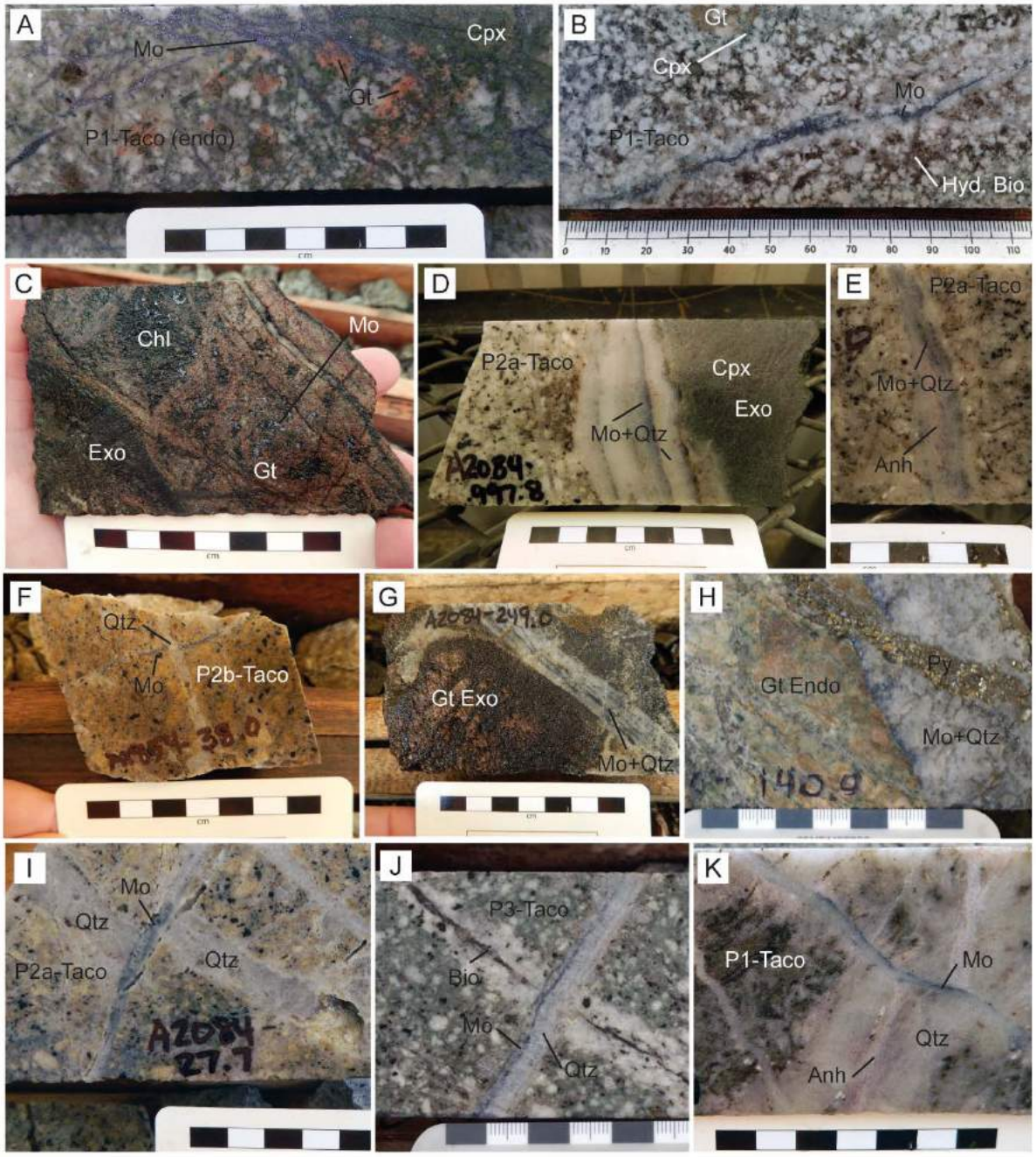

Fig. 4.8. Stage 2 and 3 molybdenite mineralisation. A-B. Stage 2 molybdenite in endoskarn. C. Stage 2 molybdenite in exoskarn. D: Stage 3 banded molybdenite veins cutting across Stage 1 porphyry and exoskarn. E. Stage 3 banded molybdenite + quartz + purple anhydrite vein cutting across Stage 1 potassic alteration. F. Stage 2 molybdenite cut by a quartz vein. G. Stage 3 molybdenite cutting across a Stage 1 exoskarn. H. Stage 3 molybdenite + quartz vein cut across by a Stage 3 pyrite vein. I. Stage 3 molybdenite cutting across earlier quartz veins. J. Stage 3 molybdenite cutting across P3-Taco and a Stage 2(?) biotite vein. K. Stage 3 molybdenite + quartz vein cutting across Stage 1 quartz + anhydrite veins in P1-Taco. Abbreviations: Anh: anhydrite; Bio: biotite; Chl: chlorite; Cpx: clinopyroxene; Exo: exoskarn; Endo: endoskarn; Gt: garnet; Mo: molybdenite; Qtz: quartz.

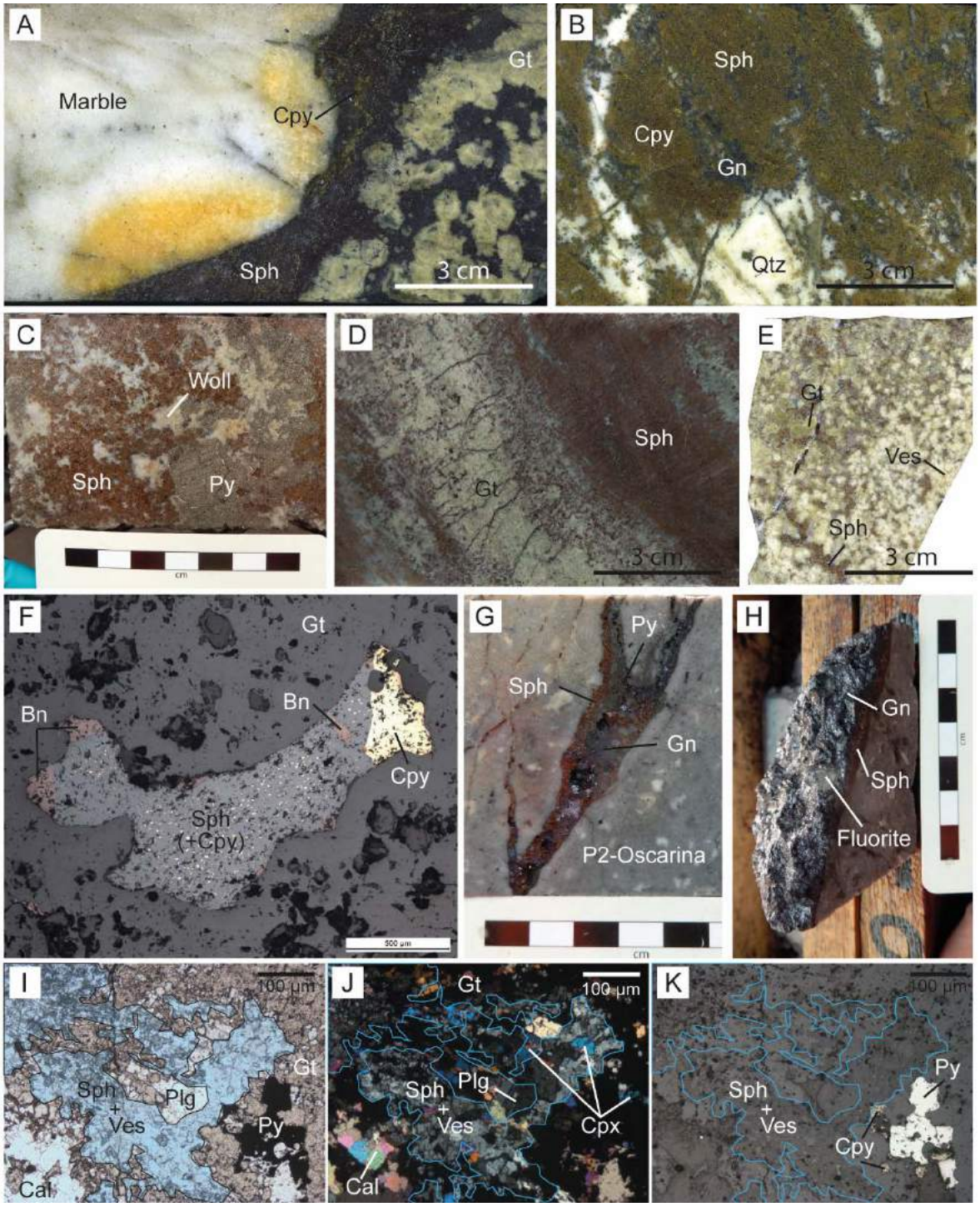

Fig. 4.9. Stage 2 retrograde mineral assemblages. A. A2669-865.9, chalcopyrite + sphalerite in exoskarn at the marble front. B-E. Examples of distal ore assemblages in exoskarn. F. Sphalerite displaying chalcopyrite disease in proximal garnet exoskarn, sample A206-299.5, Taco-Bornita zone. G-H. Sphalerite + galena ± fluorite vein cutting across P2-Oscarina dyke. I-K: Sample A1390-307.0, a Stage 2 retrograde assemblage consisting of vesuvianite intergrown with sphalerite, calcite, pyrite, and chalcopyrite cut across Stage 1 exoskarn. Abbreviations: Bn: bornite; Cal: calcite; Cpy: chalcopyrite; Gn: galena; Gt: garnet; Plg: plagioclase; Py: pyrite; Qtz: quartz; Sph: sphalerite; Ves: vesuvianite; Woll: wollastonite.

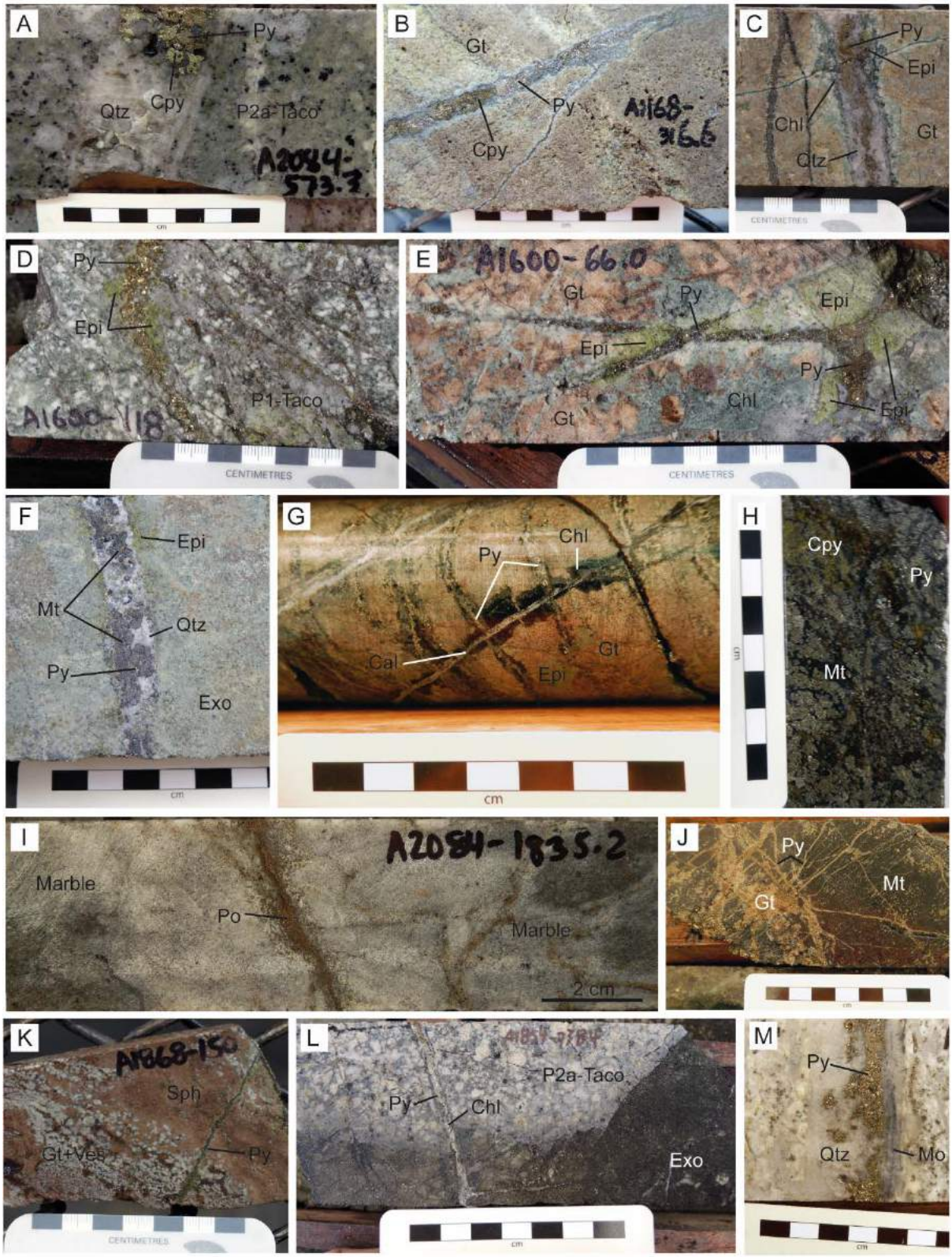

Fig. 4.10. Stage 2 and Stage 3 alteration and mineralisation assemblages. A-I: Pyrite and pyrrhotite (Stage 2), J-M: pyrite stage 3. Abbreviations: Cal: calcite; Chl: chlorite; Cpy: chalcopyrite; Epi: epidote; Exo: exoskarn; Gt: garnet; Ksp: K-feldspar; Mo: molybdenite; Mt: magnetite; Py: pyrite; Qtz: quartz; Sph: sphalerite; Ves: vesuvianite.

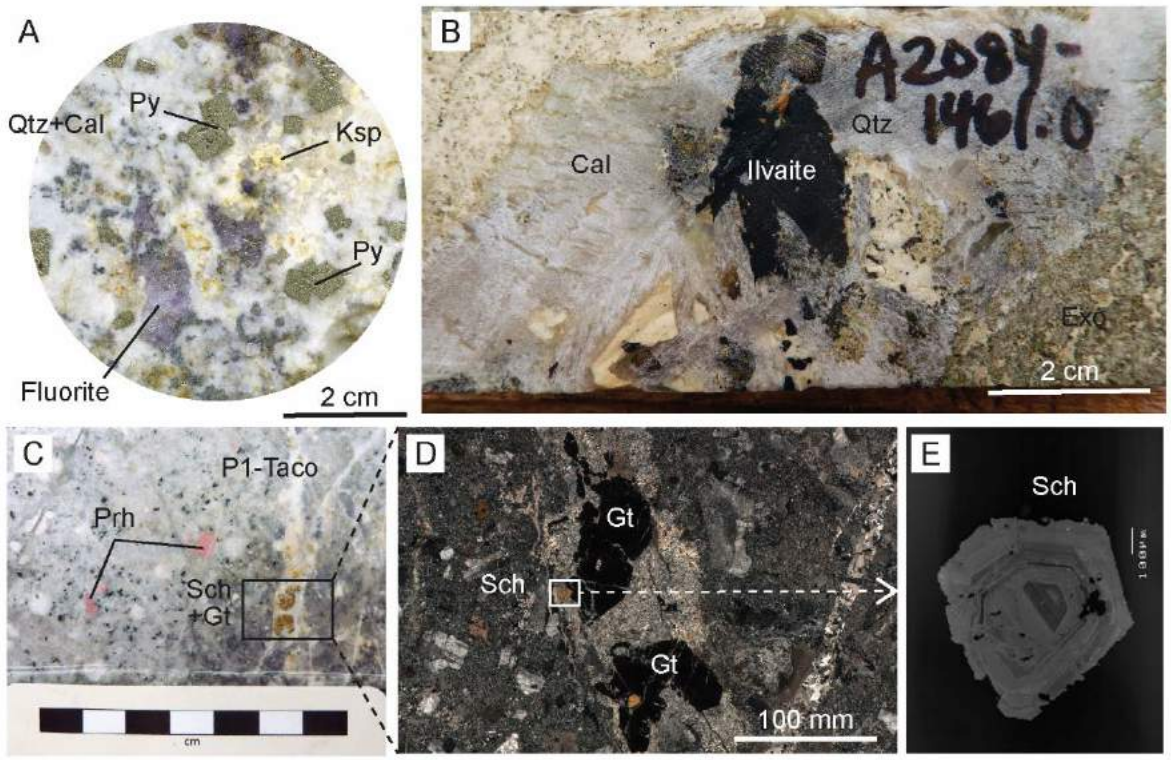

Fig. 4.11. Stage 2 and Stage 3 rare minerals. A. Sample A3053-23.4, fluorite-pyrite-quartz-K-feldspar-calcite in P2-Taco. B. Quartz-calcite-ilvaite in exoskarn. C. Sample A545-154.9, garnet + scheelite vein cuts across prehnite alteration in P1-Taco. D. Photomicrograph (crossed polars) detail of garnet + scheelite vein from (C). E. Cathodoluminescence image of a scheelite crystal from (D). Abbreviations: Anh: anhydrite; Cal: calcite; Gt: garnet; Ksp: K-feldspar; Py: pyrite; Qtz: quartz; Sch: scheelite.

The majority of mineralisation at Antamina formed during Stage 2 retrograde alteration and occurs in endoskarns, exoskarns, and in veins cutting across porphyries. A minor amount of mineralisation is noted in marble and hornfels. Copper, molybdenum, and zinc sulphides comprise the principal ore minerals; these include chalcopyrite ($CuFeS_2$), bornite (Cu_5FeS_4), molybdenite (MoS_2), and sphalerite (ZnS). Pyrite (FeS_2) and magnetite (Fe_3O_4) are common, but of lesser economic importance. Minor minerals include galena (PbS) and pyrrhotite ($Fe_{(1-x)}S$). Rare occurrences of chalcocite (Cu_2S) and wittichenite (Cu_3BiS_3) have also been noted (Fig. 4.1).

Chalcopyrite is the major host for copper at Antamina. It is widely distributed among distal and proximal skarns and porphyries, and occurs as disseminations, patchy replacements, and veins (Fig. 4.7). In distal exoskarns, chalcopyrite is typically patchy and intergrown with pyrite ± sphalerite (Fig. 4.7 A-B), whereas in proximal exoskarns it occurs with bornite and

inside sphalerite as chalcopyrite disease texture (Fig. 4.7 C-F). Veins containing chalcopyrite ± pyrite ± quartz ± calcite cut across porphyries (Fig. 4.7 B).

Bornite is locally abundant and restricted to the Bornita Zone, southwest of the Taco zone. It occurs with chalcopyrite ± quartz in the interstices between garnet ± clinopyroxene (Fig. 4.7 D). Assays from this zone show a significant enrichment in Cu and Bi. Under reflected light, bornite is purple (Bn-1) with pinkish-purple blebs (Bn-2) and displays a complex suite of cleavage-controlled exsolution minerals, including chalcocite and wittichenite (Fig. 4.7 E-F). Despite the colour difference, Bn-1 and Bn-2 both fall within the range of natural bornite solid solution (as determined by EDS), although Bn-1 is slightly enriched in Cu and Fe compared to Bn-2. Cleavage-controlled exsolution of chalcopyrite, wittichenite, chalcocite, an Ag-sulfosalt, and galena are spatially associated with Bn-1 (Fig. 4.7 E-F).

Molybdenite is the primary source of molybdenum (Mo) at Antamina. The highest Mo concentrations occur in and surrounding the Taco porphyry centre, but a considerable amount of molybdenite is also hosted in the skarns (Fig. 4.6 and Fig. 4.8). Based on Re-Os ages (Chapter 3) and field observations, molybdenite mineralisation took place over at least 3 stages spanning the formation of the Antamina deposit. Three styles of molybdenite mineralisation are observed at Antamina: Type 1 consists of early stringer veins containing molybdenum ± quartz (10.58 ± 0.07 Ma, Fig. 4.8 A-B), Type 2 early patchy replacements in exoskarns (10.44 ± 0.05 to 10.39 ± 0.05 Ma; Fig. 4.8 C), and Type 3 consists of late banded quartz + molybdenite veins (9.99 ± 0.04 Ma and 9.68 ± 0.05 Ma; Fig. 4.8 D-E). Stage 2 molybdenite ± quartz stringer veins are narrow (typically maximum 5 mm wide), discontinuous, wavy veins that cut across P1 potassic- and endoskarn-altered porphyries (Fig. 4.8 A-B). Frequently, they are cut by later quartz veins (Fig. 4.8 F). Patchy molybdenite ± chlorite is observed in exoskarns (Fig. 4.8 C). Banded molybdenum + quartz veins are described in Stage 3 of the paragenesis, as they cut across earlier mineralised skarns, porphyries, and veins, including quartz + anhydrite veins (Fig. 4.8 K).

Sphalerite is the dominant ore mineral in distal exoskarn with lesser amounts occurring in proximal exoskarn, and only rare occurrences in endoskarn (Fig. 4.5). The colour varies from light to dark brown and the crystals are typically subhedral to anhedral. Two modes of occurrence have been observed: veins and patchy to semi-massive replacements (Fig. 4.9). Disseminated, patchy, and semi-massive replacements are the most common style of Zn

mineralisation at Antamina. This style is observed in distal exoskarns and is dominated by fine to coarse grained intergrowths of sphalerite with lesser chalcopyrite ± pyrite ± galena ± calcite ± quartz ± wollastonite ± vesuvianite (Fig. 4.9). Less commonly, sphalerite occurs interstitial to green garnet with bornite, chalcopyrite, and minor quartz in the proximal exoskarns of the central Taco zone; this mode of occurrence displays "chalcopyrite disease", whereas semi-massive replacements and veins do not (Fig. 4.9 F). In drill hole A2890, sphalerite + galena + calcite + fluorite veins cut across the Oscarina dykes (Fig. 4.9 G-H). The Fe content of disseminated, patchy and semi-massive sphalerite varies from 2.4 to 5.3 wt. % (average 3.3 wt. %, n = 30) except for one sample that ranges from 6.6 to 10.2 wt. % (average 8.6 wt. %, n = 6; Digital Appendix 4.1). One interstitial sample with chalcopyrite disease has significantly lower Fe contents than the patchy and semi-massive samples, ranging from 0.3 to 0.4 wt. % (average 0.3 wt. %, n = 6; Digital Appendix 4.1).

Galena occurs as subhedral to anhedral crystals, up to a few millimetres, and is mainly intergrown with pyrite and sphalerite (Fig. 4.9). The abundance of galena is localized to distal skarns and polymetallic veins, some of which extend beyond the skarns into marble and hornfels; it also occurs in in trace amounts with the bornite exsolution assemblage (described above) observed in proximal exoskarn (Fig. 4.7 F).

Pyrite occurs in all rock types at Antamina, and it is most abundant in Stage 2 retrograde skarn alteration. Stage 2 pyrite ranges from coarse grained (up to 3 cm), euhedral cubes to subhedral patchy clusters intergrown with sphalerite, chalcopyrite, quartz, and calcite; the same assemblage also occurs as veins that cut across skarns and porphyries (Fig. 4.10 A-H). Within the skarn zones at Antamina, pyrite is the most common Fe-sulphide, however beyond the outer limits of skarn alteration, pyrrhotite becomes more abundant than pyrite. Pyrrhotite is most commonly observed as fine disseminations or veins cutting across marble, often surrounded by a bleached halo (Fig. 4.10 I). The transition from proximal pyrite (in the skarns and porphyries of Antamina) to distal pyrrhotite (in the surrounding metamorphic rocks) delineates the extent of oxidised hydrothermal fluid interaction with the reduced wall rocks.

Magnetite occurs as fine disseminations in potassic-altered porphyries along with disseminated pyrite and hydrothermal biotite; its presence is revealed by weak magnetism. In the skarns, magnetite comprises a significant proportion of retrograde ores and forms semi-

massive replacements of garnet ± clinopyroxene (Fig. 4.10 H, J). Magnetite also occurs in veins with pyrite ± quartz and an epidote selvage, cutting across exoskarn (Fig. 4.10 F).

Other rare mineral occurrences associated with Stage 2 alteration and mineralisation include fluorite (CaF_2), ilvaite ($CaFe_3(SiO_4)_2OH$), and prehnite ($Ca_2Al_2Si_3O_{10}(OH)_2$). Fluorite is typically purple, although one occurrence of green fluorite is noted in drill hole A2890 in a sphalerite + galena + pyrite vein cutting across an Oscarina dyke (Fig. 4.9 H). Fluorite also occurs in the Oscarina zone as veins and patches associated with pyrite (Fig. 4.11 A). An isolated occurrence of ilvaite was observed in the Usupallares zone with calcite + quartz + phlogopite in exoskarn. Prehnite is pink and appears to replace feldspar; its distribution is localized to the northeast corner of the APC in P1-Taco (Oscarina zone).

4.4.3. Stage 3: Late Alteration and Molybdenite Mineralisation

The last stage of alteration recognized at Antamina consists of banded molybdenum + quartz veins, pyrite + calcite + quartz + chlorite veins, and trace garnet + scheelite + sericite veins; these cut across Stage 2 alteration and mineralisation (Fig. 4.11). Banded quartz + molybdenite veins are the youngest molybdenite stage observed; these veins are 0.5 to 3 cm thick with straight walls and contain thin bands of molybdenite and sugary quartz (Fig. 4.8 D-E, G-K). They cut across Cu-mineralised skarns and P1-P3 porphyries (Fig. 4.8 G-K). In the central Taco zone (below 3,500 m above sea level), purple anhydrite was observed in some banded molybdenite + quartz veins (Fig. 4.8 E). However, banded quartz + molybdenite veins have also been observed cutting across quartz + anhydrite veins in the same zone (Fig. 4.8 K).

Stage 3 pyrite occurs in veins with molybdenite + quartz (Fig. 4.10 M). Stage 3 pyrite veins also cut across Stage 1 garnet and Stage 2 magnetite (Fig. 4.10 J), Stage 1 garnet and Stage 2 vesuvianite + sphalerite (Fig. 4.10 K), and P2a and Stage 1 exoskarn in the Taco zone (Fig. 4.10 L).

A single occurrence of scheelite is noted in a sericite + garnet vein in the Oscarina zone. This vein cuts across P1-Taco and an alteration assemblage that includes garnet + epidote + prehnite (Fig. 4.11 C-E).

4.4.4. Sulphur Isotopes

The $\delta^{34}S$ values for sulphide minerals (pyrite, sphalerite, bornite, and galena) from the Antamina deposit range from -2.8 to 4.9‰, with an average value of 1.1‰ (Fig. 4.12 and Digital Appendix 4.2). Bornite samples (n = 2) are sampled from two different locations in proximal exoskarn (in the Bornita Zone) and show $\delta^{34}S$ compositions ranging from -0.7 to -0.4‰; pyrite from the same samples is reported at -0.3‰ for both samples (Fig. 4.12 and Digital Appendix 4.2). Additional samples of pyrite and sphalerite in endoskarn and exoskarn range from -0.7 to 4.9‰. Pyrite and sphalerite from the same samples report as consecutive pairs of $\delta^{34}S$ values (Digital Appendix 4.2), which indicates they formed from the same sulphur source. Pyrite from distal hornfels returned the lowest $\delta^{34}S$ value (2.8‰; Fig. 4.12).

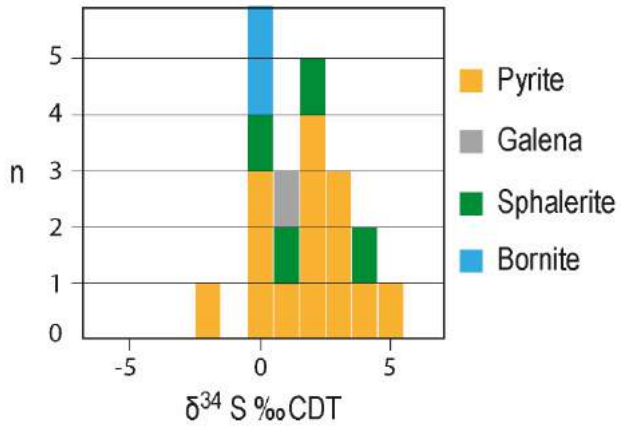

Fig. 4.12. Sulphur isotope compositions of Stage 2 sulphide minerals.

4.4.5. Alteration Zonation

At Antamina, zoning patterns of alteration and metal distribution are systematic and centred on the Taco zone, and to a lesser extent, the Usupallares zone. Alteration styles are largely controlled by the host rocks and are well-preserved, due to minimal post-mineralisation faulting. Porphyry style alteration (i.e., potassic alteration) is confined to the central intrusions, whereas skarn alteration occurs along P1 intrusion margins and in the surrounding country rock. A typical alteration zoning pattern in P1-Taco comprises a core of potassic alteration (hydrothermal biotite), which is transitional into weak endoskarn (patchy, localized

endoskarn veins), intensifying to massive and pervasive endoskarn proximal to the exoskarn contact (Fig. 4.5). In the wall rocks, exoskarn is the dominant alteration style and within exoskarn there are zoning patterns defined by mineralogy, garnet colour, and garnet-clinopyroxene composition (described in detail below). Beyond the exoskarn alteration zone, fluid escape structures in marble are the most distal expression of alteration at Antamina (Fig. 4.10 I).

4.4.6. Metal Zonation

Metal zonation is well-developed at the deposit scale, with clear patterns of proximal Mo-Cu ± Ag and distal Zn-Pb ±Ag ± Bi observed in plan view (Fig. 4.13), and grade contours of the main ore metals in plan view and cross section (Fig. 4.14). In plan view, these metals are distributed in a ring shape around the Taco porphyry centre (Fig. 4.13 and Fig. 4.14). In cross section, an inverted cup-shaped distribution is noted for these same metals in the Taco zone (Fig. 4.5); the same pattern is broadly discernible in long section (Fig. 4.14). By rock type, the highest concentrations of Zn are hosted in exoskarn, Cu in endoskarn and exoskarn, and Mo in endoskarn and P2 (Taco and Usupallares; Fig. 4.14). Bismuth displays two prominent zones of high concentration, one in the north-northeast Taco zone and another in the Bornita zone (Fig. 4.13). Bismuth in the Bornita zone is contained in the mineral wittichenite, which occurs in close association with the highest concentrations of bornite (Fig. 4.7). Silver distribution overlaps with copper and zinc, indicating that minor Ag-bearing minerals might be more common than documented, and/or that chalcopyrite, bornite, and sphalerite are enriched in Ag, to some extent (Fig. 4.13).

Zonation of the main ore minerals mostly follows the same trend as their constituent metals, with molybdenite concentrated in the Taco and Bornita porphyry centres, chalcopyrite slightly outward of molybdenite in endoskarn and exoskarn, and sphalerite outward from chalcopyrite in exoskarns. The patterns of chalcopyrite and sphalerite are similar in the Usupallares zone, however the minerals are less abundant. Bornite has a more localized distribution, occurring mostly southwest of the Taco zone in the Bornita zone (Fig. 4.15). Galena (not shown in Fig. 4.15) occurs in minor amounts in distal exoskarns where its occurrence overlaps with sphalerite. Scheelite was observed in only one occurrence in the northeast Taco/Oscarina zone, although the distribution of W indicates that it may be more common than noted in distal exoskarns.

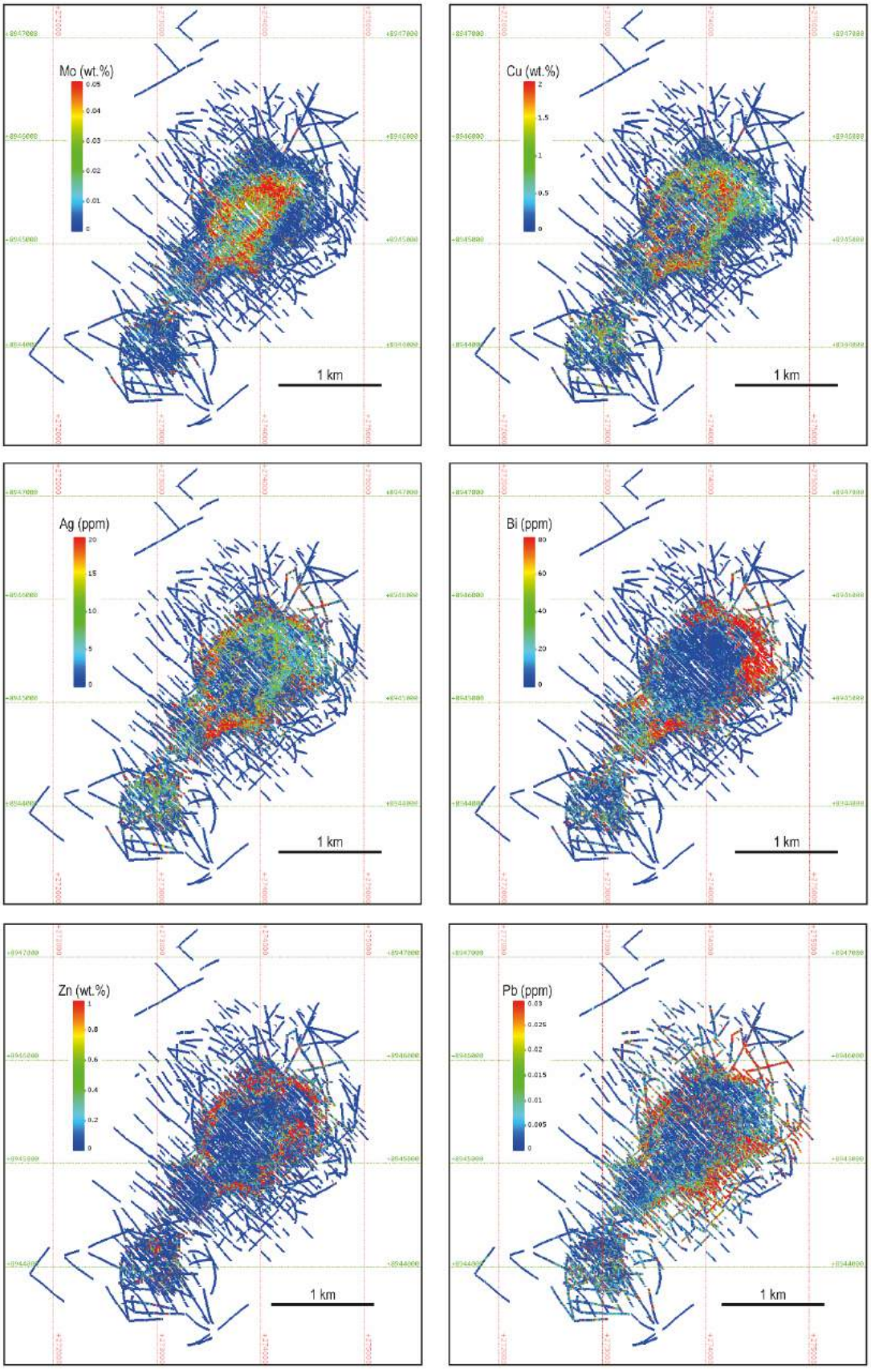

Fig. 4.13. Deposit-scale metal zonation (plan view), with drill holes projected to the surface.

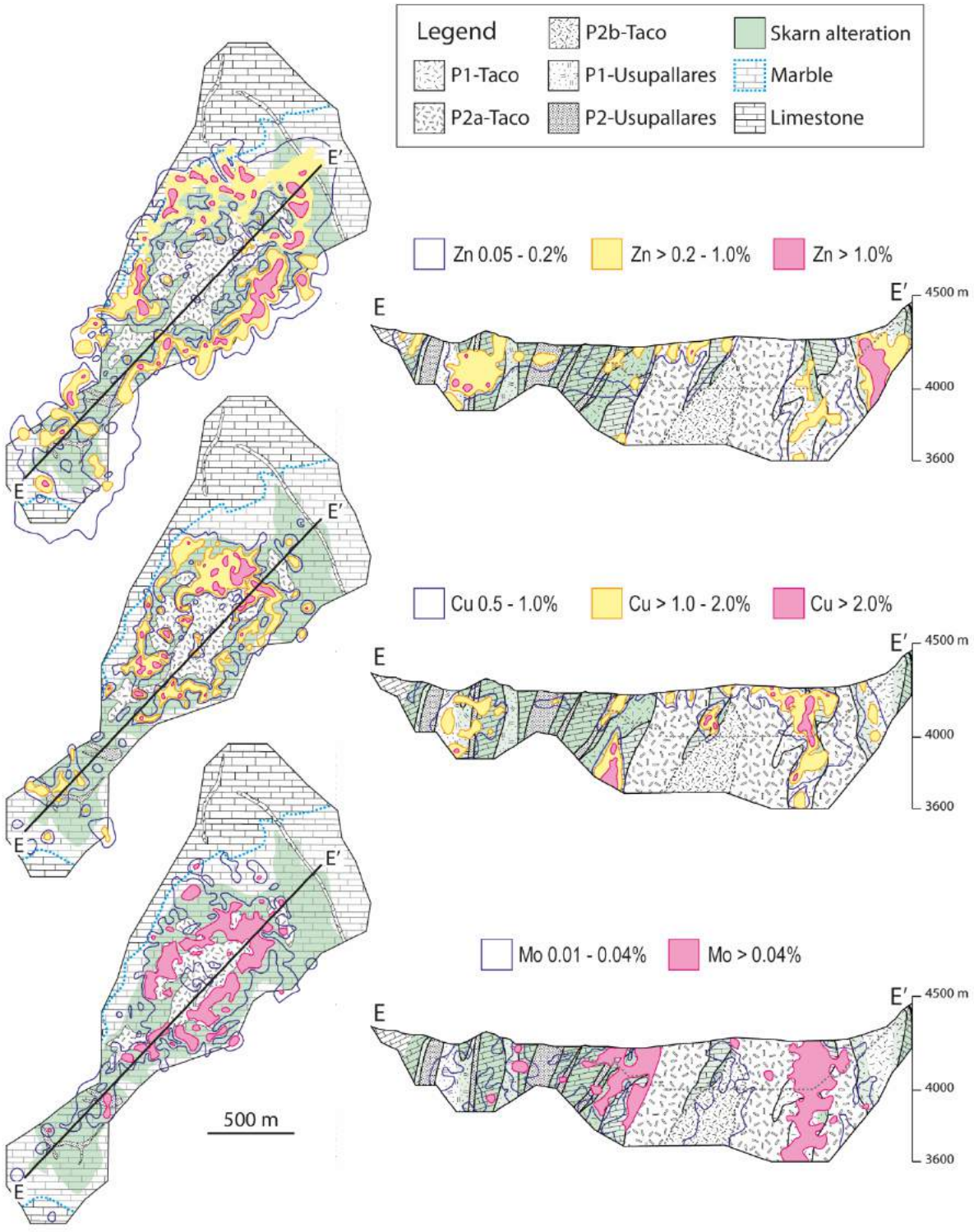

Fig. 4.14. Grade contours for Zn, Cu, and Mo in plan view (4,000 masl) and long section.

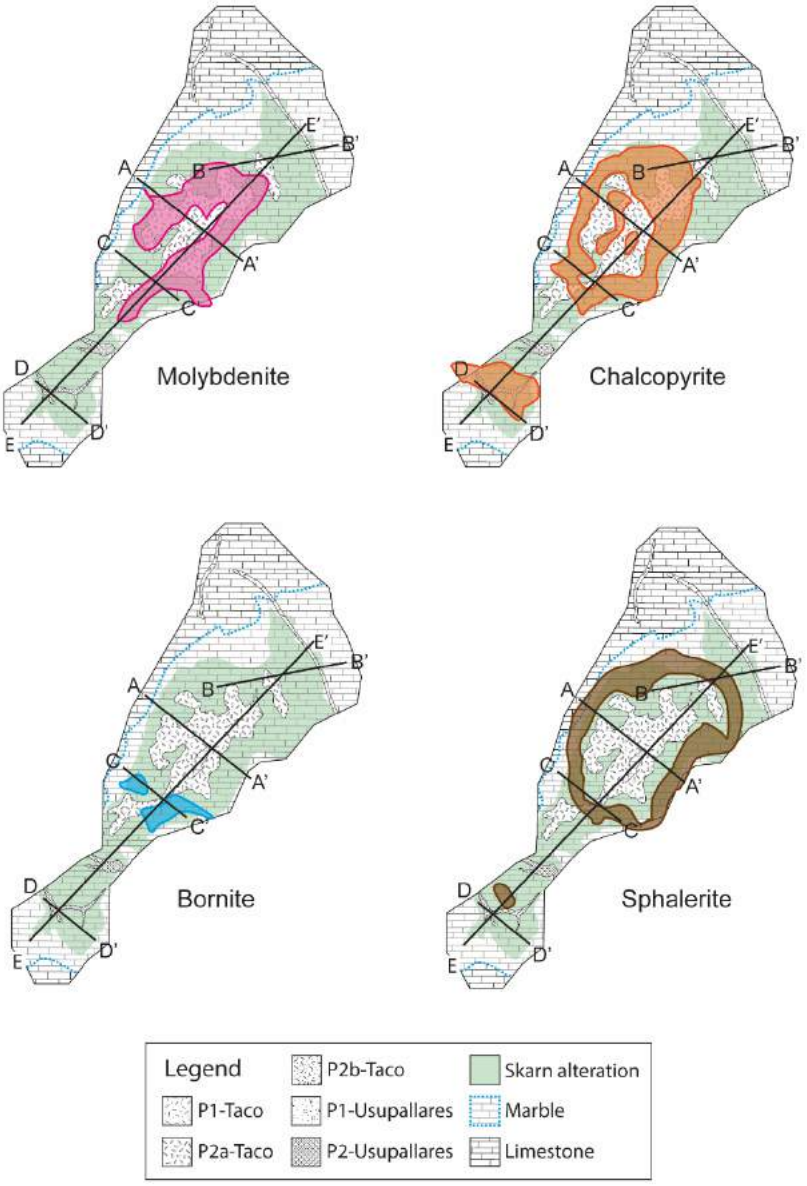

Fig. 4.15. Distribution of selected sulphide minerals in plan view (approximate, based on core logging and assays).

4.4.7. Garnet:Clinopyroxene Zonation

At Antamina, both endoskarn and exoskarn display proximal to distal mineralogical zoning patterns with respect to the porphyry-wall rock contact. Garnet is the dominant skarn mineral throughout the deposit (Fig. 4.16). However, clinopyroxene abundance increases toward the southwest with localized horizons of clinopyroxene > garnet in the Usupallares section (Fig. 4.16). In general, clinopyroxene abundance increases with depth in the Usupallares section, which appears to be correlated with the change of wall rock composition from Hd_{24} to Hd_{35} (Fig. 4.16). Wollastonite is locally abundant in distal exoskarns along the marble front, but is not a continuous mineralogical feature around the deposit.

4.4.8. Garnet Colour Zonation

In general, there is a systematic change in garnet colour from pink-red-brown-green from endoskarn to distal exoskarn (Fig. 4.17). Spatially, pink garnet occurs exclusively in endoskarn and green garnet occurs exclusively in distal exoskarn (i.e., near the marble front), whereas red and brown garnet are observed both in endoskarn and exoskarn proximal to the intrusion-wall rock contact (Fig. 4.17). Within each cross section, exoskarn garnet colour displays subtle differences with increasing depth and range (proximal to distal), while endoskarn garnet colour does not appear to change with depth or range.

In the Oscarina section, exoskarn garnet is dominantly brown with discontinuous patches of green garnet along the marble front (Fig. 4.17). The Taco section shows exoskarn garnet colour changing from red to brown to green with depth and range (Fig. 4.17). Xenoliths of exoskarn (entrained in P2 porphyry phases) contain red > pink garnet. In the Bornita section (Fig. 4.17), exoskarn garnet varies from green to brown with depth and, like the Taco section, green garnet is most abundant along the marble front (Fig. 4.17). Exoskarn garnet in the Usupallares section is dominantly brown and red with minor green garnet occurring at the top of the section in drill hole A2589 (Fig. 4.17).

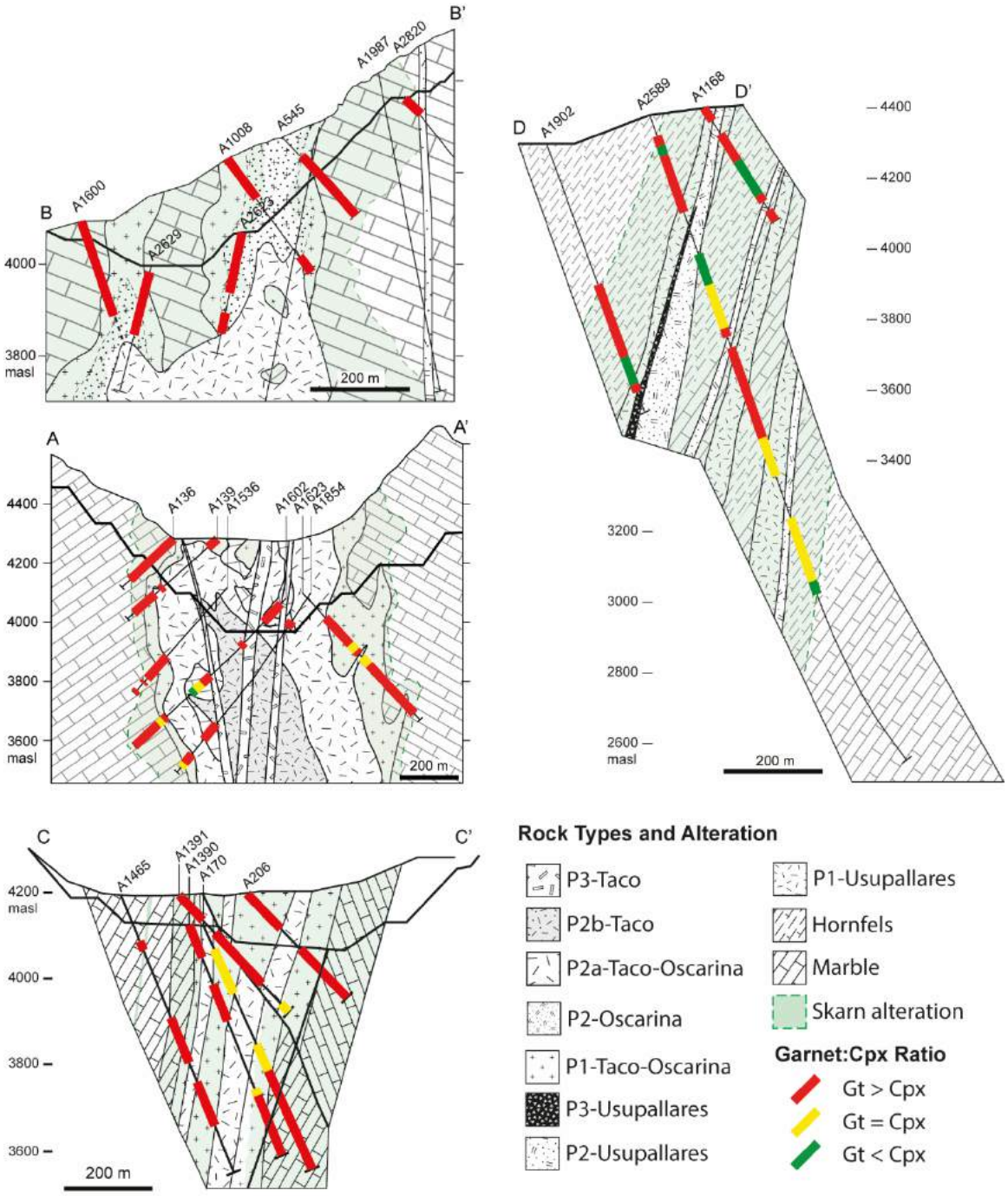

Fig. 4.16. Garnet/clinopyroxene ratios in logged drill cores from cross sections A-A' to D-D' (Fig. 1.5).

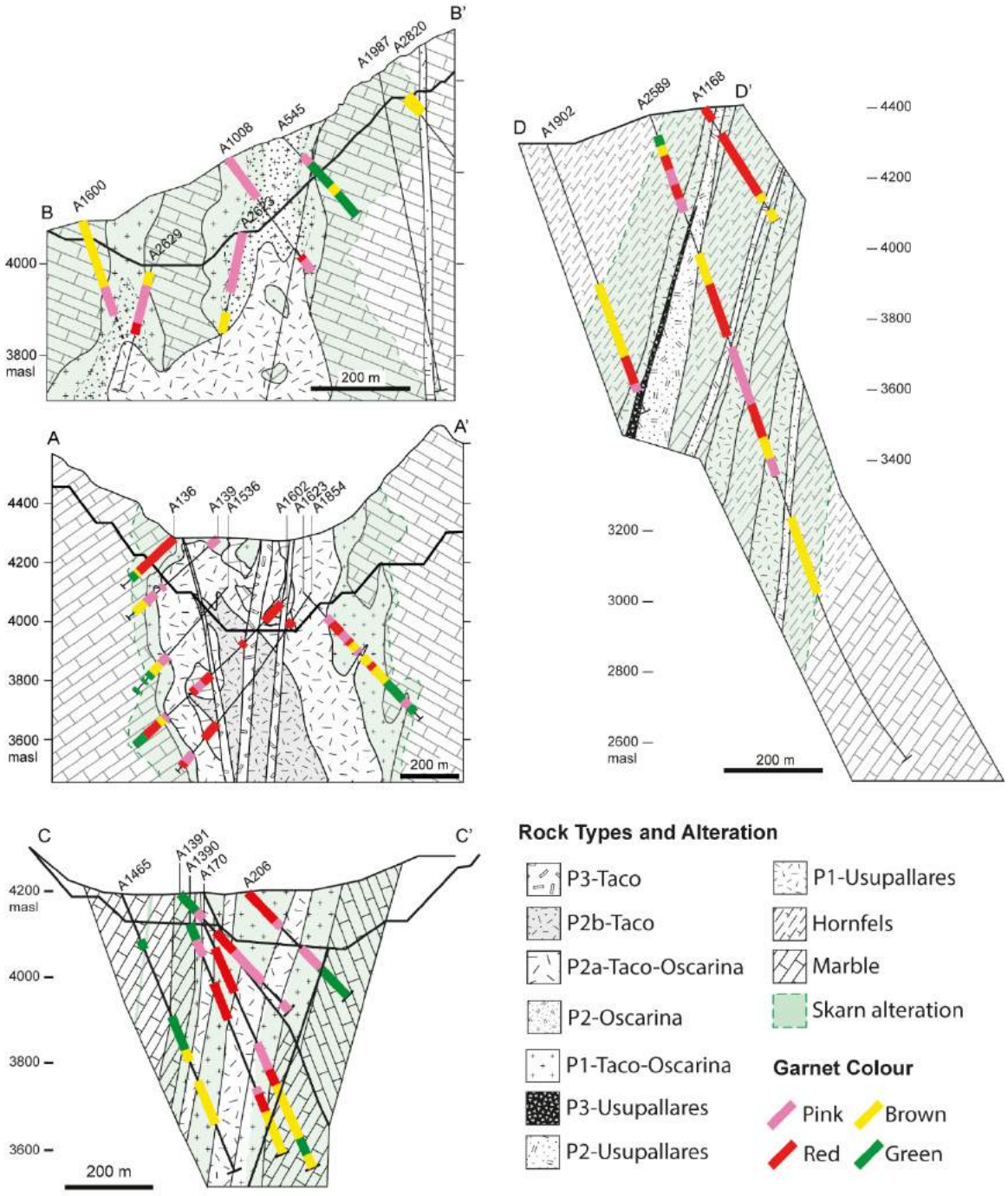

Fig. 4.17. Garnet colour in logged drill cores from cross sections A-A' to D-D' (Fig. 1.5).

4.4.9. Garnet Compositional Zoning

Garnet compositions (in terms of endmember andradite, Ad) are plotted for the Taco, Bornita, and Usupallares sections (Fig. 4.18 to Fig. 4.20). The average andradite content of garnet in exoskarn generally increases with vertical and lateral distance from the endoskarn contact in

the Bornita and Usupallares sections (Figs. 4.19-4.20). In drill hole A2589 (Usupallares section), the average andradite composition increases from Ad_{63} in endoskarn to Ad_{85} in exoskarn downhole over approximately 300 m (Fig. 4.20). In comparison, in the Bornita section the average andradite composition increases only slightly from Ad_{80} to Ad_{85} over approximately 285 m downhole (Fig. 4.19). In the Taco section, garnet compositional zoning patterns are less straightforward, however subtle patterns are detected in drill holes A1536 and A1602 where andradite content increases from Ad_{83} to Ad_{97} in exoskarn over approximately 200 m depth. One sample of endoskarn from drill hole A1854 shows an average andradite composition of Ad_{37}, which extends the lateral zonation of andradite content from Ad_{37} in endoskarn to Ad_{97} in exoskarn (drill hole A1602) over approximately 200 m. However, this endoskarn sample (Ad_{37}) is approximately 50 m deeper than the nearest exoskarn sample (Ad_{97}), which introduces some ambiguity to the relationship between garnet compositional zoning and depth in the Taco section (Fig. 4.17).

4.4.10. Clinopyroxene Compositional Zoning

Clinopyroxene compositions, measured in mol % hedenbergite (Hd) – diopside (Di) – and johanssenite (Jo) endmembers, range from $Hd_{03\text{-}55}Jo_{05(max)}$ in endoskarn to $Hd_{03\text{-}98}Jo_{10(max)}$ in exoskarn. Across the deposit, the change in clinopyroxene composition is less straightforward than the change in garnet composition due to the generally lower abundance of clinopyroxene at Antamina. The Usupallares section displays the highest abundance of clinopyroxene across the deposit, and also shows the most systematic zoning clinopyroxene patterns (Fig. 4.20). In drill hole A2589, the average clinopyroxene composition increases from Hd_{18} in endoskarn to Hd_{35} in exoskarn approximately 300 m down hole (Fig. 4.20). The Usupallares section also shows the highest variability in wall rock composition (due to interlayered marble and hornfels from the cm to m scale). A clinopyroxene composition of Hd_{32} was analysed in exoskarn near the top of the Usupallares section (A1168); this analysis does not fit the trend of increasing Hd downhole, which could be due to local compositional variations in the wall rocks. A similar pattern is noted in the Bornita section where the average clinopyroxene composition increases from Hd_{15} in endoskarn to Hd_{54} in exoskarn over approximately 400 m down hole and away from the endoskarn contact (Fig. 4.19). In the Taco section, there is limited clinopyroxene, but one sample at ~3,500 m elevation has a composition of Hd_{17}. In a nearby deep drill hole, A2491 (collared between the Taco and Bornita sections), hedenbergite

composition increases with depth from Hd_{79} at ~2,500 masl to Hd_{90} at ~2,400 masl (1,516 and 1,725 m depth along the drill trace; Fig. 4.21). These samples are located approximately 1,000 vertical m below the sample in the Taco section; taken together, these samples show a trend of increasing Hd content in clinopyroxene with depth. There is not enough systematic clinopyroxene data available from the Oscarina section to interpret compositional zoning patterns.

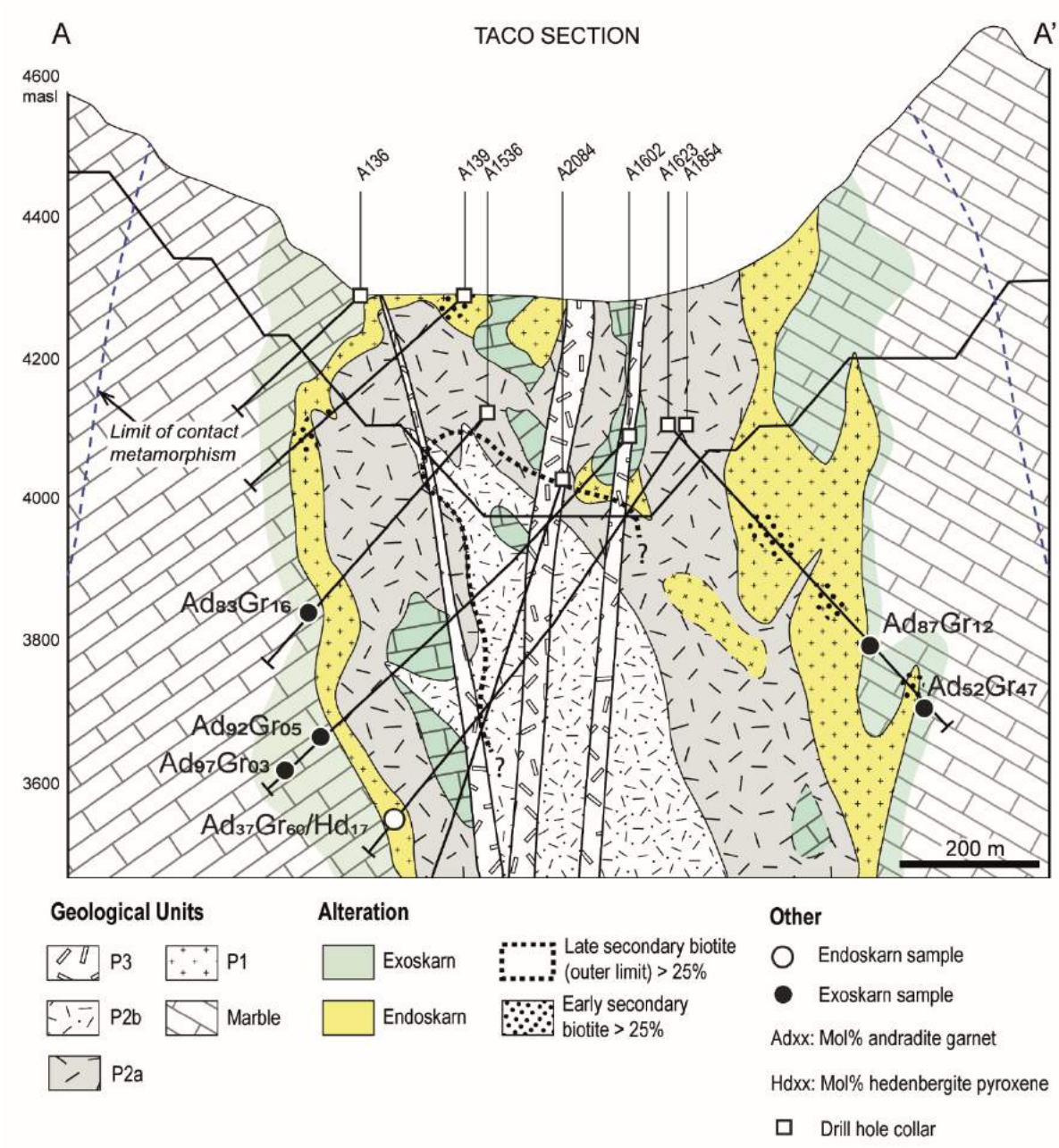

Fig. 4.18. Garnet and clinopyroxene compositional zoning in the Taco zone. See text for detail.

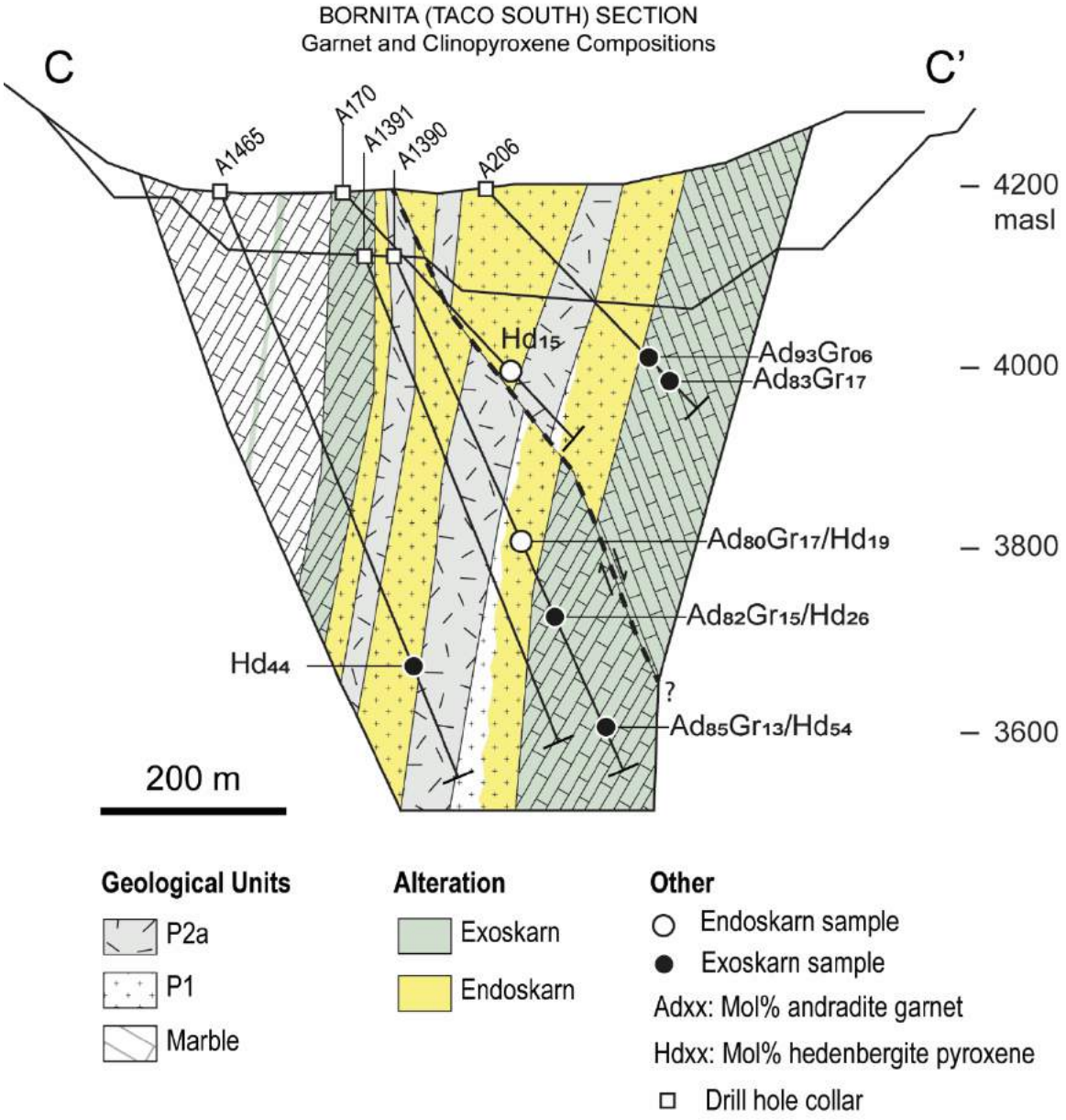

Fig. 4.19. Garnet and clinopyroxene compositional zoning in the Bornita (Taco south) zone. See text for detail.

4.4.11. Fluid Inclusion Analysis – Context and Sample Description

A sample of comb-layered quartz (UST) from drill hole A545-193.6 was selected for this fluid inclusion study. The sample is correlative with Stage 1 quartz in the mineral paragenesis and the UST structure is indicative of early fluid exsolution from P1, therefore this sample has the potential to provide insight on early magmatic-hydrothermal conditions at Antamina.

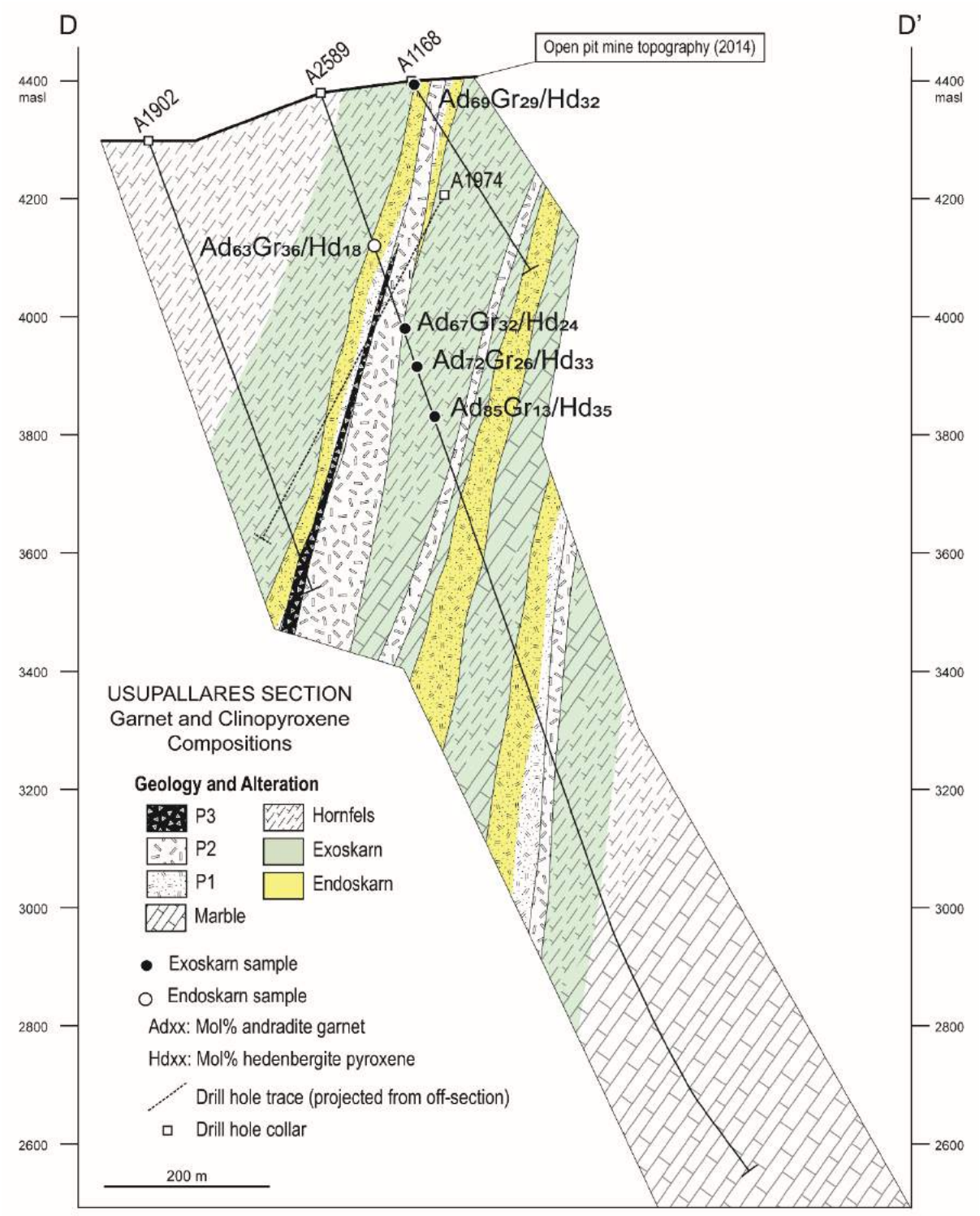

Fig. 4.20. Garnet and clinopyroxene compositional zoning in the Usupallares zone. See text for detail.

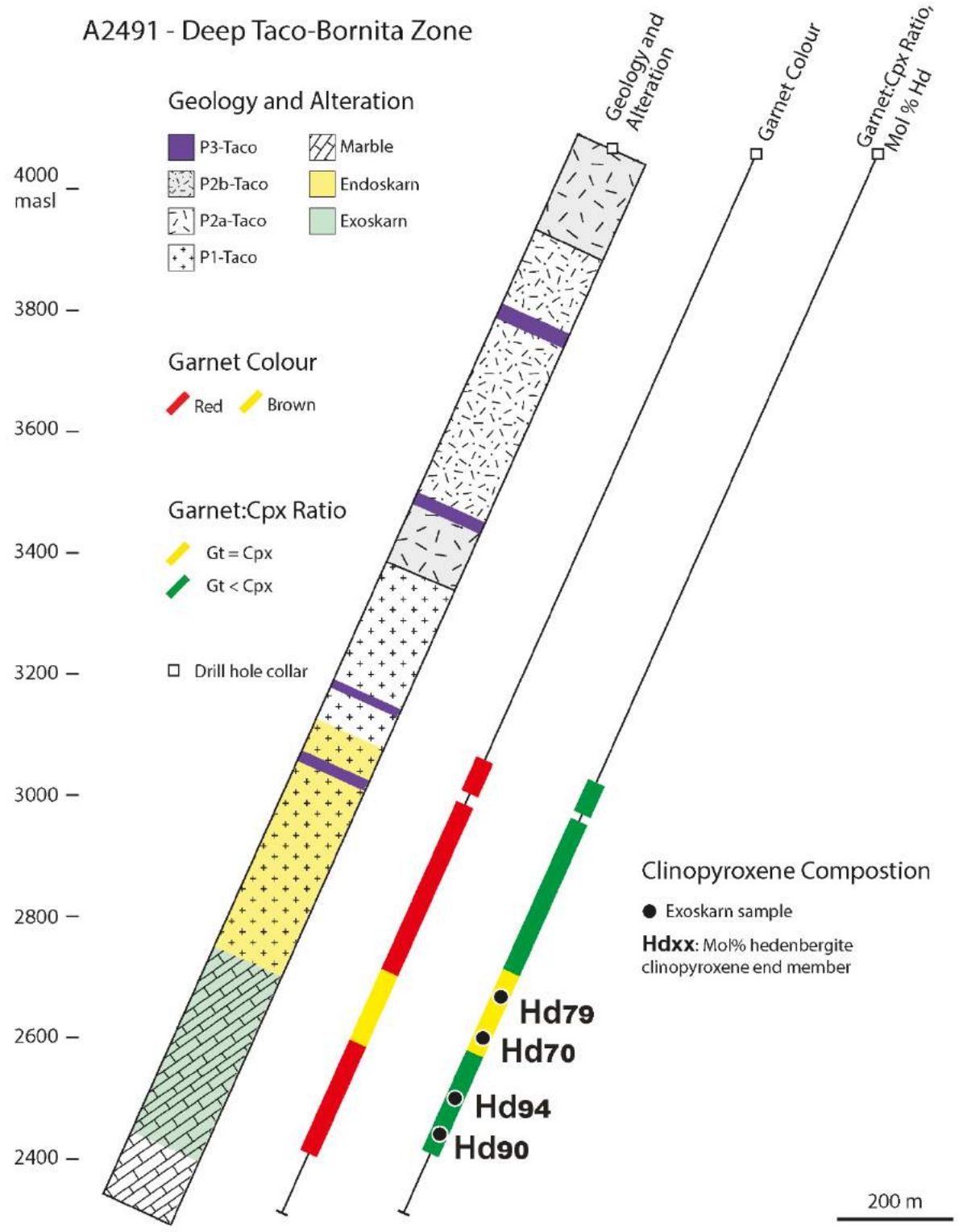

Fig. 4.21. Garnet-Clinopyroxene zonation patterns in deep drill hole A2491, Taco-Bornita zone.

The term ‘unidirectional solidification texture’ (UST) refers to several common, but volumetrically minor, oriented mineral textures that can be found in the roof zones of shallow

porphyry Mo, W, and Cu systems (e.g., Shannon et al., 1982; Kirkham and Sinclair, 1988; Lowenstern and Sinclair, 1996; Shafaroudi et al., 2015). Comb-layered quartz is a type of UST characterized by alternating layers of euhedral quartz and granitoid aplite (± phenocrysts); the quartz layers originate from a planar growth surface and their terminations point in the same direction, inward toward the centre of the crystallising intrusion. Layer thickness is variable, ranging from millim to m, as is the number of layers. Comb-layered quartz textures form via a repetitive process of pressure build up then decompression in the magma chamber (Lowenstern and Sinclair, 1996). As volatiles accumulate in the cupola, quartz nucleates along the tops and sides of the magma chamber; crystals continue to grow inward (perpendicular to the intrusion walls) until the system overpressures and aqueous fluids are released. Decompression causes fluid release, which quenches the magma, forming aplite interlayers that re-seal the system and start the process again. As the intrusion continues to cool and crystallise, the magma chamber wall migrates inward and another UST layer forms. The fluids that escape during decompression cause alteration (± mineralisation) in the adjacent and overlying rocks, hence the presence of these textures provides unique insight into the formation of some magmatic-hydrothermal ore deposits.

Because USTs form near the top of shallow magma chambers, this sample can provide a crude spatial context for microthermometry results. As in other samples of typical UST comb-quartz (e.g., Lowenstern and Sinclair, 1996), this sample displays layers of euhedral quartz crystals oriented roughly perpendicular to a sub-planar growth surface (Fig. 4.22 A-D). The individual quartz layers range from approximately 0.5 to 5 mm wide and are separated by porphyritic aplite interlayers with widths up to 3 cm (Fig. 4.22 A-B). The aplite interlayers are composed of quartz + K-feldspar and contain euhedral quartz phenocrysts, similar to those described by Lowenstern and Sinclair (1996); additional igneous phenocrysts include biotite, amphibole, plagioclase, and K-feldspar and the aplite groundmass is dominated by aphanitic (5-20 μm) quartz and K-feldspar. The sample has been subject to Stage 1 alteration, including local replacement by garnet (Ad_{72-85}) along the comb quartz veins and a weak overprint of Stage 2 prehnite + epidote + calcite that is noted in the groundmass. Despite this overprinting alteration, CL imaging reveals that primary growth zones in the UST have been largely retained, indicating that the quartz has not been recrystallized by later hydrothermal events.

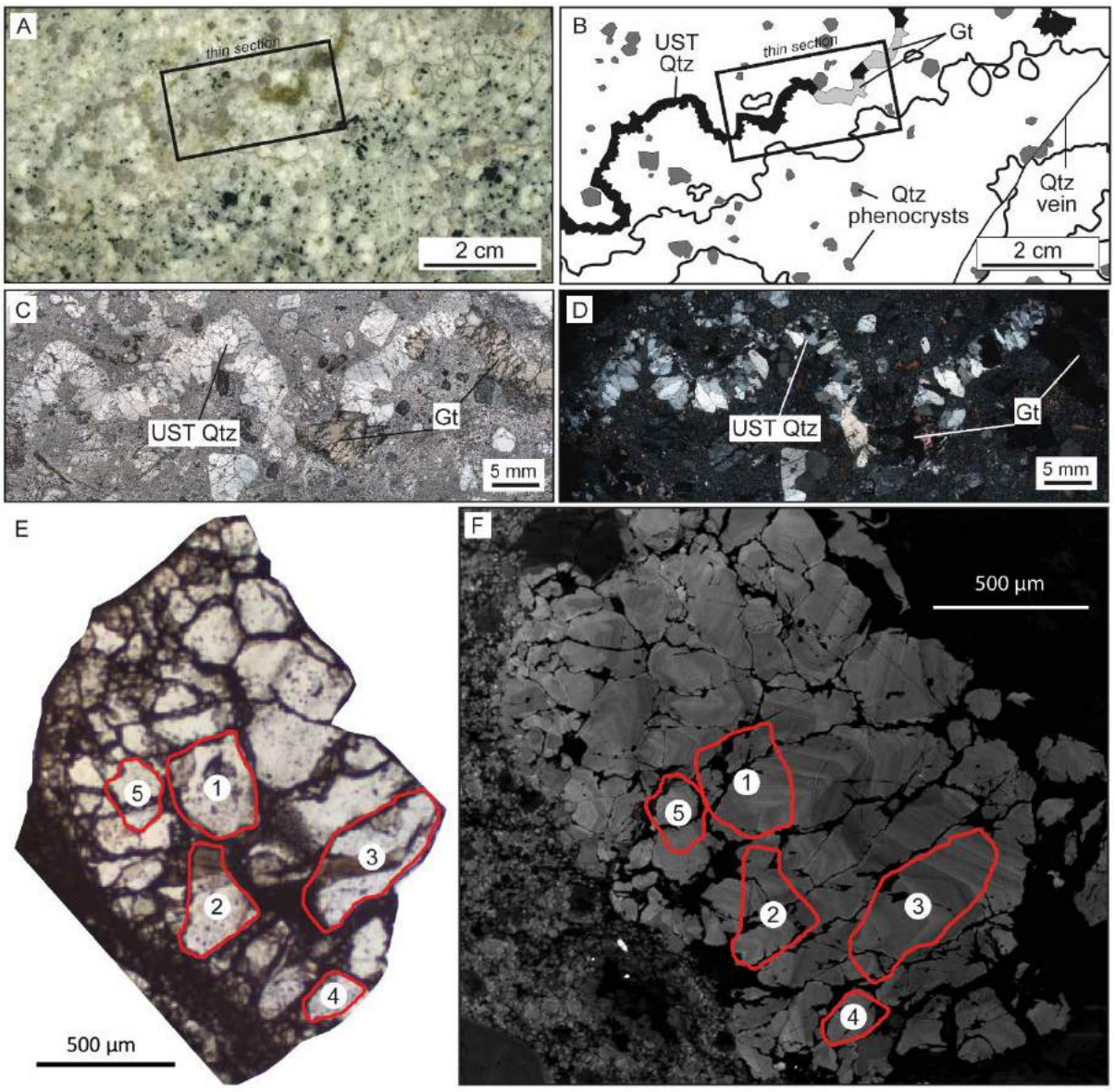

Fig. 4.22. Unidirectional solidification texture (comb quartz) in sample A545-193.6. A. core sample showing location of thin section. B. Sketch of key mineralogical and textural features from (A). C. Plane polarized light photomicrograph of the UST showing partial replacement by garnet. D. Cross-polarized light photomicrograph. E. Fluid inclusion sample showing the location of chips analysed. F. CL image of the UST showing primary magmatic zoning in the comb quartz. The approximate location of fluid inclusion chips are outlined in red.

4.4.12. Fluid Inclusion Analysis – Microthermometry Results

Fluid inclusions have been classified as four different types (I-IV) based on physical properties at room temperature (Table 4.1); the complete data set is available in Digital Appendix 4.3. Based on spatial relationships and petrographic observations, Type I inclusions are primary, and Type II likely contains a mixture of primary and secondary inclusions, and Types III and IV are most likely to be secondary. With few exceptions, temporal relationships

between the fluid inclusion types could not be established with a high degree of confidence. Isolated inclusions, which are commonly indicative of primary populations, were observed in all types. Type I inclusions are typically isolated or in clusters (Table 4.1). Trails of inclusions, which are commonly indicative of secondary inclusions, were observed in types II and III. Some type III inclusions occur in distinct trails cutting across mineral grain boundaries, indicating that they are secondary, while some Type II inclusions also occur in trails or possibly crystal growth zones; the latter scenario would indicate that they are primary. Only Type IV inclusions occur exclusively as isolated inclusions, however these comprise the smallest population and provide the most limited and inconsistent microthermometry results.

Table 4.1. Summary of fluid inclusion types, physical properties at 25°C, and microthermometry results.

Type	Components	n	Vf (%)	Sub-Type*	n	Spatial	T_mIce (°C)	T_h (°C)	Hom. Mode	T_hHalite (°C)	Salinity (wt. % $NaCl_{eq}$)	Density (g/cm^3)
I	L + V + S_{1-4} + O	10	5-20	-	-	I, C	-28.5 to -25.5	318-367	H	405-420	46.7-52.3	1.1-1.2
II	L + V + S_{1-4}	53	5-50	A	5	I,C	-28.0 to -27.0	302-345	H	405-494	49.5-51.4	1.2-1.3
				B	48	I,C,T	-36.1 to -16.5	244-413	L	N/A	29.9-66.8	0.9-1.1
III	L + V	40	10-60	-	-	I, C, T	-14.0 to -3.0	200-348	L	N/A	5.4-25.3	0.8-0.9
IV	L_2 + V	4	50-60	-	-	I	-11.0 to -4.0	N/O	N/O	N/A	7.3-20.0	N/A

*Sub-type classification is based on homogenisation mode.
Salinities were calculated using the final ice melting temperature, based on the NaCl-H_2O system (Bodnar, 1993).
Densities were calculated using the HokieFlincs spreadsheet (Steele-MacInnes et al., 2012).
Abbreviations: L = liquid; V = vapour; S = solid (translucent daughter minerals including halite); O = opaque daughter mineral; Vf = vapour fraction; I = isolated; C = cluster; T = trail; Hom. Mode = homogenization mode where H = homogenization by halite dissolution and L = homogenisation to liquid.

All fluid inclusion types recognised in this study are liquid-rich with vapour ± daughter minerals. Type I (n = 10) consists of liquid + vapour + halite + additional translucent daughter minerals other than halite (typically 1 to 2) + a triangular opaque phase. Type II (n = 53) consists of liquid + vapour + halite ± additional translucent daughter minerals. Type III (n = 40) consists of liquid + vapour. Type IV (n = 4) consists of two liquid phases (H_2O and CO_2) + vapour.

Type I inclusions display euhedral to subhedral negative crystal shapes. They range in size from 12 to 24 µm. All contain a small vapour bubble (vapour fraction ranges from 5% to 20%), and contain halite plus at least one other daughter crystal at 25°C, though up to four have been observed in a single fluid inclusion (Fig. 4.23). Halite (isotropic) is always present;

additional solid phases are colourless and cubic to tabular in shape, but the mineral species could not be identified with confidence. They may include sylvite (KCl; based on cubic shape, isotropism, low relief) and a sulfate or carbonate (based on the tabular shape and the weak birefringence). Two out of ten inclusions formed pale brown crystal masses during freezing, indicating the presence of $CaCl_2$. A triangular opaque solid, up to 3 µm, was observed in all Type I inclusions. Laser Raman analysis of these opaque solids yielded inconclusive results, possibly due to the depth of the inclusions. However, because triangular opaque daughter crystals have been confirmed as chalcopyrite in other porphyry copper deposits (i.e., Cline and Bodnar, 1994; Mavrogenes and Bodnar, 1994; Rusk et al., 2008; Vry, 2010), chalcopyrite is a contextually reasonable assumption in this case. Based on the similar physical properties of fluid inclusions containing triangular opaques (Table 4.1), they are most likely to be daughters rather than randomly trapped crystals.

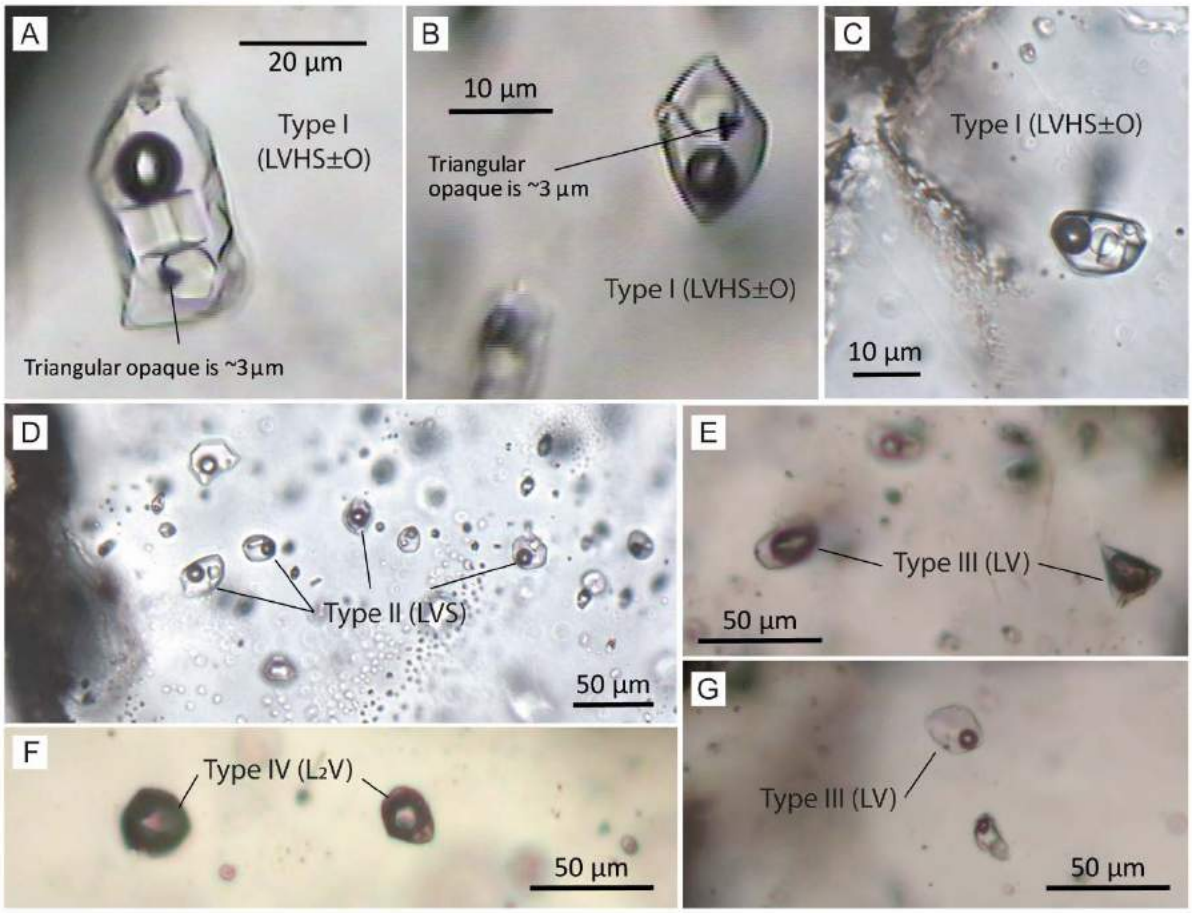

Fig. 4.23. Photomicrographs of fluid inclusion types identified in this study.

Four out of ten Type I inclusions displayed first ice melting between -28.5°C and -25.5°C (Fig. 4.24), which is below the eutectic temperature for the H_2O-NaCl system; this indicates components in addition to NaCl are present, which is consistent with the presence of other daughter minerals in addition to halite in the fluid inclusions. Calculated salinity (after Bodnar, 1993) ranges from 46.7-52.3 wt. % NaCl equivalent (based on T_mIce; Fig. 4.24, Table 4.1), which is essentially a brine. All of these inclusions homogenise by halite disappearance; that is, the liquid phase homogenizes before halite dissolves. Liquid homogenisation temperatures ranged from 318°C to 367°C, and halite homogenisation temperatures ranged from 405°C to 420°C. Opaque daughters failed to homogenise through temperatures up to 600°C, which is the upper limit for the heating stage. This behaviour is consistent with that reported by Spencer et al. (2015) and Mavrogenes and Bodnar (1994). Post-entrapment modification, specifically hydrogen diffusion into and out of the fluid inclusion, is one possible explanation for this observed behaviour (Mavrogenes and Bodnar, 1994).

Type II fluid inclusions have been subdivided according to homogenization mode; Type IIA inclusions (n = 5) homogenise by halite disappearance, while Type IIB inclusions (n = 48) homogenise to the liquid state (Table 4.1). Type IIA fluid inclusions occur as isolated inclusions and in clusters, while Type IIB occurs in clusters, trails, and as isolated inclusions. Sizes range from 12 to 48 µm (Type IIA) and 5.5 to 46.5 µm (Type IIB). The most common shapes are irregular, oblong, and rounded squares, and negative crystals. The vapour fraction ranges from 5-30% (Type IIA) and from 5-50% (Type IIB; Table 4.1). Type II inclusions always contain halite, but an additional translucent, isotropic daughter (sylvite?) was observed in 21 inclusions. Prior to microthermometry experiments (i.e., at room temperature), six of these inclusions displayed only liquid and vapour phases; however after heating up to 200°C solids (probably halite) formed and persisted throughout the remaining heating and freezing experiments. Four Type IIA inclusions, and at least 25 Type IIB inclusions formed pale brown crystals during freezing, which is attributed to the presence of $CaCl_2$. Salinity ranges from 49.5-51.4 wt. % NaCl equivalent in Type IIA inclusions, and from 29.9-66.8 wt. % NaCl equivalent in Type IIB inclusions (Fig. 4.24, Table 4.1). T_mIce measurements in Type IIA range from -28.0 to -27.0°C. T_mIce measurements in Type IIB range from -36.1°C to -16.5°C with a mode at -24.5°C (Fig. 4.24, Table 4.1). Homogenisation temperatures in Type IIA range from approximately 302-345°C, and from 244°C to 413°C (with a mode at

310°C) in Type IIB (Fig. 4.24, Table 4.1). While Type IIA fluid inclusions lack an opaque daughter, they share many similarities with Type I fluid inclusions (such as homogenisation by halite disappearance, high salinity, and spatial occurrence, among other characteristics listed in Table 4.1); this subset of Type II fluid inclusions are likely to be primary fluid inclusions that have been undergone some degree of post-entrapment modification (as indicated by the variability in daughter minerals and the presence of $CaCl_2$, as described above).

Type III inclusions contain only liquid and vapour and occur in clusters, trails, and as isolated inclusions. Shapes are variable and include round-oblong, negative crystal, and rectangular or irregular, and sizes range from 5.2 to 51 µm. The vapour fraction ranges from 10-60% and all homogenise to the liquid phase. No daughters were observed in Type III inclusions. Calculated salinity ranges from 5.4 to 25.3 wt. % NaCl equivalent based on T_mIce measurements ranging from -14°C to -3°C (Fig. 4.24, Table 4.1). Homogenization temperatures range from 200°C to 348°C (Fig. 4.24, Table 4.1).

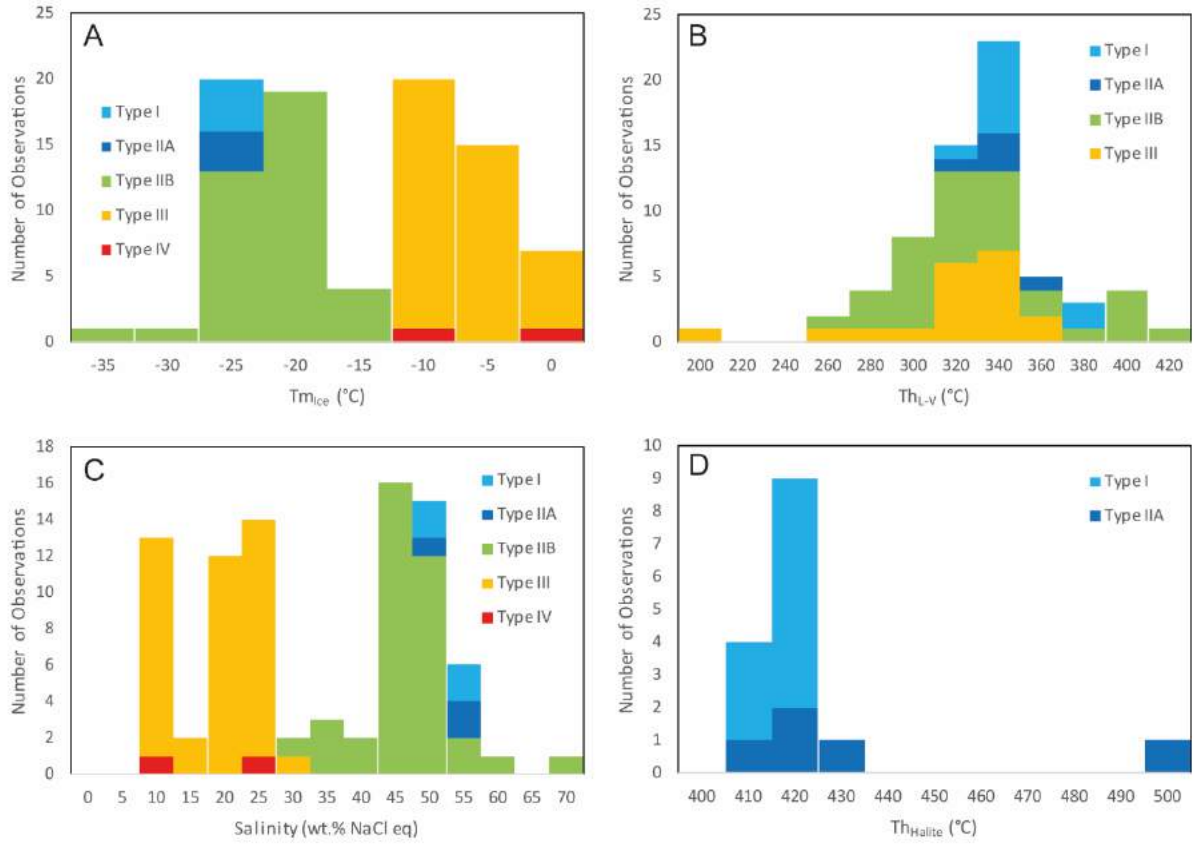

Fig. 4.24. Fluid inclusion microthermometry results.

Type IV inclusions include a small population (n = 4) of isolated inclusions containing liquid H_2O + liquid CO_2 + vapour H_2O. They range in size from 14-60 µm and display irregular shapes. These inclusions are generally dark or shadowy and therefore difficult to observe, however, the largest one (60 µm) displays a double bubble and initial melting of CO_2 was observed at -56.7°C. A double bubble was not observed in the remaining three samples, although a bubble shift was observed between -56.6°C to -56.5°C, indicating the likely presence of liquid CO_2. One of these inclusions produced a pale brown solid upon freezing to -100°C, which slowly melted between -56.7°C and -10°C; this freezing and melting behaviour indicates the presence of $CaCl_2$ and NaCl. Two measurements of T_mIce were recorded at -10°C and -4°C on two different inclusions, and the corresponding salinity was calculated at 7.3 to 20 wt. % NaCl equivalent, respectively (Fig. 4.24, Table 4.1). Homogenization temperatures were not obtained prior to decrepitation of the sample, therefore the mode of homogenisation is not known.

4.5. Discussion

4.5.1. Controls on Skarn Silicate Mineralogy and Zonation

The redox state of the wall rocks, coupled with oxidized magmatic-hydrothermal fluids, controls the distribution of garnet versus clinopyroxene in the Antamina skarns. In particular, organic carbon in the wall rocks creates reducing conditions where Fe^{2+} (i.e., reduced Fe) minerals such as clinopyroxene ($Ca(Mg,Fe^{2+})Si_2O_6$) are stable over Fe^{3+} minerals (such as andradite garnet). This is most evident in the Usupallares section (Fig. 4.20) where garnet:clinopyroxene ratios in exoskarn are < 1, compared to exoskarns in the Taco, Bornita, and Oscarina sections, which are dominated by garnet and display garnet:clinopyroxene ratios ≥ 1 (Fig. 4.16). It is suspected that exoskarns with garnet:clinopyroxene ≥ 1 formed in wall rocks with low organic carbon contents (possibly marble-dominant lithologies), and exoskarns with garnet:clinopyroxene < 1 formed in wall rocks with higher organic carbon contents, such as shale or marl. Because both the Celendín and Jumasha Formations contain marble, it is difficult to be certain about which unit hosts the garnet-dominant exoskarns; however, given that marl and shale comprise the majority of the Celendín Formation, it is likely that clinopyroxene-dominant exoskarns are hosted in the Celendín Formation. In contrast with the exoskarns, all of the endoskarns formed in relatively oxidised, magnetite-bearing intrusions, which favour the stability of Fe^{3+} minerals (i.e., andradite garnet,

$Ca(Fe^{3+})_2Si_3O_{12}$). This can explain why garnet is the dominant skarn minerals in most endoskarns.

The range of garnet and clinopyroxene compositions analysed in this study is compatible with typical Cu skarns and the low johanssenite contents of clinopyroxene distinguish Antamina from typical Zn skarns (Fig. 4.3; Meinert, 2005). At the deposit scale, skarn silicate mineral zonation shows a general increase in the hedenbergite content of clinopyroxene and the andradite content of garnet in exoskarns with increasing depth and distance from the endoskarn contact (Figs. 4.19-4.20). The highest Hd contents are observed at approximately 2,000 m elevation, near the bottom of the skarn system. The observed compositional changes can be attributed to several factors. One is the change from proximal oxidizing conditions to distal reducing conditions controlled largely by the composition of the wall rocks. The coincidence of increasing andradite and hedenbergite compositions with depth and distance from the endoskarn contact seems contradictory; however because the skarns are dominated by garnet, the overall redox state must have favoured the formation of a higher Fe^{3+} mineralogy in most cases. One possible explanation for the increasing andradite/decreasing grossularite contents of exoskarns away from the endoskarn contact is that the low solubility of Al causes grossularite to precipitate in proximal skarns (versus higher solubility Fe, which will be more likely to precipitate in distal skarn garnet). The same trend of increasing Fe contents of clinopyroxene away from the fluid source is explained using similar logic; Mg is a better fit than Fe in the clinopyroxene crystal structure, therefore Mg is preferentially incorporated into proximal diopside, whereas Fe is incorporated into distal hedenbergite.

4.5.2. Controls on Mineralisation and Fluid Composition

Ore mineral distribution and composition indicates that the Taco zone was the major hydrothermal centre for the Antamina deposit. From the central Taco porphyry complex outward to the marble front, there is a transition from high temperature/low solubility to low temperature/high solubility metals, namely proximal Mo-Cu to distal Zn-Pb (Fig. 4.13). The coexisting Cu and Zn mineralisation is unusual as skarns with such metal associations are rare (e.g., Chang and Meinert, 2004); however, aside from the abundance of Zn, Antamina displays the genetic characteristics of a Cu skarn system. The overall ore mineral zoning is consistent with that observed in typical continental arc Mo-Cu porphyries (proximal molybdenite-bornite-chalcopyrite to distal sphalerite-galena), and the narrow range of $\delta^{34}S$

values in these samples is consistent with sulphide values reported for porphyry Cu systems (range is from 1-8‰; Seal, 2006). While most of these data report in the typical porphyry Cu range, there is some minor spread towards negative $\delta^{34}S$ values, which may be indicative of reduced sedimentary sulphur mixing with magmatic sulphur with increasing distance from the magmatic source (Seal, 2006).

Outside of the central molybdenite zone, a localized concentration of bornite marks a zone of high-temperature Cu-sulphide precipitation (Fig. 4.15). At temperatures above 500°C within the Cu-Fe-S system, there are extensive regions of solid solution and high-temperature bornite can incorporate a variety of trace elements including Bi > 17 wt. % and Ag ~8,000 ppm (Cook et al., 2011). Upon cooling below 400°C, a large number of mineral phases can precipitate through exsolution, the most common of which include chalcopyrite, chalcocite, digenite, and wittichenite (if appreciable Bi is present). The observed textures and compositions indicate that bornite likely precipitated early as a high-temperature solid solution (~400-500°C), which is approaching the temperature of late-stage potassic alteration. Upon cooling, this solid solution would have exsolved into multiple lower temperature phases including chalcopyrite + wittichenite + chalcocite (Fig. 4.7). Bismuth, which was stable in solid solution, was partitioned into wittichenite. These observations are supported by the mineral paragenesis (Fig. 4.1) and are compatible with the observations of Cook et al. (2011).

Sulphide mineral zonation progresses outward from molybdenite to bornite-chalcopyrite and sphalerite ± galena. The deposition (and resultant spatial distribution) of these sulphides is likely related to a complex interplay of factors including metal solubility, transport ligands, temperature, and pH, to name a few (i.e., Wood and Samson, 1998; Williams-Jones et al., 2010; Zhong et al., 2014; Spencer et al., 2015, Shu et al., 2017; and references therein). Metal sulphide deposition patterns appear to be primarily controlled by transport distance away from the magmatic-hydrothermal centre, which is also related to falling temperatures and increasing pH (caused by neutralisation of acidic magmatic-hydrothermal fluids by interaction with carbonate-rich wall rocks). Metals with higher solubilities (i.e., Zn, Pb) were transported further than metals with low solubility (i.e., Mo, Cu). Previous studies report on the importance of chloride complexes as agents of transport in hydrothermal fluids (e.g., Sverjensky, 1987; Yardley, 2005; Spencer et al, 2015); however a recent study by Zhong et

al. (2015) demonstrates that high-salinity fluids are not always required for metal transport and deposition in high temperature deposits such as skarns and porphyries. Based on the hypersaline composition of some fluid inclusions reported in this study, and their spatial association with Cu (± Mo) mineralisation, transport of these metals was likely facilitated, at least to some degree, by chloride complexes. If Zn and Pb were also transported by chloride complexes, precipitation may have been triggered by hydrothermal fluid interaction with reduced S in meteoric water or wall rocks with increasing distance from the magmatic source (e.g., Zhong et al., 2015). Alternatively, bisulfide complexes may have played a role in transporting Zn-Pb ± Cu (based on the $\delta^{34}S$ compositions of these sulphides indicating a potential magmatic source); in this case the spatial distribution of Cu-Zn-Pb can be explained by cooling and de-complexing of S in the hydrothermal fluids (e.g., Zhong et al., 2015). The transition from pyrite (as the dominant Fe-sulphide in the porphyry-skarn zone) to pyrrhotite (in limestone near the contact metamorphic aureole; Escalante, 2008) is probably related to lower fO_2 conditions induced by organic carbon in limestone (i.e., up to 3.63 wt. % C; Chapter 2), as well as decreasing fS_2 and Fe/S with increasing distance from the magmatic fluid source.

4.5.3. Constraining the Depth of Formation

One of the aims of this study is to estimate the depth of formation of the Antamina deposit by using microthermometry measurements of fluid inclusions (FI) to calculate pressure, which can then be related to depth the equation: $P = \rho g z$, where P = pressure (Pa), ρ = density (kg/m^3), g = acceleration due to gravity (m/s^2), and z = depth (m). Because fluid inclusions can provide the data needed to calculate pressure, and because multiple populations of FI can coexist in a single sample, the selection of FI for this purpose is a non-trivial task. Each FI population records a specific geological event, therefore the first step is to identify which process is recorded by each population, as this will determine the significance of any further calculations. In this study, four types of FI were identified. Of these, Type I is most likely to be primary, whereas all other types are likely to be secondary (based on petrographic observations). In this UST sample, primary FI are most likely to have trapped early magmatic fluid compositions under pressure conditions that existed near the top of the magma chamber. Therefore, they are the most suitable FI population to use for pressure calculations relating to the depth of formation.

Table 4.2. Calculated pressure and density of fluid inclusions that homogenise by halite disappearance.

Chip ID	FI ID	Th_{NaCl} (°C)	Th_{L-V} (°C)	ρ_{BULK} (g/cm^3)	P_{hom} (kbar)
UST-002	IK-01	405	318	1.2	1.2
UST-002	IE-01	405	322	1.2	1.1
UST-002	JF-01	410	325	1.2	1.1
UST-002	IJ-01	415	328	1.2	1.1
UST-002	HD-01	420	328	1.2	1.2
UST-002	HD-02	415	332	1.2	1.1
UST-001	FF-02	410	333	1.2	1.0
UST-001	FJ-01	415	340	1.2	0.9

FI: fluid inclusion; Th: homogenisation temperature;
P_{hom}: pressure at homogenisation; ρBULK: fluid density.
All calculations after Steele-MacInnes et al. (2012).

In order to most closely approximate the trapping pressure, it is ideal to use primary FI that have not been subject to post-entrapment modification or leakage. There is some variability in the compositions of the primary FI which may indicate that post-entrapment modification or leaking has taken place. For instance, the formation of pale brown crystals during freezing was observed in 2 out of 10 primary inclusions, whereas it is a more common feature of the secondary FIs that formed temporally later. Because the primary FI in the UST should have trapped the earliest fluids to exsolve directly from the magma, the introduction of Ca into these FI may be a by-product from skarn formation, which began just slightly later than the initial release of magmatic-hydrothermal fluids from the magma chamber. Therefore, the presence of $CaCl_2$ may be indicative of open-system behaviour (i.e. post-entrapment modification), so these FI were not included in the pressure calculation because they cannot provide meaningful estimations of P-T conditions (Audétat and Günther, 1999). Another consideration is the presence of opaque daughters, which were only observed in primary inclusions. As similar FI have been observed in other porphyry and UST samples (i.e., Harris et al., 2004; Rusk et al., 2008), these are considered to provide a fair representation of early fluid compositions and so FI containing opaques, but lacking indications of $CaCl_2$, were retained for the pressure calculation.

A consistent feature of the primary FI identified in this study is homogenisation by halite disappearance. Fluid inclusions that homogenise by halite disappearance are relatively common in skarns and porphyry copper deposits (e.g., Bodnar and Beane, 1980; Dilles and

Einaudi, 1992; Cline and Bodnar, 1994; Baker and Lang, 2003; Harris et al., 2004; Rusk et al., 2008; Maydagán et al., 2015), but until recently, the interpretation of such inclusions has presented challenges due to a lack of experimental data. One of the difficulties in dealing with these types of FI is that salinity cannot be directly calculated when there is no vapour phase present during halite dissolution, as equations that relate halite dissolution temperature to salinity are only valid under vapour-saturated conditions (Lecumberri-Sanchez et al., 2012). Recent contributions on this subject (Becker et al., 2008; Lecumberri-Sanchez et al., 2012) have made it easier to constrain the PVTX properties of FI that homogenize by halite disappearance, which is directly applicable to this study. The pressure and fluid density of primary FI in this UST sample have been calculated according to the calculations of Lecumberri-Sanchez et al. (2012) by utilising the HokieFlincs spreadsheet (Steele-MacInnis et al., 2012; Table 4.2). Pressure ranges from 0.95 to 1.2 kbar and fluid density ranges from 1.1 to 1.2 g/cm^3 (Fig. 4.25). These pressures are lithostatic pressures and indicate a maximum formation depth ranging from 4.6 to 3.5 km (averaging 4.1 km) when calculated using Eq. 4.1, assuming an average bulk rock density of 2.7 g/cm^3 (Olhoeft and Johnson, 1984).

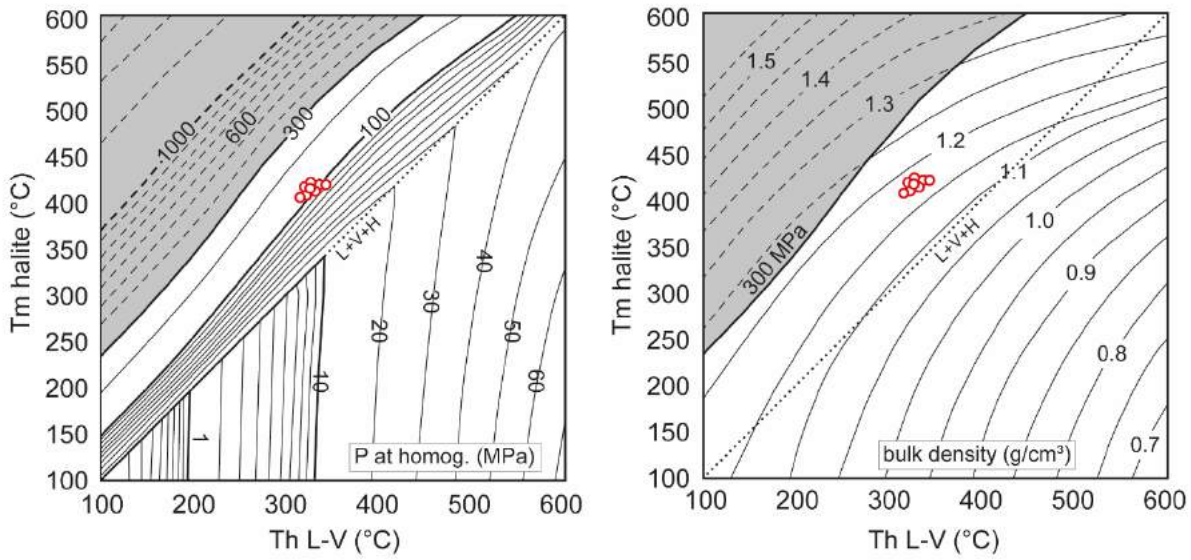

Fig. 4.25. Pressure and fluid density plots for fluid inclusions that homogenize by halite disappearance.

4.5.4. Uplift and Unroofing of the Deposit

Since the mid-Miocene, the central Andes of Peru have experienced surface uplift on the order of 3,500 m (Gregory-Wodzicki, 2000). In order to validate the depth of formation estimate, a model that incorporates uplift and glacial unroofing of the deposit is proposed.

The top of the APC was partially exposed in the Antamina cirque, beneath Lake Antamina (~4,300 masl) when the deposit was discovered. Drilling revealed USTs at ~4,200 masl; given that USTs form in the apical portions of intrusions, this indicates that the top of the system was largely intact and only minimally eroded by glaciation. Based on the depth of the cirque compared to the elevation of the surrounding peaks, it is estimated that glaciation removed up to 500 m of rock from above the deposit. Two scenarios (maximum versus minimum depth of emplacement) are proposed to constrain the depth of formation.

Scenario 1 (Fig. 4.26) utilizes the maximum calculated depth of emplacement of 4.6 km coupled with an estimated 3.5 km (3,500 m) of surface uplift since emplacement during the early Miocene; this places the top of the deposit at a depth of ~1.1 km below the present-day surface. Assuming Pleistocene glacial erosion of ~500 m, the top of the deposit would still be 0.6 km below the present-day surface, which is slightly too deep.

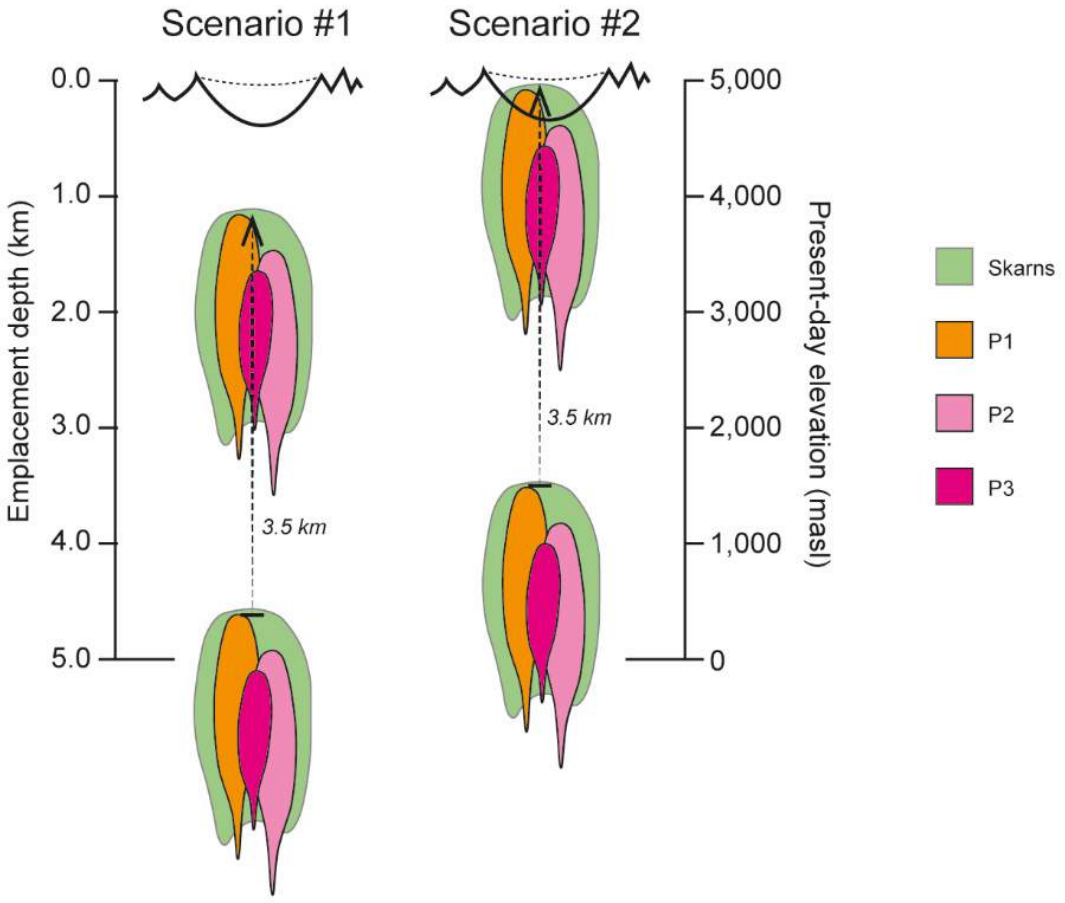

Fig. 4.26. Emplacement depth, uplift, and erosion scenarios for the Antamina deposit.

Scenario 2 (Fig. 4.26) utilizes the minimum calculated emplacement depth of 3.5 km coupled with 3.5 km of surface uplift to project the top of the deposit to the present-day surface. Again, assuming 500 m of glacial erosion, this removes the top ~500 m of the deposit, which places the top of the system more or less where it is today.

Therefore, the ideal scenario is explained by shallower depth of emplacement between ~4.0 and 3.5 km assuming maximum surface uplift of 3.5 km (since the early Miocene) and Pleistocene glacial erosion on the order of ~500 m.

4.5.5. Additional Constraints on Deposit Formation

From the highest elevation skarns exposed at the surface of the Taco-Oscarina zone, at approximately 4,500 m elevation, to the bottom of the system, at approximately 2,400 masl (Taco zone), the skarns have a vertical extension ≥ 2,100 m. In the Usupallares zone the top of the skarns outcrops at approximately 4,300 m elevation and the bottom is at least 2,700 m elevation, accounting for a vertical extension ≥ 1,800 m. In the Taco zone, the skarn has a variable width along its vertical extension, ranging from ~50 to 200 m wide between 4,200 to 3,500 masl, to 200 m wide at ~2,400 masl; this variation in width is opposite to what is expected for a skarn forming under homogeneous conditions where the skarn alteration zone should narrow with increasing depth. One possible explanation for this is a stratigraphic change in wall rock composition with depth. Assuming that the local stratigraphy is not overturned, the top of the deposit should have formed in the calcareous siltstones and silty limestones of the Celendín Formation, and the lower extension of the deposit should have formed in the relatively pure limestones of the Jumasha Formation. The width of the skarn zone is somewhat dependent on the composition of the wall rocks, and limestones are more favourable than calcareous siltstones to the development of broad skarn zones. Variations in width near the top of the skarn system may be attributed to the stratigraphic variability in the Celendín Formation, which contains rock types ranging from shale to limestone. Fluids interacting with this unit would be expected to create broad skarn zones in the more receptive limestone layers and narrow skarn zones in mudstones. Overall, the Jumasha Formation is a more receptive host rock, so skarn formation is favoured when fluids interact with this unit.

4.6. Conclusions

The Antamina deposit is comprised of a central porphyry complex surrounded by skarns with an ore mineralisation suite dominated by Cu-Mo-Zn. The system displays well-developed zoning patterns with respect to alteration, metal zonation, and skarn mineral composition. Alteration zoning pattern includes potassic alteration in the porphyry centre, transitional into endoskarn along the porphyry margins, then exoskarn and distal fluid escape structures in marble. Exoskarns are zoned with respect to garnet colour, from pink-red-brown-green (proximal to distal), and also in garnet/clinopyroxene ratio, garnet and clinopyroxene compositions, and metal endowment. Clinopyroxene and garnet compositions are mostly within the range of typical copper skarns. Hedenbergite content of clinopyroxene in exoskarn generally increases with depth and distance away from the endoskarn contact, as do andradite compositions in garnet, which indicate that skarn-forming fluids were expelled near the top of the system, rather than at varying depths. Metal zoning shows an outward progression from Mo ± Cu in the central porphyry, to Cu (± Ag, Bi)-Zn-Pb in distal exoskarns. Fluorite is locally abundant in the Oscarina zone, and scheelite occurrences have been noted; however they do not appear to be associated with respect to the mineral paragenesis. Fluid inclusions indicate that the ore fluids were highly saline. Stable isotopes ($\delta^{34}S$) indicate a magmatic source of sulphur that is consistent with $\delta^{34}S$ values observed in other porphyry Cu deposits (Seal, 2006). Pressure estimates from fluid inclusion microthermometry in the UST sample indicate that the deposit formed between 1,234 to 946 bar lithostatic pressure, which equates to a depth range of approximately 4.6 to 3.5 km. Coupled with uplift estimates for the central Andes of Peru and erosion due to glaciation, the most likely scenario is explained by depth of emplacement between ~4.0 and 3.5 km, consistent with 3.5 km of uplift and erosion from the early Miocene to present.

4.7. References

Audétat, A., and Günther, D., 1999, Mobility and H_2O loss from fluid inclusions in natural quartz crystals: Contributions to Mineralogy and Petrology, v. 137, p. 1-14.

Baker, T., and Lang, J.R., 2003, Reconciling fluid inclusion types, fluid processes, and fluid sources in skarns: and example from the Bismark Deposit, Mexico: Mineralium Deposita, v. 38, p. 474-495.

Becker, S.P., Fall, A., and Bodnar, R.J., 2008, Synthetic fluid inclusions. XVII. PVTX properties of high salinity H_2O-NaCl solutions (>30 wt% NaCl): application to fluid inclusions that homogenize by halite disappearance from porphyry copper and other hydrothermal ore deposits: Economic Geology, v. 103, p. 539-554.

Bodnar, R.J., and Beane, R.E., 1980, Fluid inclusion study of the porphyry copper prospect at Red Mountain, Arizona: Economic Geology, v. 75, p. 876-893.

Bodnar, R.J., 1993, Revised equation and table for determining the freezing point depression of H_2O-NaCl solutions: Geochimica et Cosmochimica Acta, v. 57, p. 683-684.

Burke, E.A.J., 2001, Raman microspectrometry of fluid inclusions: Lithos, v. 55, p. 139-158.

Chang, Z., and Meinert, L.D., 2004, The magmatic-hydrothermal transition – evidence from quartz phenocryst textures and endoskarn abundance in Cu-Zn skarns at the Empire Mine, Idaho, USA: Chemical Geology, v. 210, p. 149-171.

Chang, Z., and Meinert, L.D., 2008, Zoning in skarns – complexities and controlling factors: PacRim Congress, 24-26 November, 2008, p. 303-306.

Cline, J.S., and Bodnar, R.J., 1994, Direct evolution of brine from a crystallising silicic melt at the Questa, New Mexico, molybdenum deposit: Economic Geology, v. 89, p. 1780-1802.

Cook, N.J., Ciobanu, C.L., Danyushevsky, L.V., and Gilbert, S., 2011, Minor and trace elements in bornite and associated Cu-(Fe)-sulphides: A LA-ICP-MS study: Geochimica et Cosmochimica Acta, v. 75, p. 6473-6496.

Coplen, T.B., Hopple, J.A., Böhlke, J.K., Peiser, H.S., Rieder, S.E., Krouse, H.R., Rosman, K.J.R., Ding, T., Vocke, Jr., R.D., Revesz, K.M., Lamberty, A., Taylor, P., and De Bièvre, P., 2002, Compilation of minimum and maximum isotope ratios of selected elements in naturally occurring terrestrial materials and reagents: U.S. Geological Survey Water-Resources Investigations Report 01-4222, 98p.

Dilles, J.H., and Einaudi, M.T., 1992, Wall-rock alteration and hydrothermal flow paths about the Ann-Mason porphyry copper deposit, Nevada; a 6-km vertical reconstruction: Economic Geology, v. 87, p. 1963-2001.

Escalante, A.D., 2008, Patterns of distal alteration zonation around Antamina Cu-Zn skarn and Uchucchacua Ag-base metal vein deposits, Peru: Mineralogical, chemical, and isotopic evidence for fluid composition, and infiltration, and implications for mineral exploration: PhD Thesis, The University of British Columbia, Canada, 817 p.

Giesemann, A., Jager, H.J., Norman, A.L., Krouse, H.R., and Brand W.A., 1994, On-line sulfur-isotope determination using an elemental analyser coupled to a mass spectrometer: Analytical Chemistry, v. 66, p. 2816-2819.

Gregory-Wodzicki, K.M., 2000, Uplift history of the Central and Northern Andes: A Review: GSA Bulletin, v. 112, p. 1091-1105.

Gustafson, L.B., and Hunt, J.P., 1975, The porphyry deposit at El Salvador, Chile: Economic Geology, v. 70, p. 857-912.

Harris, A.C., Kamenetsky, V.S., White, N.C., and Steele, D.A., 2004, Volatile phase separation in silicic magmas at Bajo de la Alumbrera porphyry Cu-Au deposit, NW Argentina: Resource Geology, v. 54, p. 341-356.

Kirkham, R.V., and Sinclair, W.D., 1985, Comb quartz layers in felsic intrusions and their relationships to porphyry deposits: in Recent Advances in the Geology of Granite-Related Mineral Deposits, Geological Survey of Canada, Contribution 34787, p. 50-71.

Lecumberri-Sanchez, P., Steele-MacInnis, M., and Bodnar, R.J., 2012, A numerical model to estimate trapping conditions of fluid inclusions that homogenise by halite disappearance: Geochimica et Cosmochimica Acta, v. 92, p. 14-22.

Lipten, E.J., and Smith, S.W., 2005, The geology of the Antamina copper-zinc deposit, Peru, South America; in T.M. Porter (ed.), Super Porphyry Copper & Gold Deposits: A Global Perspective, PGC Publishing, Adeliade, Australia, v. 1, p. 189-204.

Lowenstern, J.B., and Sinclair, W.D., 1996, Exsolved magmatic fluid and its role in the formation of comb-layered quartz at the Cretaceous Logtung W-Mo deposit, Yukon Territory, Canada: Transactions of the Royal Society of Edinburgh, Earth Sciences, v. 87, p. 291-303.

Maydagán, L., Franchini, M., Rusk, B., Lentz, D.R., McFarlane, C., Impiccini, A., Ríos, F.J., and Rey, R., 2015, Porphyry to epithermal transition in the Altar Cu-(Au-Mo) deposit, Argentina, studied by cathodoluminescence, LA-ICP-MS, and fluid inclusion analysis: Economic Geology, v. 110, p. 889-923.

Mavrogenes, J.A., and Bodnar, R.J., 1994, Hydrogen movement into and out of fluid inclusions in quartz – experimental evidence and geologic implications: Geochimica et Cosmochimica Acta, v. 58, p. 141-148.

Meinert, L.D., Dipple, G.M., and Nicolescu, S., 2005, World Skarn Deposits: Economic Geology 100th Anniversary Volume, Society of Economic Geologists, Littleton, Colorado, p.299-336.

Meinert, L.D., 1995, Compositional variation of igneous rocks associated with skarn deposits – chemical evidence for a genetic connection between petrogenesis and mineralisation: in Magmas, Fluids, and Ore Deposits, J.F.H. Thompson (ed.), Mineralogical Association of Canada Short Course Series, v. 23, Chapter 18, p. 401-418.

Ohloeft, G.R., and Johnson, G.R., 1984, Dry bulk densities for various rock types: in R.S. Carmichael (ed.), Handbook of Physical Properties of Rocks, v. 3, CRC Press, Inc.

Rusk, B.G., Reed, M.H., and Dilles, J.H., 2008, Fluid inclusion evidence for magmatic-hydrothermal fluid evolution in the porphyry copper-molybdenum deposit at Butte, Montana: Economic Geology, v. 103, p. 307-334.

Seal II, R.R., 2006, Sulfur isotope geochemistry of sulfide minerals: Reviews in Mineralogy & Geochemistry, v. 61, p. 633-677.

Shafaroudi, A.M., Karimpour, M.H., and Stern, C.R., 2015, The Khopik porphyry copper prospect, Lut Block, Eastern Iran: Geology, alteration and mineralisation, fluid inclusion, and oxygen isotope studies: Ore Geology Reviews, v. 65, p. 522-544.

Shannon, J.R., Walker, B.M., Carten, R.B., and Geraghty, E.P., 1982, Unidirectional solidification textures and their significance in determining relative ages of intrusions at the Henderson Mine, Colourado: Geology, v. 10., p. 293-297.

Shu, Q., Chang, Z., Hammerli, J., Lai, Y., Huizenga, J-M., 2017, Composition and evolution of fluids forming the Baiyinnuo'er Zn-Pb skarn deposit, northeastern China: insights from laser ablation ICP-MS study of fluid inclusions: Economic Geology, v. 112, p. 1441-1460.

Sillitoe, R.H., 2010, Porphyry copper systems: Economic Geology, v. 105, p. 3-41.

Spencer, E.T., Wilkinson, J.J., Creaser, R.A., and Seguel, J., 2015, The distribution and timing of molybdenite mineralisation at the El Teniente Cu-Mo porphyry deposit, Chile: Economic Geology, v. 110, p. 387-421.

Spencer, E.T., Wilkinson, J.J., Nolan, J., and Berry, A.J., 2015, The controls of post-entrapment diffusion on the solubility of chalcopyrite daughter crystals in natural quartz-hosted fluid inclusions: Chemical Geology, v. 412, p. 15-25.

Steele-MacInnis, M., Lecumberri-Sanchez, P., and Bodnar, R.J., 2012, HOKIEFLINCS-H2O-NACL: A Microsoft Excel spreadsheet for interpreting microthermometric data from fluid inclusions based on PVTX properties of H_2O-NaCl: Computers and Geoscience: http://dx.doi.org/10.1016/j.cageo.2012. 01.022.

Sverjensky, D.A., 1987, The role of migrating oil field brines in the formation of sediment-hosted Cu-rich deposits: Economic Geology, v. 82, p. 1130-1141.

Titley, S.R., 1982, Advances in the geology of the porphyry copper deposits: southwestern North America. University of Arizona Press, Tucson, AZ, 560 p.

Vry, V.H., 2010, Geological and hydrothermal fluid evolution at El Teniente, Chile: Unpublished PhD thesis, Imperial College London.

Williams-Jones, A.E., Samson, I.M., Ault, K.M., Gagnon, J.E., and Fryer, B.J., 2010, The genesis of distal zinc skarns: Evidence from the Mochito deposit, Honduras: Economic Geology, v. 105, p. 1411-1440.

Wood, S.A., and Samson, I M., 1987, Solubility of ore minerals and complexation of ore metals in hydrothermal solutions: Reviews in Economic Geology, v. 10, p. 33-80.

Yardley, B.W.D., 2005, Metal concentrations in crustal fluids and their relationship to ore formation: Economic Geology, 100th Anniversary Volume, p. 613-632.

Zhong, R., Brugger, J., Chen, Y., and Li, W., 2015, Contrasting regimes of Cu, Zn and Pb transport in ore-forming hydrothermal fluids: Chemical Geology, v. 395, p. 154-164.

4.8. Appendix

Table A4.1. Drill holes logged in this study.

Drill Hole	Depth from (m)	Depth to (m)	Total meters	Zone
A1008	0	325	325	Oscarina
A1378	0	100	100	Oscarina
A1579	256	327	71	Oscarina
A1600	0	642.6	642.6	Oscarina
A1868	0	421	421	Oscarina
A2213	0	68	68	Oscarina
A2623	0	251	251	Oscarina
A2629	174	278.4	104.4	Oscarina
A2669	0	915.5	915.5	Oscarina
A2810	0	300	300	Oscarina
A2820	0	260	260	Oscarina
A2835	0	250	250	Oscarina
A2890	0	500	500	Oscarina
A545	0	300	300	Oscarina
A136	0	240	240	Taco
A139	0	406	406	Taco
A1536	0	472	472	Taco
A1602	0	601.7	601.7	Taco
A1623	0	580	580	Taco
A1854	0	750	750	Taco
A2084	0	2000	2000	Between Taco and Bornita
A2491	0	2000	2000	Between Taco and Bornita
A1390	0	616	616	Bornita
A1391	0	574	574	Bornita
A1465	0	685	685	Bornita
A170	0	355	355	Bornita
A206	0	340.1	340.1	Bornita
A2887	467	564	97	SW of Bornita
A2887	1700	2006	306	SW of Bornita
A1168	34	88	54	Usupallares
A1902	0	800	800	Usupallares
A2589	246	366	120	Usupallares
31 Drill holes			15,505.30	meters

Chapter 5:
Summary and Conclusions

5.1. Summary of Key Findings

This chapter reviews the key findings of this study and summarizes the interpretations from previous chapters to provide a comprehensive model for formation of the Antamina deposit.

In Chapter 2, I investigated the geochemical changes that take place in the host rocks during skarn formation and ways to distinguish endoskarn and exoskarn. Key findings include:

- Traditional field logging criteria, such as skarn texture and garnet colour, are less reliable that geochemical composition in the recognition of massive endoskarn and exoskarn.
- Several pairs of discriminating elements were identified from the whole rock data set: the most effective discriminating pairs are TiO_2 vs. Y, HREE; Al_2O_3 vs. HREE, Y, Ni, and Sc, plus Al_2O_3 alone (endoskarns contain > 11.5 wt. % Al_2O_3, whereas exoskarns contain < 11.5 wt. %).
- After reclassifying the skarns based on their geochemical compositions, it is found that some "endoskarn" samples should be reclassified as exoskarn, which reduces the previous estimates of high volumes of endoskarn at Antamina.
- Skarn formation (both endoskarn and exoskarn) involves relatively little mass change even though there are significant geochemical compositional changes in the host rocks (i.e., marble, intrusions).

Chapter 3 provides a detailed intrusive sequence and new geochronological constraints on the timing of porphyry emplacement, skarn formation, and mineralisation at Antamina using the U-Pb zircon (LA-ICP-MS and CA-TIMS methods), $^{40}Ar/^{39}Ar$ biotite, and Re-Os molybdenite dating techniques. The intrusive sequence was based on cross-cutting relationships observed through the logging of approximately 15 km of diamond drill core plus highwall mapping. It was found that at least 11 porphyry phases comprise the Antamina porphyry complex (and the adjacent Oscarina and Condorcocha zones). The porphyries display a similar range of compositions ranging from trachyte to andesite porphyry and all of them contain 5-15 % biotite ± 1-5 % hornblende, indicating high magmatic water contents of at least 4 wt. % (Burnham, 1997). All phases, except for the Oscarina dykes, contain at least some quartz stockwork veins and secondary biotite alteration. Furthermore, all phases except for P2-Oscarina dykes, display adakite-like compositions, which provides additional confirmation of

high magmatic water contents. All early phases (P1) and some P2 phases (except for the Oscarina dykes) contain a central zone of potassic alteration; only P1-Taco and Usupallaresphases contain endoskarn along their margins in contact with exoskarn. Because the porphyries are so similar in composition and texture, the only sure way to tell them apart is by using cross-cutting relationships.

New U-Pb zircon ages reported in this study range from 10.95 ± 0.20 Ma (P1-Taco) to 10.24 ± 0.23 Ma (P3-Usupallares), which equates to approximately 1.1 million years of magmatic activity. Hydrothermal biotite results are within the analytical error of these U-Pb zircon ages. Molybdenite occurs in two stages and Re-Os ages of molybdenite range from 10.58 ± 0.07 to 10.39 ± 0.05 Ma (Stage I), and 9.99 ± 0.04 and 9.68 ± 0.05 Ma (Stage II). The youngest molybdenite age extends that duration of magmatic-hydrothermal activity at Antamina to 1.52 million years. The molybdenite Re-Os ages and biotite Ar-Ar ages are slightly younger than the zircon U-Pb ages at the sites where the various types of high-precision dating were done by at least 0.43 million years. This is likely because zircon crystalized at higher temperatures (closure temperature > 900°C; Cherniak and Watson, 2001) early in the history of the melt evolution, before water exsolved from the melt, whereas the potassic alteration and molybdenite formation occurred later after the magmatic hydrothermal fluids exsolved from the melt and escaped from the magma chamber. The time difference is short (e.g., > 100 Ma) and is only detectable because of the young age of these rocks and the high precision of the dating method (e.g., CA-TIMS, Re-Os) used in this study. The dating methods have relatively consistent relative errors regardless of the absolute age. For example, at 0.5% relative error, the uncertainty for a 1000 Ma sample is ± 5 Ma, whereas for a 10 Ma sample the uncertainty is only ± 0.05 Ma (or 50,000 years).

Both the zircon crystallization ages and the alteration-mineralisation ages have shown that there are 3 intrusive centres in the Antamina porphyry complex, namely the Taco Zone in the NE and the main body, the smaller Usupallares Zone in the SW, and the Oscarina Zone dykes overprinting the Taco zone at the NE corner. There is another geographically separate intrusive centre, the Condorcocha Zone, ~1 km NW of the Taco Zone of the APC. The mineralisation is mainly related to hydrothermal activity associated with the Taco and Usupallares intrusions.

The dating results show a clear trend of younging towards the SW in both the zircon crysallization ages of the intrusions, and alteration-mineralisation ages. From northeast to southwest along the axis of the deposit, zircon crystallisation ages range from 10.95 ± 0.20 to 10.24 ± 0.23 Ma, Stage I molybdenite ages range from 10.58 ± 0.07 to 10.39 ± 0.05 Ma, and Stage II molybdenite ages range from 9.99 ± 0.04 to 9.68 ± 0.05 Ma. There is also a subtle younging trend with increasing depth at Usupallares. There are not enough data at other locations but it is suspected that the same trend exists throughout the deposit.

At each zone the earliest intrusions (P1s) display porphyry-style stockworks that transition outwards to endoskarns at the marginal zones of the intrusions; these intrusions are surrounded by exoskarns in the wallrocks. The later intrusions (P2-P3) display varying intensities of quartz veining/stockworking, but no endoskarn alteration. Because the late intrusions were still rich in fluids (as evidenced by the quartz stockworks and the K-alteration), these intrusions enhanced the size and metal endowment of the Antamina system by contributing more mineralisation to the existing skarns in the form of cross-cutting quartz-sulphide veins. It is also possible that these same fluids escaped through existing skarns to form new exoskarn along the marble front of the system, thereby coalescing late exoskarns with early exoskarns and enhancing the overall size and continuity of the skarn body.

Chapter 4 shows that the alteration and mineralisation patterns at Antamina are centred on the Taco-Bornita zone and that patterns in mineralogy and mineral composition change systematically from proximal to distal regions of the deposit. Key proximal to distal patterns include the change in garnet colour from pink to red to brown to green; a slight decrease in the garnet to clinopyroxene ratio (most notable in drill holes that exceed 1,500 m depth and in the Usupallares zone); and increasing Fe contents of both clinopyroxene and garnet, for which mineral colour (lighter to darker) is an rough proxy. Bornite is found exclusively in this zone, as well intense potassic alteration; these are indicative of the highest temperature zone in the deposit. Outward from this high-temperature centre, the metal distribution shows a trend towards lower temperature/higher solubility metals (from Mo-Cu ± Ag-Bi to Zn-Pb ± Ag) precipitated in the distal reaches of the deposit. Fluid inclusion results from a UST sample in the Taco zone indicate that the deposit formed between~3.5 to 4 km depth. Miocene uplift estimates of 3.5 km, coupled with glacial erosion on the order of 500 m, place the deposit at the present-day surface.

5.2. How did Antamina become a giant ore deposit?

Several geological factors contributed to the location and size of the Antamina deposit. The individual factors are not particularly unusual, however it is the precise combination of these factors in space and time that had an optimising effect on the ore forming process at Antamina. Key factors include:

- Emplacement of multiple porphyries, all with high magmatic water contents.
- A locally abundant supply of reactive carbonate wall rocks
- Ideal depth of emplacement (not too shallow, not too deep)
- A strong structural control imposed by the Valley Fault System on porphyry emplacement and hydrothermal fluid flow
- A favourable uplift and erosion history

The southwest-trending younging of porphyries emplaced along the Valley Fault, coupled with the availability of reactive carbonate rocks along this trend facilitated the lateral continunity of skarns and mineralisation. The Valley Fault system served to focus porphyry emplacement and hydrothermal fluids to concentrate ore grades in a relatively localised area. The subvertical structure and dilation of the Valley Fault, coupled with an increase in marble at depth (stratigraphic change from the Celendín to Jumasha formation at depth) may have influenced the vertical extent of the deposit, which exceeds 2 km in the Taco zone.

Multiple fertile intrusions were emplaced along a narrow structural corridor that focussed hydrothermal fluids and increased the reaction surface area between fluids and carbonate rocks, thereby promoting extensive skarn formation. In contrast, if the intrusions were emplaced in a nested geometry, the skarn-forming potential would be limited by the reduced surface area in contact with carbonate rocks. In the context of regional uplift and erosion, deeper emplacement would change the economics of mining, as more waste would need to be stripped to access the ores. Shallower emplacement coupled with uplift and erosion would have removed some of the highest ore grades. The formation of the giant Antamina deposit required all of these factors to operate in tandem at precisely the right time and location.

5.3. References

Burnham, C.W., 1997, Magmas and hydrothermal fluids, in H.L.Barnes (ed.), Geochemistry of Hydrothermal Ore Deposits, 3rd edition, John Wiley & Sons, p. 63-123.

Cherniak, D.J., and Watson, E.B., 2001, Pb diffusion in zircon: Chemical Geology, v. 172, p. 5-24.